



**OBSERVATION AND BRANCHING FRACTION  
MEASUREMENT OF  $\Xi^0 \rightarrow \Sigma^+ e^- \bar{\nu}_e$  at KTeV/E799-II,  
FERMILAB**

By

**ASHKAN ALAVI-HARATI**

A dissertation submitted in partial fulfillment of the  
requirements for the degree of

Doctor of Philosophy

(Physics)

at the

**UNIVERSITY OF WISCONSIN-MADISON**

1999

## Acknowledgments

I would like to express my deepest gratitude to my major advisor Professor Albert Erwin for his continued guidance and advice during all of the years of my research, and to my wonderful friend Theodoros Alexopoulos who taught me high energy physics, data analysis, computers, and most importantly work ethics. Theo helped me through all aspects of my work in the past three years. Life in Erwin's lab was never boring with Albert, Theo and Professor Murray Thompson around. I enjoyed every moment of their company in and out of the lab. They also provided valuable comments on this thesis.

Obviously, this work could not have been done without the efforts of many people. I am indebted to all of the KTeV collaborators and to all of the Fermilab beam division staff for setting up and performing this outstanding experiment. I would like to thank my friends A. Lath, R. Kessler, R.J. Tesarek, S. Bright and J. Graham for helping me on my chamber calibration duties. Special thanks goes to the members of the hyperon group: S. Bright, D.A. Jensen, E. Monnier, E.J. Ramberg, N. Solomey, E.C. Swallow and R. Winston. They recommended a thesis topic that turned out to be very exciting and they also helped me a lot through my analysis. I am grateful to Professor Swallow for going over parts of this thesis and making helpful comments.

It was a great pleasure to work with a brilliant group of young postdocs and grads; many of whom also shared meals, played Volleyball and spent other extra curricular time with me: S. Averitte, L. Bellantoni, A. Bellavance, J. Belz, R. Ben-David, C. Bown, S. Bright, G. Graham, K. Hagan, E. Halkiadakis, K. Hanagaki, V. Jejer, J. Jennings, A. Ledovskoy, P. Mikelsons, H. Nguyen, V. Prasad, C. Qiao, B. Quinn, M. Sadamoto, K. Senyo, P. Shanahan, P.S. Shawhan, S.A. Taegar, R.J. Tesarek, A. Tripathi and E.D. Zimmerman.

On a personal note I want to thank several people: my friends who contributed to my accomplishments with their advice and encouragement: Theo and his wife Vasso, Massoud Vakili, H.R. Farshi, N. Tahvildar-Zadeh M. Borumand (thanks for the Feynman Diagrams Majid), J. Shafii, L. Koch, L. Far, S. and M. Zaini, S. Botshekan and F. Tannazi; my aunt and my cousins who never let me feel alone during these seven years of living far from my beloved family; my fellow housemates at the “Knapp House” whose friendship and kindness made the otherwise frustrating months of thesis writing full of joy and fun; and the hardworking staff at the physics department B. Schutz, J. Buehlman, A. Lefkow and S. Kuretsky for making things really work for me.

Finally, my greatest thanks goes to my uncle and aunt, Dr. Daryush and Parvin Nowrasteh. I would not have made it to this point without their generous help and support. I don’t know how to express my appreciation to my parents Zohreh and Zabihollah and to my brothers Khashayar and Mani. Thanks for your understanding and letting me pursue my selfish dreams. I dedicate this thesis to you.

# Contents

<b>Abstract</b>	<b>xxiv</b>
<b>1 Introduction</b>	<b>1</b>
1.1 CP Violation in the Kaon System . . . . .	1
1.1.1 CP Eigenstates in the Neutral Kaon System . . . . .	4
1.1.2 Indirect CP Violation . . . . .	5
1.1.3 Direct CP Violation . . . . .	8
1.2 Rare Decay of Neutral Kaons . . . . .	10
1.3 Neutral Hyperon Physics at KTeV . . . . .	14
1.3.1 Hyperon Semi-Leptonic Decays . . . . .	14
1.3.2 Hyperon Non-Leptonic Decays . . . . .	22
1.3.3 Weak Radiative Hyperon Decays . . . . .	25
1.3.4 Three Body and other Radiative Hyperon Decays . . . . .	26
<b>2 The Beam and Detector</b>	<b>31</b>
2.1 The Beamline . . . . .	31
2.2 The E799 Detector . . . . .	36
2.3 The Spectrometer . . . . .	40
2.4 The Transition Radiation Detectors . . . . .	43

2.5	The Trigger Hodoscopes . . . . .	47
2.6	The Electromagnetic Calorimeter . . . . .	48
2.7	The Photon Veto System . . . . .	52
2.8	The Hole Counters . . . . .	56
2.9	The Hadron Anti and Muon Counters . . . . .	56
<b>3</b>	<b>Triggering and the Run</b>	<b>61</b>
3.1	Level 1 Trigger . . . . .	61
3.1.1	Drift Chamber Stretcher/OR . . . . .	62
3.1.2	Calorimeter Total Energy . . . . .	68
3.2	Level 2 Trigger . . . . .	68
3.2.1	The Stiff Track Trigger . . . . .	69
3.2.2	Hardware Cluster Counting . . . . .	71
3.3	Level 3 Trigger . . . . .	73
3.4	Hyperon Trigger . . . . .	73
3.4.1	Trigger Requirements . . . . .	73
3.5	The Run . . . . .	76
3.5.1	E799 Physics Run . . . . .	77
3.5.2	Special Runs . . . . .	77
<b>4</b>	<b>Data Acquisition</b>	<b>79</b>
4.1	The Data Acquisition System . . . . .	79
4.2	The Slow Control System . . . . .	83
4.2.1	Architecture of the KTeV-SC . . . . .	84

4.2.2	KTeV-SC Detector Subsystems . . . . .	91
4.2.3	The KTeV-CS Hardware . . . . .	99
4.2.4	The KTeV-SC Software . . . . .	106
4.2.5	Performance of the KTeV-CS . . . . .	111
<b>5</b>	<b>Event Reconstruction and Detector Calibration</b>	<b>117</b>
5.1	Track Reconstruction . . . . .	117
5.1.1	Hit pairs . . . . .	118
5.1.2	Y Tracks . . . . .	119
5.1.3	X Tracks . . . . .	120
5.1.4	Vertexing . . . . .	120
5.1.5	Track-Cluster Matching . . . . .	121
5.2	Cluster Reconstruction in the Calorimeter . . . . .	122
5.2.1	Hardware Clustering . . . . .	122
5.2.2	Software Clustering . . . . .	123
5.2.3	Energy and Position Measurements . . . . .	123
5.3	Drift Chambers Time-to-Distance Calibration . . . . .	124
5.3.1	Timing Offsets . . . . .	124
5.3.2	Time-to-Distance Relations . . . . .	126
5.3.3	Chamber Resolution . . . . .	130
5.3.4	Chamber Wire-by-Wire Efficiency . . . . .	134
5.4	Alignment of the Drift Chambers . . . . .	136
5.4.1	Relative Alignment of the Drift Chambers . . . . .	138
5.4.2	Corkscrew Rotations . . . . .	138

5.4.3	Global Alignment of the Drift Chambers . . . . .	139
<b>6</b>	<b>Data Analysis and Event Selection</b>	<b>142</b>
6.1	Data Selection . . . . .	142
6.1.1	The $\Xi^0 \rightarrow \Sigma^+ e^- \bar{\nu}_e$ Event Selection . . . . .	143
6.1.2	The $\Xi^0 \rightarrow \Lambda \pi^0$ Event Selection . . . . .	160
6.2	The $\Xi^0$ Beta Decay Events . . . . .	164
6.3	Background Studies . . . . .	167
6.3.1	$K_L^0 \rightarrow \pi^0 \pi^+ \pi^-$ . . . . .	175
6.3.2	$K_L^0 \rightarrow \pi^+ e^- \bar{\nu}_e$ . . . . .	175
6.3.3	$K_L^0 \rightarrow \pi^+ e^- \bar{\nu}_e \gamma$ . . . . .	176
6.3.4	$K_L^0 \rightarrow \pi^0 \pi^+ e^- \bar{\nu}_e$ . . . . .	177
6.3.5	$\Xi^0 \rightarrow \Lambda \pi^0$ followed by $\Lambda \rightarrow p \pi^-$ . . . . .	177
6.3.6	$\Xi^0 \rightarrow \Lambda \pi^0$ followed by $\Lambda \rightarrow p e^- \bar{\nu}_e$ . . . . .	178
6.4	Measurement of the Branching Ratio . . . . .	181
6.5	$\Lambda \rightarrow p e^- \bar{\nu}_e$ Decay, An alternative Normalization Mode . . . . .	183
6.5.1	The Reconstruction Method . . . . .	184
6.5.2	The Event Selection . . . . .	185
<b>7</b>	<b>The Monte Carlo Simulation</b>	<b>188</b>
7.1	Event Generation . . . . .	188
7.1.1	Kaon Production . . . . .	189
7.1.2	Hyperon Production . . . . .	190
7.2	Hyperon Decays . . . . .	192

7.2.1	Distribution of the Decay Products . . . . .	193
7.2.2	Polarization of the Decay Products . . . . .	194
7.3	Detector Response . . . . .	195
7.3.1	Drift Chambers . . . . .	195
7.3.2	The Trigger Hodoscopes . . . . .	196
7.3.3	CsI Calorimeter . . . . .	197
7.4	Accidental Activity . . . . .	199
<b>8</b>	<b>Systematics</b>	<b>200</b>
8.1	Hole Counters . . . . .	201
8.2	Hadron Anti . . . . .	201
8.3	Total Energy in the Calorimeter . . . . .	202
8.4	Hardware Clustering . . . . .	202
8.5	Drift Chamber Fast OR . . . . .	204
8.6	Cut Variation Studies . . . . .	208
8.7	Background Subtraction and Acceptance Correction Uncertainty . .	209
8.8	Summary of the systamatics . . . . .	212
<b>9</b>	<b>Conclusion</b>	<b>216</b>
	<b>First BR Measurement of the Decay <math>\Xi^0 \rightarrow \Sigma^+ e^- \bar{\nu}_e</math></b>	<b>218</b>
	<b>Kinematics With A Missing Particle</b>	<b>222</b>
	<b>Feynam Diagrams of Non-Leptonic and Radiative Hyperon De-</b>	
	<b>cays</b>	<b>225</b>



<b>Acronyms of Commonly Used Terms in Detector Control Systems</b>	<b>229</b>
--	------------

<b>Bibliography</b>	<b>235</b>
---------------------	------------

## List of Tables

1.1	Rare decays of $K_L$ at KTeV. . . . .	11
1.2	Rare decay of $K_L$ with a direct CP violation component at KTeV. .	12
1.3	Rare decays of $\pi^0$ at KTeV. . . . .	12
1.4	Neutral hyperon program at KTeV. $N_{event}$ is the number of events observed in the previous experiments and $N_{KTeV}$ is the number of candidates at KTeV: ? means the decay hasn't been studied yet. .	15
2.1	KTeV primary beam specification . . . . .	32
2.2	Positions and Dimensions of the detector elements. The positions are given at the front face of the detector with respect to the target.	39
2.3	Drift chamber sizes, measured in wires per sense plane. . . . .	43
2.4	Positions and Dimensions of the photon veto elements. The posi- tions are given at the front face of the detector with respect to the target. . . . .	53
4.1	RS-232 signals and their functions for the PLC. . . . .	105

6.1	Effect of each cut on the pre-selected data if all the others have been fulfilled. A large difference between the data and the simulation is indicative of the cut being mostly effective on the background and not on the signal events. Some of the cuts seem to be ineffective because of their earlier pre-selection. . . . .	161
7.1	Values of parameters describing the kaon production spectrum [80].	189
7.2	Coefficients in empirical fits for hyperon spectrum. . . . .	191
8.1	Summary of the systematic errors for the $\Xi^0 \rightarrow \Sigma^+ e^- \bar{\nu}_e$ BR measurement. . . . .	212
8.2	Branching ratio for various separated data samples. . . . .	215

## List of Figures

1.1	$K^0 \Leftrightarrow \bar{K}^0$ , $\Delta S = 2$ Box diagram in the Standard model. . . . .	6
1.2	(a) Tree level diagram contribution to $K_L \rightarrow \pi^0\pi^0$ . (b) Penguin diagram contribution to $K_L \rightarrow \pi^0\pi^0$ . . . . .	8
1.3	Sensitivity of KTeV to the rare decay of Kaons. . . . .	13
1.4	Feynman diagram for Cascade Beta Decay, $\Xi^0 \rightarrow \Sigma^+ e^- \bar{\nu}_e$ . . . . .	16
1.5	The radiative decay of $\Xi^0 \rightarrow \Sigma^0 \gamma$ for the E799-II summer run. . . . .	27
1.6	The radiative decay of $\Xi^0 \rightarrow \Lambda \gamma$ for the E799-II winter run. . . . .	28
1.7	The 3-body radiative decay of $\Lambda \rightarrow p \pi^- \gamma$ . Data corresponds to 5% of the E799-II winter run. . . . .	30
2.1	Schematic plan view of the collimation and sweeping system. . . . .	33
2.2	The momentum spectrum of $\Xi^0$ particle. Only high momentum hy- perons reach the KTeV detector. The kaon spectrum peaks at about 40 GeV/c. . . . .	35
2.3	Schematic drawing of KTeV detector (E799 configuration). The scale in the $y$ direction is expanded for clarity. . . . .	37
2.4	Three dimensional view of KTeV/E799 detector. . . . .	38
2.5	The drift chamber sense and field wire geometry, viewed from the above, along the vertical $x$ -sensing wires. . . . .	41

2.6	The schematic layout of the TRD detector. . . . .	45
2.7	Schematic drawing of $V$ and $V'$ bank front view. . . . .	47
2.8	Beam view of the KTeV CsI calorimeter array. . . . .	49
2.9	$E/p$ for electron in $K_{e3}^0$ 's, where $E$ is the energy measured at the calorimeter, and $p$ is the momentum measured by the spectrometer. . . . .	51
2.10	The calorimeter's intrinsic energy resolution measured in $K_{e3}^0$ events as a function of electron momentum. . . . .	51
2.11	A typical RC viewed from upstream, located inside the vacuum region. The RC's dimensions are shown in Table 2.4. . . . .	54
2.12	SA4 viewed from upstream. SA's and CIA had different dimensions as shown in Table 2.4. . . . .	54
2.13	The Collar Anti located just upstream of the CsI calorimeter. . . . .	55
2.14	The HA hodoscope composed of 28 scintillation counters. . . . .	58
2.15	The Muon counters. . . . .	60
3.1	Stretcher circuit. . . . .	64
3.2	Stretcher/OR logic. The hatched area shows the paddles used for the hyperon trigger. . . . .	66
3.3	Hit counting current summer circuit. . . . .	67

3.4	Diagram of STT. In the right beam hole we have a track with a sufficiently small change in slope passing through the instrumented region in all 4 chambers, so the STT result (-4) for the right side is TRUE. On the left side, the track does not pass through the instrumented region in all 4 chambers, so the STT result (10) for the left side is FALSE. Thus the event is accepted. . . . .	70
3.5	All possible hit patterns for a $2 \times 2$ array of blocks. The value assigned to each group of patterns is shown to the right. . . . .	71
4.1	Block diagram of the KTeV DAQ. . . . .	80
4.2	The overall basic KTeV Slow-Control building blocks. . . . .	85
4.3	KTeV-Slow Control software architecture. . . . .	89
4.4	Overall structure of the KTeV-SC system with the main hardware monitor/control components shown. . . . .	92
4.5	Low-Voltage Multiplexer chip. . . . .	99
4.6	Low-Voltage Multiplexer box. It uses 256 differential input with 32 differential output channels. . . . .	100
4.7	MUX unit, including a Joerger-32 ADC, MUX box, resistor board, and transition boards. . . . .	101
4.8	LVTB, top view, and stereo view. . . . .	102
4.9	KTeV RS232 communication. Here, shown only the KTeV processors that use the RS-232 communication. . . . .	104

4.10 Overall software structure of the KTeV-SC system. Also, shown are the different tasks that perform the monitoring/controlling of the KTeV detector. . . . .	107
4.11 KTeV-SC Database detailed architecture. . . . .	109
4.12 Part of the SCC database structure. . . . .	110
4.13 The main KTeV-SC screen, presenting the status of various components of the KTeV experiment. . . . .	113
4.14 The LeCroy 1440 HV status screen. . . . .	114
4.15 The CAEN HV status screen includes the DC and TRD system. . . . .	115
4.16 The PLC monitor status screen. . . . .	116
5.1 The raw distribution of TDC values for all wires in plane 1. The sharp edge corresponds to charged particles passing very close to a sense wire at high TDC values. The trigger provided a common stop for the TDC's. . . . .	127
5.2 Average RF-Level 1 timing as a function of Run for E799 summer data. The dashed vertical lines show runs for which T(0) calibrations were performed. . . . .	128
5.3 A sample Time-to-Distance Relation for plane 1. TDC counts are subtracted from a common offset (700 counts) to invert from common-stop mode. The relation is quite linear between 20 and 230 counts with a slope of about $50\mu\text{m}/\text{nsec}$ and asymptotically approaches the cell size of 6.35 mm. . . . .	131

5.4	A typical Sum-of-Distances distribution in Chamber 1, X view. The mean of the distribution should be the constructed cell size of 6.35 mm and the width is proportional to the resolution. . . . .	132
5.5	The history of the Chambers resolution for the winter run as a function of the run numbers being used for the x-t calibration. The top plot shows the resolution for the $x$ views and the bottom plot for the $y$ view. . . . .	133
5.6	The history of the Chambers resolution for the summer run as a function of the run numbers being used for the x-t calibration. The top plot shows the resolution for the $x$ views and the bottom plot for the $y$ view. . . . .	135
5.7	The wire-by-wire efficiency for one summer run in the upstream X and Y planes. . . . .	137
5.8	Corkscrew rotation as seen in Chamber 1 and 2, if Chamber 4 is rotated with respect to Chamber 1. . . . .	140
6.1	The geometry of the decay $\Xi^0 \rightarrow \Sigma^+ e^- \bar{\nu}_e$ where $\Sigma^+ \rightarrow p\pi^0$ and $\pi^0 \rightarrow \gamma\gamma$ . . . . .	144



- 6.2 Distribution of the: (a) Ratio of the energy of the electron as measured by the calorimeter to the momentum of the electron as measured by the charged spectrometer. (b) Momentum of the positive charged track, assumed to be a proton. (c) Momentum of the negative charged track, assumed to be an electron. (d) Ratio of momentum of the positive track to the momentum of the negative track. The light grey shows the accepted events after applying the cuts and the dark grey is the rejected events. . . . . 150
- 6.3 Distribution of the: (a) Square of the transverse momentum of the charged vertex. (b) Distance between the two neutral clusters (photons) in the calorimeter. (c) Distance of closest approach between the  $\Sigma^+$  reconstructed track and the electron track. (d) Separation distance between the center of the electron cluster and the track associated with that at CsI. The light grey shows the accepted events after applying the cuts and the dark grey is the rejected events. . . 151
- 6.4 Distribution of the: (a) Reconstructed  $p\pi^-\pi^0$  principal decay mass. (b) Reconstructed mass of  $\Sigma^+e^-$ . (c) Reconstructed momentum of  $\Sigma^+e^-$ . (d) Reconstructed  $\Sigma^+e^-$  lifetime in units of  $\Xi^0$  lifetime. The light grey shows the accepted events after applying the cuts and the dark grey is the rejected events. . . . . 152

- 6.5  $\Xi^0 \rightarrow \Sigma^+ e^- \bar{\nu}_e$  distribution of the: (a) longitudinal position of  $\Xi^0$  vertex inside the decay volume. (b) Longitudinal distance between the  $\Sigma^+$  and  $\Xi^0$  vertices. (c,d) Transverse position of  $\Xi^0$  beta vertex. The light grey shows the accepted events after applying the cuts and the dark grey is the rejected events. . . . . 153
- 6.6  $\Xi^0 \rightarrow \Sigma^+ e^- \bar{\nu}_e$  distribution of the reconstructed transverse momentum versus the reconstructed mass of  $\Sigma^+ e^-$ . The events above the line  $1.34 \Leftrightarrow M_{\Sigma^+ e^-} = p_t$  are rejected from data. . . . . 154
- 6.7 Monte Carlo simulation of the: (a) Ratio of the energy of the electron as measured by the calorimeter to the momentum of the electron as measured by the charged spectrometer. (b) Momentum of the positive charged track, assumed to be a proton. (c) Momentum of the negative charged track, assumed to be an electron. (d) Ratio of momentum of the positive track to the momentum of the negative track. The light grey shows the accepted events after applying the cuts and the dark grey is the rejected events. . . . . 155

- 6.8 Monte Carlo simulation of the: (a) Square of the transverse momentum of the charged vertex. (b) Distance between the two neutral clusters (photons) in the calorimeter. (c) Distance of closest approach between the  $\Sigma^+$  reconstructed track and the electron track. (d) Separation distance between the center of the electron cluster and the track associated with that at CsI. The light grey shows the accepted events after applying the cuts and the dark grey is the rejected events. . . . . 156
- 6.9 Monte Carlo simulation of the: (a) Reconstructed  $p\pi^-\pi^0$  principal decay mass. (b) Reconstructed mass of  $\Sigma^+e^-$ . (c) Reconstructed momentum of  $\Sigma^+e^-$ . (d) Reconstructed  $\Sigma^+e^-$  lifetime in units of  $\Xi^0$  lifetime. The light grey shows the accepted events after applying the cuts and the dark grey is the rejected events. . . . . 157
- 6.10 Monte Carlo simulation of the: (a) longitudinal position of  $\Xi^0$  vertex inside the decay volume. (b) Longitudinal distance between the  $\Sigma^+$  and  $\Xi^0$  vertices. (c,d) Transverse position of  $\Xi^0$  beta vertex. The light grey shows the accepted events after applying the cuts and the dark grey is the rejected events. . . . . 158
- 6.11 Monte Carlo simulation of the reconstructed transverse momentum versus the reconstructed mass of  $\Sigma^+e^-$ . The events above the line  $1.34 \Leftrightarrow M_{\Sigma^+e^-} = p_t$  rejected from data. . . . . 159

- 6.12 The  $\Sigma^+$  mass peak with all the cuts applied except one.  $z_{\Sigma^+} \Leftrightarrow z_{\Xi^0}$ , reconstructed transverse momentum of  $e^-\Sigma^+$ ,  $p\pi^-\pi^0$  mass and the reconstructed mass of  $e^-\Sigma^+$  are the strongest cuts as shown in table 6.1. . . . . 162
- 6.13 The geometry of the dominant decay of  $\Xi^0 \rightarrow \Lambda\pi^0$  where  $\Lambda \rightarrow p\pi^-$  and  $\pi^0 \rightarrow \gamma\gamma$ . This decay was used as the normalization mode. . . 163
- 6.14 Distribution of the reconstructed  $\Xi^0$  mass from  $\Xi^0 \rightarrow \Lambda\pi^0$  candidates. 165
- 6.15  $\Xi^0 \rightarrow \Lambda\pi^0$  decay's distribution of the: (a) Longitudinal distance between the  $\Lambda$  and  $\Xi^0$  vertices. (b) Square of the transverse momentum of the charged vertex. (c) Ratio of energy of the  $\pi^-$  as measured by the calorimeter to the momentum of the  $\pi^-$  as measured by the charged spectrometer. (d) Reconstructed  $p\pi^-$  mass. Dots are data and the histogram is MC in each plot. . . . . 166
- 6.16 Reconstructed  $p\pi^0$  mass distribution for the events selected for the  $\Xi^0$  beta decay branching ratio measurement. The parameters of a Gaussian fit on the data distribution are given. . . . . 168
- 6.17 Proper time distribution of  $\Sigma^+$  from the  $\Xi^0$  beta decay event candidates, in  $\Sigma^+$  lifetime units. The plotted points are data (statistical errors only). The histogram is the corresponding MC distribution normalized to the number of data events. No acceptance correction has been applied. The results of an exponential fit done on the data and on the simulation are shown. . . . . 169

- 6.18  $\Xi^0 \rightarrow \Sigma^+ e^- \bar{\nu}_e$  distribution of the: (a) Ratio of the energy of the electron as measured by the calorimeter to the momentum of the electron as measured by the charged spectrometer. (b) Momentum of the positive charged track, assumed to be a proton. (c) Momentum of the negative charged track, assumed to be an electron. (d) Ratio of momentum of the positive track to the momentum of the negative track. Dots are data and the histogram is MC in each plot. 170
- 6.19 Distribution of the: (a) Total energy of the cluster deposited in the CsI calorimeter. (b) Distance between the two neutral clusters (photons) in the calorimeter. (c) Distance of closest approach between the  $\Sigma^+$  reconstructed track and the electron track. (d) Separation distance between the center of the electron cluster and the track associated with that at CsI. Dots are data and the histogram is MC in each plot. . . . . 171
- 6.20  $\Xi^0 \rightarrow \Sigma^+ e^- \bar{\nu}_e$  distribution of the: (a) Reconstructed  $p\pi^-\pi^0$  principal decay mass. (b) Reconstructed mass of  $\Sigma^+ e^-$  beta decay. (c) Reconstructed momentum of  $\Sigma^+ e^-$  beta decay. (d) Reconstructed  $\Sigma^+ e^-$  lifetime in units of  $\Xi^0$  lifetime. Dots are data and the histogram is MC in each plot. . . . . 172
- 6.21 Distribution of the: (a) longitudinal position of  $\Xi^0$  vertex inside the decay volume. (b) Longitudinal distance between the  $\Sigma^+$  and  $\Xi^0$  vertices. (c,d) Transverse position of  $\Xi^0$  beta vertex. Dots are data and the histogram is MC in each plot. . . . . 173

6.22	Distribution of the: (a) Square of the transverse momentum of the charged vertex. (b) Square of the transverse momentum of the reconstructed $\Xi^0$ beta vertex. (c,d) Projection of the 2-dimensional distribution of transverse momentum vs reconstructed mass of $\Sigma^+e^-$ on the mass and transverse momentum axis respectively. Dots are data and the histogram is MC in each plot. . . . .	174
6.23	The geometry of the decays $K_L \rightarrow \pi^+\pi^-\pi^0$ and $K_L^0 \rightarrow \pi^+e^-\nu_e\gamma$ (+ an accidental photon). . . . .	176
6.24	Monte Carlo simulation of $\Xi^0 \rightarrow \Lambda\pi^0$ for: (a) Reconstructed $\Xi^0$ mass. (b) Reconstructed mass of $\Sigma^+e^-$ . (c) Longitudinal distance between the $\Sigma^+$ and $\Xi^0$ vertices. (d) Square of the transverse momentum of the charged vertex. The light grey shows the accepted events after applying the cuts and the dark grey is the rejected events. . . . .	179
6.25	Reconstructed $p\pi^0$ mass distribution for the $\Xi^0$ beta events. The MC simulated background normalized to the flux is shown in dark grey. . . . .	180
6.26	The geometry of the decay $\Xi^0 \rightarrow \Lambda\pi^0$ where $\Lambda \rightarrow pe^-\bar{\nu}_e$ . . . . .	185
6.27	The reconstructed mass of $\Xi^0$ for the decay $\Xi^0 \rightarrow \Lambda\pi^0$ where $\Lambda \rightarrow pe^-\bar{\nu}_e$ and $\pi^0 \rightarrow \gamma\gamma$ . . . . .	186
8.1	Energy total and HCC efficiency . . . . .	203

- 8.2 Drift chamber FAST-OR efficiency. Upper plots: hit wire distribution for track traveling down the left (west) and right (east) holes. Shaded, the corresponding distribution is shown for the tracks with no FAST-OR trigger latch bits set. Bottom plots: Same distribution for the OR of the holes and calculated inefficiencies in % from these previous three plots. . . . . 206
- 8.3 A DC signal from a real track is in coincidence with an RF signal. The top plot shows a track passing very close to a sense wire in the  $X$  plane of a chamber causing an early hit. The same track would be close to the edge of a cell in the  $X'$  plane causing a late hit. A noisy wire can set the FAST-OR on too early making the real hit miss the RF bucket. FAST-OR stretches a signal to about 90 nsec to cover any hits in a DC cell. . . . . 207
- 8.4 The distribution of branching ratio for 100 different sets of cuts applied on the data. The peak is around the measured branching ratio for the nominal set of cuts and the width of the gaussian fit is a measure of the systematic error. . . . . 210
- 8.5 The distribution of branching ratio for 100 different sets of cuts applied on a Monte Carlo simulated sample. The width of the gaussian fit is a measure of the Monte Carlo imperfection. . . . . 211
- 8.6 The measured branching ratio of  $\Xi^0 \rightarrow \Sigma^+ e^- \bar{\nu}_e$  decay as a function of time for 14 different run-ranges. The error bars are statistical only. The first point is the measured value for the full sample. . . . 214

A.1	Reconstructed $p\pi^0$ mass distribution for the events selected for the first $\Xi^0$ beta decay branching ratio measurement in the winter data.	
	The parameters of a Gaussian fit on the data distribution are given.	219
A.2	Distribution of the reconstructed $\Xi^0$ mass from $\Xi^0 \rightarrow \Lambda^0\pi^0$ candidates.	220
C.1	$\Xi^0 \rightarrow \Lambda\pi^0$ . . . . .	226
C.2	$\Lambda \rightarrow p\pi^-$ . . . . .	227
C.3	$\Xi^0 \rightarrow \Lambda\gamma$ and $\Xi^0 \rightarrow \Sigma^0\gamma$ . . . . .	228



### Abstract

We present a branching fraction measurement of Cascade Beta Decay,  $\Xi^0 \rightarrow \Sigma^+ e^- \bar{\nu}_e$  based on the E799-II experiment data-taking in the Summer of 1997 at KTeV, Fermilab. We used the principal decay of  $\Xi^0 \rightarrow \Lambda \pi^0$  where  $\Lambda$  decays to a proton and a  $\pi^-$  as the flux normalization mode. This is the first observation of this interesting decay mode which under d and s quark interchange, is the direct analogue of the well measured Neutron Beta Decay,  $n \rightarrow p e^- \bar{\nu}_e$ . For 626 events with an expected  $45 \pm 18$  background events, we measured the branching fraction of  $\Xi^0 \rightarrow \Sigma^+ e^- \bar{\nu}_e$  decay to be  $(2.60 \pm 0.11_{(stat.)} \pm 0.16_{(sys.)}) \times 10^{-4}$  in good agreement with predictions based on SU(3) flavor symmetry models.

## Chapter 1

### Introduction

Though the neutral kaon system has been studied for many years, it remains a rich hunting ground for possible new discoveries. The KTeV experiment at Fermilab [1] was armed with an intense source of high-energy kaon decays together with a state-of-the-art detector. Its two main objectives were to measure the value of the  $CP$ -violation parameter  $Re(\epsilon'/\epsilon)$  with a very high precision of order  $1 \times 10^{-4}$ , and to study rare decays of  $K_L$  and  $\pi^0$  particles. The neutral beam however, contained a copious amount of neutral hyperons,  $\Lambda$  and  $\Xi^0$  which made KTeV a unique facility to study the rare decay of these particles as well.

This thesis will focus on the hyperon physics at KTeV, especially the beta decay of  $\Xi^0$ . In this chapter, we present an overview of some topics in neutral kaon and hyperon physics which have been addressed by KTeV.

#### 1.1 CP Violation in the Kaon System

Symmetries and invariance principles within physical systems have contributed a great deal to our understanding of those systems at the most fundamental levels. Indeed, some of the greatest insights have stemmed from experiments that have

discovered an unexpected invariance principle, or have discovered a violation where a symmetry was expected. As an example for the former, the Michelson-Morely null experiment led to the invariance of the speed of light as one of the principles of Einstein's special theory of relativity.

In the study of elementary particles and their interactions, searches for symmetries have had invaluable consequences. Of particular interest in quantum field theory are three discrete symmetries; charge conjugation ( $C$ ), parity ( $P$ ) and time reversal ( $T$ ). According to the  $CPT$  theorem [2, 3], particle interactions are invariant under the combined operation of these three operators. This  $CPT$  symmetry leads to some very basic predictions, such as the equality of the masses, lifetimes and magnitude of electric charge of particles and anti-particles [4].

Perhaps the intuitive way of preserving  $CPT$  symmetry of particle interactions would be to have interactions that were invariant under each of three individual operators  $C$ ,  $P$  and  $T$ , as they were believed to be valid symmetries of the nature.

However, in 1956 Lee and Yang [5] proposed that parity violation could explain the  $\tau \leftrightarrow \theta$  puzzle, where two otherwise identical particles decayed into both a  $P$  even  $2\pi$  state and a  $P$  odd  $3\pi$  state. Both  $\tau$  and  $\theta$  were later known to be the same particle,  $K^+$ . They suggested that the parity nonconservation could be established by observation of an angular asymmetry in the  $\beta$  decay of polarized nuclei, or the decay chain  $\pi \rightarrow \mu + \bar{\nu}_\mu$  and  $\mu \rightarrow e + \bar{\nu}_e + \nu_\mu$ . This proof was furnished in the following year in the famous  $^{60}\text{Co}$  experiment of Wu *et. al.* [6], and shortly thereafter, in the pion decay sequence by Garwin *et. al.* [7] and Friedman and Telegdi [8]. The confirmation of parity violation led to the recognition of the V-A

nature of the weak interaction [9, 10].

A consequence of the  $CPT$  theorem is that if one of the operations,  $C$ ,  $P$  or  $T$  is not conserved, then at least one of the other two is not conserved either [11]. Landau pointed out that the parity-violating weak interactions were invariant under the combined operation of  $C$  and  $P$  [12]. For example,  $CP$  transforms the left-handed neutrinos to right-handed anti-neutrinos and these two states are physically observable. On the other hand, operation of  $C$  or  $P$  alone transforms the neutrino into one of the charge conjugate states, which has not been observed. In 1964, however, the notion of  $CP$  invariance and  $T$  invariance had to be abandoned by the discovery of  $CP$  violation in decays of long lived component of the neutral kaon demonstrated by Christenson, Cronin, Fitch and Turley [13]. Since then,  $C$ ,  $P$ , and  $CP$  violation have been observed only in the weak interactions. The strong and electromagnetic interactions are invariant under these operations in all experiments to date.

It has been almost 35 years since the initial discovery of  $CP$  violation, yet we don't completely understand the true origin of this phenomena. The origin of  $C$  and  $P$  violation is less a mystery. They arise from the left-handed nature of the interactions of the  $W$  boson. While the Standard Model might be able to explain the phenomena of  $CP$  violation by introducing a  $CP$  violating phase, we would still lack the knowledge of the origin of this phase. It is also possible to explain  $CP$  violation from interactions beyond the Standard Model.

### 1.1.1 CP Eigenstates in the Neutral Kaon System

Let us look at some elements of phenomenology of the neutral kaon system and summarize the experimental results. The strong interaction produces the  $K^0$  and  $\bar{K}^0$  mesons which are eigenstates of strangeness.  $K^0$  are produced for example through strangeness conserving interactions such as:

$$\pi^- + p \rightarrow K^0 + \Lambda$$

$K^0$  and  $\bar{K}^0$  are  $CP$  conjugates of one another. With an appropriate choice of phase we can write:

$$\begin{aligned} CP|K^0\rangle &= |\bar{K}^0\rangle \\ CP|\bar{K}^0\rangle &= |K^0\rangle \end{aligned} \tag{1.1}$$

From these however, one can construct the  $CP$  eigenstates:

$$\begin{aligned} |K_1\rangle &= \frac{1}{\sqrt{2}}(|K^0\rangle + |\bar{K}^0\rangle) & CP &= +1 \\ |K_2\rangle &= \frac{1}{\sqrt{2}}(|K^0\rangle - |\bar{K}^0\rangle) & CP &= -1 \end{aligned} \tag{1.2}$$

If  $CP$  were conserved by the weak interaction then  $|K_1\rangle$  and  $|K_2\rangle$  would be the weak eigenstates in which case they would have well defined masses and lifetimes with the following  $CP$ -conserving decays:

$$\begin{aligned} |K_1\rangle &\rightarrow \pi^0 \pi^0 & CP &= +1 \\ |K_1\rangle &\rightarrow \pi^+ \pi^- & CP &= +1 \\ |K_2\rangle &\rightarrow \pi^0 \pi^0 \pi^0 & CP &= -1 \end{aligned} \tag{1.3}$$

in addition to other decays to non-eigenstates of  $CP$ . Because of the large phase space for the  $\pi\pi$  final state, the  $|K_1\rangle$  would have a much shorter lifetime than the  $|K_2\rangle$ . In fact  $K_1$  and  $K_2$  were known as the short lived and long lived kaons respectively until the discovery of  $CP$  violation in which the decay of the long lived kaons into two-pion final states was observed.

### 1.1.2 Indirect $CP$ Violation

One method to explain  $CP$  violation is to suppose the short lived and long lived kaons are mixtures of  $K_1$  and  $K_2$  [14]. The tiny  $CP$  violation is then a result of the opposite eigenstate admixture in a nearly  $CP$  eigenstate. The mixing can occur through virtual  $\Delta S = 2$  as shown in Fig. 1.1.

Let us examine the mixing of eigenstates in more detail. For clarity, we assume  $CPT$  is conserved in what follows. We begin this kaon phenomenology with an effective second order Hamiltonian  $H_{eff}$  [15, 16, 17] on a two-state system with time dependent amplitudes  $\Psi$  and  $\bar{\Psi}$  for  $K^0$  and  $\bar{K}^0$  states, respectively. The  $H_{eff}$  has to contain terms second order in the weak Hamiltonian in order to incorporate  $\Delta S = 2$  that mixes  $K^0$  and  $\bar{K}^0$  and should satisfy the Schrödinger equation

$$i \frac{d}{dt} \begin{pmatrix} \Psi \\ \bar{\Psi} \end{pmatrix} = H_{eff} \begin{pmatrix} \Psi \\ \bar{\Psi} \end{pmatrix}. \quad (1.4)$$

$H_{eff}$  is a  $2 \times 2$  matrix connecting  $K^0$  and  $\bar{K}^0$  states, which can be written as the combination of two separately Hermitian matrices,  $M$  and  $\Gamma$ :

$$H_{eff} = M - \frac{i}{2} \Gamma \quad (1.5)$$

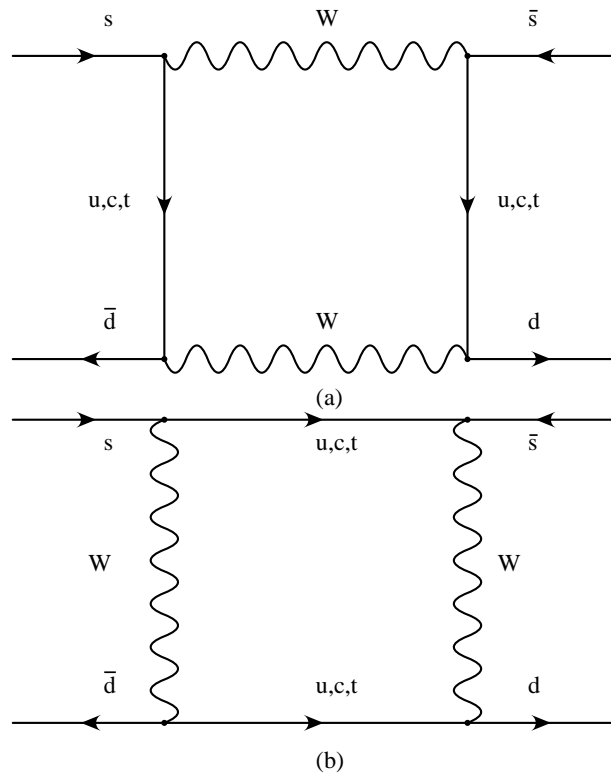


Figure 1.1:  $K^0 \leftrightarrow \bar{K}^0$ ,  $\Delta S = 2$  Box diagram in the Standard model.

where  $M$  and  $\Gamma$  are the  $2 \times 2$  mass and decay matrices in the  $K^0$  and  $\bar{K}^0$  basis.

One finds the eigenstates are

$$\begin{aligned} |K_L\rangle &= \frac{1}{\sqrt{2(1+\epsilon^2)}}((1+\epsilon)|K^0\rangle \leftrightarrow (1\leftrightarrow\epsilon)|\bar{K}^0\rangle) \\ |K_S\rangle &= \frac{1}{\sqrt{2(1+\epsilon^2)}}((1+\epsilon)|K^0\rangle + (1\leftrightarrow\epsilon)|\bar{K}^0\rangle), \end{aligned} \quad (1.6)$$

and in terms of  $K_1$  and  $K_2$  :

$$\begin{aligned} |K_L\rangle &= \frac{1}{\sqrt{1+\epsilon^2}}(|K_2\rangle + \epsilon|K_1\rangle) \\ |K_S\rangle &= \frac{1}{\sqrt{1+\epsilon^2}}(|K_1\rangle + \epsilon|K_2\rangle) \end{aligned} \quad (1.7)$$

where the mixing parameter,  $\epsilon$ , is given by

$$\epsilon = \frac{\langle \bar{K}^0 | H_{eff} | K^0 \rangle \leftrightarrow \langle K^0 | H_{eff} | \bar{K}^0 \rangle}{2(m_L \leftrightarrow m_S) + i(\Gamma_S \leftrightarrow \Gamma_L)}, \quad (1.8)$$

with  $m_{L,S}$  ( $K_{L,S}$  mass) and  $\Gamma_{L,S}$  ( $K_{L,S}$  decay rate) the eigenvalues of  $M$  and  $\Gamma$ , respectively. As we can see the non-zero  $CP$ -violating parameter arises from nonequal off-diagonal elements of the Hamiltonian, meaning an asymmetry in the rate of particle-antiparticle transitions.

$\epsilon$  is measured to be a very small parameter with amplitude:

$$|\epsilon| = (2.25 \pm 0.08) \times 10^{-3} \quad (1.9)$$

So the interpretation of Eqs. 1.7 is that  $K_L(K_S)$  is mostly dominated by  $CP$  odd (even) amplitude  $K_2(K_1)$  and the  $CP$  violation is due to the  $K_1(K_2)$  contamination.  $\epsilon$  determines the size of the  $CP$ -violation contamination. The  $K_1$  contamination in the  $K_L$  decays into the two-pion final state.

This  $CP$  violation due to the asymmetric  $K^0 \leftrightarrow \bar{K}^0$  mixing is called “indirect  $CP$  violation”.



### 1.1.3 Direct CP Violation

There is another possible channel for  $CP$  violation called the “direct  $CP$  violation”. In this case the  $CP$ -odd state  $K_2$  can decay directly to the  $CP$ -even final state of two pions. This  $\Delta S = 1$  transition predicted by the Standard Model is shown in Fig. 1.2 for the decay  $K_L \rightarrow \pi^0 \pi^0$ . Diagram (b) shows the strong penguin diagram contribution to this decay. The electroweak counterpart in which the gluon is replaced by a photon or a  $Z$  boson, also contributes. The diagrams for the decay  $K_L \rightarrow \pi^+ \pi^-$  are similar.

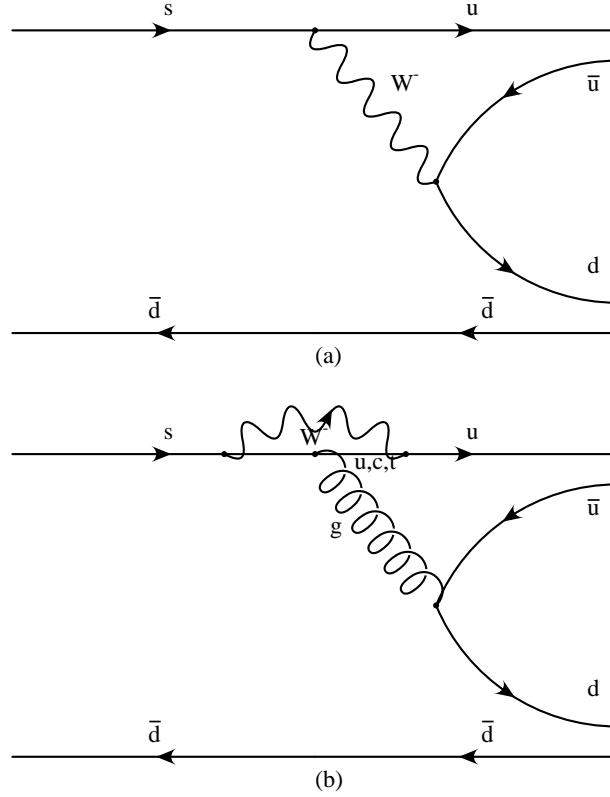


Figure 1.2: (a) Tree level diagram contribution to  $K_L \rightarrow \pi^0 \pi^0$ . (b) Penguin diagram contribution to  $K_L \rightarrow \pi^0 \pi^0$ .

The strength of this transition is conventionally expressed by means of the parameter  $\epsilon'$  defined by the expression

$$\epsilon' \equiv \frac{i}{\sqrt{2}} e^{i(\delta_2 - \delta_0)} \text{Im}\left(\frac{A_2}{A_0}\right) \quad (1.10)$$

where  $\delta_j$  are the  $\pi\pi$  phase shifts at the  $K^0$  mass for a state with isospin  $j$  and the  $A_j$  are defined in terms of the  $K^0$  decay amplitude by

$$\langle I = j | H_{eff} | K^0 \rangle \equiv A_j e^{i\delta_j} \quad (1.11)$$

and similarly for the  $\bar{K}^0$

$$\langle I = j | H_{eff} | \bar{K}^0 \rangle \equiv A_j^* e^{i\delta_j}. \quad (1.12)$$

If we define  $\eta$  as the ratio of the decay amplitude  $K_L \rightarrow \pi\pi$  to that of  $K_S \rightarrow \pi\pi$ ,

$$\begin{aligned} \eta_{+-} &= \frac{\langle \pi^+ \pi^- | H_{eff} | K_L \rangle}{\langle \pi^+ \pi^- | H_{eff} | K_S \rangle} \\ \eta_{00} &= \frac{\langle \pi^0 \pi^0 | H_{eff} | K_L \rangle}{\langle \pi^0 \pi^0 | H_{eff} | K_S \rangle}, \end{aligned} \quad (1.13)$$

then from equations 1.11 to 1.10, one finds

$$\begin{aligned} \eta_{+-} &= \epsilon + \epsilon' \\ \eta_{00} &= \epsilon \Leftrightarrow 2\epsilon'. \end{aligned} \quad (1.14)$$

The value of  $Re(\epsilon'/\epsilon)$  can be found by measuring the double ratio of the four  $K_{L,S} \rightarrow 2\pi$  decay rates:

$$\begin{aligned} & \frac{, (K_L \rightarrow \pi^+ \pi^-) / , (K_S \rightarrow \pi^+ \pi^-)}{, (K_L \rightarrow \pi^0 \pi^0) / , (K_S \rightarrow \pi^0 \pi^0)} = \frac{|\eta_{+-}|^2}{|\eta_{00}|^2} \\ &= \left| \frac{\epsilon + \epsilon'}{\epsilon \Leftrightarrow 2\epsilon'} \right|^2 \approx \left| 1 + 3\frac{\epsilon'}{\epsilon} \right|^2 \approx 1 + 6Re\left(\frac{\epsilon'}{\epsilon}\right) \end{aligned} \quad (1.15)$$

The most recent values of  $Re(\epsilon'/\epsilon)$  have been measured by two groups. NA31 [18] at CERN reported

$$Re(\frac{\epsilon'}{\epsilon}) = [23 \pm 3.4_{(stat.)} \pm 5.5_{(syst.)}] \times 10^{-4}, \quad (1.16)$$

a three-sigma deviation from zero. However E731 [19] at Fermilab reported

$$Re(\frac{\epsilon'}{\epsilon}) = [7.4 \pm 5.2_{(stat.)} \pm 2.9_{(syst.)}] \times 10^{-4} \quad (1.17)$$

consistent with zero.

Improved versions of these experiments, KTeV/E832 at Fermilab and NA48 at CERN, were designed to measure  $Re(\epsilon'/\epsilon)$  with an accuracy of order  $10^{-4}$ .

## 1.2 Rare Decay of Neutral Kaons

Besides the  $\pi\pi$  decays of the  $K_L$  and  $K_S$ , some rare decays of  $K_L$  containing  $CP$ -violating amplitudes could yield information regarding direct and/or indirect  $CP$  violation. Of special interest are the three highly suppressed decays of  $K_L$  to  $\pi^0 e^+ e^-$ ,  $\pi^0 \mu^+ \mu^-$  and  $\pi^0 \nu \bar{\nu}$  which have large “direct”  $CP$ -violating amplitudes. The third one,  $K_L \rightarrow \pi^0 \nu \bar{\nu}$ , is essentially purely direct  $CP$ -violating in the Standard Model. A detailed status report of this decay mode can be found in [20].

A list of decays of  $K_L$  and  $\pi^0$  being studied by the KTeV collaboration is presented in tables 1.1 to 1.3. The overview of the rare decays can be found in the KTeV design report [1]. Some of the rare decays are highly suppressed and beyond the experimental reach at present. Figure 1.3 presents the branching ratio of the observed rare decays and the known limit as well as sensitivity of KTeV to the unobserved rare decays of  $K_L$ .

Table 1.1: Rare decays of  $K_L$  at KTeV.

Decay Mode	Interest
$K_L \rightarrow \pi^0 e^+ e^- \gamma$	Background to $K_L \rightarrow \pi^0 e^+ e^-$
$K_L \rightarrow e^+ e^- \gamma \gamma$	Background to $K_L \rightarrow \pi^0 e^+ e^-$
$K_L \rightarrow e^+ e^- e^+ e^-$	Form Factor
$K_L \rightarrow \pi^0 \gamma \gamma, \pi^0 \rightarrow e^+ e^- \gamma$	Chiral Perturbation Theory
$K_L \rightarrow \pi^0 \pi^0 \gamma, \pi^0 \rightarrow e^+ e^- \gamma$	Chiral Perturbation Theory
$K_L \rightarrow \pi^0 \pi^0 \gamma \gamma, \pi^0 \rightarrow e^+ e^- \gamma$	Chiral Perturbation Theory
$K_L \rightarrow \pi^0 \pi^0 e^+ e^-$	Chiral Perturbation Theory
$K_L \rightarrow 2\pi^0, \pi^0 \rightarrow e^+ e^- \gamma$	Normalization
$K_L \rightarrow e^+ e^-$	Unitarity
$K_L \rightarrow e^+ e^- \gamma$	$\gamma^* \gamma$ Form Factor
$K_L \rightarrow \pi^+ \pi^- e^+ e^-$	CP & T violation
$K_L \rightarrow \pi^\pm \pi^\pm e^\mp e^\mp$	Lepton number violation
$K_L \rightarrow K^\pm e^\mp \nu(\bar{\nu}), K^\pm \rightarrow \pi^\pm \pi^\pm \pi^\mp$	$V_{ud}$ measurement ( $K_L$ beta decay)
$K_L \rightarrow \pi^\pm \pi^\pm \pi^\mp e^\mp \nu(\bar{\nu})$ ( $K_{e5}$ )	Chiral Perturbation Theory
$K_L \rightarrow \mu^+ \mu^-$	$\rho$ measurement in CKM matrix
$K_L \rightarrow \mu^+ \mu^- \gamma$	Form Factor
$K_L \rightarrow e^+ e^- \mu^+ \mu^-$	Form Factor
$K_L \rightarrow \mu^+ \mu^- \mu^+ \mu^-$	Form Factor
$K_L \rightarrow \pi^0 e^\pm \mu^\mp$	Lepton number violation

Table 1.2: Rare decay of  $K_L$  with a direct CP violation component at KTeV.

Decay Mode	Interest
$K_L \rightarrow \pi^0 e^+ e^-$	CP violation ( $\epsilon'/\epsilon \approx 1$ )
$K_L \rightarrow \pi^0 \mu^+ \mu^-$	CP violation ( $\epsilon'/\epsilon \approx 1$ )
$K_L \rightarrow \pi^0 \nu \bar{\nu}$ , $\pi^0 \rightarrow e^+ e^- \gamma$	CP violation ( $\epsilon'/\epsilon \gg 1$ )
$K_L \rightarrow \pi^0 \nu \bar{\nu}$ , $\pi^0 \rightarrow \gamma \gamma$	CP violation ( $\epsilon'/\epsilon \gg 1$ )

Table 1.3: Rare decays of  $\pi^0$  at KTeV.

Decay Mode	Interest
$K_L \rightarrow 3\pi^0$ , $\pi^0 \rightarrow e^+ e^-$	Unitarity
$K_L \rightarrow 3\pi^0$ , $\pi^0 \rightarrow e^+ e^- \gamma$	Form Factor of $\pi^0$
$K_L \rightarrow 3\pi^0$ , $\pi^0 \rightarrow e^+ e^- e^+ e^-$	Parity of $\pi^0$
$K_L \rightarrow 3\pi^0$ , $\pi^0 \rightarrow e^+ e^- \gamma \gamma$	Radiative Corr. for $\pi^0 \rightarrow e^+ e^- \gamma$
$K_L \rightarrow 3\pi^0$ , $\pi^0 \rightarrow e^\pm \mu^\mp$	Lepton number violation

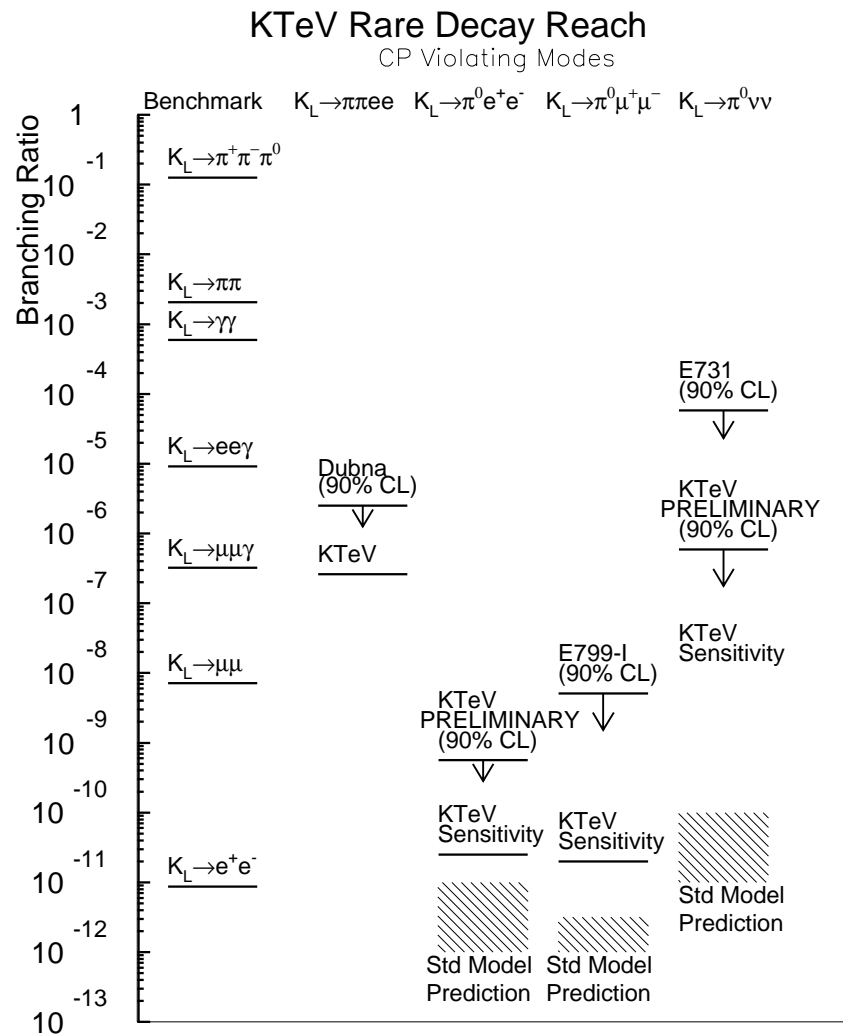


Figure 1.3: Sensitivity of KTeV to the rare decay of Kaons.

### 1.3 Neutral Hyperon Physics at KTeV

KTeV experiment was mainly designed to study the Kaon system. The detector was far (about 94 m) from the production target to ensure mostly  $K_L$  in the neutral beam would reach the detector. However, a copious amount of neutrons, and some very high momentum hyperons<sup>1</sup> entered the detector along with  $K_L$ 's. The Lambda and the Cascade were the only two hyperons with lifetimes long enough to be observable at KTeV. Table 1.4 presents a list of some hyperon topics which have been studied at KTeV. The last column in the table shows the main physics interest of the decay, like Branching Ratio (BR) measurement, form factors, and etc. In this section we briefly describe the motivations for studying these decays and some recent results [22]. The semi-leptonic decays of hyperons which is the main focus of this thesis will be overviewed in more detail. The two-body non-leptonic decays which are the dominant decay modes of hyperons will be discussed as well.

#### 1.3.1 Hyperon Semi-Leptonic Decays

Though the weak interaction is assumed to be well understood, the decay properties of strange quarks inside hadrons are not, because the strong force has not yet been accommodated in the standard model of electroweak interactions. One way of studying strange quark decay is through the hyperon decays. In this section, we overview our knowledge of Hyperon Semi-leptonic Decays (HSD). These decays known also as beta decays are represented by  $A \rightarrow B l \nu_l$ , where  $l$  can be either an

---

<sup>1</sup>Hyperons are baryons which contain at least one strange quark.

Table 1.4: Neutral hyperon program at KTeV.  $N_{event}$  is the number of events observed in the previous experiments and  $N_{KTeV}$  is the number of candidates at KTeV: ? means the decay hasn't been studied yet.

Decay mode	$N_{event}$	$N_{KTeV}$	Physics Interest
$\Xi^0 \rightarrow \Sigma^+ e^- \bar{\nu}_e$	0	1100	BR, Form Factors
$\bar{\Xi}^0 \rightarrow \bar{\Sigma}^+ e^+ \nu_e$	0	66	BR, Form Factors
$\Xi^0 \rightarrow \Sigma^+ \mu^- \bar{\nu}_\mu$	0	5	BR
$\Xi^0 \rightarrow \Lambda \pi^0, \Lambda \rightarrow p e^- \bar{\nu}_e$	Many	6000	Form Factors
$\Xi^0 \rightarrow \Lambda \pi^0, \Lambda \rightarrow p \mu^- \bar{\nu}_\mu$	28	?	BR, Form Factors
$\Xi^0 \rightarrow \Sigma^0 \gamma$	85	7000	BR, Asymmetries
$\Xi^0 \rightarrow \Lambda \gamma$	116	1000	BR, Asymmetries
$\Xi^0 \rightarrow \Lambda \pi^0 \gamma$	0	?	BR
$\Lambda^0 \rightarrow p \pi^- \gamma$	72	7000	BR
$\Sigma^0 \rightarrow \Lambda e^+ e^-$	314	10	BR, $\Sigma^0$ Parity
$\Sigma^0 \rightarrow \Lambda \gamma \gamma$	0	?	BR
$\Xi^0 \rightarrow \Lambda \pi^0$ and $\bar{\Xi}^0 \rightarrow \bar{\Lambda} \pi^0$	Many	Many	Precise mass, Polarization
$\Xi^0 \rightarrow p \pi^-, \bar{\Xi}^0 \rightarrow \bar{p} \pi^+$	0	0	$\Delta S = 2$ (SM test)



electron or a muon, are similar to the familiar and well understood nuclear beta decay,  $n \rightarrow pe^- \bar{\nu}_e$ . Figure 1.4 shows the Feynman diagram for the decay of our interest  $\Xi^0 \rightarrow \Sigma^+ e^- \bar{\nu}_e$ . The muon channel of this decay is also possible and being studied at KTeV [23, 24].

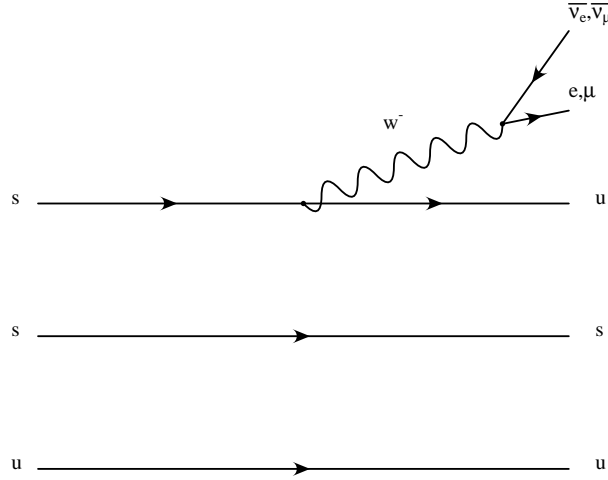


Figure 1.4: Feynman diagram for Cascade Beta Decay,  $\Xi^0 \rightarrow \Sigma^+ e^- \bar{\nu}_e$ .

The fact that hyperons carry  $\frac{1}{2}$  spin, contain one or more strange quarks and the mass difference between the parent and daughter baryons are large, makes their semi-leptonic decays rich sources of information on the role of strong force in the decay processes. HSD can be conveniently described by the older V-A theory which includes more than electroweak theory. For  $\Xi^0 \rightarrow \Sigma^+ e^- \bar{\nu}_e$  the transition amplitude in the V-A theory can be written most generally: <sup>2</sup>

$$\mathcal{M} = \frac{G_F}{\sqrt{2}} \langle \Sigma^+ | J_\alpha | \Xi^0 \rangle \bar{u}_e \gamma^\alpha (1 + \gamma_5) u_\nu \quad (1.18)$$

---

<sup>2</sup>The presented formalism can easily be extended to other HSD,  $A \rightarrow B l \nu_l$ .

where  $G_F$  is the universal weak coupling constant. In Eq. 1.18 the leptonic current is left-handed and the hadronic current can be expressed in terms of vector and axial vector components as follows:

$$\langle \Sigma^+ | J_\alpha | \Xi^0 \rangle = V_{us} \bar{u}(\Sigma^+) (V_\alpha + A_\alpha) u(\Xi^0) \quad (1.19)$$

where  $V_{us}$ <sup>3</sup> is the Cabibbo-Kobayashi-Maskawa matrix element [21] for strangeness changing  $\Delta S=1$  decays.  $u(\Xi^0)$  and  $u(\Sigma^+)$  are the Dirac spinors of the initial and final baryons. The vector and axial vector currents can be written as:

$$V_\alpha = f_1(q^2)\gamma_\alpha + \frac{f_2(q^2)}{M_{\Xi^0}}\sigma_{\alpha\beta}q^\beta + \frac{f_3(q^2)}{M_{\Xi^0}}q_\alpha \quad (1.20)$$

$$A_\alpha = (g_1(q^2)\gamma_\alpha + \frac{g_2(q^2)}{M_{\Xi^0}}\sigma_{\alpha\beta}q^\beta + \frac{g_3(q^2)}{M_{\Xi^0}}q_\alpha)\gamma_5 \quad (1.21)$$

$$q^\alpha = (p_e + p_\nu)^\alpha = (p_{\Xi^0} \leftrightarrow p_{\Sigma^+})^\alpha \quad (1.22)$$

There are 3 vector form factors  $f_1$  (vector),  $f_2$  (weak magnetism) and  $f_3$  (induced scalar); plus 3 axial-vector form factors  $g_1$  (axial-vector),  $g_2$  (weak electricity) and  $g_3$  (induced pseudo-scalar) which are functions of the baryons momentum transfer squared,  $q^2$ . Time reversal invariance implies that all of them are real. Determination of these form factors will shed light on the internal strong force that keeps the quarks together as well as its interplay with the electroweak force which is responsible for the decay of the hyperons.  $f_3$  and  $g_3$  are suppressed by the mass of the lepton and can be ignored in the case of decays to an electron.

---

<sup>3</sup> $V_{us} = \sin(\theta_C)$  to a very good approximation. For  $\Delta S=0$  decays,  $V_{ud} = \cos(\theta_C)$ .  $\theta_C$  is called the Cabibbo mixing angle.

## Integrated Observables

Because of the low statistics of HSD, one has to lump events together to produce certain integrated observables; namely, the total decay rate (or alternatively the branching ratio), lepton-neutrino angular correlation, the asymmetry coefficients in the decay of a polarized initial baryon, and the polarization of the decay baryon in its own rest frame for an unpolarized initial baryon. These experimentally measurable quantities have the advantage that their definitions do not assume any particular theoretical approach. We follow the calculations of Garcia and Kielanowski [25] to summarize some of these variables. In the following relations  $\Delta M$  is the mass difference between the initial and final baryons and  $\delta$  is defined as  $(\Delta M/M_{\Xi^0})$ . For the decay  $\Xi^0 \rightarrow \Sigma^+ e^- \bar{\nu}_e$ ,  $\Delta M = 125.5 \pm 0.6$  MeV/c and  $\delta = 0.0954 \pm 0.0005$ . For convenience, we keep terms only through the first order of  $\delta$ . Detailed calculations of these variables can also be found in reference [26].

The total decay rate can be extracted from the branching ratio measurement of the decay. It is a function of the form factors:

$$Rate = \frac{G_F^2 (\Delta M)^5}{60\pi^3} \left( (1 \leftrightarrow \frac{3}{2}\delta) f_1^2 + (3 \leftrightarrow \frac{9}{2}\delta) g_1^2 \leftrightarrow 4\delta g_1 g_2 \right) \quad (1.23)$$

The polarization of the  $\Sigma^+$  is observed via its two body decay  $\Sigma^+ \rightarrow p\pi^0$  (see Sec. 1.3.2 for definitions) which has a large asymmetry  $\alpha_\Sigma = \approx 0.98$ . The distribution of the cosine of the angle between the proton and the  $e^-$  in the  $\Sigma^+$  frame is

$$\frac{1}{4\pi} \frac{d}{d\Omega_p} = \frac{1}{4\pi} (1 + S_e \alpha_\Sigma \hat{p} \cdot \hat{e}), \quad (1.24)$$

where  $S_e$  is the  $\Sigma^+$  polarization in the electron direction averaged over phase space

and

$$\begin{aligned} Rate \times \mathcal{S}_e = \frac{G_F^2(\Delta M)^5}{60\pi^3} & ((2 \Leftrightarrow \frac{10}{3}\delta)g_1^2 + (2 \Leftrightarrow \frac{7}{3}\delta)f_1g_1 \Leftrightarrow \frac{1}{3}\delta f_1^2 \\ & \Leftrightarrow \frac{2}{3}\delta f_1f_2 + \frac{2}{3}\delta f_2g_1 \Leftrightarrow \frac{2}{3}\delta f_1g_2 \Leftrightarrow \frac{10}{3}\delta g_1g_2). \end{aligned} \quad (1.25)$$

Similarly, the  $\Sigma^+$  polarization in the neutrino direction averaged over phase space is

$$\begin{aligned} Rate \times \mathcal{S}_\nu = \frac{G_F^2(\Delta M)^5}{60\pi^3} & ((\frac{10}{3}\delta \Leftrightarrow 2)g_1^2 + (2 \Leftrightarrow \frac{7}{3}\delta)f_1g_1 + \frac{1}{3}\delta f_1^2 \\ & + \frac{2}{3}\delta f_1f_2 + \frac{2}{3}\delta f_2g_1 \Leftrightarrow \frac{2}{3}\delta f_1g_2 + \frac{10}{3}\delta g_1g_2). \end{aligned} \quad (1.26)$$

We can also measure the  $e \Leftrightarrow \nu$  correlation, defined as

$$\alpha_{e\nu} = 2 \frac{N(\cos(\hat{e}, \hat{\nu}) > 0) \Leftrightarrow N(\cos(\hat{e}, \hat{\nu}) < 0)}{N(\cos(\hat{e}, \hat{\nu}) > 0) + N(\cos(\hat{e}, \hat{\nu}) < 0)}. \quad (1.27)$$

In terms of the form factors we have:

$$\begin{aligned} Rate \times \alpha_{e\nu} = \frac{G_F^2(\Delta M)^5}{60\pi^3} & ((1 \Leftrightarrow \frac{5}{2}\delta)f_1^2 \Leftrightarrow (1 + \frac{3}{2}\delta)g_1^2 \\ & + 4\delta g_1g_2). \end{aligned} \quad (1.28)$$

From these equations we can see the dominant effects come from the 'direct' vector and axial-vector form factors  $f_1$  and  $g_1$ .  $f_2$  and  $g_2$  give rise to smaller contributions proportional to  $\delta$ .

## Cabibbo Hypothesis

The Cabibbo theory (CT) [27] is based on the V-A theory, assuming perfect SU(3) symmetry. It also postulates that only first-class hadronic operators <sup>4</sup> participate

---

<sup>4</sup>First and second class currents are defined based on their transformation properties under G-parity.

in weak interactions,  $V_\alpha$  and  $A_\alpha$  are octet SU(3) operators where  $V_\alpha$  is also related to the electromagnetic current through conserved vector current (CVC) hypothesis, and the universality of weak interactions is determined by an angle  $\theta_C$ .

With these postulates, CT relates the form factors of different HSD to one another by SU(3) flavor symmetry. In this limit  $g_2$  vanishes (no second-class current) and the remaining three form factors for e-mode processes at  $q^2 = 0$  are of the form

$$\begin{aligned} f_1(0) &= C_F F_1 + C_D D_1 \\ f_2(0) &= C_F F_2 + C_D D_2 \\ g_1(0) &= C_F F + C_D D \end{aligned} \tag{1.29}$$

where  $F$ 's and  $D$ 's are the reduced form factors and  $C_F$  and  $C_D$  are products of SU(3) Clebsch-Gordon coefficients. Since the weak vector current and the electromagnetic current are assumed to be members of the same SU(3) octet, the vector form factors are related to electric charges and the anomalous magnetic moments of the nucleons. This results in

$$f_1(0) = 1 \tag{1.30}$$

$$f_2(0) = \frac{M_{\Xi^0}}{2M_p}(\mu_p \leftrightarrow \mu_n) = 2.60 \tag{1.31}$$

for  $\Xi^0 \rightarrow \Sigma^+ e^- \bar{\nu}_e$ .  $\mu_p$  and  $\mu_n$  are anomalous magnetic moment of the proton and the neutron, respectively [28].

No similar connection can be made for  $g_1$ . Therefore, the value of  $F$  and  $D$  are undetermined. The three free parameters of  $F$ ,  $D$  and  $\theta_C$  in CT are to be fixed within HSD. For Cascade beta decay  $g_1 = F + D$ , which is similar dependence as

the well studied neutron beta decay. Thus, in the flavor symmetric quark model, differences between these two decays arise only from the differing particle masses and CKM matrix elements ( $V_{us}$  rather than  $V_{ud}$ ).

From the neutron beta decay the ratio  $g_1/f_1 = 1.2670 \pm 0.0035$  and from  $K_{e3}^0$  decays, the best measured value of  $V_{us}$  is  $|V_{us}| = 0.2196 \pm 0.0023$  [28]. Based on the SU(3) flavor symmetry assumption, a branching ratio of  $(2.61 \pm 0.11) \times 10^{-4}$  can be predicted for Cascade beta decay [29]. With an order of 1000  $\Xi^0 \rightarrow \Sigma^+ e^- \bar{\nu}_e$  events,  $g_1/f_1$  can be measured to about 0.2.

### SU(3) symmetry breaking in HSD

The postulate of SU(3) flavor symmetry in CT is the weakest of all the postulates. Since we know SU(3) is not an exact symmetry in the real world, one must eventually find discrepancies between CT and experiment. An application of the Ademollo-Gatto theorem [30] protects  $f_1$  and  $V_{us}$  to first order in the SU(3) symmetry breaking. However, the second order corrections may be needed to check the consistency between the value of  $V_{us}$  measured from  $K_{e3}^0$  decays and HSD. The symmetry breaking effects for  $g_1$  are of the first order. Recently, several models have been proposed to predict the SU(3) symmetry breaking corrections to the form factors (see for example [31, 32, 33, 34]) in HSD and  $\Xi^0 \rightarrow \Sigma^+ e^- \bar{\nu}_e$  decay in particular. They calculate a 20  $\Leftrightarrow$  30% correction to the form factors. An independent and precise measurement of  $f_1$  and  $g_1$  can either verify or rule out these models.

Perhaps  $g_2$  would be the most interesting form factor to measure, provided high

statistics experiments can be performed. Given  $SU(3)$  is broken,  $g_2$  is also subject to an expected  $20 \Leftrightarrow 30\%$  correction, predicting a nonzero value. The possibility of having a larger  $g_2$ , implies the existence of second-class currents which is not accommodated in the Standard Model. Several models exist that try to predict the value of  $g_2$ . This value is very sensitive to the models. In the case of  $\Xi^0 \rightarrow \Sigma^+ e^- \bar{\nu}_e$  decay, for instance, the non-zero prediction of  $g_2$  ranges from  $\sim 0.05$  to  $\sim 1.1$ . Experimental data are certainly needed to guide the theory [35]. The beta decay of  $\Lambda$  would be a more desirable decay for  $g_2$  measurements since they can be produced with a fairly large statistics, and the mass difference between the initial and final baryons is large ( $\delta \approx 0.2$ ).

### 1.3.2 Hyperon Non-Leptonic Decays

The dominant decay of hyperons is for a strange quark (s) in the parent hyperon to be converted into an up (u) or a down (d) quark as the hyperon itself decays into a meson and a baryon. The dominant decay modes for spin- $\frac{1}{2}$  hyperons, except for  $\Sigma^0$  which decays electromagnetically, all have a  $\pi$  meson in the final state, and therefore the decays are usually represented by  $B \rightarrow B'\pi$ , where  $B$  and  $B'$  are initial and final state baryons. The basic Feynman diagrams for the two non-leptonic decays,  $\Xi^0 \rightarrow \Lambda\pi^0$  and  $\Lambda \rightarrow p\pi^-$  observable at KTeV are shown in Appendix C.

Because of the complications of the strong interaction, one needs an effective weak Hamiltonian to describe these decays. When a spin- $\frac{1}{2}$  hyperon decays non-leptonically, the daughter baryon is also a spin- $\frac{1}{2}$  particle while the daughter meson

has spin zero. Conservation of angular momentum implies this Hamiltonian is restricted to having only  $l = 0$  (s-wave) and  $l = 1$  (p-wave) components. The most general decay amplitude that satisfies Lorentz invariance, must be a sum of scalar and pseudo-scalar quantities and can be written [36]

$$\mathcal{M} = \bar{u}'(A + B\gamma_5)u \quad (1.32)$$

where A and B are the s-wave and p-wave amplitudes respectively. Since the final state pion is a pseudo-scalar and has negative parity, the  $\bar{u}'B\gamma_5u$  term which is also a pseudo-scalar is called the parity conserving amplitude. The term  $\bar{u}'Au$  is a scalar and has a positive parity and is called the parity violating amplitude.

We now define  $s = A$  and  $p = (E' \leftrightarrow M')/(E' + M')B$  for the s-wave and p-wave parts.  $s$  and  $p$  have the advantage that they appear in an analogous manner in the decay rate and asymmetry formulae [37].  $E'$  and  $M'$  being the energy and mass of the daughter baryon in the rest frame of the parent particle. Using these definitions and Eq. 1.32 the decay rate becomes [38]

$$\Gamma = \frac{|q|}{4\pi} (|s|^2 + |p|^2) \frac{(E' + M')}{M} \quad (1.33)$$

where M is the parent hyperon mass and  $|q|$  is the momentum transfer of the decay.

Other quantities of interest are the so called decay asymmetry parameters which describe the angular distribution of the daughter baryon and its polarization. The decay parameters can be written in terms of  $s$  and  $p$  amplitudes

$$\alpha = \frac{2\text{Re}(s^*p)}{|s|^2 + |p|^2} \quad (1.34)$$



$$\beta = \frac{2\text{Im}(s^*p)}{|s|^2 + |p|^2} \quad (1.35)$$

$$\gamma = \frac{|s|^2 \Leftrightarrow |p|^2}{|s|^2 + |p|^2}, \quad (1.36)$$

with the normalization condition  $\alpha^2 + \beta^2 + \gamma^2 = 1$ . The angular distribution of the daughter baryon in the rest frame of the parent hyperon can be written as:

$$\frac{1}{d\Omega} \frac{d}{d\Omega} = \frac{1}{4\pi} (1 + \alpha_B \vec{P}_B \cdot \hat{p}_{B'}) \quad (1.37)$$

where  $\vec{P}_B$  is the polarization of the decaying baryon and  $\hat{p}_{B'}$  is a unit vector along the momentum direction of the daughter baryon in the rest frame of the parent hyperon. It is known that some hyperons are produced with a significant polarization [39, 40, 41]. Equation 1.37 can be used to measure the polarization of  $\Lambda$ ,  $\bar{\Lambda}$ ,  $\Xi^0$ ,  $\bar{\Xi}^0$ , if  $\alpha$  is known.

The polarization of the daughter baryon in its own rest frame is

$$\vec{P}_{B'} = \frac{(\alpha + \vec{P}_B \cdot \hat{p}_{B'})\hat{p}_{B'} + \beta(\vec{P}_B \times \hat{p}_{B'}) + \gamma[\hat{p}_{B'} \times (\vec{P}_B \times \hat{p}_{B'})]}{1 + \alpha\vec{P}_B \cdot \hat{p}_{B'}} \quad (1.38)$$

which simplifies to

$$\vec{P}_{B'} = \alpha\hat{p}_{B'}, \quad (1.39)$$

if the parent hyperon is unpolarized. Note that a polarization vector is only simply well defined in the rest frame of the polarized particle, and so the polarization terms in the left hand side of the above equations are measured in the daughter particle rest frame, while those on the right hand side are measured in the decaying particle.

Experimental measurements of  $\beta$  and  $\gamma$  are difficult, requiring measurement of both parent and daughter polarization. However, the measurement of  $\alpha$  can be

made simple, in the case when the daughter baryon itself decays. As an example let's consider the decay of  $\Xi^0 \rightarrow \Lambda \pi^0$  with the subsequent decay of  $\Lambda \rightarrow p \pi^-$ . For the sake of simplicity, we assume  $\Xi^0$  is unpolarized. From Eq. 1.39, the  $\Lambda$  polarization is known to be

$$\vec{P}_\Lambda = \alpha_\Xi \hat{p}_\Lambda. \quad (1.40)$$

The  $\Lambda$  decays in turn to a proton and  $\pi$ , with the proton distribution given by Eq. 1.37

$$\frac{1}{4\pi} \frac{d}{d\Omega} = \frac{1}{4\pi} (1 + \alpha_\Lambda \vec{P}_\Lambda \cdot \hat{p}_p) \quad (1.41)$$

This equation is independent of  $\phi$  angle and can be integrated over this angle. Therefore, using 1.40, Eq. 1.41 can be rewritten as

$$\begin{aligned} \frac{1}{2} \frac{d}{d(\cos\theta)} &= \frac{1}{2} (1 + \alpha_\Lambda \alpha_\Xi \hat{p}_p \cdot \hat{P}_\Lambda) \\ &= \frac{1}{2} (1 + \alpha_\Lambda \alpha_\Xi \hat{P}_\Lambda \cos(\theta)) \end{aligned} \quad (1.42)$$

where  $\hat{P}_\Lambda$  is the unit vector in the direction of  $\Lambda$  polarization in the  $\Lambda$  rest frame. The decay parameter product  $\alpha_\Lambda \alpha_\Xi$  is extracted by measuring the slope of the decay angle  $\theta$  distribution.

### 1.3.3 Weak Radiative Hyperon Decays

Despite their seeming simplicity, weak radiative hyperon decays (WRHD) are theoretically unexplained, and limited experimental data are available [42]. Experimentally, there are only two quantities relevant to the measurement of these decays: their branching fraction and the asymmetry of the photon emission with respect

to the initial spin direction. Despite this, there is only one accurate measurement of a WRHD asymmetry - the decay  $\Sigma^+ \rightarrow p\gamma$ , where the asymmetry is unexpectedly large and negative. [43] Theoretically, these decays are difficult because of the involvement of weak, electromagnetic and strong forces. One recent attempt has indicated that experimental measurements of the two  $\Xi^\circ$  WRHD ( $\Xi^\circ \rightarrow \Sigma^0\gamma$  and  $\Xi^\circ \rightarrow \Lambda\gamma$ ) may resolve some of the questions surrounding this topic [44].

$\Xi^\circ \rightarrow \Sigma^0\gamma$  was measured in 1989, with 85 events observed [45]. The measurement of the branching ratio and asymmetry of the decay was three standard deviations away from the closest theoretical prediction. We observed about 5000 events on top of a background of 1400 at KTeV which hopefully will lead to a more precise branching ratio and asymmetry measurement [46]. Fig 1.5 shows the invariant mass for our data.

A measurement of  $\Xi^\circ \rightarrow \Lambda\gamma$  decay rate was reported in 1990, with 115 signal events [47]. The measurement of the branching ratio and asymmetry differed from the expectation at the  $1\sigma$  level. We collected about 1100 of these events at KTeV during the E799 winter run (Fig 1.6).

#### 1.3.4 Three Body and other Radiative Hyperon Decays

Besides the weak radiative decays, KTeV did well on the other hyperon decays where photons are emitted. A three body hyperon decay is basically an inner bremsstrahlung of the corresponding two body decay mode [48]. We study both Lambda and Cascade three body radiative decays at KTeV. Fig 1.7 shows the mass peak for  $\Lambda \rightarrow p\pi^-\gamma$  for the one day of E799 winter data. Based on the

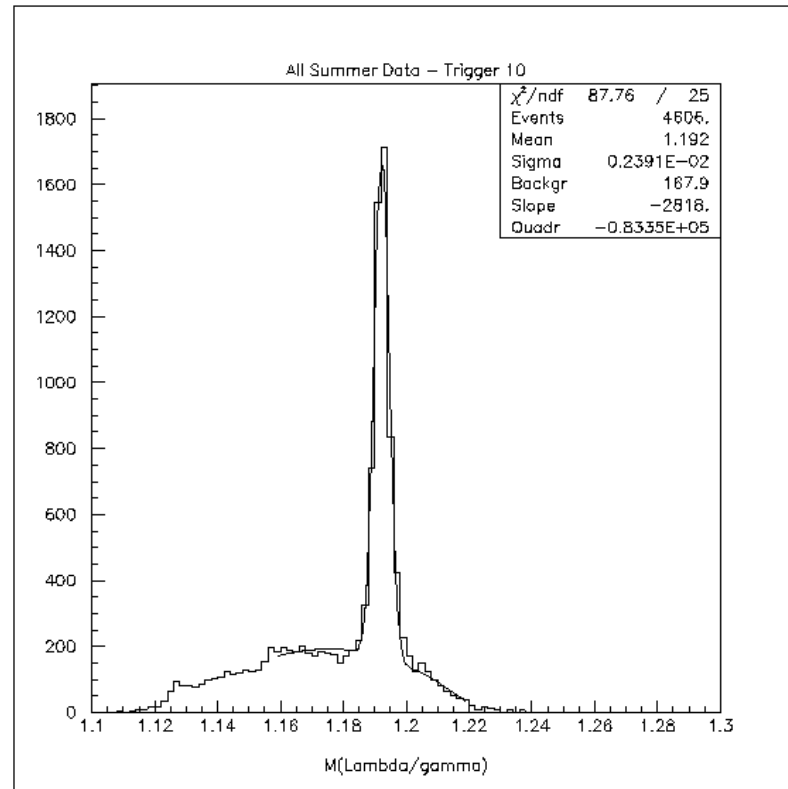


Figure 1.5: The radiative decay of  $\Xi^0 \rightarrow \Sigma^0 \gamma$  for the E799-II summer run.

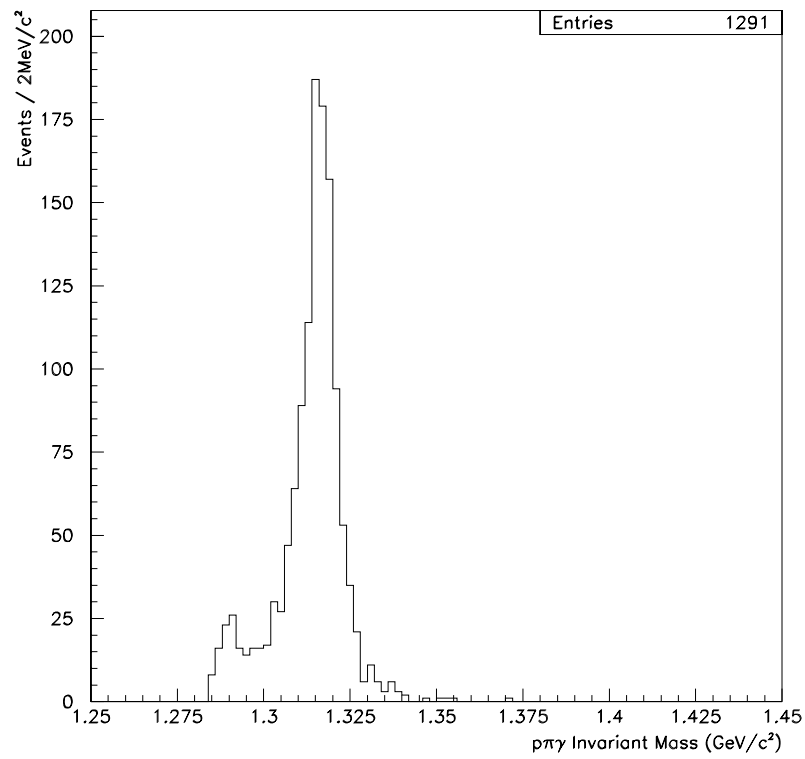


Figure 1.6: The radiative decay of  $\Xi^0 \rightarrow \Lambda\gamma$  for the E799-II winter run.

yield, we estimate about 5000 of these events observable at KTeV. The previous measurement saw 72 events [49].

$\Xi^0 \rightarrow \Lambda \pi^0 \gamma$  decay contrasts with the previous one in that both the final state particles are neutral and thus the inner bremsstrahlung process is presumably not applicable. This means that the branching rate is dominated by direct emission processes. No previous observation or limit has been placed on this decay <sup>5</sup> and little theoretical work has been performed on it [50].

Finally, KTeV was even sensitive to decays of the  $\Sigma^0$  neutral hyperon. None survived from production at the primary target, since they decay at that point and the final state products would not pass all of the filtering, sweeping and collimation of our beamline. However, because we saw more than 5000 events of the type  $\Xi^0 \rightarrow \Sigma^0 \gamma$ , we could use this decay chain to tag rare decays of the  $\Sigma^0$  with a BR down to the  $10^{-3}$  level. One interesting decay to look for is  $\Sigma^0 \rightarrow \Lambda e^+ e^-$ . There is no BR measurement of this decay mode, although an experimental observation of 314 events was made in 1965 [51]. This decay is interesting in that it can be used to measure the relative parity between the  $\Sigma^0$  and the  $\Lambda$ . Alff *et al.*, measured this relative parity to be even. However, they were not able to measure the BR of the decay. KTeV can use the decay  $\Sigma^0 \rightarrow \Lambda \gamma$  followed by dalitz decay of  $\pi^0$  to  $e^+ e^- \gamma$  as the flux normalization mode for the BR measurement. There is one QED prediction from 1958 of the branching ratio to be 0.00545 [52].

---

<sup>5</sup>This decay is not listed in PDG [28]

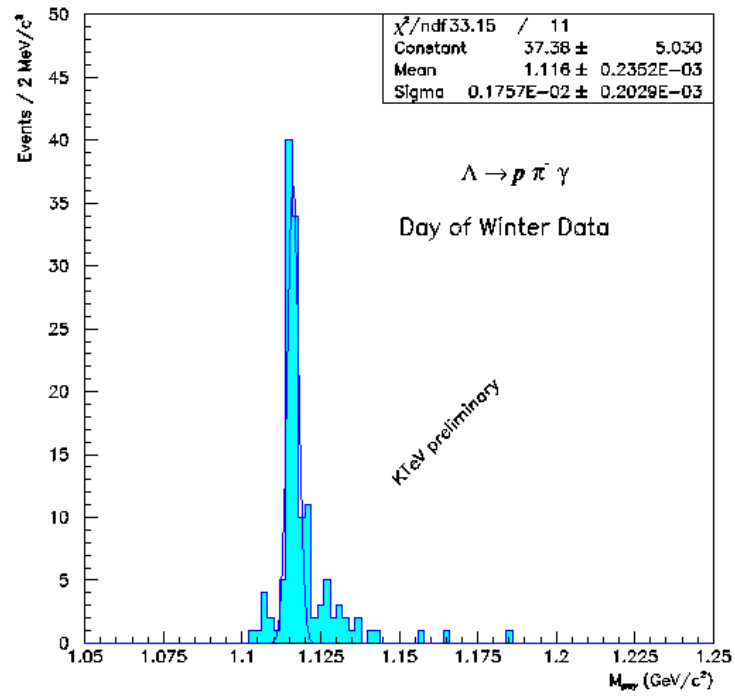


Figure 1.7: The 3-body radiative decay of  $\Lambda \rightarrow p \pi^- \gamma$ . Data corresponds to 5% of the E799-II winter run.

## Chapter 2

# The Beam and Detector

This chapter will describe the beamline and the detector used in this measurement as part of Fermilab E799-II experiment. Both E799-II which was designed to study rare decays of kaons and hyperons and E832 whose goal was to measure the direct CP violating parameter  $\epsilon'$  are referred to as “ the KTeV” experiment. They used the same beamline and detector with slightly different setups.

The E799 data were collected in two periods, from January to March of 1997 (known as the “winter run”) and from August to September of 1997 (known as the “summer run”).

## 2.1 The Beamline

The Fermilab Tevatron supplied 800 GeV protons during a  $\sim 23$  second period “spill”, approximately once every minute. Within each spill, there was a 53 MHz “bucket” structure due to the accelerator radio frequency (RF) of the Tevatron. This RF signal was used in our experiment so that the trigger could be synchronous with this substructure in the spills. The buckets were separated by 19 nsec, and the protons arrived in a 2 nsec period at the beginning of each bucket. The target



typically received  $4.5 \Leftrightarrow 5.0 \times 10^{12}$  protons per spill for the winter run, and  $3.5 \times 10^{12}$  for the summer run.

The primary beam of protons then were tuned to be incident on a beryllium oxide target which was 30.5 cm long ( $\sim 0.9$  nuclear interaction lengths) with a cross section of  $3.0 \text{ mm} \times 3.0 \text{ mm}$ . The targeting angle was chosen to be 4.8 mrad in the vertical plane so that we could eliminate most of neutrons from the beam and still maintain a high neutral kaon flux to reach the decay volume of the experiment. The horizontal targeting angle was set to be very small (less than 0.02 mrad). It was essential that the beam impinge accurately on the target and be stable. Table 2.1 summarizes the specification of the KTeV primary beam. [53]

Table 2.1: KTeV primary beam specification

Proton beam energy	800 GeV
Proton intensity	$5.0 \times 10^{12}$
Length of run	1 year
Targeting angle	-4.8 mr (vertical), <0.02mr (horizontal)
Targeting angle variability	-4.0 mr to -5.6 mr
Beam size at the target	$\leq 250\mu\text{m}$ (horizontal and vertical)
Beam spot stability	$\leq \pm 50\mu\text{m}$ (horizontal and vertical)
Beam position stability	$\leq \pm 100\mu\text{m}$ (horizontal and vertical)
Beam angle stability	$\leq \pm 25\mu\text{m}$ (horizontal and vertical)

Secondary particles leaving the target were formed into two nearly parallel

neutral beams by a series of collimators, absorbers, and sweeping magnets located downstream of the target as shown in Fig. 2.1.

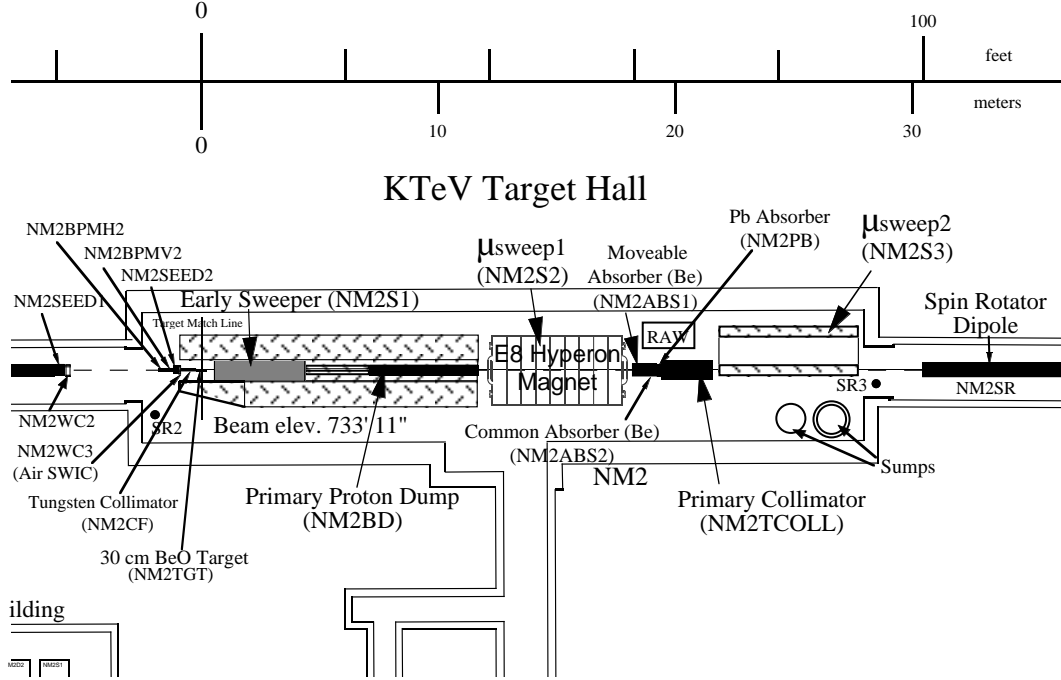


Figure 2.1: Schematic plan view of the collimation and sweeping system.

A lead absorber was placed at 18.5 m downstream of two sweeping magnets and a copper beam dump to convert photons to electron-positron pairs which would be removed by other two sweeping magnets. Two nearly parallel neutral beams were then defined by the “primary collimator”, at  $z=19.8$  m. There was two holes,  $1.09 \text{ cm} \times 1.09 \text{ cm}$  each, at the upstream end of the collimator where the centers of the holes were separated by 3.19 cm.

We used two different sizes of beam. For the winter run, the solid angle of each beam was collimated to  $0.5 \text{ mrad} \times 0.5 \text{ mrad}$  known as “small beam”. For the

summer run, this angle was increased to  $0.7 \text{ mrad} \times 0.7 \text{ mrad}$ , known as “large beam”.

There were two more collimators further downstream (not shown in the figure). The “slab collimator” was used to eliminate particles with high transverse momentum which could cross-over the beams. The “defining collimator” at  $z=85.0 \text{ m}$  was placed to trim and define the edges of the two beams.

The “spin rotator” dipole magnet (shown in the picture) was the only magnet whose magnetic field pointed in the horizontal direction (defined as  $x$  axis). All the four sweeping magnets had their magnetic field downwards in the vertical direction. Knowing that  $\Xi^0$  and  $\Lambda$  hyperons are produced polarized, with their polarization being perpendicular to the production plane, the sweeping magnets could be tuned to rotate the polarization vector in the beam direction (defined as  $z$  axis). The spin rotator could then be used to rotate this vector into the vertical direction, allowing the measurement of the hyperon polarization (see Sec. 1.3.2). The polarity of this magnet was flipped on a daily basis.

Finally, there was a “final sweeping magnet” at  $z=90 \text{ m}$  just upstream of the decay volume to sweep all the remaining charge particles in the beams. Short lived particles in the neutral beam, like  $K_S$  ( $c\tau \sim 2.7 \text{ cm}$ ) and to a lesser extent  $\Lambda$  ( $c\tau \sim 7.9 \text{ cm}$ ) and  $\Xi^0$  ( $c\tau \sim 8.7 \text{ cm}$ ), decayed before reaching the decay volume of the experiment about  $94 \text{ m}$  downstream of the target, enhancing the percentage of  $K_L$  ( $c\tau \sim 15.5 \text{ m}$ ). The ratio of the number of neutrons to the number of  $K_L$ 's was about 3 for E799 beam. Flux calculations show, the number of  $\Lambda$ 's and  $\Xi^0$ 's reaching the decay volume were approximately 2% and 0.2% of the number

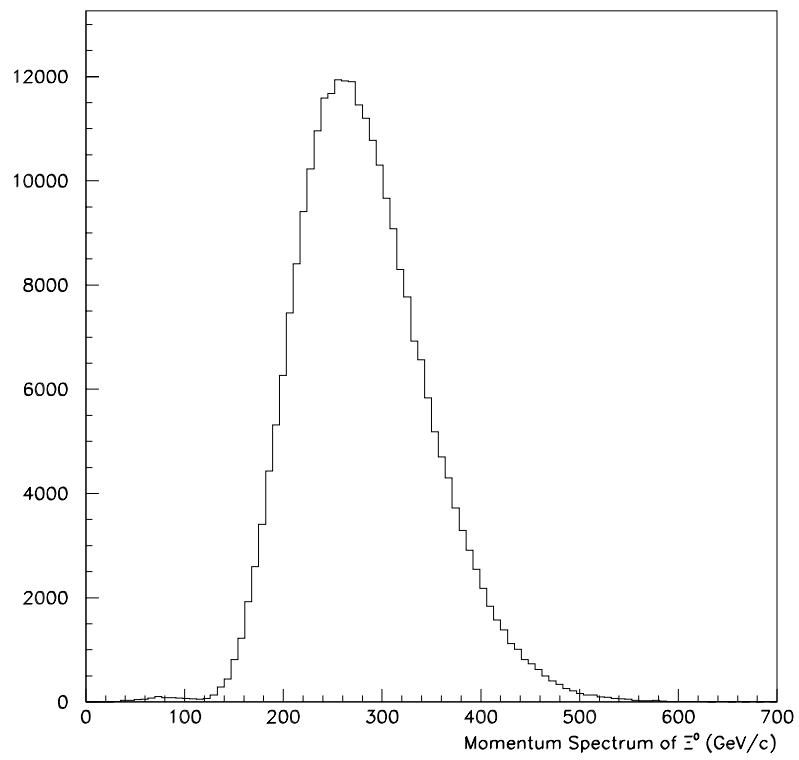


Figure 2.2: The momentum spectrum of  $\Xi^0$  particle. Only high momentum hyperons reach the KTeV detector. The kaon spectrum peaks at about 40 GeV/c.

of  $K_L$ 's, respectively. Due to their short life time, only high momentum  $\Lambda$ 's and  $\Xi^0$ 's survived at this point. Figure 2.2 shows the momentum spectrum of  $\Xi^0$  in the decay volume of the experiment.

In order to reduce the interaction of the beam with materials, the decay volume was in a vacuum with a pressure  $\sim 1.0 \times 10^{-6}$  Torr. In fact, the vacuum tank started at  $z=50$  m. The end of the tank was sealed by a window with a diameter of 0.9 m made of Kevlar and aluminized mylar, referred as the “vacuum window”.

## 2.2 The E799 Detector

The detector is shown in Figs. 2.3 and 2.4, and the  $z$  positions and the transverse dimensions of the detector elements most relevant for hyperon analysis are listed in Table 2.2.

We first define the coordinate system used. The origin of the coordinate system was center of the production target, and the line from the production target to the center of the CsI electromagnetic calorimeter is defined as the  $z$  axis. The neutral beam travels in positive  $z$  directions. The  $y$  coordinate is defined to be vertical, with upward direction to be positive, and the positive  $x$  direction is then towards the left (or “west”) when viewed from upstream to require a right-handed coordinate system.

The individual elements of the detector are described below.

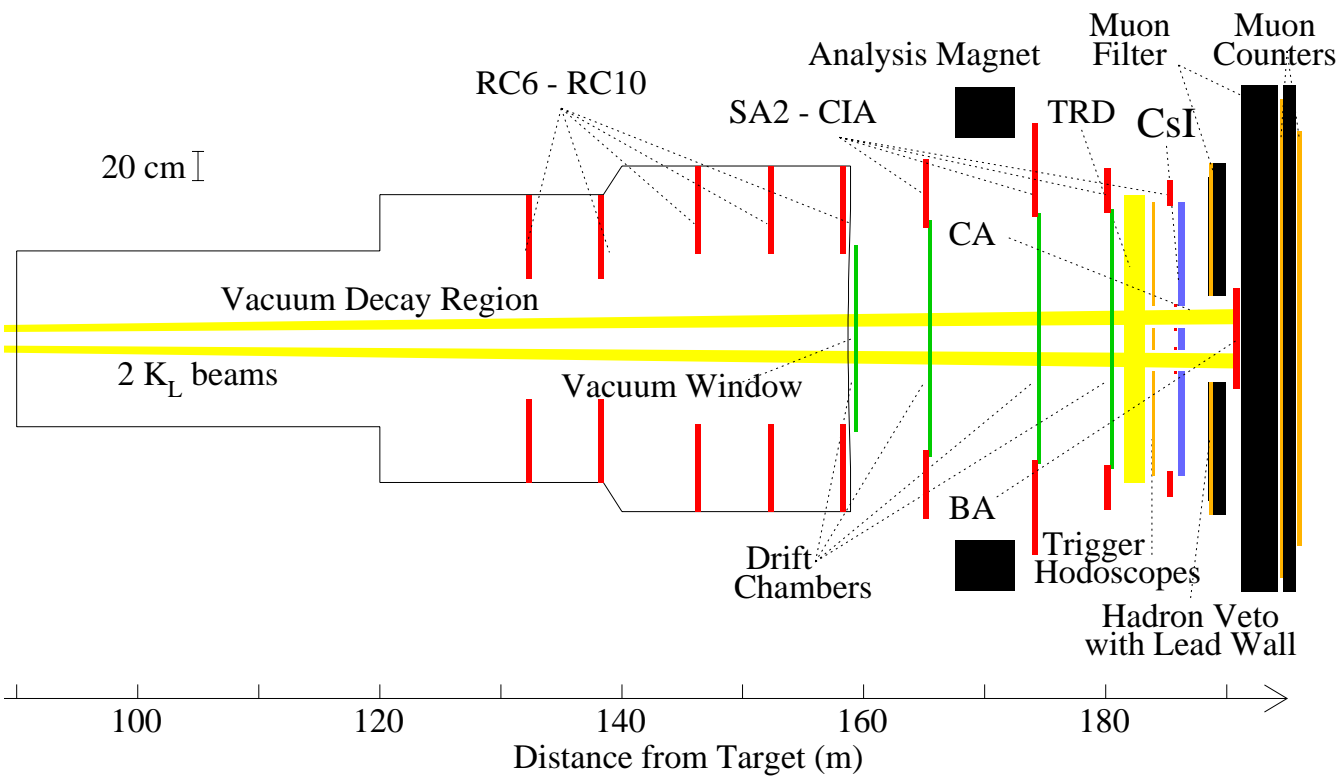


Figure 2.3: Schematic drawing of KTeV detector (E799 configuration). The scale in the  $y$  direction is expanded for clarity.

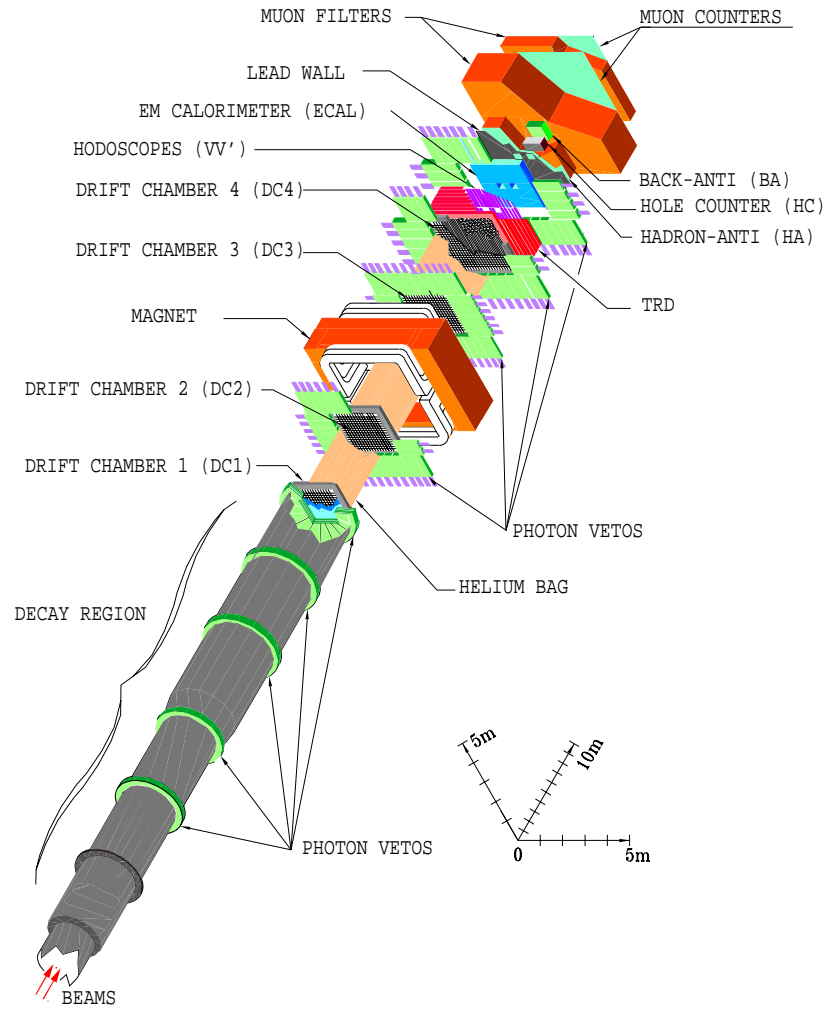


Figure 2.4: Three dimensional view of KTeV/E799 detector.

Table 2.2: Positions and Dimensions of the detector elements. The positions are given at the front face of the detector with respect to the target.

Detector Element	Position(m)	Transverse Size(m)
Vacuum Window	158.89	-
DC1( $x$ plane)	159.42	$1.30 \times 1.30$
DC2( $x$ plane)	165.56	$1.64 \times 1.44$
Analyzing Magnet	170.01	inner: $2.9 \times 2.0$
DC3( $x$ plane)	174.59	$1.74 \times 1.64$
DC4( $x$ plane)	180.49	$1.90 \times 1.90$
TRD1	181.17	$2.18 \times 2.18$
TRD8	183.36	$2.18 \times 2.18$
V bank	183.90	$1.90 \times 1.90$
V' bank	183.95	$1.90 \times 1.90$
CsI	186.01	$1.90 \times 1.90$
HA	188.97	$2.24 \times 2.24$
Mu2	194.83	$3.93 \times 2.99$
Mu3X	196.59	$3.93 \times 2.99$
Mu3Y	196.63	$3.93 \times 2.99$



## 2.3 The Spectrometer

The main measurement apparatus for charged particles was a charged spectrometer which consisted of four drift chambers (DC's), two on each side of an analyzing magnet as shown in Figs. 2.3 and 2.4. Helium bags were placed between the drift chambers to reduce the effects of multiple scattering on the measurement of particle trajectories and momenta.

Each chamber contained four planes of sense wires, two each in the  $x$  and  $y$  views referred to as  $X$ ,  $X'$ ,  $Y$ , and  $Y'$  planes. The sense wires were  $25\text{ }\mu\text{m}$  gold-plated tungsten, while the field shaping wires were made of  $100\text{ }\mu\text{m}$  gold-plated aluminum. The field wires formed a hexagonal "cell" around each sense wire as shown in Fig. 2.5.

The wires in a sense plane were separated by 12.7 mm. The two sense planes in each view, offset by 6.35 mm or a cell size <sup>1</sup>, were staggered to resolve the two-fold ambiguity that results from ionization drifting towards the nearest wire, rather than in a specific direction. The four chambers were of different sizes (Table 2.3), with the largest downstream, to increase acceptance for high angle tracks.

The chambers were filled with a mixture of 49.75% Argon, 49.75% Ethane, and 0.5% isopropyl alcohol by volume. For the summer run we changed the mixture to 49.5% Argon and 49.5% Ethane with 1.0% isopropyl alcohol for additional

---

<sup>1</sup>A cell size is sometimes defined as the distance between two adjacent sense wires in a plane (or the diameter in the hexagonal cell) which is 12.7 mm. However, half of this distance which is the distance between a field wire and a sense wire at the center of the hexagonal, corresponds to the maximum drift distance for our chambers and therefore a more natural unit to refer to.

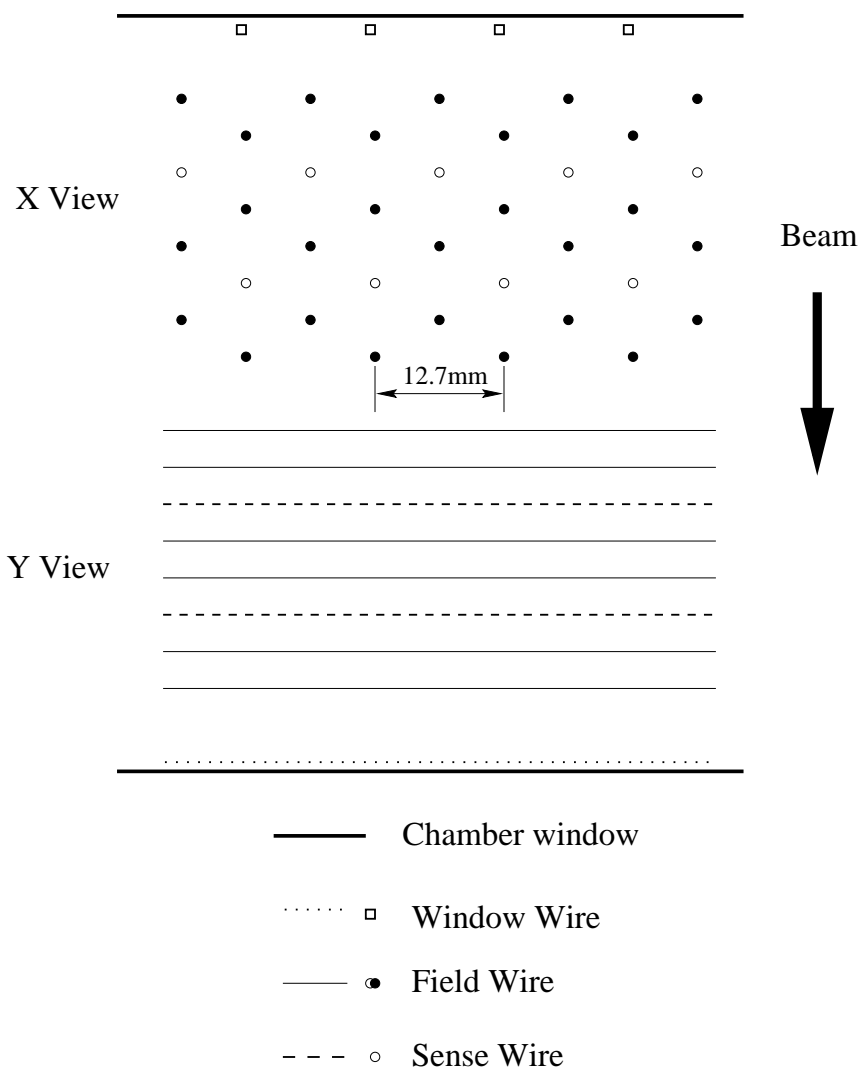


Figure 2.5: The drift chamber sense and field wire geometry, viewed from the above, along the vertical  $x$ -sensing wires.

quenching. When charged particles passed through the gas, they produced a trail of electron-ion pairs, electrons being drifted towards the sense wires, while the ions drifted towards the field wires. With the typical applied voltage of -2450 to -2550V to the field wires relative to the sense wires, the electron drift velocity was of the order of  $50 \mu\text{m}/\text{nsec}$  and was roughly constant over much of the active chamber volume.

The signals from the drift chambers were then amplified and discriminated by electronics located on cards mounted on the chambers' frames [54]. The discriminated signals with 40 nsec width were fanned out to the trigger system and a set of LeCroy 3377 Time-to-Digital converters (TDC's) with a resolution of 0.5 nsec. A common stop was provided to the TDC's by the Level 1 trigger signal.

By converting the drift time measured at the TDC's to a drift distance, a position measurement could be made from each chamber wire hit with an accuracy of about  $100 \mu\text{m}$ . The details of the chambers' calibration, alignment and performance are discussed in Chapter 5.

The  $2.9 \times 2.0 \text{ m}$  analyzing magnet applied a nominal  $p_t$  (transverse momentum) kick of 205 MeV to the charged particles corresponding to a vertical field of about 2 kG. The magnet, located at  $z = 170.00\text{m}$ , was placed between DC2 and DC3. The magnetic field would simply bend the straight  $x$ -view tracks between the two chambers and the momentum of charged particles could be measured from this bending angle.

The drift chambers' intrinsic resolution was measured to be

$$\frac{\sigma_p}{p} = 0.016\% \times p + 0.38\% \quad (2.1)$$

Table 2.3: Drift chamber sizes, measured in wires per sense plane.

DC number	View	Number of sense wires per plane
1	X	101
1	Y	101
2	X	128
2	Y	112
3	X	136
3	Y	128
4	X	140
4	Y	140

where  $p$  is the momentum of a charged particle in GeV/c. The first term comes from multiple scattering in the spectrometer and the second term from the spatial resolution of the chambers.

## 2.4 The Transition Radiation Detectors

The main particle identification for the  $\Xi^0 \rightarrow \Sigma^+ e^- \bar{\nu}_e$  analysis came from the CsI calorimeter for which the  $\pi/e$  discrimination was better than 500:1 for 90% electron acceptance. The E799 detector used a Transition Radiation Detector (TRD) system to enhance  $\pi/e$  discrimination by adding a 276:1 rejection for 90% electron acceptance. This extra factor was necessary to increase the sensitivity for some kaon rare decays such as  $K_L \rightarrow \pi^0 e^+ e^-$ . It was also necessary to identify and tag

$\Lambda \rightarrow pe^- \bar{\nu}_e$  decays from the principal decay of  $\Xi^0$ ,  $\Xi^0 \rightarrow \Lambda \pi^0$  whose decay topology is almost exactly similar to the dominant decay of  $\Lambda \rightarrow p\pi^-$  (Sec. 6.5). We could use the TRD's to remove some background events of the decay  $\Xi^0 \rightarrow \Sigma^+ e^- \bar{\nu}_e$ . However, since the background was small and fairly well under control, and the Monte Carlo simulation of TRD's was not implemented completely at the time, we decided not to use them for the BR measurement.

Eight TRD's of  $2.1 \text{ m} \times 2.1 \text{ m}$  were placed between drift chambers and the trigger hodoscopes. Figure 2.6 shows the schematic layout of the TRD design. The details of construction and performance of the TRD's can be found in the final design report [55]. Presented here is only a brief description of the most important features of this detector system [56].

Each TRD consisted of a radiator, an active MWPC volume, and two buffered gas volumes. The radiator to produce 10 keV TR X-rays was a 15 cm thick polypropylene fiber mat (density of  $0.5 \text{ g/cm}^3$ ). There were two beam holes in the radiator with a size of  $15.5 \text{ cm} \times 15.5 \text{ cm}$  each to reduce beam interactions. The gas volumes and radiators were segmented by aluminized mylar, called the entrance window. MWPC consisted of vertically mounted cathodes and anodes. The cathode was a wire plane consisting of  $85 \text{ }\mu\text{m}$  diameter Be-Cu wires with 2.5 mm spacing. The entrance window was kept at a slightly higher voltage than the cathode forming a 1.5 mm mini-drift gap. The anode to cathode gap was 6.5 mm, and the anode was a wire plane consisting of  $25 \text{ }\mu\text{m}$  diameter gold plated tungsten wires with a 5 mm spacing. The planes were lined up so that each anode wire sat directly behind a cathode wire. The anode wires were ganged into

channels consisting of two wires each in the central 60 cm covering the two beam holes with an effective pitch of 1 cm. In the outer region, 4 wires were summed into a channel with an effective pitch of 2 cm. This gave a total of 112 channels/plane, or 224 channels/chamber. Therefore, there were 1792 channels for the 8 chambers.

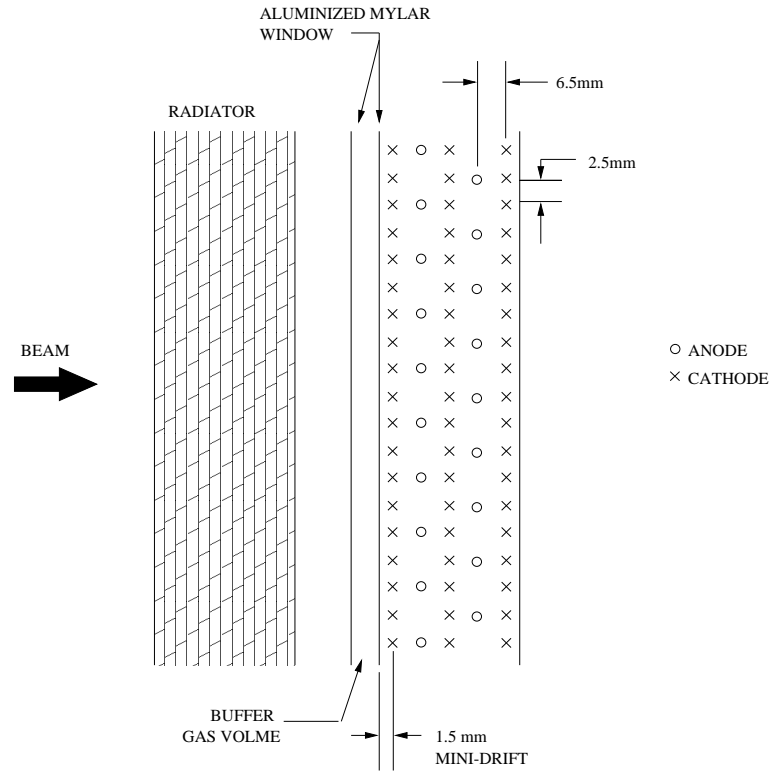


Figure 2.6: The schematic layout of the TRD detector.

The gaseous detector needed at least 24 mm of Xenon gas for good X-ray detection. The ionization energy loss could fake a TR signal and reduce the  $\pi/e$  separation ability. To achieve a high yield of TR and to minimize the ionizing energy deposit, a gas mixture of 80% Xe and 20%  $\text{CO}_2$  was chosen. Since a 0.1%

change in concentration of main components could result in a 1% change in gain, the composition of active volume gas was monitored by gas chromatography system at 100 ppm levels. With the operating high voltage of -2400V, the gas mixture gave a drift velocity of 5 cm/ $\mu$ sec. The voltage was automatically regulated by monitoring the gas pressure so that each chamber maintained the same gain. This was necessary for two reasons. First, since a TRD is a detector that measures the pulse height to look for X-rays above a minimum ionization signal, any variation in gain would have caused changes in the  $\pi/e$  rejection and the performance for particle identification would vary with temperature and pressure variations. Secondly, the TRD system also used the pulse height information on-line to generate a level 2 trigger. Variation of the gain would cause changes in trigger condition which would be unacceptable for physics analysis.

The buffer volume was filled with a safe gas of  $C_2F_6$  that was X-ray transparent and had the same order of density as Xenon so that it helped to support the entrance window. This kept the inner aluminized window flat to within 100  $\mu$ m.

The pulse from each channel was sent to the preamp mounted directly on the chamber. The preamp amplified the current pulse to produce an output voltage directly proportional to the input charge. It had a high gain of  $\sim 40$ . The output of the preamp was differential to improve noise rejection, and was passed into a postamp by a cable whose length was a part of time delay requirement of the trigger system. The postamp first translated the differential input into a single-ended signal. Next, the pulse was shaped so that the length of the pulse tail was reduced. That would keep the ADC gate width as narrow as possible to

minimize accidentals. The shaped pulse was finally sent to a low gain amplifier stage. This additional stage of amplification allowed the signal channel to be tuned for optimizing its gain.

After the second amplification, an output was sensed by Analog-to-Digital-Convertors (ADC) (LeCroy 4300B FERA ADC) with a gate width of 300 nsec through co-axial RG-58 cables. Another output after the pulse shaping was discriminated also at the front end of TRD, and used to form a second level trigger signal.

## 2.5 The Trigger Hodoscopes

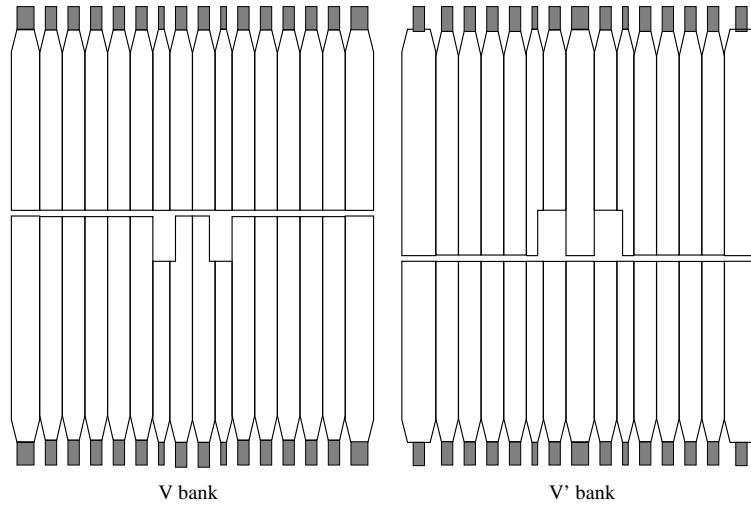


Figure 2.7: Schematic drawing of  $V$  and  $V'$  bank front view.

The first level trigger used two planes of vertical scintillator hodoscopes, labeled as  $V$  and  $V'$  bank counters, upstream of the CsI calorimeter. The hodoscopes could count the number of charged particles reaching the calorimeter.



Figure 2.7 shows the geometry of the hodoscopes. They had a dimension of  $1.9 \text{ m} \times 1.9 \text{ m}$  with two beam holes cut in the counters. Five different width counters were used: 9.92 cm, 11.82 cm, 13.74 cm, 15.63 cm and 17.76 cm. Both  $V$  and  $V'$  banks consisted of 1 cm thick scintillators viewed by PMT's mounted through light guides.

## 2.6 The Electromagnetic Calorimeter

The electromagnetic calorimeter consisted of 3100 blocks of pure CsI crystals. Each crystal had a length of 50 cm (about 27 radiation lengths and 1.4 nuclear interaction lengths). 2232 of the crystals in the inner region ( $1.2 \text{ m} \times 1.2 \text{ m}$ ), had a cross section of  $2.5 \text{ cm} \times 2.5 \text{ cm}$  with two beam holes of size  $15 \text{ cm} \times 15 \text{ cm}$  as shown in Fig. 2.8. The beam holes allowed the neutral beam to pass through without interacting. The other 868 crystals in the outer region had a cross section of  $5 \text{ cm} \times 5 \text{ cm}$ . The length of the crystals was chosen to achieve excellent energy resolution and linearity. However, the difficulties in manufacturing such long crystals required that about 80% of them were processed from two halves (25 cm long each) glued with Epo-Tek 305 epoxy, which was chosen for its high UV transmission. The rest were uniform single crystals.

In a totally active calorimeter, the parameters which affect the energy resolution and linearity are scintillation light yield and scintillation uniformity. On average, the actual light yield for the crystals were 20 photo-electrons per MeV which resulted in a less than 0.4% of energy resolution for energies greater than 3 GeV. The individual crystals were wrapped by mylar with thickness of  $13 \mu\text{m}$

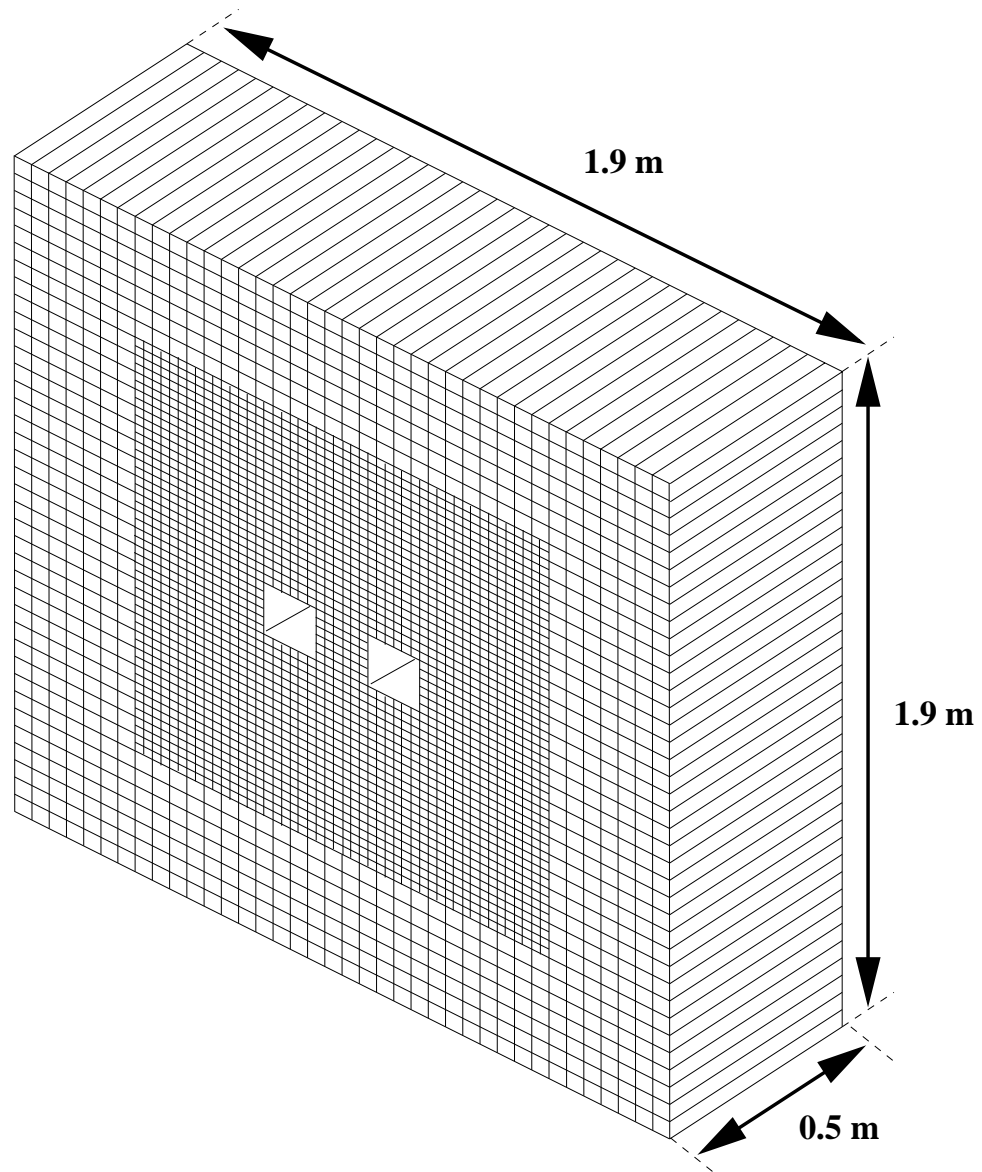


Figure 2.8: Beam view of the KTeV CsI calorimeter array.

to optically isolate each crystal and optimize the uniformity of the scintillation response [57].

The scintillation spectrum could be approximately characterized by a “fast” and a “slow” component. The fast spectrum peaked at a wavelength of 315 nm with a time constant of  $\sim 20$  nsec, while the slow component peaked at 420 nm and had a time constant of  $\sim 1$   $\mu$ sec. From 80% to 90% of the scintillation light was emitted within 100 nsec.

The CsI array was housed in a light-tight blockhouse where the temperature was controlled to  $\pm 0.1^\circ\text{C}$ . This would reduce the gain fluctuations due to the temperature variations. Besides, the blockhouse environment was kept dry with a humidity of 4% or lower to protect the crystals which were slightly hygroscopic. The temperature and humidity of the blockhouse were monitored at several locations and displayed by the KTeV slow control system described in Sec. 4.2.

The scintillation light produced by electromagnetic showers in the CsI crystal was detected by a photomultiplier tube (PMT) mounted on the back of each crystal. The large crystals used six-stage-dynode 1/2 inch Hamamatsu R5330 PMT's, and the small crystals used five-stage-dynode 3/4 inch Hamamatsu R5364's. Both types of the PMT's had a gain of 5000 with a typical high voltage of  $\approx 1200$  V.

The signals from each crystal were then digitized by a Digital PMT base, or DPMT [58]. The DPMT was an auto-ranging device, with eight binary ranges. The input current,  $I$ , was split into eight binary ranges, *i.e.* into  $I/2$ ,  $I/4$ ,  $I/8$ ,  $I/16$ ,  $I/32$ ,  $I/64$ ,  $I/128$ , and  $I/256$ . Then each of the eight split currents were integrated, with a clock speed up to 53 MHz. Next, it was determined which of

the eight binary ranges were *inrange*, and the integrated current from this range was digitized with an 8-bit FADC. Thus the DPMT produced an 8 bit mantissa and a 3 bit exponent, for 16 bits of dynamic range. The DPMT's had a very low noise level (less than 1MeV), and they had a wide dynamic range. The DPMT's were calibrated using a laser flasher system. After calibration, additional nonlinearity due to the DPMT was well under 1%.

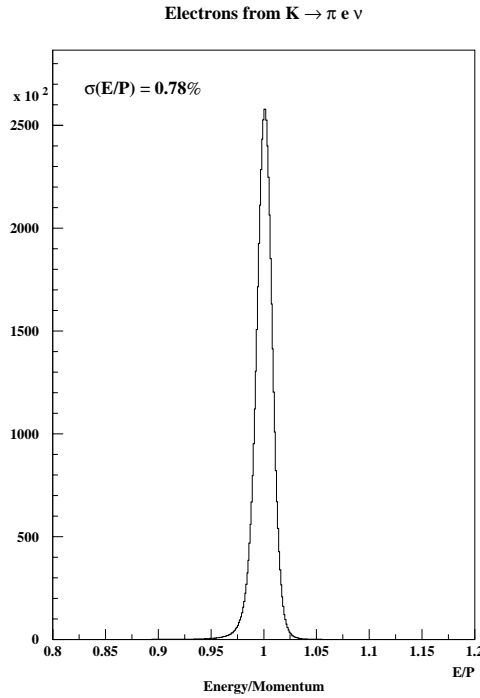


Figure 2.9:  $E/p$  for electron in  $K_{e3}^0$ 's, where  $E$  is the energy measured at the calorimeter, and  $p$  is the momentum measured by the spectrometer.

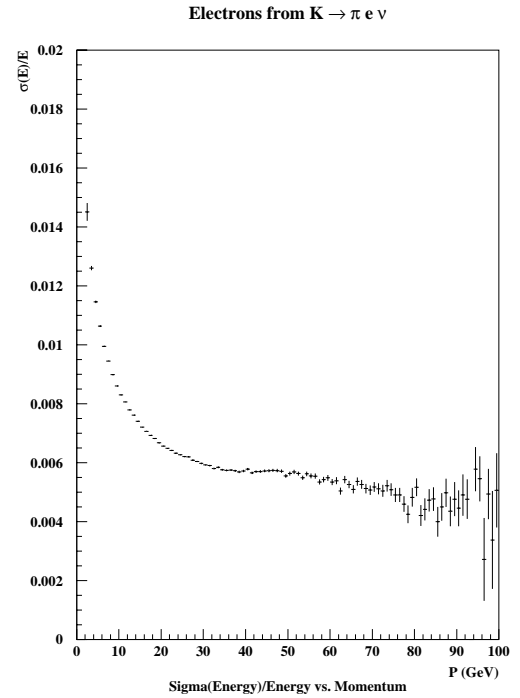


Figure 2.10: The calorimeter's intrinsic energy resolution measured in  $K_{e3}^0$  events as a function of electron momentum.

The CsI calorimeter was used to measure the energy and position of electrons

and photons. It was also used as a particle identification detector for  $e/\pi$  separation. Figure 2.9 shows  $E/p$  for electron in  $K_{e3}^0$  events, where  $E$  is the energy measured by the CsI calorimeter and  $p$  represents the electron momentum measured by the spectrometer. Since the CsI crystals were 27 radiation lengths long, electrons deposited almost all of their energy in the calorimeter and had a peak of unity in the  $E/p$  distribution. Due to a finite resolution in momentum measurements, the  $E/p$  was smeared with the resolution expressed in Eq. 2.1. Subtracting the resolutions in  $p$  in quadratures, the intrinsic resolution of the calorimeter is shown in Fig. 2.10 as a function of electron momentum. The energy dependence had a form of

$$\frac{\sigma_E}{E} = 0.45\% + \frac{2.0\%}{\sqrt{E}} .$$

The  $1/\sqrt{E}$  dependence resulted from photo-statistics in scintillation light. The constant term of 0.45% accommodated other effects such as non-uniformity in light collection efficiency, uncorrected light leakage, internal calibration error, fluctuation of light yield due to temperature variation, electronic noise etc [59].

In summary, the CsI calorimeter was able to measure the position of the electromagnetic showers with a precision better than 1.0 mm. The energy resolution was better than 1% for energies above 4 GeV, and the  $e/\pi$  rejection was about 500 : 1.

## 2.7 The Photon Veto System

We used various photon veto elements to insure that no photon or charged particle could escape the fiducial volume of the detector. We describe the four types of

photon veto counters used in E799 in this section [20].

Table 2.4: Positions and Dimensions of the photon veto elements. The positions are given at the front face of the detector with respect to the target.

Veto Element	Position(m)	Transverse Size(m)
RC6	132.60	inner: $0.84 \times 0.84$ , outer radius: 1.00
RC7	138.60	inner: $0.84 \times 0.84$ , outer radius: 1.00
RC8	146.60	inner: $1.18 \times 1.18$ , outer radius: 1.44
RC9	152.60	inner: $1.18 \times 1.18$ , outer radius: 1.44
RC10	158.60	inner: $1.18 \times 1.18$ , outer radius: 1.44
SA2	165.12	inner: $1.540 \times 1.366$ , outer: $2.500 \times 2.500$
SA3	173.99	inner: $1.692 \times 1.600$ , outer: $3.000 \times 2.400$
SA4	180.02	inner: $1.754 \times 1.754$ , outer: $2.372 \times 2.372$
CIA	185.19	inner: $1.842 \times 1.842$ , outer: $2.200 \times 2.200$
CA	185.91	inner: $0.150 \times 0.150$ , outer: $0.180 \times 0.180$
BA	191.09	$0.60 \times 0.30$

Table 2.4 lists the z positions and the transverse dimensions of the photon veto elements. Each photon veto counter had a sandwich structure of radiators and scintillators. The light yield in the scintillator was detected by PMT's. Five "Ring Counters" (RC6-RC10) were located inside the vacuum decay volume, upstream of all other detectors. They had a round shape at outside, to fit the shape of the cylindrical vacuum tank as shown in Fig. 2.11. They consisted of 24 layer

scintillator tiles with a thickness of 2.5 mm followed by lead sheets. For the first 16 layers, the lead sheets were 0.5 radiation lengths ( $X_0$ ) each. For the rest of 8 layers, the lead was 1  $X_0$  thick each, resulting in a total amount of lead to be 16  $X_0$ .

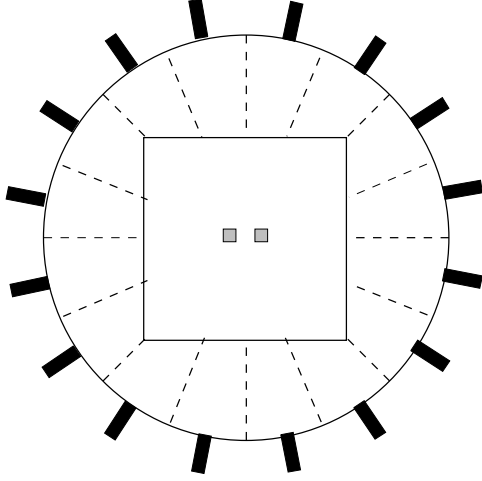


Figure 2.11: A typical RC viewed from upstream, located inside the vacuum region. The RC's dimensions are shown in Table 2.4.

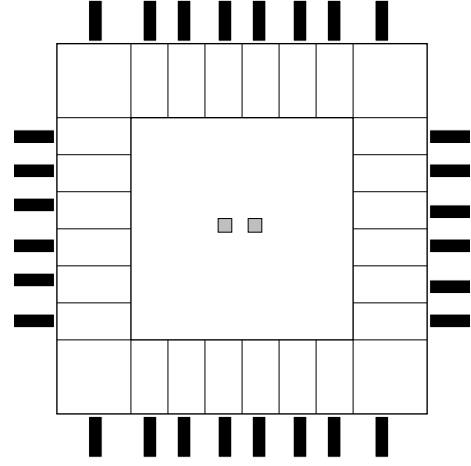


Figure 2.12: SA4 viewed from upstream. SA's and CIA had different dimensions as shown in Table 2.4.

There were three “Spectrometer Antis” (SA2-SA4) outside and just upstream of drift chambers 2 to chamber 4. The CsI Anti (CIA) covered outside of the CsI calorimeter. The rectangular shape of SA and CIA matched the outer shape of the drift chambers and the CsI calorimeter as shown in Fig. 2.12. The general configuration of the three SA's and the CIA were the same. Their sandwich structure consisted of 32 layers of lead sheets with a thickness of 0.5  $X_0$  each, and scintillators with a thickness of 2.5 mm, leading to 16  $X_0$  lead in total similar to

the RC's.

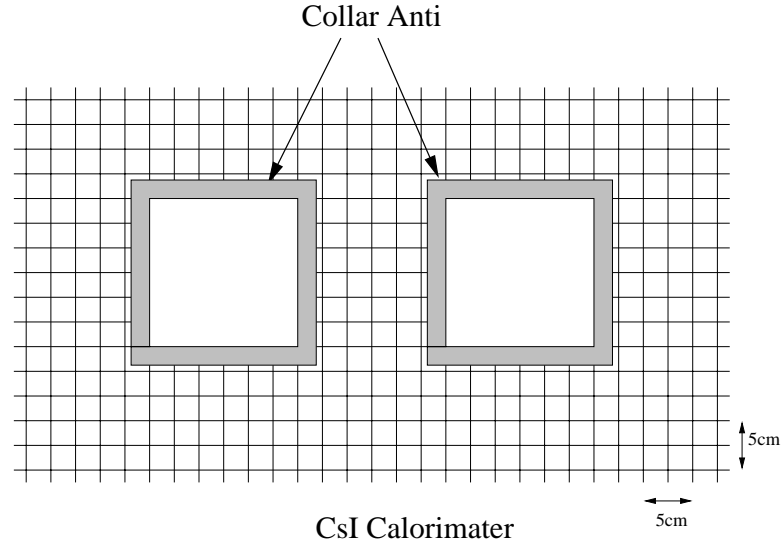


Figure 2.13: The Collar Anti located just upstream of the CsI calorimeter.

The “Collar Anti” (CA) was located in front of the calorimeter and just around the beam holes like a picture frame (Fig. 2.13) to catch the events that wouldn’t deposit energy in the CsI completely. It consisted of 3 layers of 1 cm thick scintillator followed by a layer of  $2.9 X_0$  tungsten.

The “Back Anti” (BA) was placed downstream of the calorimeter and in the beam region to detect the photons and charged particles going down the beam holes. It was composed of a 60 layer lead-scintillator sandwich, and a total depth of lead of 30 radiation lengths or one nuclear interaction length. BA was divided into 3 parts, 10 radiation lengths each, longitudinally to distinguish electromagnetic and hadronic showers from their shower shapes. The first two sections were to detect photons and the last to detect hadrons.



## 2.8 The Hole Counters

A typical hyperon decay at KTeV produced a high momentum proton (or anti-proton) which stayed in the beamline. In order to trigger on such events, a small fast scintillator counter, known as a “Hole Counter” (HC) was placed in each beamline in back of the CsI calorimeter in the hole of the Hadron Anti (Sec. 2.9) steel filter [60]. Each counter was  $6.296 \times 6.296 \text{ in}^2$  ( $16 \times 16 \text{ cm}^2$ ), and 0.0625 inch thick. The scintillator material was Bicron 404 plastic organic scintillator. Lucite light pipes of 0.0625 in thickness made of 10 fingers of various widths, from 7/16 to 3/4 inch, were glued to the upper edge of the scintillator with Bicron 600 UV optical glue. The lucite light pipes were bent at a right angle and then twisted by heat treatment to map on the 0.75 inch diameter photo cathode of a Hamamatsu R3082 photo tube. The HC’s were operated 50 V above the plateau point which was done with a cosmic ray telescope trigger. The typical operating voltage used at KTeV was 1250 V. The  $z$  location from the target of these counters were 189.6 meters, with a large error of .01 meters. Each counter was wrapped in two layers of black mylar, 0.5 mil thick, that had an  $0.008 \mu\text{m}$  reflective Aluminum coating on the side facing the scintillator material.

## 2.9 The Hadron Anti and Muon Counters

A bank of scintillator hodoscopes, called “Hadron Anti” (HA), was located downstream of the CsI calorimeter immediately after a lead wall (at  $z=188.5 \text{ m}$ ) [61]. The HA was used to reduce the trigger rate by vetoing the events producing charged pions or muons. In particular, for the hyperon trigger, HA reduced the

trigger rate by a factor of about 3.5 by vetoing on the pions from the decay of  $\Lambda$ ,  $\Lambda \rightarrow p\pi^-$ . Figure 2.14 shows HA's configuration and dimensions. The HA was placed upstream of the BA as far as possible to minimize the rate due to backplash radiation from the BA and the neutral beam dump. Both the lead wall and the HA had a single large ( $34 \text{ cm} \times 64 \text{ cm}$ ) beam hole to let the photons going into beam holes be detected by the BA (sec. 2.7). Also, there was a 1 m thick steel wall with a proportionally large hole placed downstream of the HA to shield it from the backplash. The lead wall was used to produce hadron showers and to absorb leakage of electromagnetic showers from the calorimeter. The thickness of that was chosen to be 15 cm (0.9 interaction lengths). The light yield produced by the scintillation counter was detected by PMT's. The first level trigger used an analog sum from all the HA counters as an input.

The three Muon Counters (MU2, MU3Y and MU3X) were the most downstream detector elements in the experiment [62].

The MU2 hodoscope consisting of vertical scintillation counters was placed downstream of the BA after the neutral beam dump and an additional 3 m thick steel. Mostly muons were expected to survive such a large amount of material. MU2 was designed to reduce the trigger rate by rejecting events decaying to muons. It had to have a very large transverse dimension to be able to catch the muons which were further scattered in the steel. The other two hodoscopes, MU3Y and MU3X consisting of horizontal and vertical counters respectively, were placed farther downstream followed by another layer of 1 m thick filtering steel. They were used at trigger level.

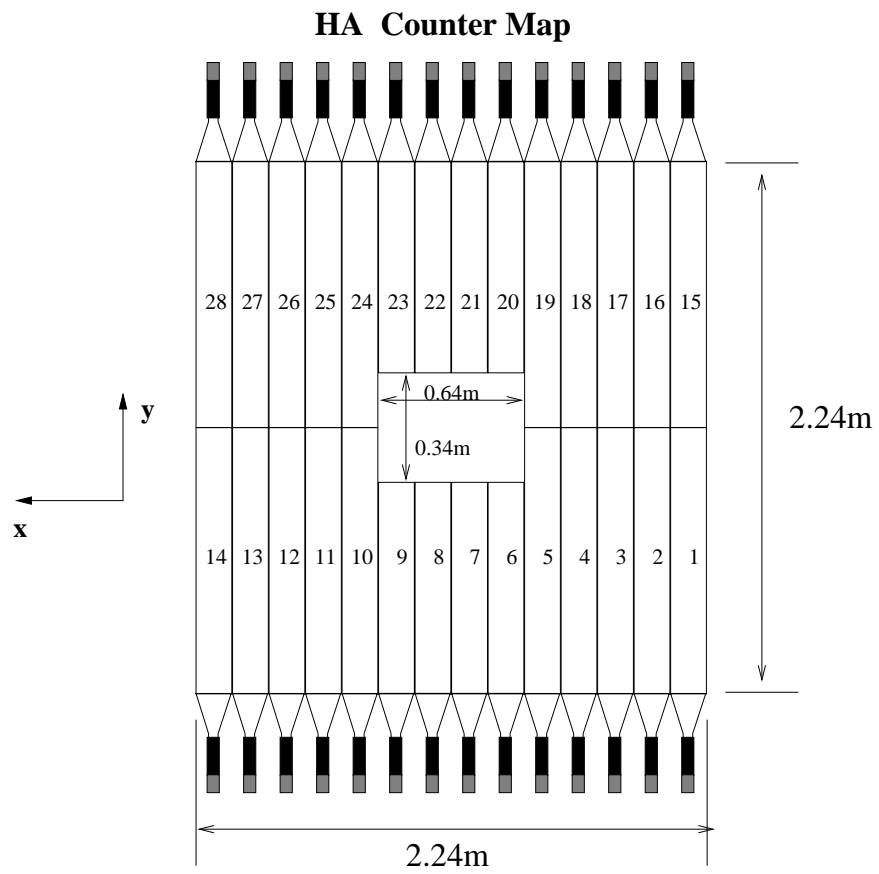


Figure 2.14: The HA hodoscope composed of 28 scintillation counters.

Being the most downstream, the Muon Counters had the largest dimensions of all the detectors. The number of scintillation counters as well as the dimensions of each hodoscope is shown in Fig. 2.15. Individual counters had dimensions of  $15\text{ cm} \times 150\text{ cm}$ . The two counters forming one paddle were overlapped by 1 cm to reduce the inefficiency for the muon going through the gap between the two counters.

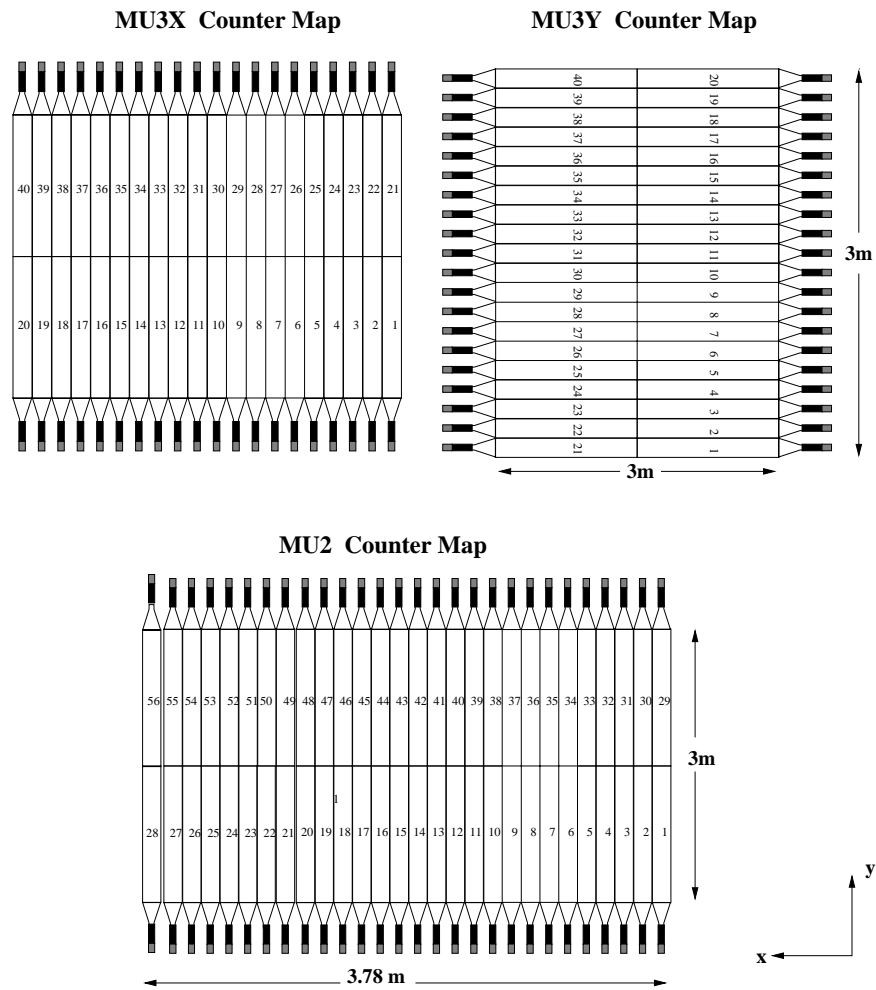


Figure 2.15: The Muon counters.

## Chapter 3

# Triggering and the Run

The trigger for E799 employed a three-level system. The first and second levels used the logic constructed from only electronic hardware, while the last level, carried out on-line event reconstruction computing to filter the events. There were two types of three-level triggers. The “CALIBRATION Triggers” designed to collect data for cosmic muons, pedestal measurements and the CsI laser calibration. The “BEAM Triggers” designed for the physics trigger. Each of the 16 beam triggers was optimized to collect one or more specific rare decays.

### 3.1 Level 1 Trigger

The first level trigger used prompt signals from the detector, like scintillator counters, calorimeter total energy sum and the logical OR of the drift chamber signals to make a quick decision on cutting the rate from  $\sim 80$  kHz to  $\sim 20$  kHz. Hence, it was very fast and available for each 19 nsec bucket (no dead time) in the spill structure.

The 16 beam triggers used different combinations of 80 Level 1 logic sources. These trigger sources were sent to a series of LeCroy 4508 Programmable Lookup

Units (PLU) and LeCroy 4516 Programmable Logic (PL), which were programmed and could be changed via CAMAC. At the same time, the RF signal provided by the accelerator was passed into the PLU and PL to strobe the trigger sources. We call the time strobed RF bucket as “in-time” bucket. A combination of PLU and PL generated an output signal by looking at the firing pattern of the Level 1 trigger sources [63].

Finally, decays with high rate were prescaled before reaching the second level, which means 1 out of the prescale factor would be selected at random.

### 3.1.1 Drift Chamber Stretcher/OR

The purpose of the Stretcher/OR (also known as DC FAST-OR) modules was to monitor discriminated drift chamber signals and to prepare them for use in the level one trigger. A level one trigger would then reject events which didn’t have enough qualifying drift chamber hits for adequate tracking.

The Stretcher/OR module performed several tasks for this purpose. It monitored the drift chamber output ECL signals on the twisted-flat ribbons with high impedance amplifiers so as not to degrade those signals as they passed by the Stretcher/OR inputs. It stretched the 40 nsec drift chamber pulse to 90 nsec, about 10 nsec greater than half the nominal maximum drift time. Outputs from the  $X \Leftrightarrow X'$  ( $Y \Leftrightarrow Y'$ ) planes were added in groups to form effective hodoscope “paddles” for use in the trigger logic at NIM levels [64, 65].

The front end of the Stretcher/OR circuit is shown in Fig. 3.1. A 10114 ECL line receiver was used to pick off the signals on the twisted-flat ribbon from the

drift chamber discriminators. Since the circuitry which follows the input was DC coupled, a 10114 was used which was always in a definite logic state.

The Stretcher/OR circuit accepted two input ribbons of 16 twisted pairs each. One ribbon handled signals from wires of the  $X$ -plane and the other handled signals from the  $X'$ -plane immediately behind those handled by the corresponding  $X$  ribbon. The OR circuits are combined to form two “paddle” outputs, A and B, such as:

$$\begin{aligned} A = & X_1 + X_2 + X_3 + X_4 + X_5 + X_6 + X_7 + X_8 \\ & + X'_1 + X'_2 + X'_3 + X'_4 + X'_5 + X'_6 + X'_7 + X'_8, \end{aligned} \quad (3.1)$$

or in the case of  $Y$  sense wires:

$$\begin{aligned} A = & Y_1 + Y_2 + Y_3 + Y_4 + Y_5 + Y_6 + Y_7 + Y_8 \\ & + Y'_1 + Y'_2 + Y'_3 + Y'_4 + Y'_5 + Y'_6 + Y'_7 + Y'_8, \end{aligned} \quad (3.2)$$

and

$$\begin{aligned} B = & X_9 + X_{10} + X_{11} + X_{12} + X_{13} + X_{14} + X_{15} + X_{16} \\ & + X'_9 + X'_{10} + X'_{11} + X'_{12} + X'_{13} + X'_{14} + X'_{15} + X'_{16}, \end{aligned} \quad (3.3)$$

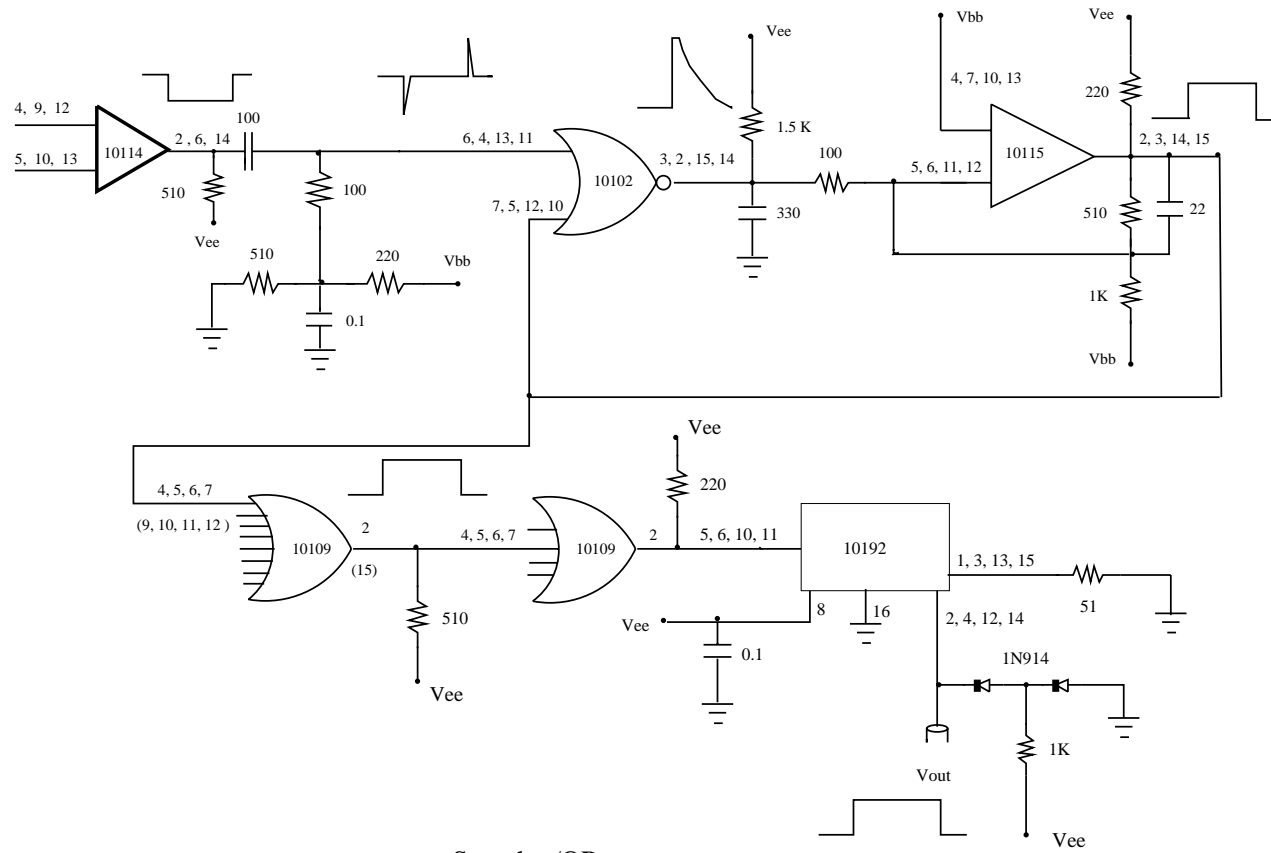
or in the case of  $Y$  sense wires:

$$\begin{aligned} B = & Y_9 + Y_{10} + Y_{11} + Y_{12} + Y_{13} + Y_{14} + Y_{15} + Y_{16} \\ & + Y'_9 + Y'_{10} + Y'_{11} + Y'_{12} + Y'_{13} + Y'_{14} + Y'_{15} + Y'_{16}. \end{aligned} \quad (3.4)$$

Therefore each chamber could be represented as a collection of “paddles” eight sense wires wide (10.16 cm paddle width). The first three pairs (DC1Y, DC1X



Figure 3.1: Stretcher circuit.



Stretcher/OR

and DC2Y) required 7 Stretcher/OR modules each (14 paddles wide), and the last plane pair (DC2X) required 8 modules (16 paddles wide) since there were different numbers of sense wires per chamber plane, as shown in table 2.3. The first level trigger used the Stretcher/OR for the upstream magnet chambers only (DC1 and DC2). Figure 3.2 shows the symbolic representation of the Stretcher/OR logic. The hatched central modules in  $X \Leftrightarrow X'$  planes of DC1 and DC2 were used in the hyperon trigger as described in section 3.4.

### Hit Counting Discriminator

Each of the 14 (16) Stretcher/OR modules provided a 90 nsec NIM output pulse when the corresponding paddle in a drift chamber plane was hit by a particle. All the paddle outputs of a plane were then examined by a discriminator to search for a combination of in-time hits. A custom designed module was built to do this task. The circuit is shown in Fig. 3.3.

The transistor summed all of the switched currents and produced an output voltage at its collector proportional to the number of switched inputs “on” at any give time. The output of the summing transistor was then fed to a single LeCroy MVL407 chip with 4 comparators. Each comparator was biased to switch at a level between two sum values. Switches were set to give outputs for number of hits greater than 0, 1, 2, and 3. Provision was made to give each multiplicity value up to 2 NIM level fanouts. Total transit time of the signal was about 9 nsec.

Since overlap widths were always smaller than the 90 nsec output of the Stretcher/OR modules, the probability of an accidental coincidence with a given

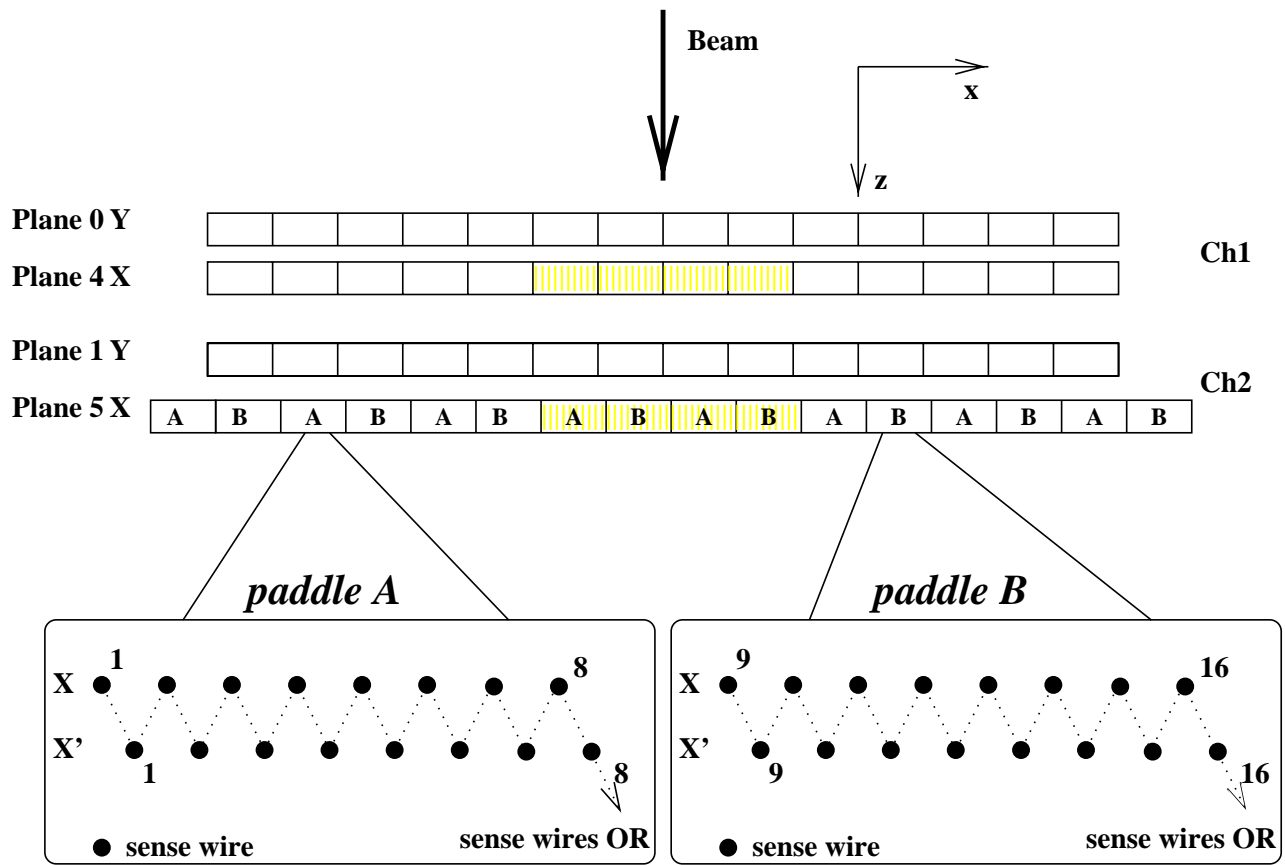


Figure 3.2: Stretcher/OR logic. The hatched area shows the paddles used for the hyperon trigger.

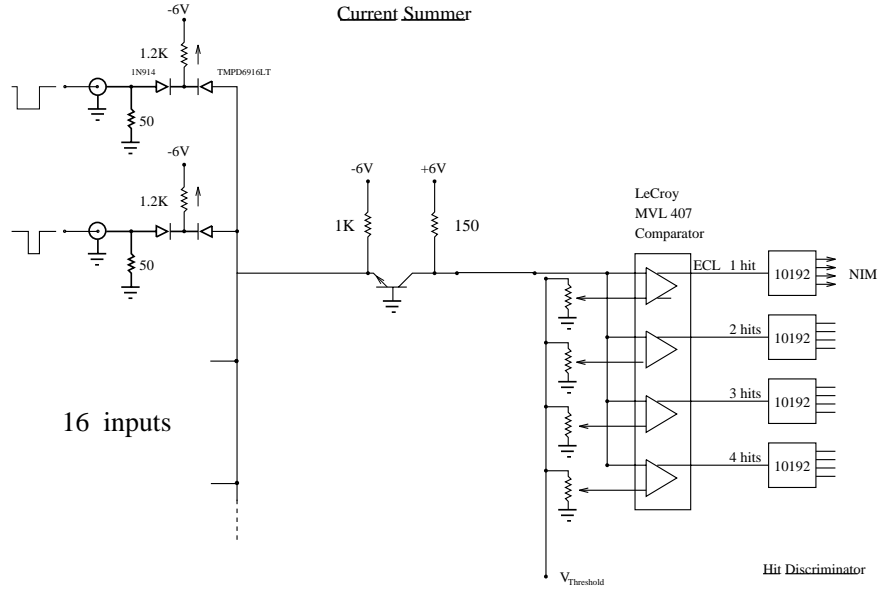


Figure 3.3: Hit counting current summer circuit.

RF bucket became smaller as the required hit multiplicity was increased. For example, the requirement of 3 or more in-time hits (for a 4 track decay, say) was less likely to be satisfied by out of time hits than the requirement of 1 or more hits.

The I-sum circuit was built on a board to mount in the crate with the Stretcher/OR modules. A small, low current supply was appended to this crate to provide the positive voltage needed by the summing transistor. Since the Stretcher/OR inputs were at the front of the rack and outputs were at the back, we put I-sum inputs at the back and outputs at the front to minimize overall transit time. The I-sum module resided in the middle of the cluster of Stretcher/OR modules that fed it, further reducing transit times.

### 3.1.2 Calorimeter Total Energy

A very rapid measurement of the total energy,  $E_t$ , deposited in the CsI calorimeter was used as a trigger source signal in the first level trigger.

The summing system consisted of sixty first level sum boards, each of which generated a sum of between 19 and 57 input channels. These first level sums were further summed, on the second level sum boards, to provide quadrant and full analog sums [66].

The input to this system was a dynode signal from the photomultiplier tubes, which was roughly 16 pC per GeV energy deposited in the crystal. The  $E_t$  system would also provide a hit crystal information to cluster counting system described in Section 3.2.2. It tagged those RF buckets for which the crystal in question had an energy deposit in excess of a preset threshold as a so called HCC bit.

## 3.2 Level 2 Trigger

The second level trigger consisted of DC hit counting, CsI hardware cluster counting and the TRD information to reduce the rate of the events that satisfied the Level 1 requirements to  $\sim 2$  kHz. It took the level 2 a longer time, about  $3 \mu\text{sec}$ , to respond due to delay in the pattern recognition for the CsI Hardware Cluster Counting and BANANA/KUMQUAT hit counting of the drift chambers. That corresponded to a  $\sim 26\%$  dead time at level 2.

The input signals from Level 2 sources were sent to another series of PLU's (LeCroy 2373) with a Level 1 signal. When the event satisfied the Level 2 requirements, each PLU generated the outputs, which were used to form a 16 bit

trigger mask; the bitwise-AND of all the lookup units was the final 16 bit trigger mask [67].

### 3.2.1 The Stiff Track Trigger

All the hyperon decay modes accessible to KTeV were characterized by the production of a high momentum proton collinear with the beam axis and since few high rate kaon decay modes had such a characteristic, a “Stiff Track Trigger” (STT) was designed to identify such stiff tracks at the second level as fast as possible [68, 69]. The STT was used to select events with a high momentum track ( $\geq 50$  GeV/c) going down the left or the right beam hole to determine the track’s change in slope before and after the analysis magnet from the pattern of latched drift chamber hits in the center of the beam hole regions in the horizontal view. These latched hits were provided by specialized modules (so-called “kumquat” for the drift chambers 1,3 and 4 and so-called “banana” for the second drift chamber). The STT was based on several electronics modules that combined inputs received from 52 wires of the drift chambers in each beam hole, with 11 wires from the first and the second chambers and 15 wires from the third and the fourth chambers.

The logic of the STT trigger was the following. If there were either 1 or 2 adjacent wires hit in the instrumented area for each chamber, the STT computed the corresponding horizontal position, “ $x_{DCn}$ ”, in each drift chamber and then calculate the quantity “ $(x_{DC4} \Leftrightarrow x_{DC3}) \Leftrightarrow (x_{DC2} \Leftrightarrow x_{DC1})$ ”. This quantity is proportional to the change in slope of the track. If its value was between -7 and +7 inclusive, the event was selected by the STT, otherwise the event was rejected.

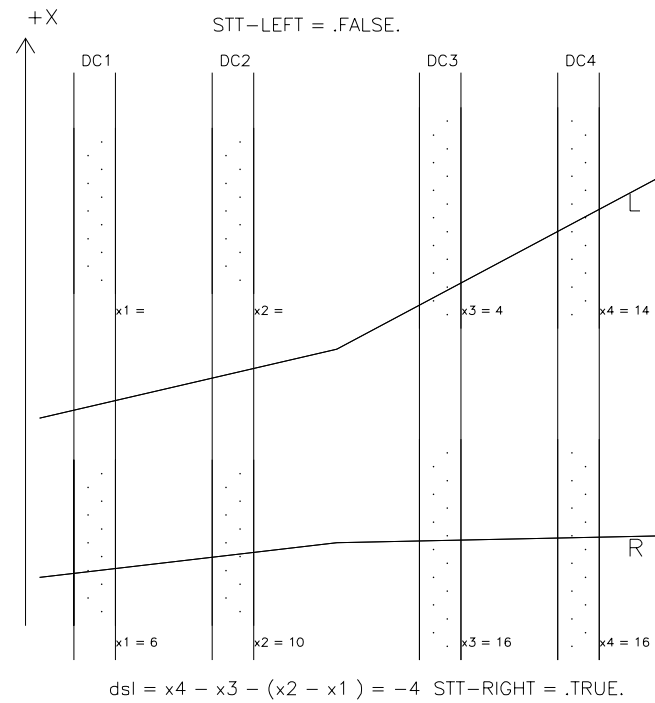


Figure 3.4: Diagram of STT. In the right beam hole we have a track with a sufficiently small change in slope passing through the instrumented region in all 4 chambers, so the STT result (-4) for the right side is TRUE. On the left side, the track does not pass through the instrumented region in all 4 chambers, so the STT result (10) for the left side is FALSE. Thus the event is accepted.

Any other combination of inputs caused the STT to reject the event. Therefore, if for example the negative track traveled through the area instrumented by the STT, the event would be rejected. Accidental in-time activity in the instrumented area would as well cause the STT to reject the event. It was also possible for a track to travel down the beam hole and miss the area instrumented by the STT.

### 3.2.2 Hardware Cluster Counting

The second level trigger used a hardware cluster counting (HCC) that determined the number of isolated showers deposited in the CsI calorimeter. The cluster finding algorithm took advantage of a pattern recognition and parallel processing technique to reach a relatively fast decision under  $2 \mu\text{sec}$ . The details of the algorithm and the HCC can be found in [70].

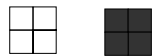




Patterns of Struck Blocks	Pattern Value
	0- No turns
	+1 -one right turn
	0- No turns
	-2 - Two right turns
	-1 -one left turn

Figure 3.5: All possible hit patterns for a  $2 \times 2$  array of blocks. The value assigned to each group of patterns is shown to the right.



The idea for the cluster finder is that an isolated cluster could be enclosed by a continuous perimeter. To define the perimeter, we considered only the crystals which contained the energy above 1 GeV, based on the information from the  $E_t$  board. If one were to travel in a given direction around the perimeter of a cluster, one would complete a  $360^\circ$  turn upon returning to the starting position. In the CsI calorimeter which consisted of rectangular blocks, a circle around any cluster corresponds to four  $90^\circ$  turns. While traveling clockwise around the perimeter, if we assign a +1 for every right turn and  $\Leftrightarrow 1$  for every left turn, the sum of right turn minus left turn should be four. Applying this procedure to the whole calorimeter, we could simply count the number of right turns and subtract the number of left turns. The resulting is four times the number of clusters.

Right or left turns were determined by examining the pattern of the hits in  $2 \times 2$  arrays. Figure 3.5 shows all the possible configuration of hits in such a group and the assigned number for each pattern. Since each crystal belonged to four different  $2 \times 2$  grids, each crystal was used to determine four different pattern values. The sum of all  $2 \times 2$  pattern value was four times the number of isolated clusters in the arrays. The outer edge of the calorimeter as well as the boundary of the small and large blocks of CsI in which the  $2 \times 2$  arrays contained a mixture of the two different sizes were treated in a special manner.

The Hardware Cluster Counting Unit then produced 4-bit cluster count which was sent to the trigger system.

### 3.3 Level 3 Trigger

The last stage of the triggering used software filter codes on-line to reconstruct and write the tagged events on the magnetic tapes (DLT's). A total of 24 Challenge SGI CPU's (200 MHz  $\simeq$  160 MIPs each) was used to process and filter the events. The resulting time to process was 3 msec per event.

### 3.4 Hyperon Trigger

Three bits (out of 16) of the beam trigger were dedicated to the hyperon data in E799. There was a "Hyperon Minimum Bias" trigger (bit 12) with a large prescale of 20 000 and loose trigger condition to study the efficiency of the other two hyperon triggers. The " $\Lambda$ -trigger" (bit 11) was built to trigger on hyperon shape events and selected mainly  $\Lambda \rightarrow p\pi^-$  events and  $\Xi^0 \rightarrow \Lambda\pi^0$  events where  $\Lambda \rightarrow p\pi^-$ . It had a prescale of 50 and was mostly used to study the principal decay of  $\Xi^0$ 's as the normalization mode for most of the  $\Xi^0$  rare decays. The main hyperon trigger (bit 10), called " $\Xi^0$ -beta-trigger" was a subset of the " $\Lambda$ -trigger" to select hyperon beta decays. It was modified several times during the run as we learned how to reconstruct Cascade beta events efficiently. Also the prescale of 2 at the beginning of the run was removed for the last three weeks of the winter run and subsequently for the entire summer run.

#### 3.4.1 Trigger Requirements

The first and second trigger requirements for the hyperon triggers were:

- Trigger 10

$$1V * L1HOLETRK * ET_2 * \overline{HADC} * \overline{PHV1} * \overline{CA} \quad (Level\ 1)$$

$$*2HCY * 2HCY\_LOOSE * LAMBDA\_RA * HCC\_GE2 \quad (Level\ 2),$$

- Trigger 11

$$1V * L1HOLETRK * ET_1 * \overline{PHV1} \quad (Level\ 1)$$

$$*LAMBDA\_RA * HCCDUM \quad (Level\ 2),$$

- Trigger 12

$$1V * HC \quad (Level\ 1)$$

$$*HCCDUM \quad (Level\ 2),$$

where each required element means:

- 1V- A hit in one of the two hodoscope planes.
- *L1HOLETRK*- A track down the beam hole. A fast OR of the vertical wires in the beam region in the first and second drift chambers is performed and combined with the activity in the hole counters. A track is said to have gone down the beam hole if there is a least one hit in each of the two first chambers and enough activity in the hole counters. For the minimum bias trigger, only activity in the hole counters is required. This beam hole requirement in addition to 1V means that at least two charge tracks are in the event.

- $\overline{PHV1}$ - The various photon vetoes – ring counters (RC), CsI calorimeter anti (CIA), spectrometer anti (SA) – are quiet, according to the standard minimum ionizing particle thresholds used. It means that no photon or charged particle has escaped the fiducial volume of the detector.
- $LAMBDA\_RA$ -There is a high probability to have a high momentum track down the beam hole. This is the Stiff Track Trigger explained in section 3.2.1. It is not used in the minimum bias trigger.
- $ET_2(ET_1)$ - There is at least a total of 18 GeV (11 GeV) of energy deposited in the electromagnetic calorimeter. The lower threshold of  $ET_1$  was used for the beta trigger in the winter as well, but it was raised to  $ET_2$  since Cascade beta events deposit a total energy of typically greater than 20 GeV in the CsI.
- $\overline{HAD\overline{C}}$ - There is no activity in the hadronic scintillator plane named the hadronic anti (no energy deposited above the lower threshold). This means that the event has no hadronic activity in the fiducial region but in the beam region.
- $HCC\_GE2$ - There are at least two on-line hardware clusters in the calorimeter.
- $2HCY*2HCY\_LOOSE$ - There are two hits in each drift chamber horizontal wire planes, with a possible hit missing in one of the two upstream chambers.

The third level trigger performed the reconstruction of the events selected by the previous trigger levels and applied more refined selection criteria on them. The

events finally recorded on tapes were either those selected by the minimum bias trigger which bypassed the third level or those selected by the “ $\Xi^0$ -beta-trigger” or by the “ $\Lambda$ -trigger” that fulfilled the following criteria:

- At least two good tracks with some possible sharing between the hits in the chambers’ vertical wire planes that form a two track vertex.

- The highest momentum track points down the beam hole and the other one to the calorimeter.

- A track momentum ratio (high/low) of at least 2.5 (characteristic of hyperon decays).

- At least one track with a momentum greater than 90 GeV/c (modified to 85 GeV/c during the data taking).

- The charged vertex (assuming  $\Lambda$ ) has to be at less than 16  $c\tau_\Lambda$  from the target <sup>1</sup>.

- 1 out of 250 events that fulfilled the first two trigger levels are selected randomly to bypass the above requirements. These events are used to check the efficiency of the third level trigger for the “ $\Xi^0$ -beta-trigger” or for the “ $\Lambda$ -trigger”.

### 3.5 The Run

The E799-II data taking focused on collecting physics data to study rare decays of kaons and hyperons. The physics runs took up most of the run time. However, we were also taking some special runs for the purpose of detector calibration,

---

<sup>1</sup>The charged vertex proper time is defined in terms of the reconstructed mass, momentum and lifetime of  $\Lambda$ , and its traveled distance as:  $ct/c\tau_\Lambda = m_{p\pi} z_{vertex}/(c\tau_\Lambda p_{p\pi})$ .

diagnostics, monitoring and etc.

### 3.5.1 E799 Physics Run

A typical E799 run took a few hours during which the data collected from different trigger sources were being written out onto 10 DLT tapes simultaneously. The raw data on about 950 tapes were then “split” off-line based on trigger types and level 3 tags. We collected about 200 million events on 91 tapes from the hyperon triggers, 60 of which came from the summer run. The split data were further “crunched” to smaller subsets onto Data Summary Tapes (DST’s) for the final analysis. The length of the runs were limited to the capacity of the DLT tapes (about 15 GBytes), a maximum of 12 hours. The runs ended automatically when the tapes were full and had to be replaced by fresh ones. They were also stopped when a problem occurred with the detector or with the beam. An average E799 run lasted between 4 to 5 hours. We used a higher intensity beam for the winter run (about  $5 \times 10^{12}$  protons per spill) than for the summer run (about  $3.5 \times 10^{12}$  protons per spill). However, the beam size was wider for the summer run ( $12 \text{ cm} \times 12 \text{ cm}$  at CsI) than for the winter run ( $10 \text{ cm} \times 10 \text{ cm}$  at CsI).

### 3.5.2 Special Runs

The main special runs taken in E799 were “Muon Runs”, “Pedestal Runs”, and “Laser Runs”.

In order to perform the relative alignment of the drift chambers (section 5.4), straight through trajectories were needed. Short muon runs (about 10 min) were taken on a daily basis to collect an order of 100 000 events for this purpose.

Also, these runs were used for the on-line calibration and monitoring of the time-to-distance relations (section 5.3). Muon beams were obtained by placing two beamstops, made of 28.5 cm and 21.1 cm thickness steel and located at  $z=46.4$  m and  $z=50.1$  m, respectively, in the beam line. Most of the hadrons were absorbed in the beamstops, and only muons could enter the fiducial region. Muon runs had a different set up than the normal hadron runs in that the intensity was lower (typically  $3 \leftrightarrow 4 \times 10^{11}$  protons per spill) and the main analyzing magnet was off. The muon events were triggered by the coincidence hits in any  $V$ ,  $V'$ , and the muon counters, which were also used to study the gain of the muon counters and to calibrate them.

Pedestal runs were taken occasionally for pedestal measurements. Although the pedestal data were collected during the off-spills on physics runs, there were some cases which needed much more pedestal data, *e.g.* after swapping some modules of the detectors, etc. We tried to take the pedestals during the beam down times as much as possible, to save beam for the physics runs.

Finally, Laser Runs were taken for calibrating DPMT's as described in section 2.6. These data were also collected during the off-spill, but sometimes larger samples were needed. Especially, after swapping DPMT's laser runs were carried out to test the result of the repair before resuming physics runs.

## Chapter 4

# Data Acquisition

This chapter describes the KTeV Data Acquisition (DAQ) system [75]. The KTeV DAQ consisted of a high rate data collection system as well as a slow control system to monitor and control the detector. The KTeV Fast DAQ was capable of a maximum average throughput rate of 160 MB/sec into the level 3 trigger, had 3600 MIPs for full on-line event reconstruction and level 3 software trigger, and could output to DLT tapes at 18 MB/sec. The KTeV Slow DAQ system ran independently of the main DA and was an automated system for monitoring and controlling various technical aspects of the experiment such as high voltages, low voltages, environmental parameters and gas systems, for reporting and acting on changes in the status of the detector and for maintaining the safety of the experimental equipment.

### 4.1 The Data Acquisition System

The Fermilab Tevatron delivered 800 GeV protons to the fixed target program in a 60 spill structure. Each spill protons were delivered in 19 nsec contiguous rf buckets for  $\sim 23$  seconds, and no beam was delivered for the remaining 37 seconds



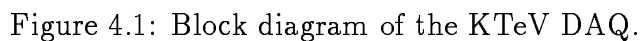


Figure 4.1 shows a block diagram of the KTeV DAQ. Data from sub-detector systems flowed into the memory nodes along one of 6 “streams” of RS485 cables,

with a maximum bandwidth of 40 MB/sec/stream. Thus the maximum total data flow along the streams was 240 MB/sec. The data from each stream were buffered in dual ported VME/VSB memory while being shipped to a Challenge L deskside server via a VME to VME interface. There were a total of 4 sets (or “planes”) of VME crate/Challenge machine pairs, giving a total of 24 memory nodes (4.62 GB total memory) in the DAQ matrix. The RS485 cables into each plane were daisy chained, allowing data on the cable to be sent to any specific plane or combination of planes.

Figure 4.1 also shows a block diagram of one stream on one plane of the KTeV DAQ. There were many different types of front end crates and modules in the experiment, but each crate was read out over a FERA bus by a FERA readout module designed and built by Fermilab (DYC3 or CTIRC). On receipt of a level 2 trigger, the data from each crate was read into the FIFO of this module, and the data from all crates in a stream were pushed serially onto the RS485 cable. Each RS485 stream was daisy chained to a memory node on each plane, connecting four nodes in total. Each memory node consisted of 3 VME/VSB dual ported memory modules, a board containing a DM115 receiver device and a DC2 controller device.

Data would flow up the RS485 cables to the memory node, consisting of a DM115/DC2 pair, a triple width VSB bus, and 3 VSB/VME Dual Ported memories. The combination DM115/DC2 was a commercial board, made by Access Dynamics, which plugged into the VSB bus at the back of the VME crate. The DM115 accepts RS485 data and pushes them into an 8 kb FIFO. The DC2 did a data DMA over the VSB bus from the FIFO into the dual ported memory, made

by Micro Memory, Inc. In addition to controlling the DMA, the DC2 attached the sub-event size to the top of each event, made a table of event VME address in the memory and kept a counter of the total number of sub-events processes. The slowest step in this process was the DMA step and access to the memory, which went at about 22 MB/sec. Because of this limitation, in order to push each stream up to its maximum of 40 MB/sec, it was important to be able to switch planes on an event by event basis. By doing this, each DC2 saw only one out of three events and thus the maximum aggregate rate per stream was limited only by the RS485 rate.

The data were pulled from the VME crates into the SGI Challenges over a VME to VME interface (PTI940). In order to achieve high VME DMA rates, sub-events were blocked in groups of roughly 1000 (“super-events”) for pulling into the Challenge. The six super-events, one from each stream, were then sent to one of the 8 level 3 filtering jobs running in parallel. The individual events were fully reconstructed and selected for off-line analysis according to the on-line level 3 criteria. The computing power for this filtering corresponded to about 3600 MIPs with three SGI Challenge computers. The fourth plane (VME crate + SGI Challenge) was used for processing calibration events and for detailed on-line monitoring of a percentage of the physics data.

After the level 3 selected an event, it built the event (*i.e.* copied it to contiguous memory space) and sent it to a separate process which handled the tape media I/O. The built event was then written to a specific tape drive depending on trigger type.

The level 3 processes analyzed events in parallel. Histograms of relevant parameters for the filtering were made independently on each CPU with HBOOK, and stored in shared memory. A separate process dumped all the contents of the shared memory, plus a sum of all histograms in shared memory, to a file on an NFS mounted disk. Thus monitoring of the histograms could be done on a CPU by CPU basis, plane by plane basis or summed over all planes, to check for inefficiencies in any one process or global problems in detectors. In addition to physics parameters, DAQ parameters such as CPU usage per process per spill and event sizes per crate or stream were also histogrammed.

## 4.2 The Slow Control System

The KTeV experiment operated an automated system for monitoring and controlling various technical aspects of the detector, such as high and low voltages, environmental parameters, gas pressures, etc. This automated system, called KTeV Slow-Control (KTeV-SC) or Slow-Data Acquisition (SDAQ) system, was used for reporting and acting on changes in the status of the detector, and for maintaining the safety of the experimental equipments.

The KTeV-SC system was flexible, easy to reconfigure or modify, extensible, and scalable. This system provided a fully automated package to collect, store, present and distribute monitored data.

The KTeV detector was located in an underground area whereas the control room was located in a surface building. For a smooth running conditions KTeV-SC provided a relatively low-cost system of remote monitoring and control. The

KTeV-SC monitored the experimental conditions locally and then generated alarm signals in the control room when problems were detected, in order to alert users in the control room to take some actions manually or remotely via the provided KTeV-SC graphical interfaces.

Monitoring several parameters of the KTeV experiment was critical not only for the off-line reconstruction but also for the safe operation of the experiment. For this reason, the KTeV-SC ran independent of the main KTeV Data Acquisition System (Sec. 4.1).

The complete system was built as a number of independent subsystems, which was integrated at the KTeV experimental Hall. During the commissioning and operation phase of the experiment, the KTeV-SC was partitioned to allow different subsystems to work independently in order to minimize possible interferences. Furthermore, all the subsystems used the same underlying KTeV-SC services (data display and visualization, alarm handler, database, etc.) to create an efficient monitor/control system.

#### **4.2.1 Architecture of the KTeV-SC**

The KTeV-SC comprised a physical hardware and a software layer. The physical hardware front-end layer was built from CAMAC hardware crates, I/O boards, etc. The software layer drove the hardware elements directly or through a variety of standard buses such as IEEE-488 (GPIB), RS232, RS422/RS488. The physical back-end was implemented on SGI workstations running UNIX. These layers were connected by an ethernet network.

In this section the different building blocks of the KTeV-SC hardware and software configuration will be described.

### Hardware Architecture of the KTeV-SC

The basic KTeV Slow-Control (KTeV-SC) system hardware building block configuration consisted of the operator interfaces (OPI's), I/O controllers (IOC's) and a local area network (LAN) communication link. This configuration is presented in Fig. 4.2.

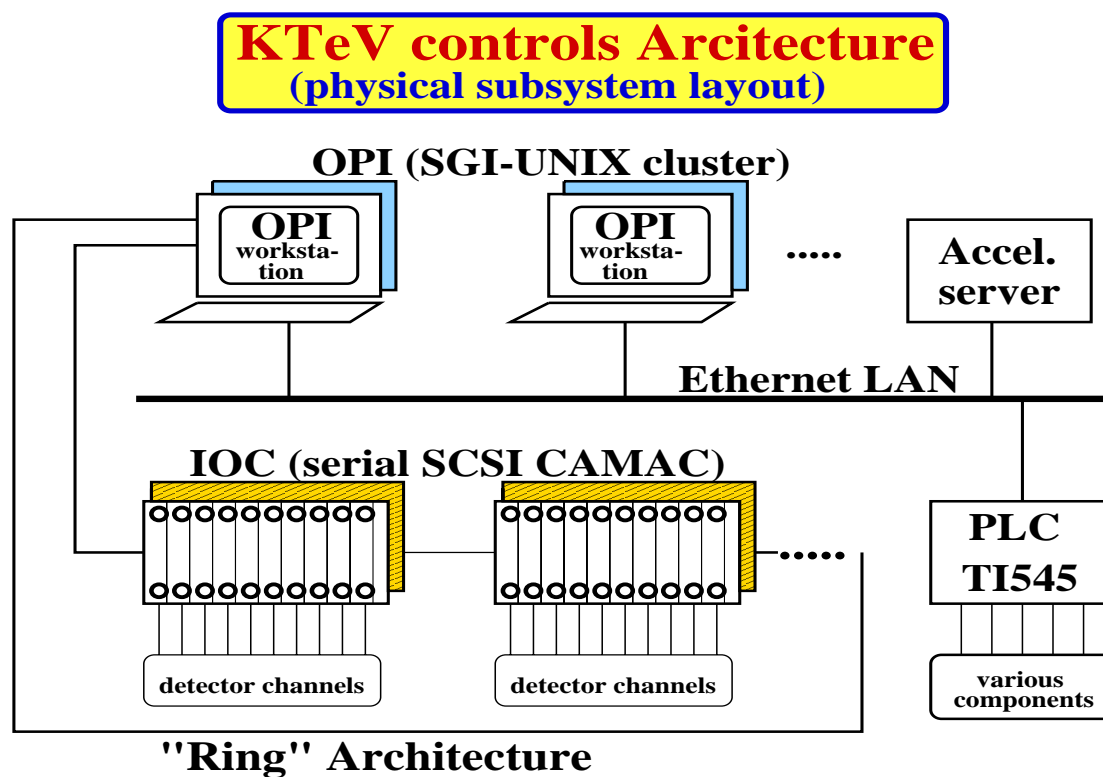


Figure 4.2: The overall basic KTeV Slow-Control building blocks.

Each OPI ran on a color graphics UNIX workstation which was an INDY

workstation from Silicon Graphics Inc. running IRIX UNIX and used the X-Window manager.

The KTeV detector electronic systems were interfaced to front-end I/O controllers. The I/O controllers included three CAMAC Serial Highway systems (IEEE Std. 595) configured in a “Ring Architecture”. The CAMAC Serial Highway had proven to be a valuable method for implementing multi-crate CAMAC systems. Each CAMAC Serial Highway could support up to 62 CAMAC crates for total lengths of about 300 meters. The JY411S (Jorway) SCSI version of the Jorway 411 CAMAC Highway was used. The Jorway UNIBUS and QBUS CAMAC Branch interfaces had been used before at various experiments in FNAL. These modules were upgraded to run from the SCSI bus of the OPIs as well.

Furthermore, the I/O controllers included three Programmable Logic Controllers (PLC’s). These were connected to the LAN via a local PC, running Windows95. The programming of the PLC’s was done by the DMACS interface tool. The DMACS interface provided the user with alarm, data logging and supervisory control capabilities. The PLC’s were SIMATIC TI545 (from Siemens Industrial Automation Inc.) controllers that integrate logic control, continuous control and advanced mathematics. The PLC’s executed user-generated programs to make decisions based on the state of input sensors (*i.e.* limit switches, etc.) and control output actuators (*i.e.* relays motors, etc.).

Finally, data from the Accelerator Monitor and Control system were provided to data servers with the help of the Simple Acquisition of Data services (SAD).

The SAD services were designed to fulfill the need of the KTeV and other Fixed

Target experiments to perform Epicure (for EPICS User Resource Enhancement) data acquisition from their experiments' computers in a simple and computer platform independent manner.

SAD acted as an intermediary between an application on a foreign node and the data acquisition services on an Epicure node. It utilized the Remote Procedure Call (RPC) facility to implement client/server communication between a VAX/VMS system running Epicure and the KTeV's UNIX OPI. RPC simplified the task by using XDR (eXternal Data Representation) to transparently convert data formats between platforms and by allowing the client/server communication to be written as simple function calls. The SAD client was linked into the KTeV application. Data acquisition services were remotely invoked by making User Task Interface (UTI) function calls. The UTI functions were actually simple wrapper routines around RPC code which packed the function parameters into a single structure and unpacked the returned data from the remote procedure if needed. The UTI also performed any necessary deallocation of RPC allocated memory. The SAD server ran on a VAX/VMS node with Epicure and Data Acquisition Requester server (DAR) installed and executed the procedure functions. These remote procedures would call normal Epicure data acquisition services exactly like a standard Epicure application and return the data to the client.

The LAN communication link was standard Ethernet which tied the IOC's and OPI's together to form a network. The same LAN was used by the main KTeV-DAQ to provide the connectivity with the KTeV-SC, Epicure Accelerator control/monitor system, etc.



## Software Architecture of the KTeV-SC

The basic KTeV Slow-Control (KTeV-SC) system software configuration is shown in a simplified form in Fig. 4.3. The software was entirely developed in house. It was written in a mixture of C, FORTRAN, the Tool Command Language (TCL) language, and the EXPECT language. TCL has two features. It is a scripting language and an interpreter for that language which made it easy to be embedded into a KTeV application. EXPECT is a TCL-based toolkit for automating interactive programs. The Graphical User Interface (GUI) was written in Tool Kit (TK) language (based on TCL), which is the TCL associated X window toolkit, and in Bell Labs Tool (BLT) module, which is an extension of the TK language.

The KTeV-SC was multi-tasking and was based upon a main software component process called *SDAQ Control Task*. This process was responsible for controlling of and communication between the various tasks that were launched by it. Several of these launched tasks were responsible for data acquisition and handling, such as: polling controllers, alarm checking, logging, archiving, and displaying different sets of parameters. The exchange of information between the *SDAQ Control Task* and the various launched task processes was performed via pipeline inter-process communication.

The configuration of the *SDAQ Control Task* was implemented with the help of an input ASCII parameter files where one could add or remove a task process, add or remove different monitoring channels, etc.

In addition, trending facility was provided by the KTeV-SC system. The *display manager graphics* was the graphical front used to create displays containing

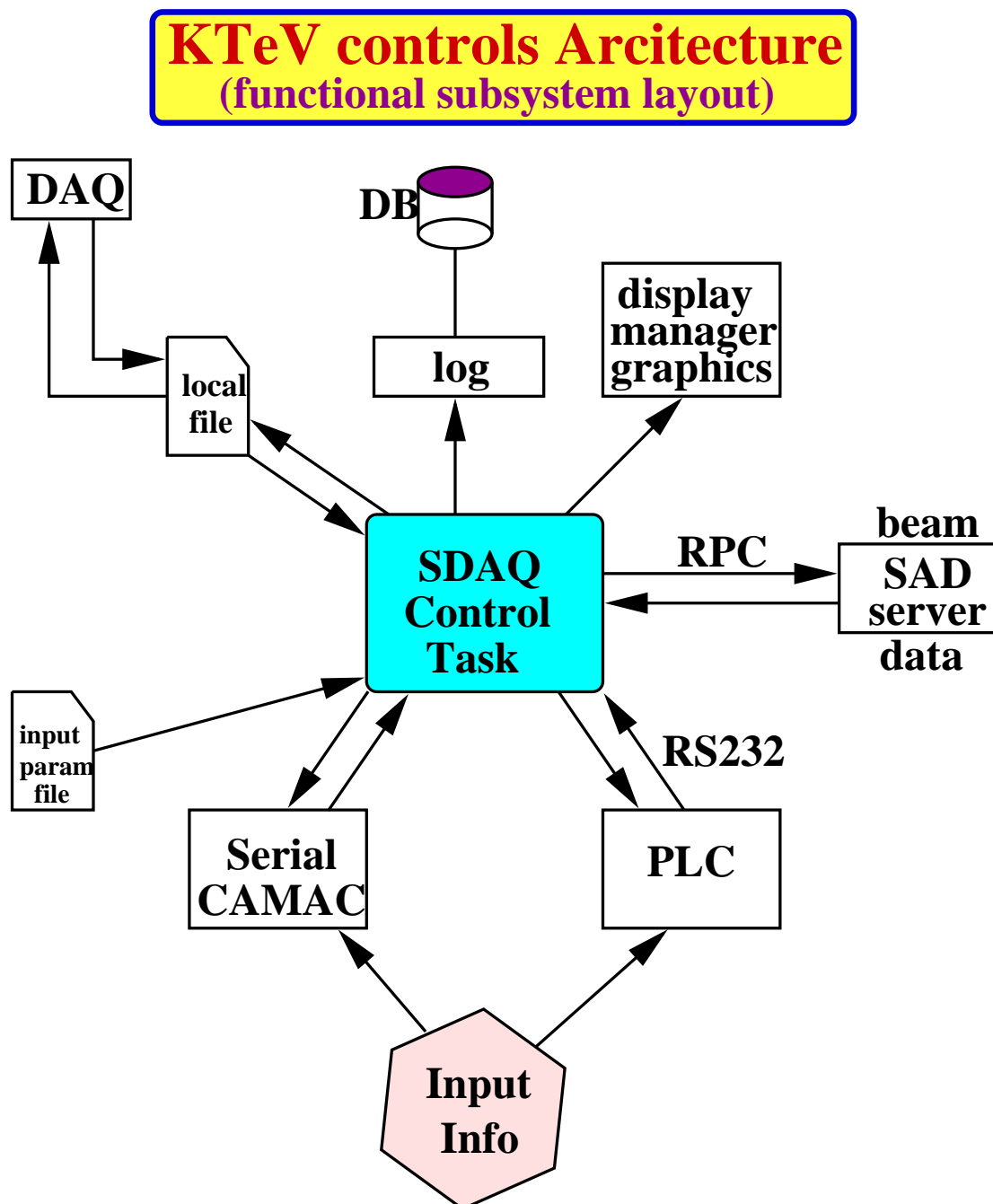


Figure 4.3: KTeV-Slow Control software architecture.

trends, symbol values, and bar graphics. The parameters to be trended in a specific chart or in a real-time and historical trending graph, could be predefined or defined on-line. Also, several features were provided by the system: historical trending was possible for some of the archived subsystem parameters; zooming and scrolling functions were provided; parameter values at the cursor position could be displayed. Most of the trending features were provided by the BLT GUI module.

The handling of alarms was performed centrally by the *SDAQ Control Task*. All the various task processes were transmitting the alarm information into the central *SDAQ Control Task*; the alarm information existed in only one place and all users would see the same status. Then the various error messages were presented to the user by the display manager graphics task. It warned the user when the alarm occurred and provided alarm viewing and logging.

The logging of data was performed once per spill on disk for most of the parameters, or on a set frequency that is predefined in an input ASCII parameter file. The logged data was spill-run number stamped in the database, as will be described in Sec. 4.2.4.

The communication with the main KTeV-DAQ was done through local ASCII files that were written/read by the *SDAQ Control Task* and the main KTeV-DAQ as well. In this architecture, the integration with the KTeV-DAQ allowed only message passing (data and actions), since the two systems were operationally independent, and they relied on different architecture and technologies.

Finally, a communication protocol was defined which used Remote Procedure Calls (RPC's) to send data between the Epicure Accelerator Monitor/Control

system and the KTeV-SC system, as described in Sec. 4.2.1.

#### 4.2.2 KTeV-SC Detector Subsystems

We now describe the slow control aspect of the various KTeV detector subsystems (see Chapter 2).

The high voltage was supplied by the LeCroy-1440, CAEN SY527, and Berkeley COW high voltage units. The monitoring of temperature, humidity, and various other environmental variables was performed by the KTeV low voltage multiplexer system. The overall structure of the KTeV-SC system is summarized in Fig. 4.4.

##### CsI Calorimeter

A TI545 PLC was used to perform the control algorithms for the blockhouse (the system that houses the CsI electromagnetic Calorimeter) and its electrical/environmental systems. We maintained the temperature of the CsI crystals to  $\pm 0.1^\circ \text{C}$ , and maintained a dry environment inside the blockhouse.

In order to protect personnel, CsI crystals and electronics, an extensive system of interlocks and alarms was established. The interlocks and alarms were of hardware and software variety. There were five software interlocks on the PLC to protect the electronics and the photomultipliers (PMT's), in case the fire alarm system went into an alarm state, the humidity parameter was high, or a high temperature developed, etc. The software interlocks and alarms were handled by the DMACS interface between the TI544 PLC and the local PC, as described in Sec. 4.2.1.

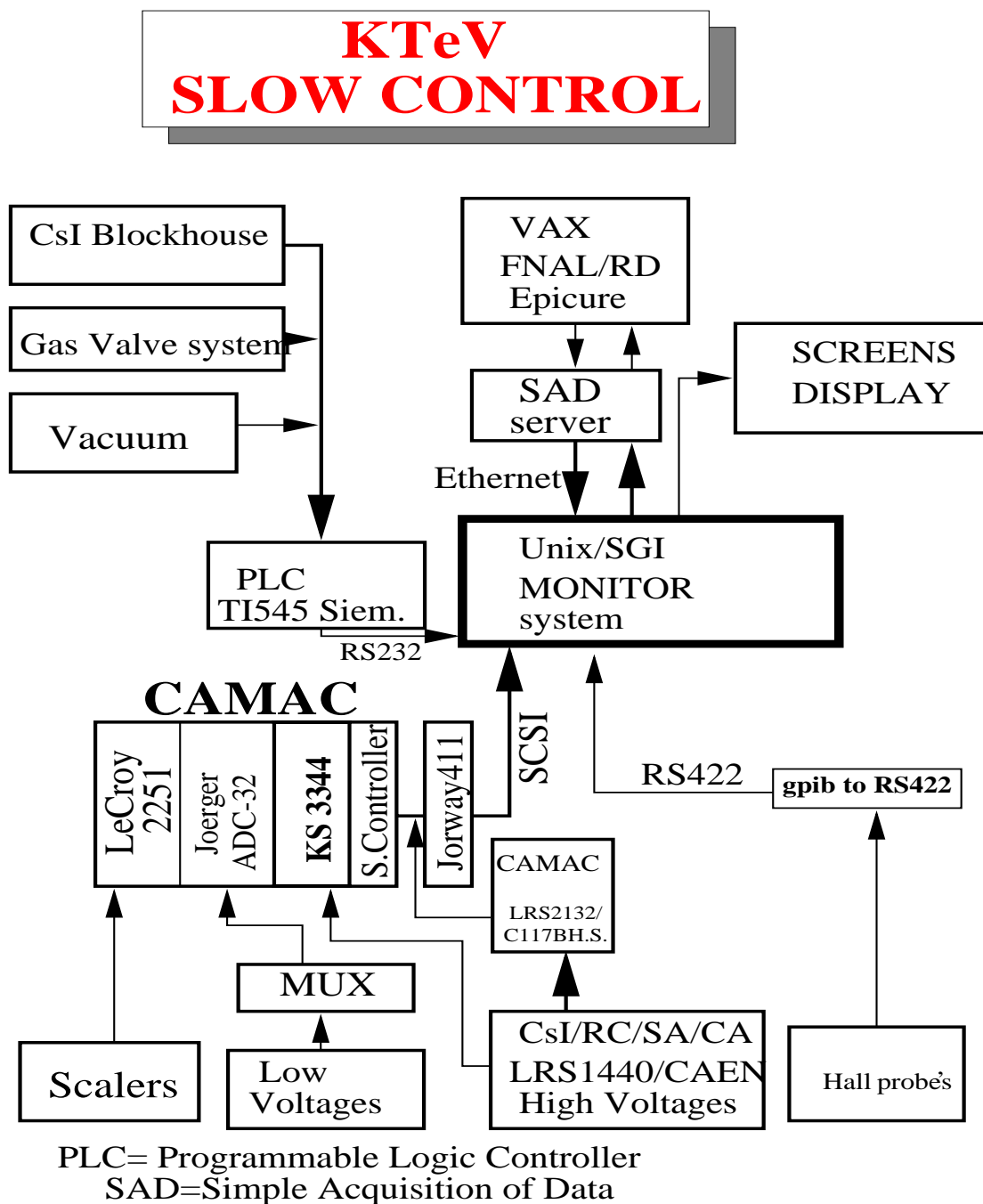


Figure 4.4: Overall structure of the KTeV-SC system with the main hardware monitor/control components shown.

The TI545 and the rack of control modules with which it communicates were connected to a battery driven Uninterruptable Power Supply (UPS) so that the humidity, temperatures, and various alarms were available even during short power outages.

More than 60 monitoring parameters were transmitted every 10 seconds by the TI454 PLC to the KTeV cluster main frames via the RS-232 serial communication link between them.

The PMT high voltage of the 3,100 CsI crystals was provided by 13 LeCroy 1440 high voltage units. The communication between the LeCroy high voltage units and the KTeV-SC was performed via the SCSI CAMAC LeCroy-2132 controller. A digital voltmeter with a IEEE-488 GPIB interface was used for a more precise measurement of the CsI detector high voltage than that could be provided by the LeCroy-1440. The digital voltmeter was read out via a CAMAC KS 3344 module from Kinetic Systems Inc.

The monitor/control of the CsI RF fanout system status was performed via a CAMAC task process.

### **Drift Chambers**

The DC's used the CAEN SY527 power supplies to provide high voltage for the anode drift field and the cathode window wires, a total number of 16 channels. The CAEN SY527 power supplies were controlled/monitored by using the CAMAC CAEN-117B High Speed controller. DC's high voltage was lowered during off spill time period to increase their lifetime. Also, whenever a DC high voltage tripped

due to a large current drawn by an excessive ionization in the chamber, the operator was informed for further action.

Low voltage for the needed pre- and post-amplifiers was monitored by the KTeV Low Voltage system as is described in Sec. 4.2.3.

The drift and special buffer window gases were supplied by a special system controlled/monitored by a TI454 PLC node, in a similar way as in the CsI calorimeter as well as in the vacuum system case.

## TRD

A CAEN SY527 power supply provided the High Voltage of the TRD's. 20 high voltage and current channels were monitored and controller by using the C117HS CAMAC interface module to the CAEN SY527 power supply.

The performance of the KTeV TRD's depended on the exact composition of the gas mixture in the active volume of the chambers. In particular, the gain of the TRD's was highly sensitive to changes in the ratio of the main components of the mixture ( $80\%Xe + 20\%CO_2$ ), and to the level of contaminant gases present in the active volume. A 541GC gas chromatograph (GC) system from Tremetics, Inc., was used by interfacing to a local PC, to monitor the purity of the gas mixture.

Also, 9 channels of 2341 LeCroy CAMAC register module were used to monitor the current status of the valves on the gas system.

## Vacuum System

In order to minimize backgrounds due to interactions of the neutral beam with the residual material, the decay region (vessel) was under vacuum with pressure

$< 10^{-4}$  Torr.

The monitoring and controlling of the vacuum system were performed by a TI545 PLC similar to the CsI case. In order to protect personnel and the rest of the experimental hardware, an extensive system of interlocks and alarms of more than 40 channels was established for the vacuum system. The interlocks and alarms were of hardware and software variety controlling and monitoring several diffusion, roughing, and ion pumps.

### **Photon Veto**

The photon veto counters consisted of 210 channels. All the PMT high voltages were supplied by the COW Berkeley high voltage units. We monitored these high voltages through the low voltage multiplexer system, as described in Sec. 4.2.3.

### **Muon Detector**

The High voltage of the 164 PMT channels of the muon counters was supplied by the COW Berkeley high voltage units. The monitoring of the high voltage of these channels was performed through the low voltage multiplexer system.

### **Analyzing Magnet**

The analyzing magnet was read out by a Hall probe (located in the magnetic field), measuring its magnetic field as well as its temperature. The Hall probe voltage was digitized by a DTM-141 Digital Teslameter unit with an IEEE-388 GPIB interface from GMW, located close to the analyzing magnet. Then, the digitized information was transmitted to the KTeV cluster via GPIB↔RS-485 controller



from National Instruments. Magnetic field and temperature readings were taken every 10 seconds during the spill.

### Active Regenerator

The role of the active regenerator in E832 part of the KTeV experiment was to provide a  $K_S$  beam from the  $K_L$  beam. The regenerator resided inside the vacuum vessel.

We monitored/controlled the 180 LeCroy 1440 high voltage PMT base channels and 256 PMT base temperature sensors. The LeCroy 1440 High Voltage system (180 channels) was read out the same way that the CsI HV system was read. The monitoring of the temperature sensors was controlled by a Motorola controller 68110 unit, that multiplexed the information and broadcast the monitored temperature parameters via a serial RS232/RS422 communication protocol to the KTeV cluster, as it will be described in Sec. 4.2.3.

### Beam Line Monitors

The KTeV beam system consisted of the primary beam transport, secondary beam production system, primary beam dump, neutral beam collimation system, filter and absorbers (Sec. 2.1).

The controlling and monitoring of the beam elements was done through the beam Epicure system.

The monitoring of the beam position was performed with the use of the Segmented Wire Ionization Chambers (SWIC). KTeV experiment used six SWIC

devices. Each SWIC was made of 48 horizontal and 48 vertical wires, and was read 10 times during a spill (10 samples 2 secs apart), consisting of 1024 *bytes*.

The on-line beam shape monitor used a photon beam with a pair of  $x$  and  $y$  scanning scintillators for each beam to map the beam profile. The motion control of the scanning scintillators was performed with a TMC-1110 servo control from Thompson Industries, and the communication of the KTeV-SC with the TMC controller was performed via an RS-232 interface, as described in Sec. 4.2.3.

## Other Systems

Monitoring was also performed for the fastbus, NIM, CAMAC, VME crate power supplies, various electronics low voltage, temperature and humidity at various places around the KTeV experimental hall. This low voltage monitoring covered a total number of more than 3 000 channels. Also, monitoring was performed for the KTeV SGI cluster operation as well as the status of the run condition; this monitoring includes disk and memory usage, etc.

Furthermore, the CAMAC dataway operation was monitored continuously for malfunctioning CAMAC crates using the CAMAC DTM-299/399 modules located in each CAMAC crate. A task process monitored the Address (A), Function (F), Read (R), and Write (W) lines in each CAMAC crate throughout the KTeV experiment. We operated a total number of 69 CAMAC crates distributed in three CAMAC serial highway systems in the detector as well as in the counting hall. All CAMAC crates used a type L-2 Serial CAMAC Controller (SCC) as an interface to the Jorway 411S SCSI branch drive. The crates were connected via RS422 cable.

In each SCC the data and clock signals were received and re-transmitted by active components. The effect of failure of these components and/or their power supplies was limited by using the SCC in conjunction with a separate bypass device, so the continuity of the signal path would not be lost because of some failure in a local CAMAC crate. To avoid the discontinuity of the SCC in the power failure case, we used the Jorway 176 serial bypass module in each CAMAC crate, which was a single width CAMAC module that provided the ability to bypass the type L-2 serial crate controllers operating in the *byte* serial mode. As a result of power down of the crate and controller, the model 176 “bypasses”, the serial D port highway input signals directly to the serial port highway outputs. Relays in the model 176 switched out the 100 Ohm highway terminations when the CAMAC crate was bypassed. The serial highway signal inputs were buffered by differential receivers within the model 176 to eliminate the 100 Ohm termination of the L-2 from being seen by the bypassed highway.

Also, the FERA ADC CAMAC module pedestals were monitored and loaded via the serial CAMAC system during off-spill periods.

Finally, the rates from various KTeV detector elements were monitored via the CAMAC LeCroy 1151 scaler modules. The KTeV-SC provided a feature to the user for on-line creation of “software” scaler channels: arbitrary arithmetic functions of hardware scaler values and real numbers.

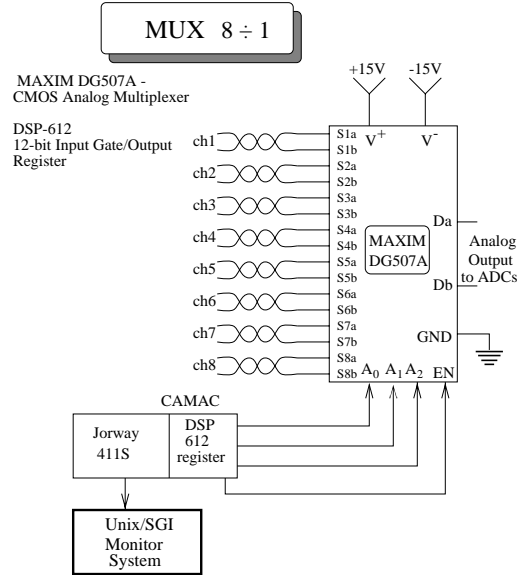


Figure 4.5: Low-Voltage Multiplexer chip.

### 4.2.3 The KTeV-CS Hardware

#### Low-Voltage Multiplexer System

All low voltage channels ( $> 1500$  channels) were routed, through twisted pairs, to several low voltage interface stations, Low-Voltage Transition Boards (LVTB) that will be described in the next section. The voltages were read through 6 CAMAC controlled 8-to-1 multiplexer boxes into 6 Joerger ADC-32 CAMAC AVM. Each multiplexer unit box used MAXIM DG507A-CMOS Analog Multiplexer and a single CAMAC DSP-612 I/O register module, as shown in Figs. 4.5 and 4.6. The MAXIM DG507A (Fig. 4.5) was a differential 8 channel multiplexer.

Each of the 8 input channels was selected by a DSP-612 I/O Output Register, using the 3 bits  $A_0$ ,  $A_1$ ,  $A_2$ . If EN (ENable) bit was high, the channel selection was determined by the binary word input to the  $A_0$ ,  $A_1$ , and  $A_2$  inputs. If EN was low,

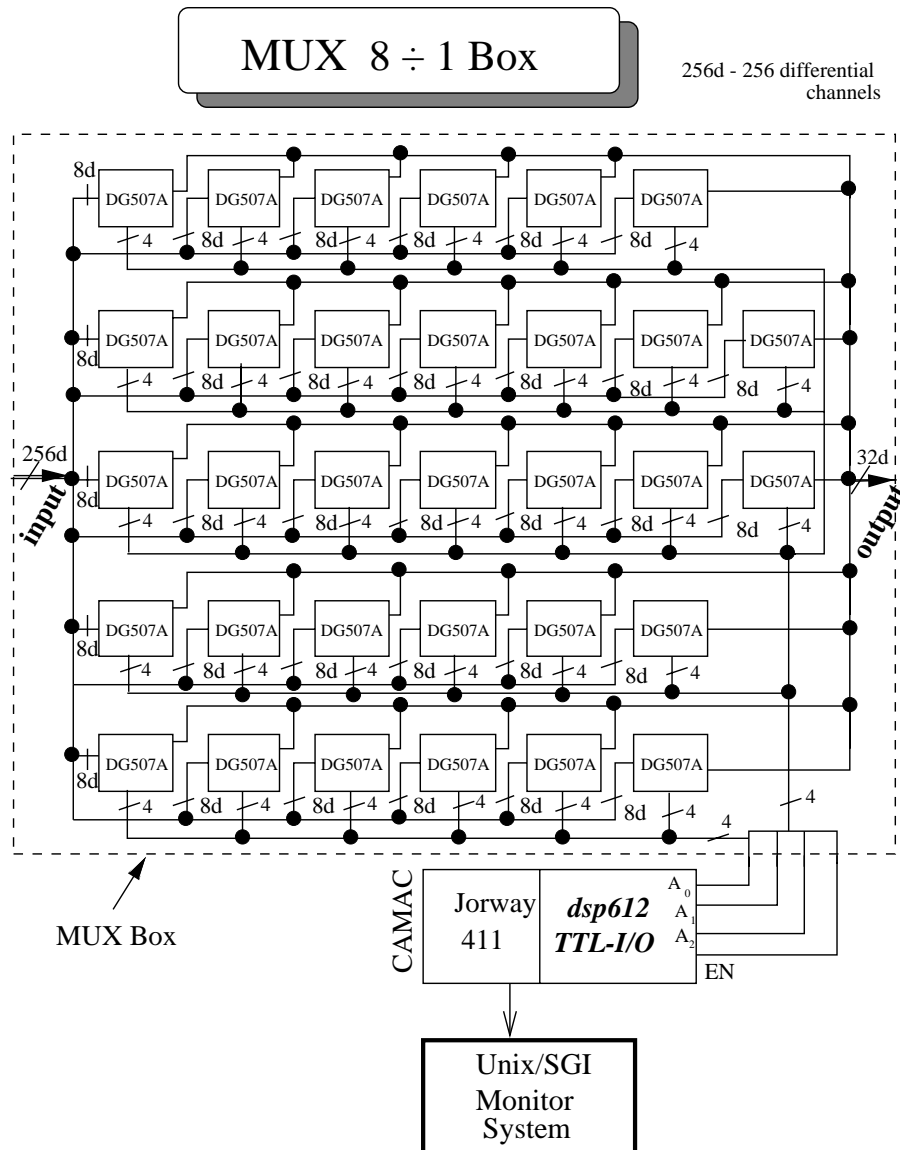


Figure 4.6: Low-Voltage Multiplexer box. It uses 256 differential input with 32 differential output channels.

no channel would be selected. Each Multiplexer 8-to-1 Box contained 32 MAXIM DG507A chips, so it multiplexed 256 input channels getting 32 output channels, as shown in Fig. 4.6. Also each DG507A multiplexer chip included 8 differential inputs, 4 selection inputs and one output channel; therefore, the output number of the MUX box was 32 channels. Thus, each multiplexer box was served by one Joerger ADC-32 AVM.

### Low-Voltage Transition Boards

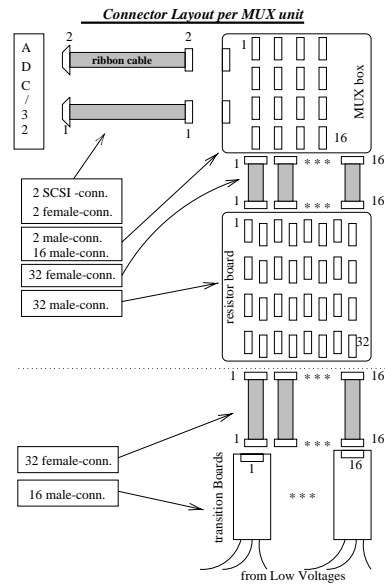


Figure 4.7: MUX unit, including a Joerger-32 ADC, MUX box, resistor board, and transition boards.

As was described in the previous section, the monitoring of the low voltage system used a combination of MUX boxes and resistor divider boards. We define a MUX unit as a combination of a Joerger ADC-32, a MUX box, and a resistor divider

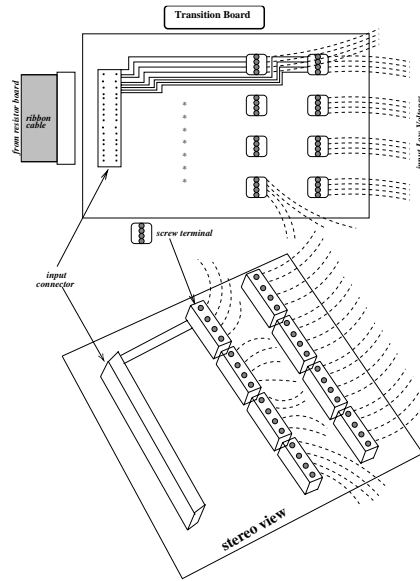


Figure 4.8: LVTB, top view, and stereo view.

board as shown in Fig. 4.7. The interface of the various low-voltage sources (NIM, CAMAC crates etc.) to the resistor board was performed by introducing several LVTB's. Each of these transition boards served 16 input low-voltage channels as shown in Fig. 4.7 and Fig. 4.8; therefore, one or a couple of these transition boards were used to serve a local Relay Rack. On the other side of the transition board a ribbon cable was used to interface the resistor divider board. Each input low-voltage channel was plugged into a screw terminal input as shown in two different views in Fig. 4.8. This solution was flexible, clean, stable and scalable by adding new transition boards to monitoring needed low voltage channels.

## Serial Communication at KTeV-SC

The RS-232 port communications of the various KTeV sub-systems and the KTeV computer cluster was designed to accept commonly used serial cables.

The KTeV sub-systems that used serial communication were:

- Beam Shape Monitor (BSM),
- Analyzing Magnet Hall probe,
- PLC for CsI, DC gas, and Vacuum system, and
- Regenerator Temperature system

as shown in Fig. 4.9. For all the needed RS-232 to RS-422/485 conversion we used model 485 adaptor from Amplicon-liveline which was a compact, plug-in unit providing bidirectional conversion of serial communications signals between RS-232↔RS-422, and RS-232↔RS-485.

It should be emphasized that many of the signals defined by the RS-232 standard table 4.1 were rarely used. The following table lists the signals that were important in our discussion (in the PLC case).

Only two of the nine pins were used for data transmission:

*2 Transmit Data*

*3 Receive Data.*

These two lines were used differently by computers and other device line modems. The RS-232 standard defines two types of equipment: Data Terminal Equipment (DTE) and Data Communications Equipment (DCE). Most computers (like the SGI KTeV cluster processors) were DTE. Also, the PLC was a DCE node.



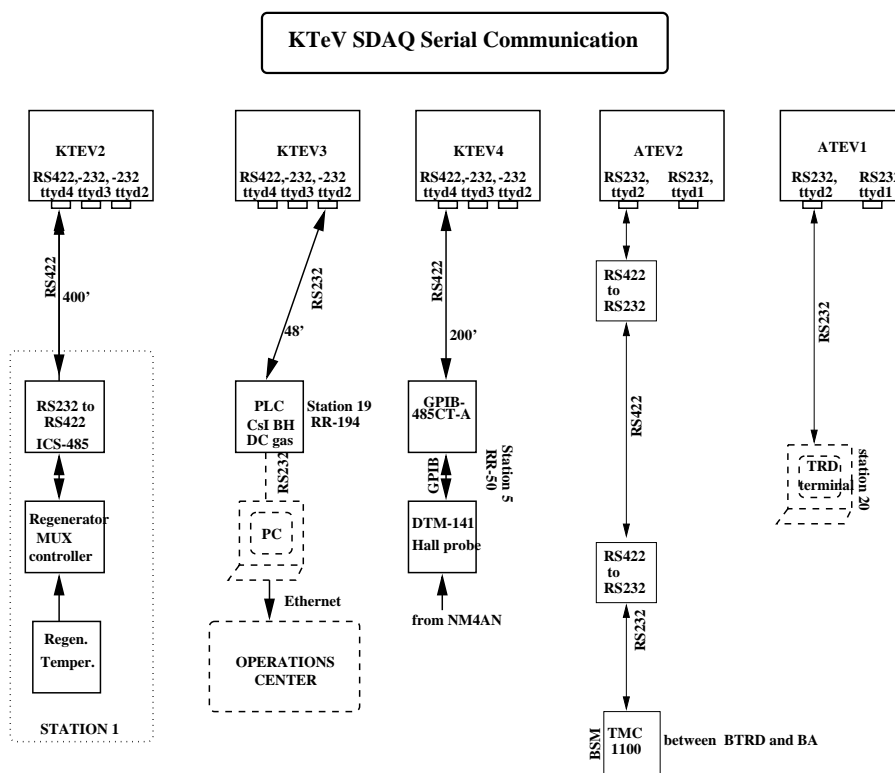


Figure 4.9: KTeV RS232 communication. Here, shown only the KTeV processors that use the RS-232 communication.

Table 4.1: RS-232 signals and their functions for the PLC.

Pin Number	Function
1	Data Carrier Detect (DCD)
2	Receive Data (RX)
3	Transmit Data (TX)
4	Data Terminal Ready (DTR)
5	Signal Ground (GND)
6	Data Set Ready (DSR)
7	Request To Send (RTS)
8	Clear To Send (CTS)
9	Frame Ground

#### 4.2.4 The KTeV-SC Software

The overall software structure of the KTeV-SC system is presented in Fig. 4.10. As shown in this figure, the system was highly modular and highly distributed with many task processes running on all KTeV cluster processors. Many advantages came from the design of the KTeV-SC in a highly modular fashion, with different subsystems running in different processes, and with well defined interfaces between them. This modular construction rendered the overall system robustness against problems in every area, so that a problematic process or task would affect only the sub-system that was controlled/monitored.

Most of the KTeV-SC task processes were of a generic nature, so, if possible, minimum software development was implemented. Most of the tasks (the ones needed to probe CAMAC) were physically running in the dedicated KTeV-SC workstations (atev1 and atev2), since the serial CAMAC system was attached to these stations. The rest of the task processes were distributed among the KTeV-DAQ available processors.

#### KTeV-SC Database

The logging and archiving of the KTeV-SC system used the HEPDB CERN database product. The database files contained all the necessary information for monitoring and controlling the experiment.

The HEPDB package is built upon one big ZEBRA RZ file that contains all the information. The ZEBRA RZ package uses random access files which reside on direct access devices or in memory. RZ files are organized in a hierarchical

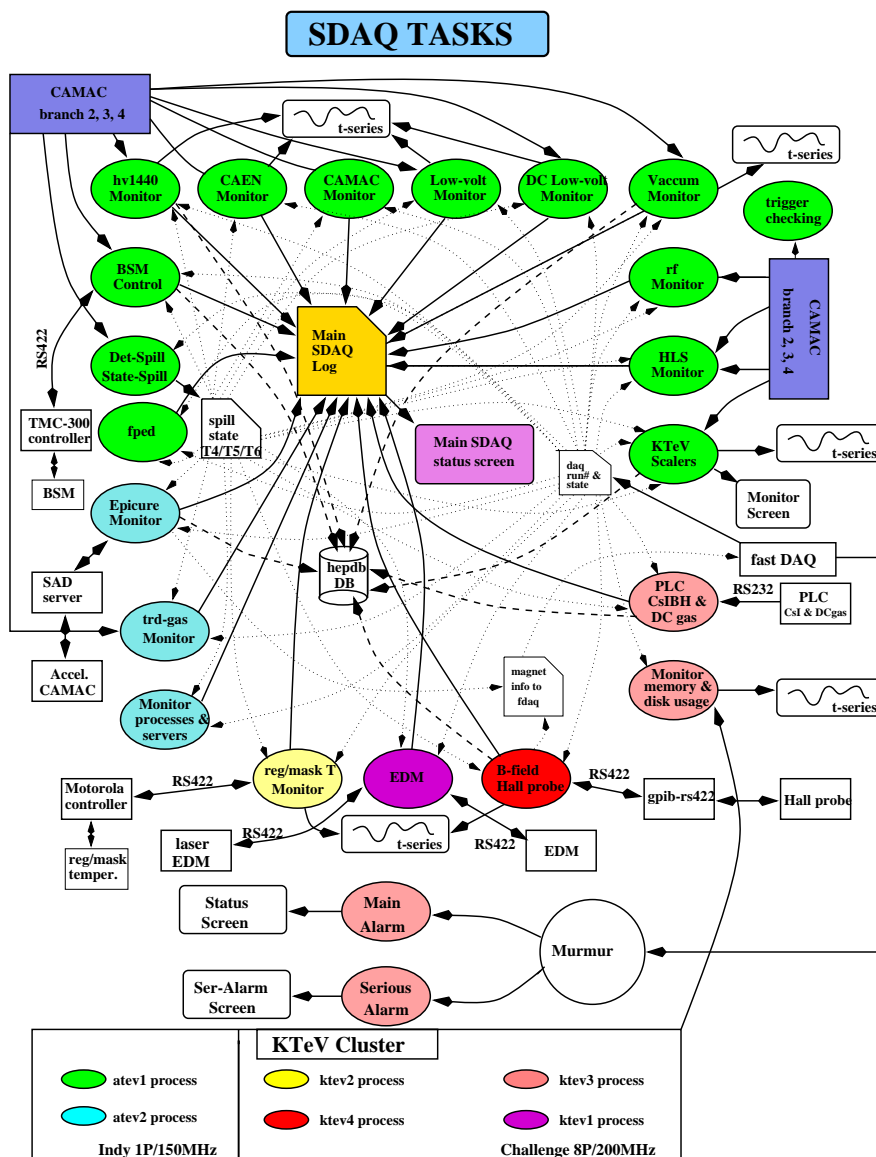


Figure 4.10: Overall software structure of the KTeV-SC system. Also, shown are the different tasks that perform the monitoring/controlling of the KTeV detector.

manner, similarly to the Unix file system. Thus, in the ZEBRA file there are ZEBRA subdirectories where the records are stored. There was no particular limit on the number and levels of subdirectories. The data, either from different detectors/systems or from different types of data for one detector, like High Voltage, Low Voltage, were stored in different subdirectories.

While in a usual database package everything that can be used to select a particular record is called a *key*, HEPDB distinguishes between *validity range pairs* and *keys* to access the data. The validity range pairs were well suited for the run/spill-related data we usually had. The pairs defined a window of a particular record. For the Slow-Daq database we defined 2 range-pair: the run and spill number. In addition, there were 10 keys automatically defined by the HEPDB package with predefined meanings, referred to as *system keys*. All other keys are called *user keys*. While the number of *validity range pairs* is a database constant, the number of *user keys* is a property of the subdirectory. Additional user keys could also be added.

For the purpose of logging and archiving, it was convenient to class the information that described the status of the KTeV detector according to the frequency with which it was updated. Thus, we separate the KTeV-SC system into two major components:

- Slow Control/Monitor (SC) (that included the HV/LV/PLC/ Analyzing Magnet Hall probes/Regenerator Temperature monitor etc.),
- End of Spill information (EOS) (that included the Accelerator Epicure/SAD data).

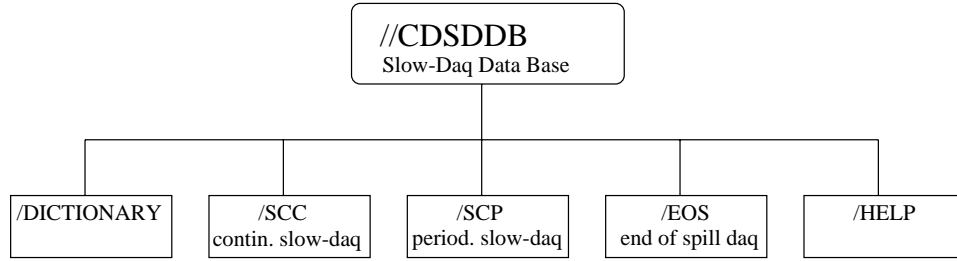


Figure 4.11: KTeV-SC Database detailed architecture.

In addition, the Slow Control/Monitor (SC) class was separated in two more subcomponents:

- Slow Control/Monitor Continuous (SCC), where these systems monitored the detector components continuously,
- Slow Control/Monitor Aperiodic (SCP), where these systems monitored some of the detector systems in aperiodic time intervals.

The KTeV Slow-Control database (SCDB) architecture is shown in Fig. 4.11.

A part of the SCDB structure was the SCC structure that is presented in Fig.4.12. Down from `/SCC` subdirectory there were 5 more subdirectories, `//CDSddb/SCC/HV` (high voltage), `//CDSddb/SCC/LV` (low voltage), `//CDSddb/SCC/PLC` (PLC data), `//CDSddb/SCC/DW` (dataway monitor), and `//CDSddb/SCC/CONSTANT` (constant data). In addition down from the `//CDSddb/SCC/HV` (high voltage), `//CDSddb/SCC/LV` (low voltage), and `//CDSddb/SCC/PLC` (PLC data) subdirectories more directories were holding the various detector data.

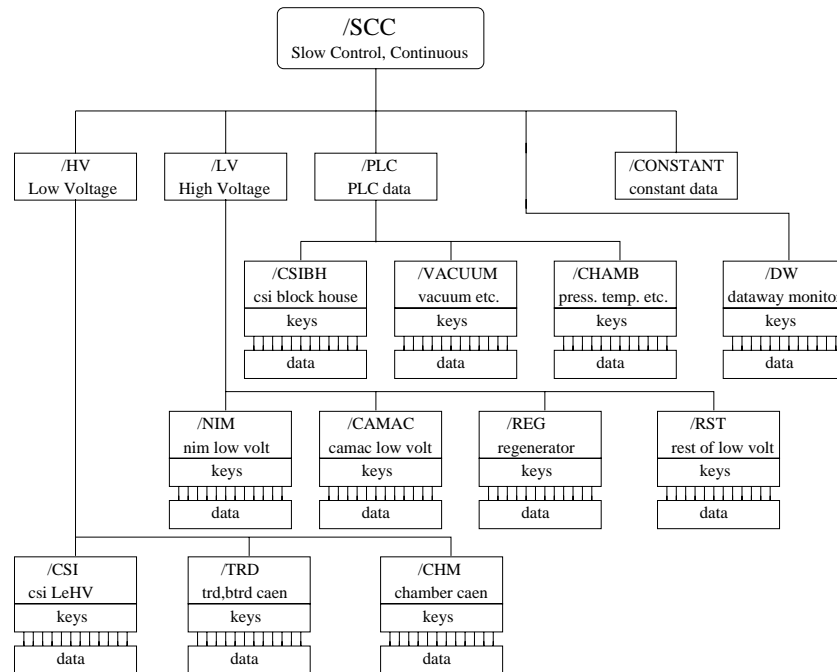


Figure 4.12: Part of the SCC database structure.

#### 4.2.5 Performance of the KTeV-CS

The KTeV Slow-Control system appeared to the user as an integrated system. Once started, there was no need to type commands into a terminal window or to start any other process. The shift crew was presented permanently with a graphical display showing the current status of the KTeV-SC, which was implemented on a color OPI in the SGI cluster. This graphical display included rows of buttons corresponding to each sub-system of the KTeV-SC as shown in Fig. 4.13. Clicking on these buttons would open up a new window to present more information about the status of the corresponding sub-system.

Several other color graphical displays were presented more information about the status of individual sub-systems of the KTeV detector. Namely, Figs. 4.14, 4.15 were the status screens of the LeCroy 1440, CAEN SY527 units, where one could control/monitor the high voltage of different sub-detectors, such as CsI calorimeter, DC's, TRD's, regenerator, etc. Furthermore, Fig. 4.16 was the status screen of the CsI blockhouse, and DC gases monitor, which was presenting information about the temperature, humidity, pressures, etc.

We used consistent color coding of icons and buttons throughout the system. Input parameters to which the user was denied access are grayed out.

Alarms were graded into two levels:

- normal state, where the system operates normally and all parameters were within the given tolerance values (green color button or icon).
- fault state, where it implies that some action was required to restore the equipment to its normal state (red color button or icon).



The KTeV-SC system was proved to be a useful and reliable system during the KTeV run , where almost all the KTeV sub-detectors were using this system. It caught numerous potential problems, and flagged error states before they occurred by observing various parameter trend-graphs.

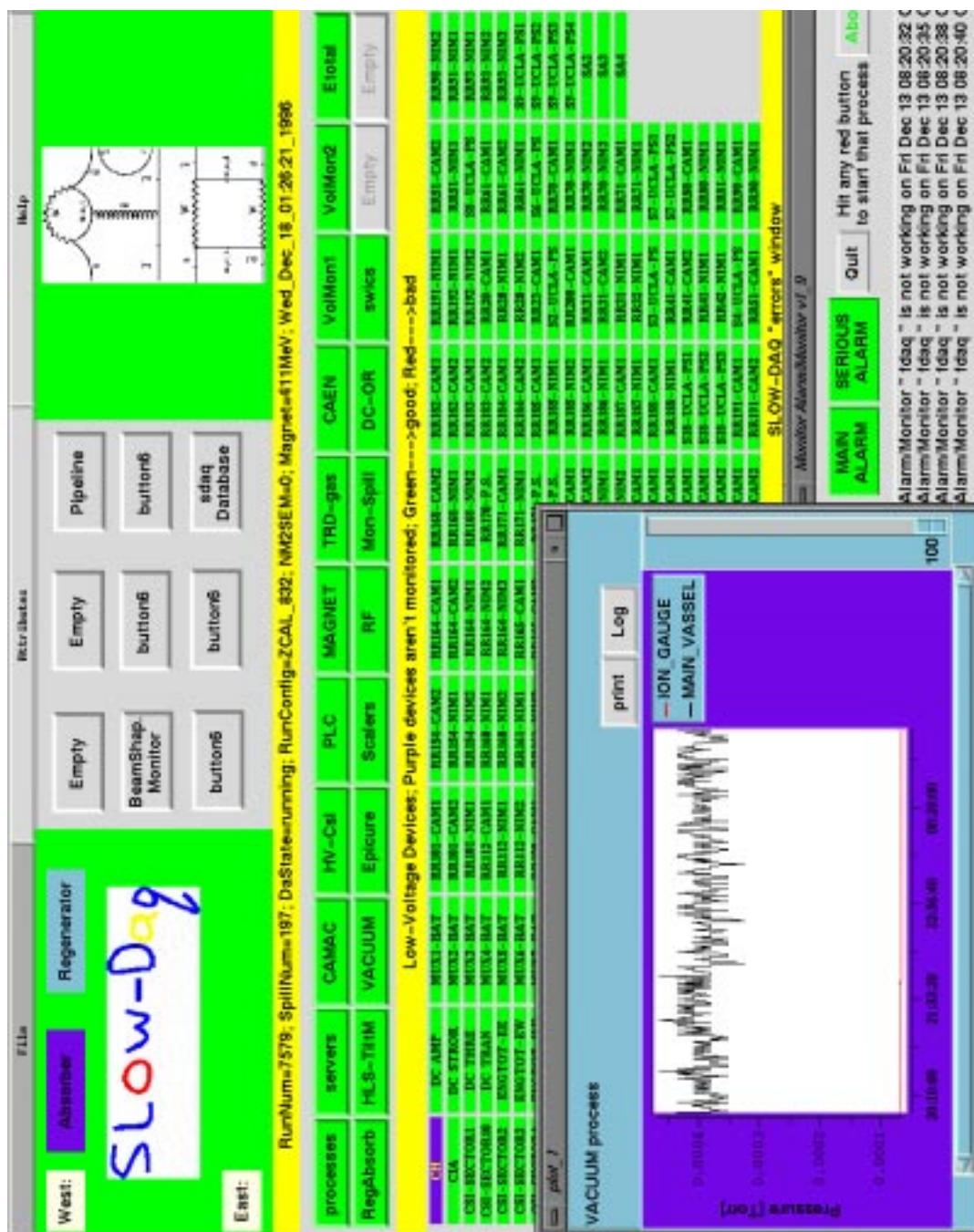


Figure 4.13: The main KTeV-SC screen, presenting the status of various components of the KTeV experiment.

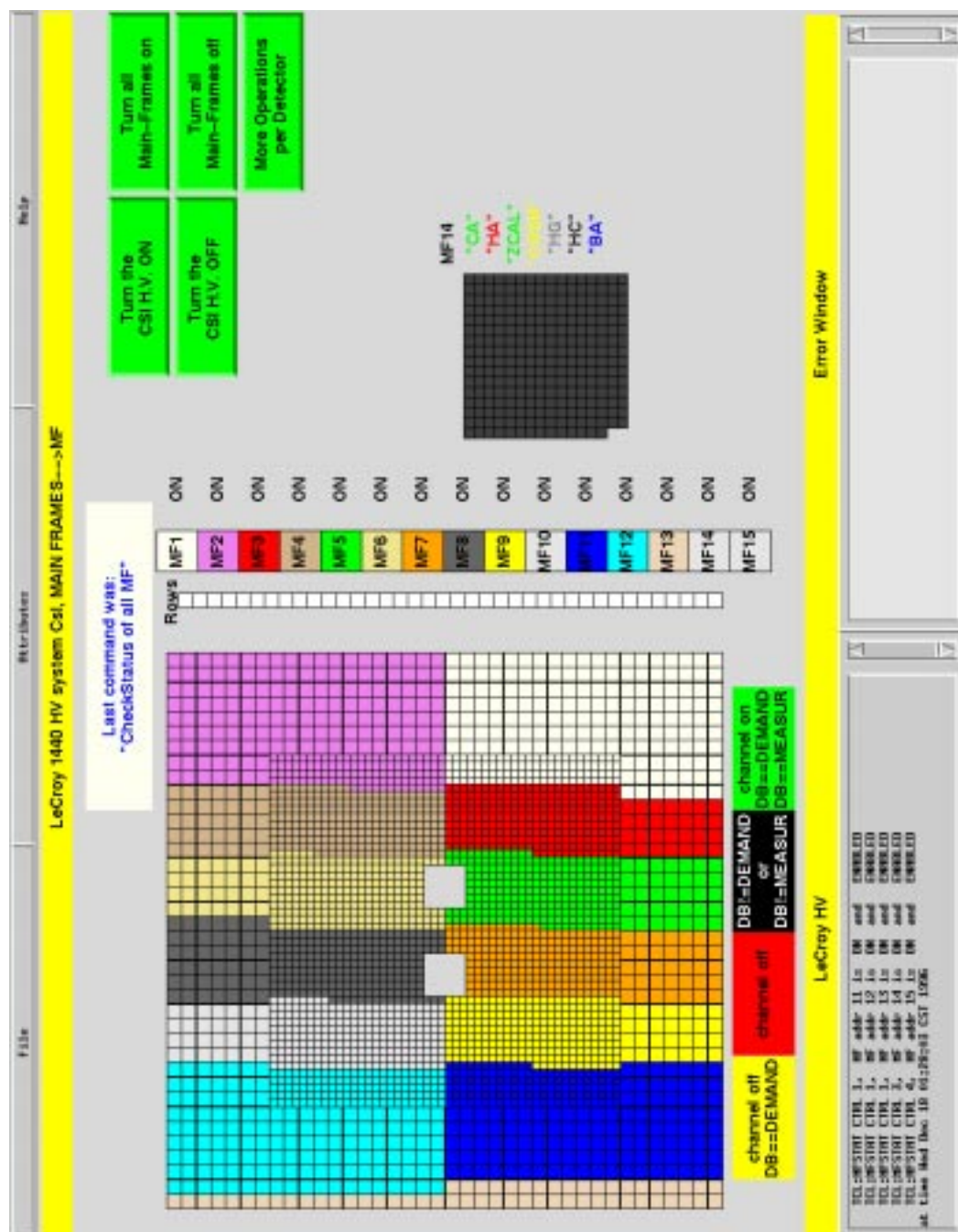


Figure 4.14: The LeCroy 1440 HV status screen.

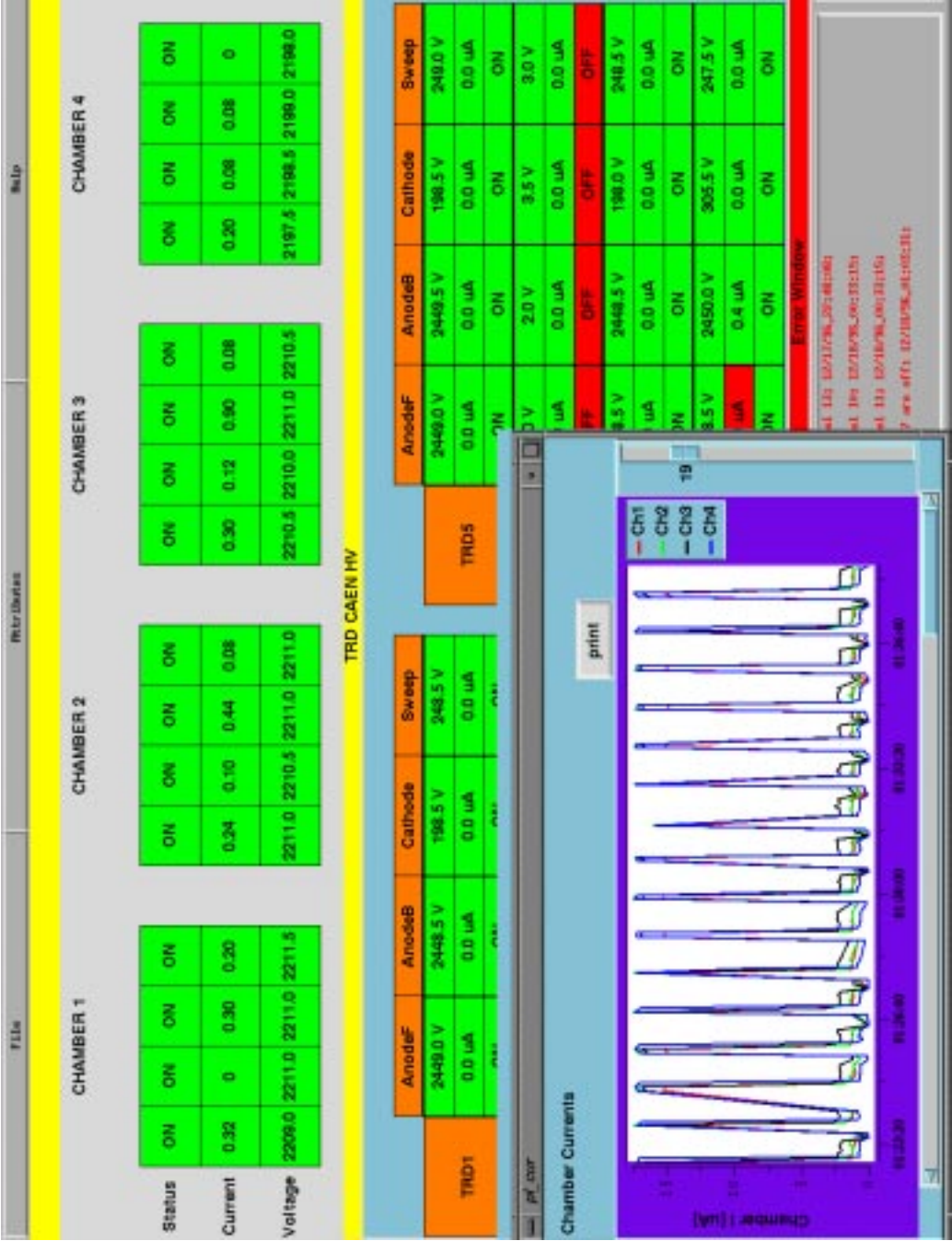


Figure 4.15: The CAEN HV status screen includes the DC and TRD system.



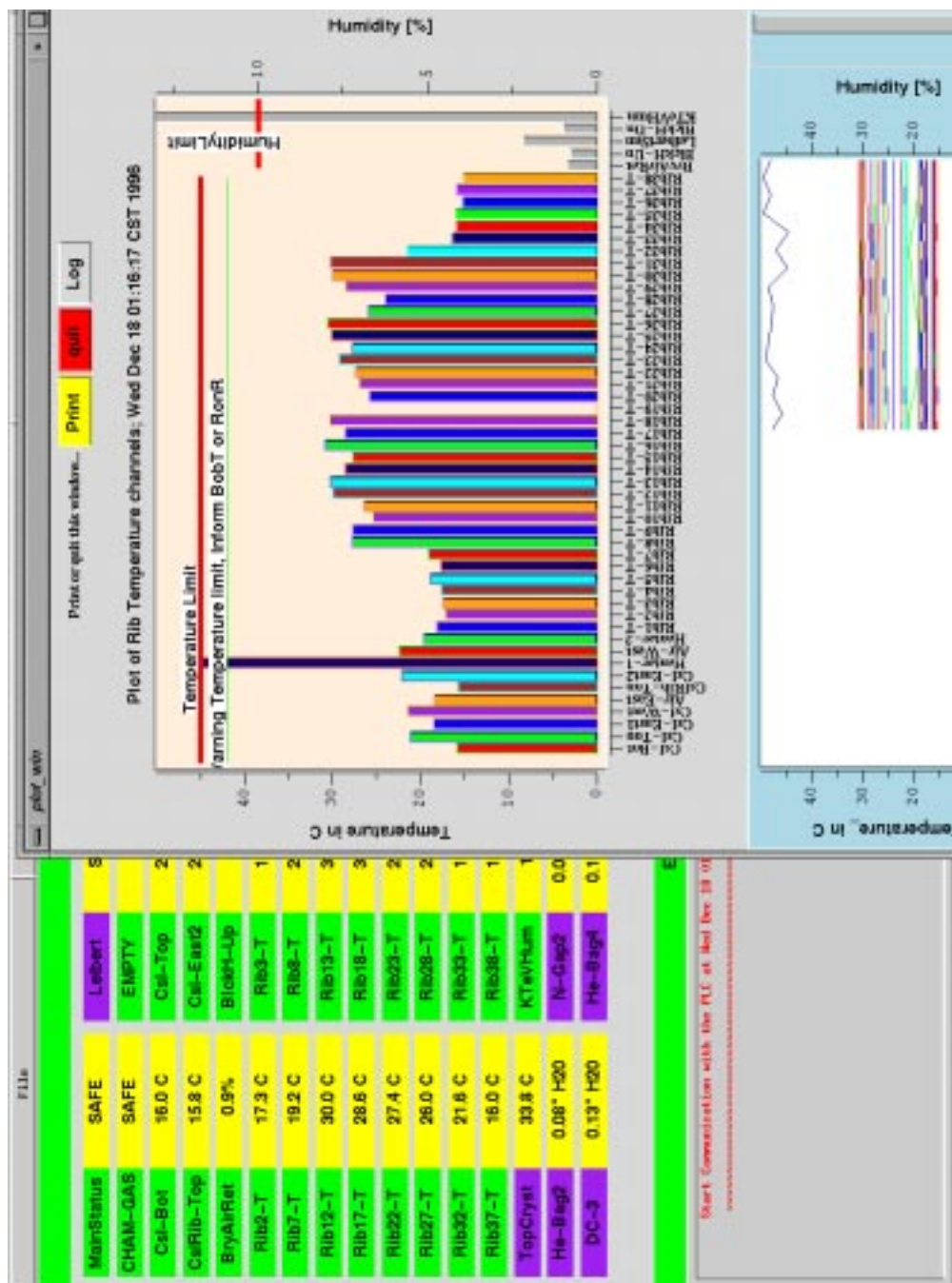


Figure 4.16: The PLC monitor status screen.

## Chapter 5

# Event Reconstruction and Detector Calibration

This chapter describes how the raw data read out from the detector components is processed for the data analysis. It consists of two parts.

We first overview the algorithms used for tracking in the drift chambers, clustering in the CsI electromagnetic calorimeter, and the matching of tracks to the clusters which were the building blocks of any data analysis at KTeV. Emphasis is made on the analysis of the hyperon decays which generally featured one stiff track going down the CsI beam holes.

Calibration of the detector was also a crucial task. The analyses of charged particles were sensitive to the performance of the drift chambers. We describe the calibration procedures for the chambers and address some related alignment issues.

## 5.1 Track Reconstruction

We first describe how the charged particle tracks in the spectrometer are reconstructed. Details of the tracking algorithm can be found in reference [71].

Track candidates were searched for in the  $x$  and  $y$  views of the drift chambers

independently with no attempt to match them. The matching between the two views were performed after the clustering (Sec. 5.2), because the cluster positions at the CsI calorimeter were needed to resolve the ambiguity in the  $x$ - $y$  matching (Sec. 5.1.4). The tracking algorithms differed substantially between the  $x$  and the  $y$  views because of the track bend at the analyzing magnet in the  $x$  view. Tracking in both views began by identifying and classifying drift chamber hits. In the  $x$  view, upstream and downstream segments were then identified, and these segments were matched at the center of the magnet to form complete tracks. In the  $y$  view, more stringent requirements could be used because these tracks formed a straight line through the four tracks.

### 5.1.1 Hit pairs

First, the hits in the drift chambers were sorted and classified as either single hits or hit pairs, where a pair means one hit in each complementary plane,  $x \leftrightarrow x'$  or  $y \leftrightarrow y'$ , as defined in Sec. 2.3. The probability of having a single hit, namely the hit in the complementary plane is missing, was very small due to the high efficiency of the chambers (see Sec. 5.3.4). These single hits were treated differently by the tracking algorithm. If hits were found in both planes, the position measurement from the two hits could be checked for consistency by calculating the some of the distances (SOD) between the sense wires and the point where the charged particle hit the chamber (see Sec. 5.3 for a detailed description of the time to distance conversion). Since the known spacing between the two wires in the complementary planes was 6.35 mm (the cell size), the difference between the SOD and 6.35 mm was required

to be within 1 mm for  $x$  view of the two upstream chambers and  $y$  view of all chambers and within 1.5 mm for  $x$  view of the two downstream chambers. A SOD significantly higher than the cell size suggested a track which arrived in an RF bucket before the formation of the trigger.

If the SOD was low, this suggested a late out-of-time track. However, another cause of a low SOD was the production of  $\delta$ -rays. Energetic charged particles passing through the material inside or outside of the chambers can knock out electron and produce the so called  $\delta$ -rays. If these  $\delta$ -rays were sufficiently energetic, they could produce their own ionization in the chamber close to the primary track. If both the  $\delta$ -ray and the primary track passed through the same drift chamber cell, the sense wires saw first the ionization from the closest ionization track, either the primary or the  $\delta$ -ray. Since the chamber TDC's registered the first hit only, the effect was a low SOD measurement from  $\delta$ -rays which can be observed in the sum-of-distances plots (see Fig. 5.3).

### 5.1.2 Y Tracks

Once hit pairs were found in each chamber, the sets of pairs in  $y$  views were grouped into linear track segments. For each combination of a chamber 1 pair and a chamber 4 pair, the track position was projected to the chambers 2 and 3, and those chambers were checked for pairs which lie within a distance of 5 mm of the projected track. For those pairs which lie near a straight line, a least squares fit for the difference between the projected position and hit position at the chamber plane 2 and 3 was carried out. If the  $\chi^2$  per degree of freedom of the fit was less



than  $4 \text{ mm}^2$ , this would be accepted as a  $y$ -track.

### 5.1.3 X Tracks

The  $x$ -view tracking was done differently. Since the analyzing magnet between the upstream chambers 1 and 2 and the downstream chambers 3 and 4 applied a momentum kick to the charged particles in  $x$  direction, the hit pairs in the  $x$ -view of the upstream and downstream chambers had to be examined independently.

The tracking algorithm made a list of all possible upstream segments in the  $x$ -view. An upstream segment was defined as a pair in chamber 1 plus a pair in chamber 2 which originated from the beam and whose angle was less than 100 milliradians. The same procedure was repeated to find the downstream segments in chambers 3 and 4. The  $x$ -track candidate was then defined as any combination of a downstream segment with an upstream segment which matched at the plane of the magnet kick with a separation distance smaller than 6 mm.

### 5.1.4 Vertexing

After finding  $x$ -track and  $y$ -track candidates, one could check for a two-track vertex, *i.e.* two  $x$ -tracks and two  $y$ -tracks which might originate from a common point within the decay region. For each pair of  $y$ -track candidates that were allowed to coexist, we projected their upstream segments back into the decay region and found the range of  $z$  positions at which they might intersect. If they might intersect within the decay region, we labeled them as  $y$ -intersection candidates and proceeded to do the same for the  $x$ -track candidates. We then looked for a combination of  $x$ -intersection and  $y$ -intersection candidates for which the ranges

of allowed  $z$  values overlapped. Any such combination would be a two-track vertex candidate.

### 5.1.5 Track-Cluster Matching

Matching between  $x$ -track and  $y$ -track candidates that pointed within the CsI calorimeter arrays could be done using the energy clusters in the calorimeter. The algorithm would find the closest cluster to the projected position at the CsI of each  $x$ -track/ $y$ -track combination. The distance separation between the position of the track  $(x,y)$  at the calorimeter and the position of the cluster (known as track-cluster separation) was required to be less than 7 cm, in order to accept the matching.

The list of vertex candidates were then examined to determine, for each one, whether the tracks matched to clusters in either (or both) of the two X-Y matching cases. For hyperon decays, one (and only one) track had to go down the beam holes in order to be triggered. In this case an  $x$ -track and a  $y$ -track were matched within a beam hole and no CsI cluster could be used.

Any cluster with energy above some threshold (3 GeV for Cascade beta decay) and not matched to a track was counted as an “extra cluster”<sup>1</sup>. Extra clusters were candidates for photons.

---

<sup>1</sup>The energy threshold reduces the chance of extra clusters being created by soft bremsstrahlung, accidental photons, or tails of hadronic showers.

## 5.2 Cluster Reconstruction in the Calorimeter

A two-pass CsI reconstruction algorithm was used to find clusters of energy deposits in the CsI calorimeter (Sec. 2.6). The first pass used information from the HCC (Sec. 3.2.2) to find *hardware* clusters. The second pass used settable block and cluster thresholds to find lower energy *software* clusters. Once found, hardware and software clusters were treated in the same way. The energy and position of each cluster were then extracted with some corrections [72].

### 5.2.1 Hardware Clustering

The hardware clustering searched for local maxima among the crystals which had the HCC bit set by the second level trigger. All crystals with the HCC bit set, were compared in energy against the neighboring crystals (adjacent or diagonal) which also had the HCC bit set. The crystals with the greatest energy of all the neighbors were made a cluster seeds. The crystals around the seed with energy greater than the read out threshold were considered as part of the cluster. For crystals near the boundary between large and small crystals, four  $2.5\text{ cm} \times 2.5\text{ cm}$  crystals were grouped together and regarded as one  $5.0\text{ cm} \times 5.0\text{ cm}$  crystal. The maximum size of a cluster was  $7 \times 7$  crystals centered around the seed block for  $2.5\text{ cm} \times 2.5\text{ cm}$  crystals, and it was  $3 \times 3$  crystals in the case of  $5.0\text{ cm} \times 5.0\text{ cm}$  crystals.

### 5.2.2 Software Clustering

The software clustering formed clusters by searching for crystals whose energy was above a seed threshold, and were local maxima. The algorithm searched for seeds only among the crystals which had not already been included in a hardware cluster. Crystals above the seed threshold were compared against their neighbors in a similar fashion to the hardware clustering except that the HCC bit was off. All Crystals which were local maxima were software cluster seeds. Clusters were formed of fixed size square regions exactly as hardware clusters, however, there was also a cluster threshold below which the cluster would be thrown out.

### 5.2.3 Energy and Position Measurements

Once the clusters were found, we used two sets of lookup tables to reconstruct the energy and position of the incident particles. The first was the “Transverse” lookup, which contained the average transverse energy distribution of the showers. The second was the “Position” lookup, used to determine the cluster position.

The energy of a cluster was found by simply adding up the energy of each crystal in the cluster. For regions near the beam hole or near the outside edge, the energy leakage was corrected for by using the lookup table created from  $K_{e3}^0$  events. Overlapping clusters were separated, *i.e.* the crystals which had contributions from multiple particles had their energy split by also looking at the same table. Finally, the total energy of the cluster was corrected for the energy leakage outside of  $7 \times 7$  crystal array (for small crystals), back of those crystals, and energy loss in the wrapping materials based on a study by using GEANT simulation. The fraction

of the missing energy were independent of the energy of the incident particle, and depended only on the size of crystals, 1.042 for the  $7 \times 7$  small and 1.059 for the  $3 \times 3$  large crystals (also for boundary region of large and small crystals), respectively.

The position lookup contained a map from the ratio of energy in adjacent rows or columns of a cluster to the position of that cluster. There were a total of 12 lookup tables, 6 for the small crystals, and 6 for the large ones, covering 6 different energy regimes. To make these lookup tables, electrons from  $K_{e3}^0$ 's whose momenta and positions were well measured by the spectrometer were used. The resulting resolution in position was estimated to be roughly 1 mm for 15 GeV photons.

### 5.3 Drift Chambers Time-to-Distance Calibration

In this chapter, we discuss the process of calibrating and alignment of the charged spectrometer [73, 74] system as well as the performance of the drift chambers during E799-II winter and summer runs.

#### 5.3.1 Timing Offsets

In order to do precision tracking with the chambers, one needs to be able to determine the drift distances by measuring the drift time in the chambers. We used LeCroy 3377 time to digital converters (TDC's) to get the signals from the drift chambers after being amplified and discriminated in front end cards mounted on the drift chambers. The TDC's were self-calibrating so that each TDC count corresponded to 0.5 nsec. However, to obtain the drift distances from the outputs of the TDC's, it is first necessary to know the TDC value for each wire that

corresponds to zero drift distance. Then, by knowing the relationship between drift times and drift distances, known as  $X(t)$  relation, one can make precise position measurements in the chambers.

There are several mechanisms that might introduce wire-to-wire variations in the value corresponding to a zero drift distance. For instance, varying cable length, different pulse height and shape, and channel-to-channel or module-to-module variations in the TDC's; and most importantly, the common stop delivered to the TDC's can all give timing differences between wires. In order to remove such differences, we used a simple technique.

Figure 5.1 shows the raw TDC distribution for hits on tracks for all wires in plane 1. The in-time window was defined as TDC counts between 230 and 700 (corresponding to 115-350 ns) and the timing edge comes from the prompt hits passing very close to a sense wire. Because the level one trigger, which provided a common stop for the TDC's, was correlated with activity in the chambers, one could use the absolute position of the timing edge to measure the zero drift TDC value. By comparing the position of the edge for each individual wire, a set of timing offsets for each were generated. This method had the advantage of not even requiring the tracks be found in the chambers. Therefore, this timing offset measurement technique could be used before any chamber alignment had been performed.

The procedure for calculating these timing shifts was to compare the shape near the timing edge for an individual wire with the edge from the sum of the 16 wires in its cable, and similarly to compare each cable in its plane with the overall

shape for the whole plane. By sliding these two timing edge distributions past one another and looking for the minimum in the  $\chi^2$  for the two distributions to match, one could then find the correct timing offset for that wire or cable. We used the two-track trigger (mostly  $K_{e3}^0$ 's) with about a million events to remove the T(0) offsets.

The largest components to shifts in the timing offsets were global shifts in Level 1 common stop delivered to the TDC's by the trigger and the global shifts in the beam timing with respect to the RF signal delivered to the experiment by the Tevatron. Figure 5.2 shows the RF-L1 timing versus run numbers. The T(0)'s were recalculated after large shifts in the timing.

### 5.3.2 Time-to-Distance Relations

Once any wire timing offsets had been removed, the chamber was treated as a unit to determine the relationship between drift distances and drift times (the “ $X(t)$  relation”) in the chamber. This was a valid assumption because parameters which affect this relation, such as the cell geometry, DC voltages, and gas mixture were identical for each sense wire in the chamber. Although, there was some evidence that rate effects were different in the beam region than the outside of the beam region, no attempt was made to account for these effects in E799. The procedure relies on the fact that on average, the illumination across each cell for an entire plane pair is uniform. In fact, even if the illumination varies linearly with position in the chamber, it will be higher on one side of a given wire, and lower on the other side in a symmetric way, hence cancelling locally. Given this uniform illumination,

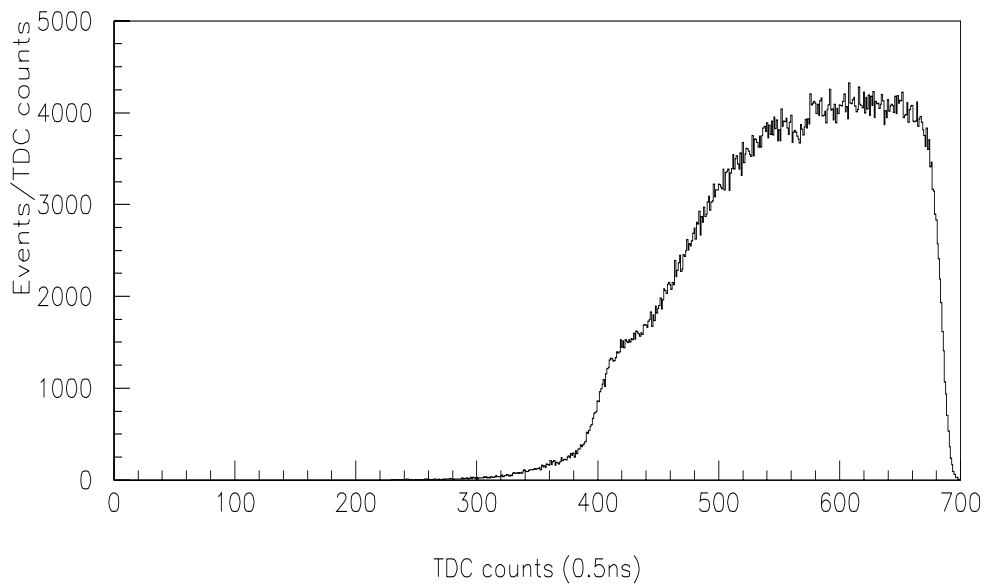


Figure 5.1: The raw distribution of TDC values for all wires in plane 1. The sharp edge corresponds to charged particles passing very close to a sense wire at high TDC values. The trigger provided a common stop for the TDC's.



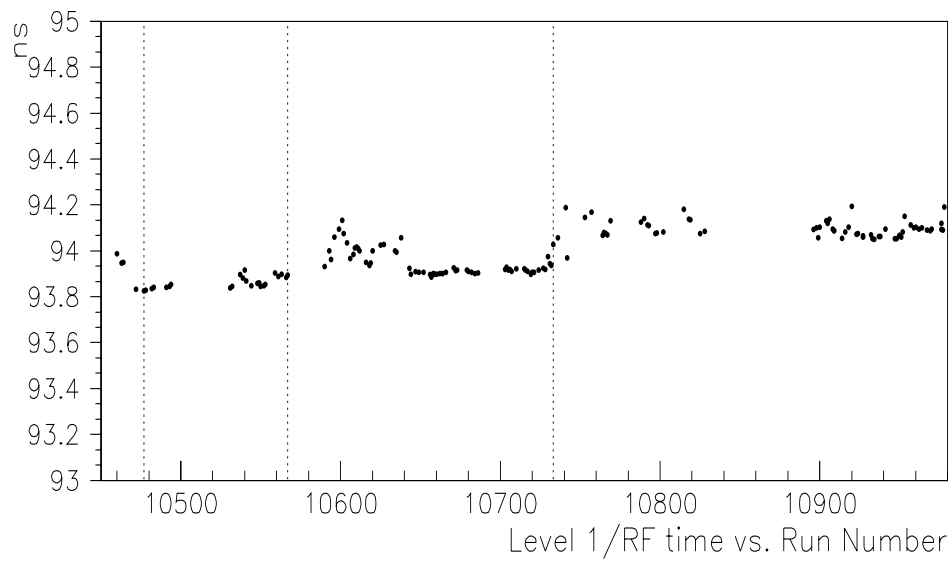


Figure 5.2: Average RF-Level 1 timing as a function of Run for E799 summer data.

The dashed vertical lines show runs for which  $T(0)$  calibrations were performed.

one can convert the distribution of the observed time into a lookup table from time to distance. Since the  $X(t)$  relation was assumed to be independent of location in the chamber, it was possible to determine this relation without using the tracks. Any sample of real hits in the drift chambers from charged particles in-time with the trigger can be used to extract the  $X(t)$  relation. However, in practice it was necessary to use hits on tracks in order to avoid backgrounds from out-of-time hits and from chamber noise.

For on-line  $X(t)$  calibration, we used samples of about 100 000 single track soft muons. Short muon runs were taken several times a week and saved on the local computer disks for the purpose of chamber calibrations and alignment. We checked the sum-of-distances (SOD) distribution and plane-by-plane resolutions (discussed in Sec. 5.3.3) following each muon run. A new  $X(t)$  map was generated and installed in the database, if there was any significant changes in the SOD distribution or chamber resolutions. Especially, it was necessary to update the maps after any long shut down, change of drift chambers' voltages or any access to the experimental hall which required any repair work on the chambers.

The two track  $K_{e3}^0$  samples (approximately 200 000 events) were used off-line to do this calibration. The runs for which an  $X(t)$  map was made, were the longest runs evenly spaced in the run period. Each track was required to have an in-time hit in the trigger counters and matched to a cluster in the CsI. The TDC distribution for hits on tracks was collected for each of the 16 drift chamber planes. The times were corrected for the propagation delay along the wire (6.8 TDC counts per meter). Missing hits were another concern because inefficiencies

are often correlated with the track position in the drift cell, leading to a bias. The method to correct for this, is to track the number of missing hits in terms of the hit on the complementary plane. When a pair was found with one of the hits having the same time as one of these singles, the other hit of the pair replaced the missing partner of that single hit. Thus, the data itself was used to find, on average, the times of the missing hits.

The time-to-distance relation is then given by

$$X(t) = d_{cell} \times \frac{\sum_{t_0}^t N(t)}{\sum_{t_0}^{t_m} N(t)} \quad (5.1)$$

where  $d_{cell}$  is the cell size of 6.35 mm corresponding to the maximum drift distance, and we are summing over the number of events  $N(t)$  in each 0.5 ns bin,  $t_0=0$  and  $t_m=240$  nsec. We have assumed that the distribution of times is ordered so that larger times are larger distances. Figure 5.3 shows a typical  $X(t)$  map for the drift chambers. This procedure was iterated a few times since the track-finding algorithm depends weakly on the  $X(t)$  tables used.

### 5.3.3 Chamber Resolution

Figure 5.4 shows a typical sum-of-distances plot. The low-side tail is due to  $\delta$ -rays produced when the tracks passed through material inside or outside the chamber which created a second track through chambers and the high-side tail is the result of the so called “hi-SOD” problem in the experiment, hence causing an asymmetric sod distribution. The central region of the peak (6.10-6.50 mm) was fit to a Gaussian distribution whose mean should be the cell size, 6.35 mm. The chamber

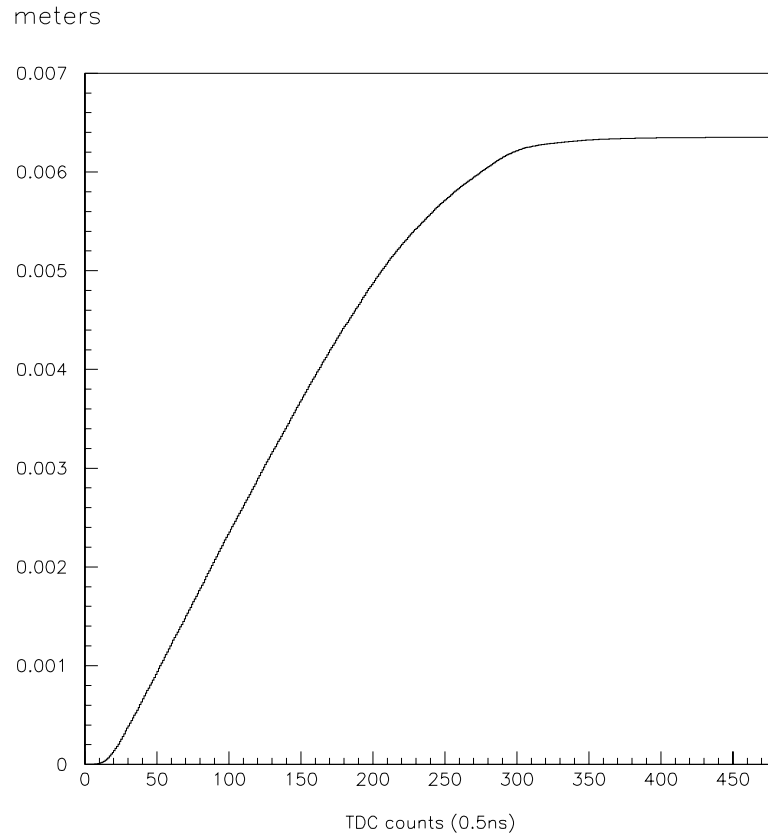


Figure 5.3: A sample Time-to-Distance Relation for plane 1. TDC counts are subtracted from a common offset (700 counts) to invert from common-stop mode. The relation is quite linear between 20 and 230 counts with a slope of about  $50\mu\text{m}/\text{nsec}$  and asymptotically approaches the cell size of 6.35 mm.

resolution defined as the standard deviation of the Gaussian distribution divided by  $\sqrt{2}$ , was measured for all the runs used for the  $X(t)$  calibration.

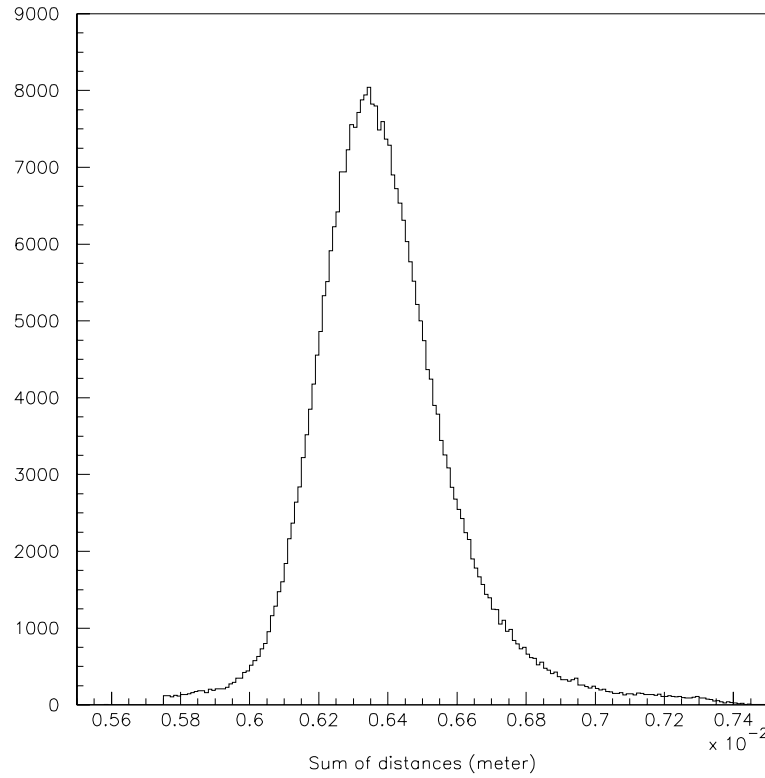


Figure 5.4: A typical Sum-of-Distances distribution in Chamber 1, X view. The mean of the distribution should be the constructed cell size of 6.35 mm and the width is proportional to the resolution.

Figures 5.5 and 5.6 show the history of the drift chambers resolution for the winter and summer of E799 data-taking respectively. These resolutions varied between 90  $\mu\text{m}$  and 130  $\mu\text{m}$  and were largely constant with time. The observed

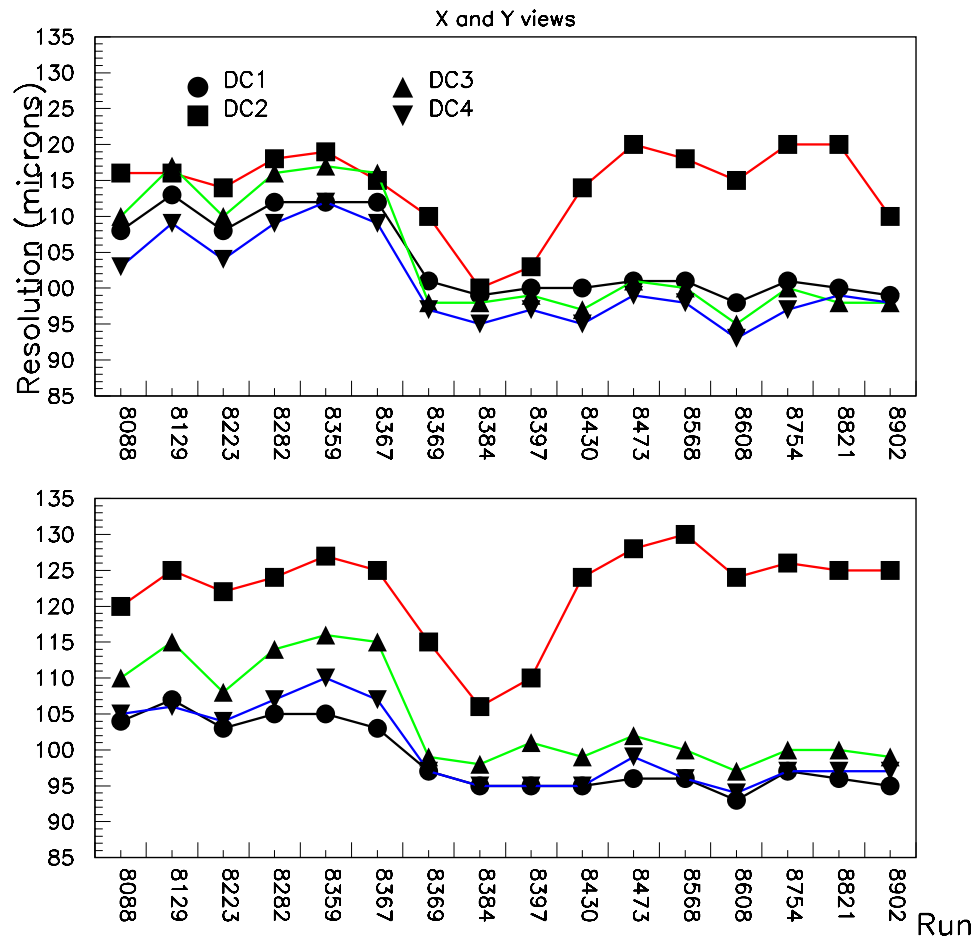


Figure 5.5: The history of the Chambers resolution for the winter run as a function of the run numbers being used for the  $x$ - $t$  calibration. The top plot shows the resolution for the  $x$  views and the bottom plot for the  $y$  view.

significant variations corresponds to change of the high voltage at various points. At the beginning of the winter run all the 4 DC's were being operated at 2450 V (up to run 8367), then the voltages were increased to 2500 V. However, DC2 was not able to hold that high voltage for a long time and its voltage was decreased back to 2450 V (after run 8429). DC2 was repaired during a long shut down and for the summer run all the DC's started with 2500 V of voltage. DC1 was problematic in the summer and we had to increase its voltage (after run 10488) to 2550 V, in order to improve the resolution.

### 5.3.4 Chamber Wire-by-Wire Efficiency

In order to understand the trigger efficiencies and reconstruction algorithms using the chambers, it was necessary to measure the wire-by-wire efficiency of the drift chambers. This was done using a very simple method.  $K_{e3}^0$  events from the two track trigger with identified electron and pion tracks were checked for tracks with missing hits in the chambers. The tracking algorithm used for this check was slightly different from what used in the analysis code in that explicit cuts were not applied to the sum of distances to avoid a bias from  $\delta$ -rays, high SOD's or accidental hits in determination of the efficiency. Every track found with this modified algorithm was checked for missing hits. If a missing hit was found, the wire on which that hit would have been was detected using the remaining track information. Efficiencies for each wire were then simply the fraction of missing hits on that wire compared to the total number of hits observed. We could also calculate the overall efficiency of each plane in a similar fashion. The

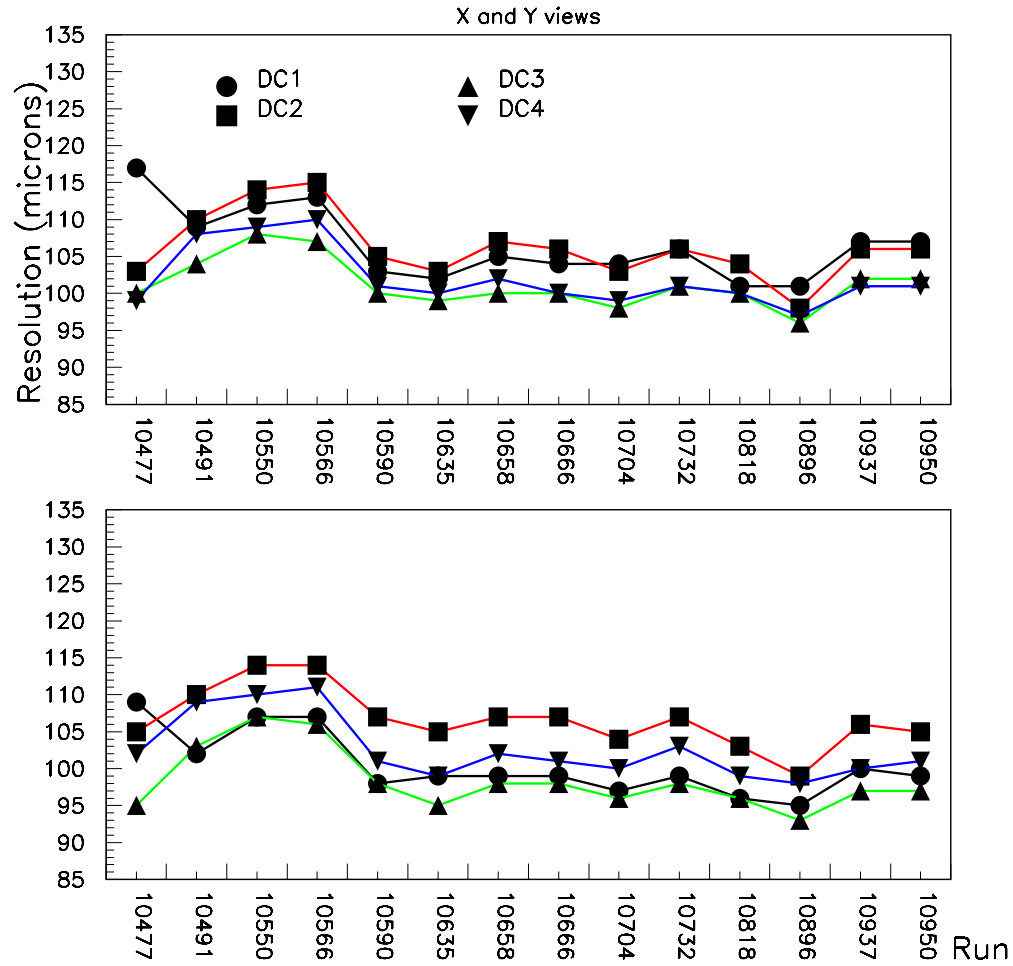


Figure 5.6: The history of the Chambers resolution for the summer run as a function of the run numbers being used for the  $x$ - $t$  calibration. The top plot shows the resolution for the  $x$  views and the bottom plot for the  $y$  view.



individual wire efficiencies, known also as the intrinsic efficiencies, were written in the database files for use in the Monte Carlo simulations.

A sample plot of wire-by-wire efficiencies is shown in Fig. 5.7. In general, chamber efficiencies did not vary significantly by run. For most wires the efficiency was above 99.5% which made the plane efficiencies better than 99.0%. The wires inside the beam region have a smaller efficiency than the wires outside the beam region, due to high rate effects.

## 5.4 Alignment of the Drift Chambers

Once the timing offsets for each drift chamber wire is removed and the  $X(t)$  relations are determined, precision position measurements can be made, and one can proceed to the task of aligning the chamber system.

The internal alignment of the chambers is done in two steps. First, we determine the relative transverse offsets and relative rotations for each plane. This step involves assuming positions for two chambers, *e.g.* 1 and 4. We then determine the relative rotation between these two chambers.

Finally, the global alignment of the chambers, can be done to determine the absolute transverse positions referenced to the target and the calorimeter. The chambers were carefully surveyed in place to be perpendicular to  $z$  and the alignment is not sensitive to small rotations in  $x \leftrightarrow z$  and  $y \leftrightarrow z$  planes.

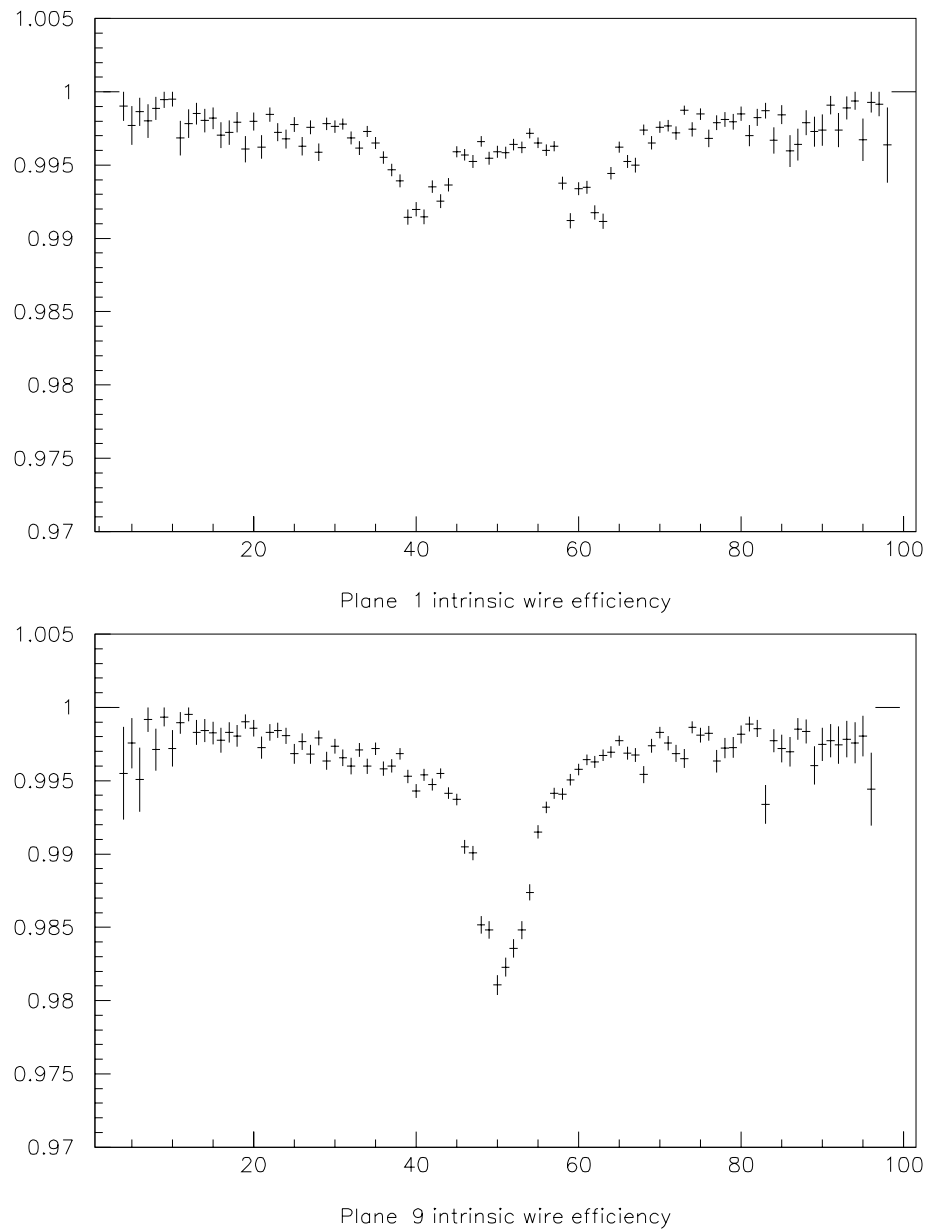


Figure 5.7: The wire-by-wire efficiency for one summer run in the upstream X and Y planes.

### 5.4.1 Relative Alignment of the Drift Chambers

Muon runs with the analysis magnet off were taken approximately once a day. Using about  $10^5$  events of these straight-through muon tracks, one could determine the offsets in  $x$  and  $y$  and rotations in the  $x \leftrightarrow y$  plane of any two drift chambers (*e.g.* 2 and 3) relative to the position of the other two chambers. We selected in-time single muon tracks with no missing hits and used the hits in chambers 1 and 4 to predict the location of the hits in chambers 2 and 3. By simply interpolating the straight line fit to the hits in chambers 1 and 4, we calculated the offset between the interpolated position and the measured position at 2 and 3 chambers. To determine the relative offsets and rotations among the planes in chambers 1 and 3, the same muon data could be used, but this time using tracking information only from chambers 2 and 3 and extrapolating the tracks to chambers 1 and 4.

### 5.4.2 Corkscrew Rotations

There is one remaining degree of freedom in the internal chamber system that can not be determined from single track events. In the proceeding procedure, it was assumed that the fixed chambers 1 and 4 had no relative rotation about the  $z$  axis. Such a rotation would introduce rotations, known as “Corkscrew Rotations”, in chambers 2 and 3 whose magnitude is proportional to the distances between the chambers. To understand this effect, imagine that chamber 4 is rotated by angle  $\phi$  with respect to chamber 1. For simplicity, assume that the chambers are evenly spaced along  $z$ , and chambers 2 and 3 are set exactly orthogonal to the axes. The straight-through muon calibration procedure described above will then

mistakenly find chambers 2 and 3 are rotated by  $\Leftrightarrow\phi/3$  and  $\Leftrightarrow2\phi/3$  about  $z$  due to the incorrect assumption that chambers 1 and 4 were exactly orthogonal to the axes. The corkscrew rotations can be corrected using two-track events like  $K_{e3}^0$ 's. Because the two tracks originate from a common vertex, they define a plane. If the reconstructed two tracks in two chambers are non-planar, we can infer and correct the residual rotation between the two chambers by measuring the apparent separation of the tracks at the vertex. We need only measure the relative rotation between the first two chambers to ascertain the rotation per unit distance and correct for the other two. This has the advantage of allowing us to use the regular data with the analysis magnet on. Figure 5.8 illustrates the corkscrew correction procedure. We construct two vectors  $\vec{r}_1$  and  $\vec{r}_2$  which connect the points of intersection of the two tracks with chambers 1 and 2 respectively. If two track decays are planar, then  $\vec{r}_1 \times \vec{r}_2 = 0$ . But if there is a residual corkscrew rotation, then  $\vec{r}_1 \times \vec{r}_2 = |\vec{r}_1||\vec{r}_2|\sin\phi$ , where  $\phi$  is the corkscrew rotation between chambers 1 and 2. By plotting  $\vec{r}_1 \times \vec{r}_2$  vs  $|\vec{r}_1||\vec{r}_2|$ , we can determine the angle  $\phi$  and then the angle per unit  $z$  distance.

### 5.4.3 Global Alignment of the Drift Chambers

Once the internal alignment of the drift chambers was complete, the entire system could be aligned to the external fixed elements like the production target and the CsI calorimeter. To find the position of the target, we can reconstruct  $\Lambda \rightarrow p\pi^-$  or  $K_L \rightarrow \pi^+\pi^-$  and point the momentum vector back to the target. Using  $\Lambda \rightarrow p\pi^-$  events takes advantage of very high momentum  $\Lambda$ 's, thus reducing the multiple

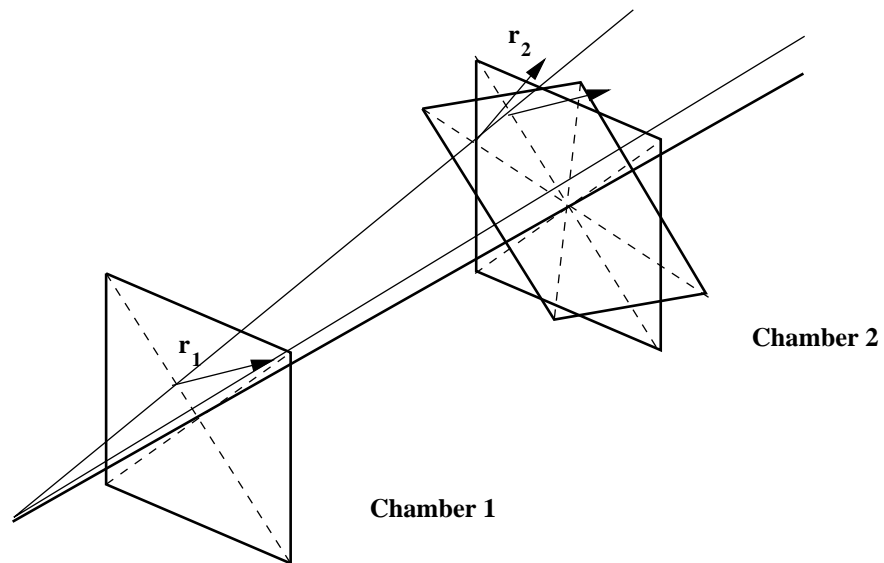


Figure 5.8: Corkscrew rotation as seen in Chamber 1 and 2, if Chamber 4 is rotated with respect to Chamber 1.

scattering contributions in error in finding the location of the target.

The coordinate system can then be fixed to the calorimeter in the  $x$  and  $y$  directions. This was accomplished with a clean sample of identified electrons in  $K_{e3}^0$  events. One could examine the residuals between the projected tracks and the reconstructed cluster centers.

## Chapter 6

# Data Analysis and Event Selection

This chapter describes the analysis of  $\Xi^0 \rightarrow \Sigma^+ e^- \bar{\nu}_e$  decay in the E799-II summer data. The first observation of this decay mode was made during the E799-II winter run [77, 78]. A brief review of the first measurement of this decay based on the winter data set at KTeV is presented in Appendix A. With some modifications in the hyperon trigger configuration which improved the bandwidth, we collected about 700  $\Xi^0 \rightarrow \Sigma^+ e^- \bar{\nu}_e$  decays (about a factor of four more data) in the summer run. The extraction of the  $\Xi^0 \rightarrow \Sigma^+ e^- \bar{\nu}_e$  branching ratio (BR) based on the summer data is also described in this chapter. The evaluation of systematic errors is discussed in Chapter 8. Version 4.11 of the KTeV analysis code and Monte Carlo simulation, and the most updated database at the end of 1998 were used.

## 6.1 Data Selection

We collected about 100 million events on 60 DLT tapes from the hyperon triggers during the Summer of 1997 run. Because of this large amount of data, it was necessary to perform an initial reduction of data. Since signal events contain a  $\pi^0$ , only events with two electromagnetic neutral clusters above 3 GeV energy were

kept. This reduced the data volume by a factor of 10 to roughly 11 million events on 6 DLT tapes. We further crunched this to about 3.4 million events on a single DLT tape by applying some specific Cascade beta analysis kinematical cuts in a loose manner. A complete analysis has then been performed on the remaining events.

### 6.1.1 The $\Xi^0 \rightarrow \Sigma^+ e^- \bar{\nu}_e$ Event Selection

To ease the process of analysis, the Cascade beta analysis code was run on the above DLT tape with some more filtering. Only events selected on-line by the “ $\Xi^0 \Leftrightarrow \text{beta} \Leftrightarrow \text{trigger}$ ” and tagged as a beta decay, with two reconstructed tracks were kept. The negative track would be an electron candidate based on the calorimeter  $e/\pi$  discrimination. Finally, three in-time hardware clusters were required corresponding to the electron and two photons from the decay of  $\pi^0$ . The last two requirements will be described later in this section. The final data sample was reduced to a manageable volume of about 594 000 events. We refer to this data set as the “pre-selected” events.

Figure 6.1 shows the topology of the decay in KTeV apparatus. The detectable final state of the decay is a high momentum proton which remains in the neutral beam and goes down a CsI beam hole, an electron and two photons which deposit their energy in the CsI calorimeter. We search for the sequence of events  $\Xi^0 \rightarrow \Sigma^+ e^- \bar{\nu}_e$  where  $\Sigma^+ \rightarrow p\pi^0$  (BR=51.57%) and  $\pi^0 \rightarrow \gamma\gamma$  (BR=98.80%) and reconstruct the event from downstream to upstream. In what follows, we discuss the method used to reconstruct Cascade beta events.



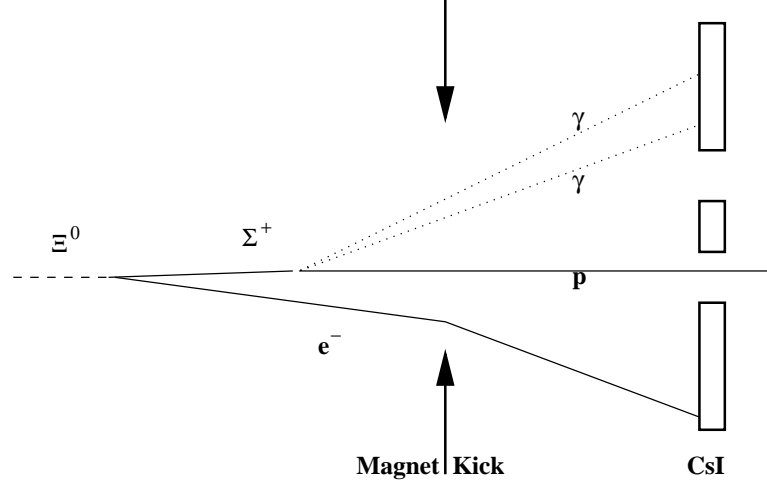


Figure 6.1: The geometry of the decay  $\Xi^0 \rightarrow \Sigma^+ e^- \bar{\nu}_e$  where  $\Sigma^+ \rightarrow p \pi^0$  and  $\pi^0 \rightarrow \gamma \gamma$ .

Besides processing the reconstruction technique, one has to come up with a set of quality cuts to reduce background events without losing too much of the signal. Even though the choice of cuts are suggested by the Monte Carlo (MC) simulations of the signal events as well as the possible background events, the exact choice of cut boundaries are somewhat arbitrary. One can adjust the values to achieve the best signal to noise ratio. Presented here, is a “nominal” set of cuts we applied to the data to select the  $\Xi^0 \rightarrow \Sigma^+ e^- \bar{\nu}_e$  signal events for the purpose of BR measurements. We assign a systematic error to this “arbitrariness” of the cut values. This will be discussed in section 8.6. In order to have a better idea of the effect of each cut, their distributions have been represented in Figs. 6.2 to 6.6 for “ $\Xi^0$ -beta-trigger” events that passed the mentioned pre-selection criteria. The corresponding distributions for the simulated  $\Xi^0 \rightarrow \Sigma^+ e^- \bar{\nu}_e$  events have been given

as well on Figs. 6.7 to 6.11.

What we observe in the detector as a final product of an event which passed the trigger requirements are a positive track going down one of the CsI beam holes of the calorimeter, a negative track associated with one of the electromagnetic clusters in the calorimeter, and two extra clusters not associated with any tracks. Assuming these two extra clusters are decay products of a  $\pi^0$ , one can use the following approximation to fix the  $z$  position of the  $\pi^0$  vertex

$$z = \left( \frac{\Delta}{m_{\pi^0}} \right) \sqrt{E_1 E_2} \quad (6.1)$$

where  $E_1$  and  $E_2$  are the energies of the photons measured by the calorimeter,  $\Delta$  is the distance between the photons at CsI and  $m_{\pi^0}$  is the invariant mass of  $\pi^0$ <sup>1</sup>. The decay vertex of the  $\pi^0$  is calculated to be the point where the positive momentum track supposed as a proton, intercepts the vertical plane on which the  $\pi^0$  vertex is located. Since the  $\pi^0$  decays electromagnetically, it has a very short lifetime of  $8.4 \times 10^{-17}$  sec and one can assume that the  $\Sigma^+$  vertex is coincident with the  $\pi^0$  vertex.

In order to eliminate accidental clusters in the calorimeter, the cluster energies have to be greater than 3 GeV. To avoid ambiguities in the  $\pi^0$  mass reconstruction, a minimum distance of 0.15 m between the two neutral clusters was required (Figs. 6.3-(b) and 6.8-(b)). The magnitude of the positive track momentum (proton) has to be larger than the magnitude of the negative track momentum

---

<sup>1</sup>This approximation works if the opening angle between the photons is very small, which is a valid assumption here. However, we used a numerical routine for the exact calculation of  $z$  in very good agreement with Eq. 6.1

(electron). The opposite would be either an anti-hyperon decay or a kaon decay. The proton momentum is required to be above 110 GeV/c and below 400 GeV/c (Figs. 6.2-(b) and 6.7-(b)). Knowing the 4-momentum of the proton and the reconstructed  $\pi^0$ , the  $\Sigma^+$  4-momentum can be calculated in the laboratory frame.

Then the  $\Xi^0$  vertex can be reconstructed as the mid-point of the distance of closest approach (DOCA) between the  $\Sigma^+$  flight path and the low momentum negative track trajectory (electron candidate). A cut at 0.01 m is applied on this closest approach distance (Figs. 6.3-(c) and 6.8-(c)).

We used the CsI calorimeter with a  $e/\pi$  rejection factor of 500:1 to identify electrons from pions. The ratio of the energy deposited by the low momentum track in the calorimeter to its momentum (measured by the spectrometer) was chosen to be between 0.93 and 1.07 (Figs. 6.2-(a) and 6.7-(a)). Since the CsI crystals are  $\sim 27$  radiation lengths, an electron would deposit all its energy in the calorimeter, and this ratio is around one for electrons. Thus this track has a high probability to be an electron which is reinforced by requiring its momentum to be above 2.5 GeV/c and below 50 GeV/c (Figs. 6.2-(c) and 6.7-(c)). Furthermore, to ensure that the negative momentum track corresponds to the electromagnetic cluster produced by the electron, the distance between the track and the center of the cluster at CsI is required to be less than 0.02 m (Figs. 6.3-(d) and 6.8-(d)). The energy over momentum ratio for the proton should be 0 in principle, since it is not supposed to hit the calorimeter at all. We alternatively required the positive track trajectory to pass through the beam holes at the CsI face. To reject the background of decays producing two identical but opposite charged particles, only

events that have a “proton” to “electron” momentum ratio above 3.5 are selected (Figs. 6.2-(d) and 6.7-(d)). This cut predominantly removes kaon background events that decay symmetrically into a particle-antiparticle pairs, for example.

With the same reconstruction technique we calculate a “ $\Xi^0$ ” mass with the hypothesis that it decayed into a  $\pi^0$  and a  $\Lambda$ . If this mass is above  $1.33 \text{ GeV}/c^2$ , we reject these events that correspond to the dominant  $\Xi^0$  decay mode,  $\Xi^0 \rightarrow \Lambda\pi^0$  (Figs. 6.4-(a) and 6.9-(a)). The reconstructed  $\Sigma^+$  mass from these background events is slightly off the  $\Sigma^+$  mass peak region, and can easily be distinguished as we will show later (see Fig. 6.12, for instance). However, their elimination using this explicit mass cut reduces the final event sample and helps reduce the background level near the  $\Sigma^+$  peak.

Since signal events produce a  $\Sigma^+$  that originates from a  $\Xi^0$  decay, the distance along the beam direction between the reconstructed  $\Sigma^+$  and  $\Xi^0$  vertex positions has to be at least positive. In order to reject the background of events that produce two tracks and a  $\pi^0$  within the same vertex (*e.g.*  $K_L \rightarrow \pi^+\pi^-\pi^0$ ), we cut on this distance to be between 1 m and 20 m (Figs. 6.5-(b) and 6.10-(b)). The last two cuts are very efficient in rejecting the backgrounds. Also the  $z$  position of  $\Xi^0$  vertex has to be inside the decay volume of the experiment between 95 m and 150 m (Figs. 6.5-(a) and 6.10-(a)). The decay volume in fact, extends to  $z=159$  m (where the vacuum window is located). Cutting at 150 m reduces more  $K_L$ 's than  $\Xi^0$ 's because of the  $K_L$ 's longer lifetime.

Fiducial cuts are then applied on the position of the  $\Xi^0$  vertex. It is required to be at  $\pm 5$  cm of each of the two beam hole centers along the horizontal and

the vertical axis (Figs. 6.5-(c),(d) and 6.10-(c),(d)). In order to be sure that there is no energy leakage from the beam hole regions inside the edge of the CsI calorimeter, we remove events that deposit more than 1 GeV energy in the Collar Anti scintillators (Sec. 2.7).

Kinematics cuts are applied on the remaining events. The tracking routine in the analysis code (Sec. 5.1) tries to find a vertex for the two tracks known as the “charged vertex”. A charged vertex with a low transverse momentum most probably characterizes the decay of a particle coming from the target (*e.g.*  $\Lambda \rightarrow p\pi^-$ ). Therefore, we require the squared transverse momentum of the charged vertex to be above  $0.006 (GeV/c)^2$  to reject the background from these direct two body decays (Figs. 6.3-(a) and 6.8-(a)). In order to reject the background of events with superimposed accidental activities that can fake our signal, the events have been selected with exactly three off-line hardware clusters (which are in-time by construction). Such a cut is extremely efficient to reject the lambda beta decay ( $\Lambda \rightarrow pe^- \bar{\nu}_e$ ) background and the  $K_{e3}^0$  ( $K_L^0 \rightarrow \pi^+ e^- \nu_e$ ) background.

Finally, the reconstructed  $e^-\Sigma^+$  momentum has to be between 160 GeV and 500 GeV, its reconstructed mass has to be between  $1.20 \text{ GeV}/c^2$  and  $1.32 \text{ GeV}/c^2$ , and its reconstructed lifetime, defined in  $\Xi^0$  lifetime unit as  $z_{e^-\Sigma^+} \times M_{\Xi^0} / (p_{e^-\Sigma^+} \times c\tau_{\Xi^0})$  has to be less than 10 (Figs. 6.4-(b),(c),(d) and 6.9-(b),(c),(d)).

The neutrino in the  $\Xi^0 \rightarrow \Sigma^+ e^- \bar{\nu}_e$  decay can not be detected. Assuming that  $\Xi^0$  particle originated from the target, the direction of the  $\Xi^0$  momentum is known and one could solve for the magnitude of its momentum and also reconstruct the momentum of the missing neutrino analytically up to a two-fold ambiguity.

Appendix B presents the details of this calculation. However, the neutrino reconstruction is unnecessary for a BR measurement, because  $\Xi^0 \rightarrow \Sigma^+ e^- \bar{\nu}_e$  was the only decay at KTeV that could produce a  $\Sigma^+$  particle. Hence, identifying a  $\Sigma^+$  mass peak in the data is an indirect but certain evidence of a Cascade beta decay.

Since the neutrino is massless, its maximum transverse momentum has to be smaller than the difference between the PDG  $\Xi^0$  invariant mass ( $1.315 \text{ GeV}/c^2$ ) and the reconstructed  $e^- \Sigma^+$  mass plus a safety margin of  $25 \text{ MeV}/c$  to cope with the reconstruction resolution (Figs. 6.6 and 6.11). This is the most systematically uncertain cut due to the sensitivity of transverse momentum calculations to factors like detector calibrations; however, it is vital to reduce the background level significantly. The systematic uncertainties due to the selection of the cuts will be discussed in Chapter 8

*A total of 778 events passed all the selection criteria.*

The above cuts have been summarized in table 6.1 with their individual effect on the pre-selected events that passed all the other cuts. Some cuts such as the  $E/p$  of the electron don't seem to be very effective. This is due to the pre-selection criteria, explained at the beginning of this section, that already implemented these cuts in a looser manner. For all these distributions and numbers, a large difference between the data and the simulation is indicative of the cut being mostly effective on the background than on the signal events. For the four most effective cuts, Fig. 6.12 shows the signal peak with all the other cuts applied.

Some further cross checks with respect to the hyperon trigger have been done on these selected events. As foreseen, all of the positive tracks are well contained

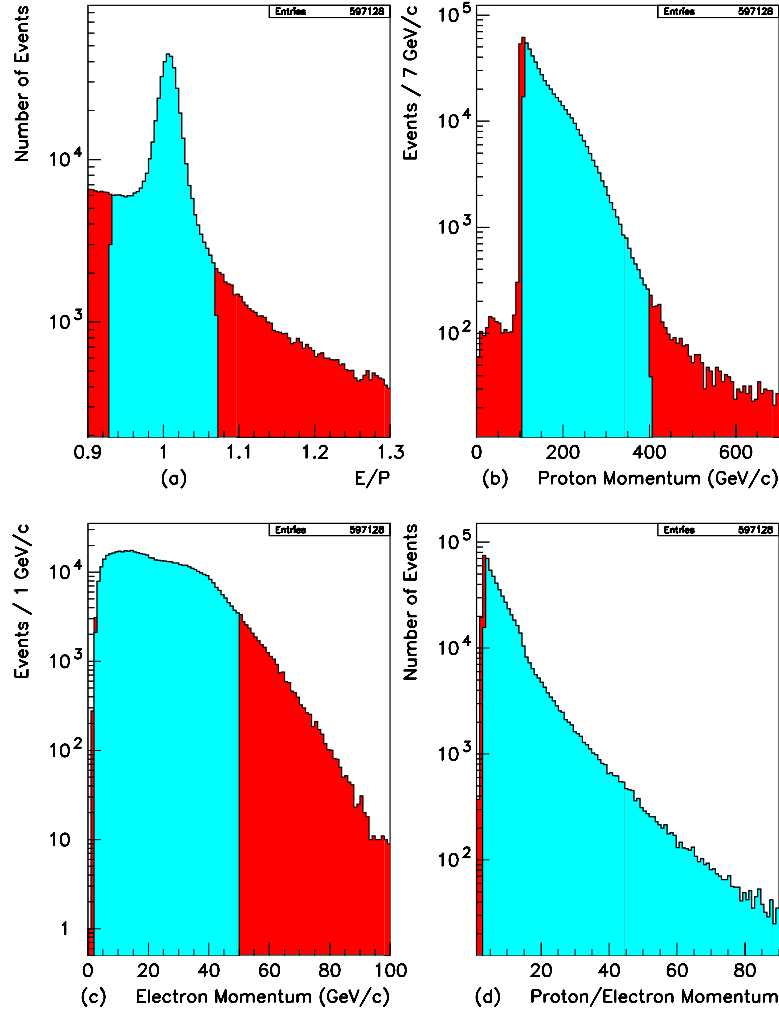


Figure 6.2: Distribution of the: (a) Ratio of the energy of the electron as measured by the calorimeter to the momentum of the electron as measured by the charged spectrometer. (b) Momentum of the positive charged track, assumed to be a proton. (c) Momentum of the negative charged track, assumed to be an electron. (d) Ratio of momentum of the positive track to the momentum of the negative track. The light grey shows the accepted events after applying the cuts and the dark grey is the rejected events.

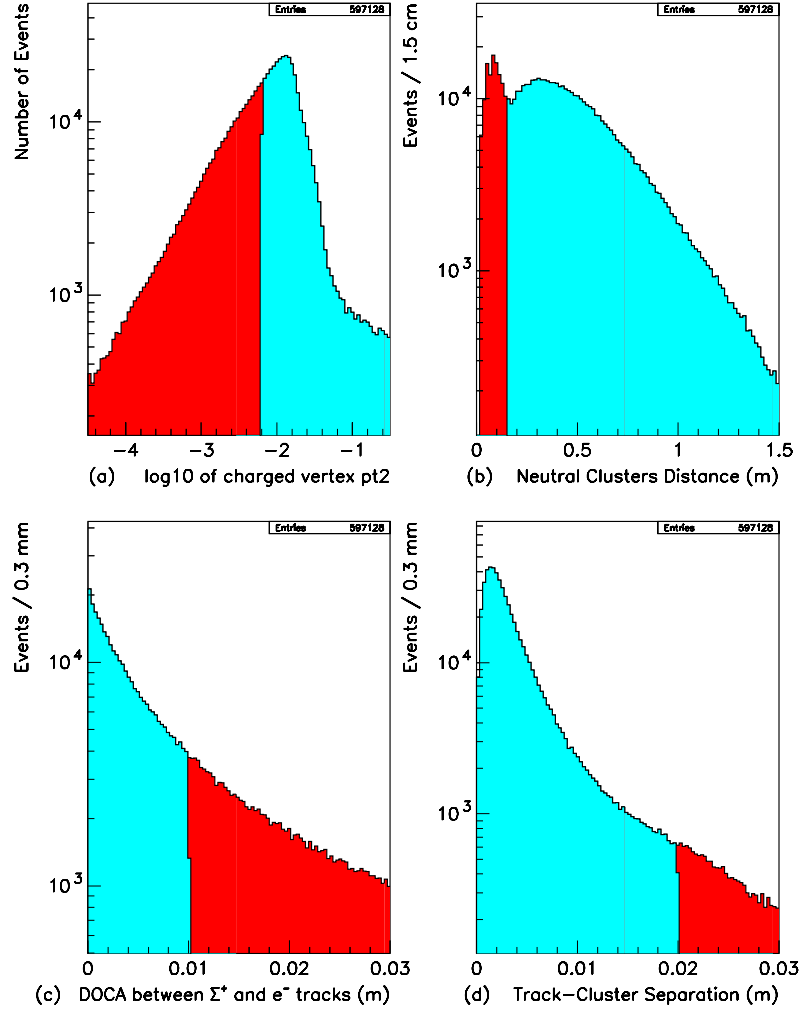


Figure 6.3: Distribution of the: (a) Square of the transverse momentum of the charged vertex. (b) Distance between the two neutral clusters (photons) in the calorimeter. (c) Distance of closest approach between the  $\Sigma^+$  reconstructed track and the electron track. (d) Separation distance between the center of the electron cluster and the track associated with that at CsI. The light grey shows the accepted events after applying the cuts and the dark grey is the rejected events.



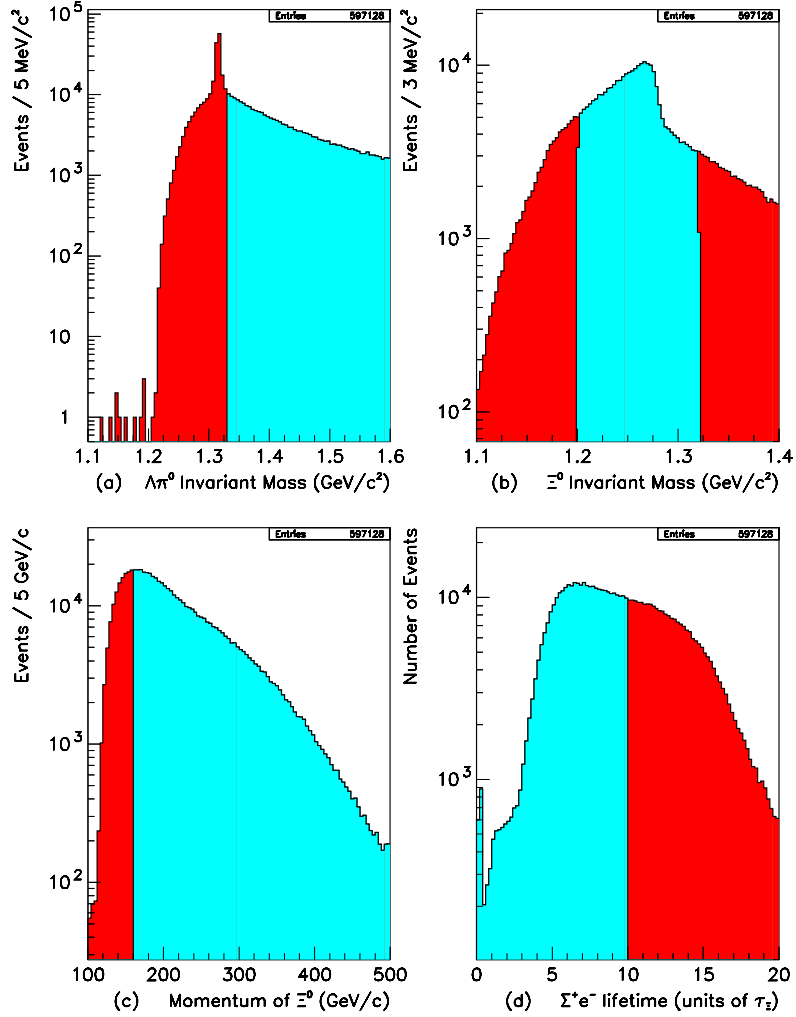


Figure 6.4: Distribution of the: (a) Reconstructed  $p\pi^-\pi^0$  principal decay mass. (b) Reconstructed mass of  $\Sigma^+e^-$ . (c) Reconstructed momentum of  $\Sigma^+e^-$ . (d) Reconstructed  $\Sigma^+e^-$  lifetime in units of  $\Xi^0$  lifetime. The light grey shows the accepted events after applying the cuts and the dark grey is the rejected events.

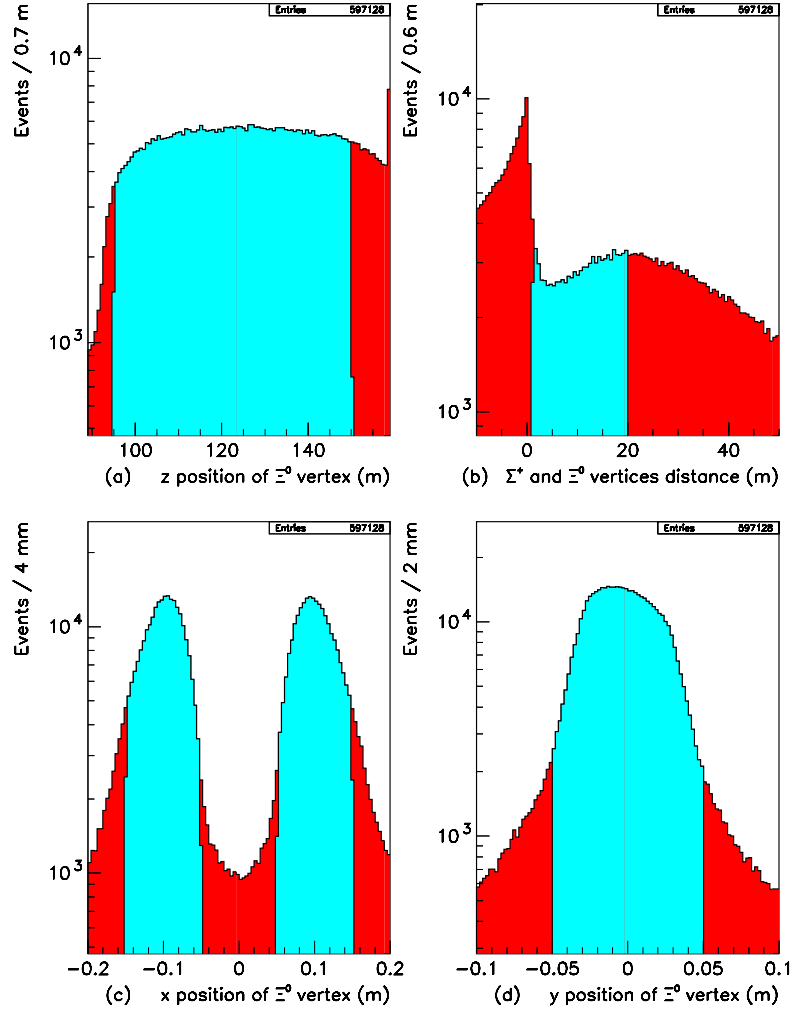


Figure 6.5:  $\Xi^0 \rightarrow \Sigma^+ e^- \bar{\nu}_e$  distribution of the: (a) longitudinal position of  $\Xi^0$  vertex inside the decay volume. (b) Longitudinal distance between the  $\Sigma^+$  and  $\Xi^0$  vertices. (c,d) Transverse position of  $\Xi^0$  beta vertex. The light grey shows the accepted events after applying the cuts and the dark grey is the rejected events.

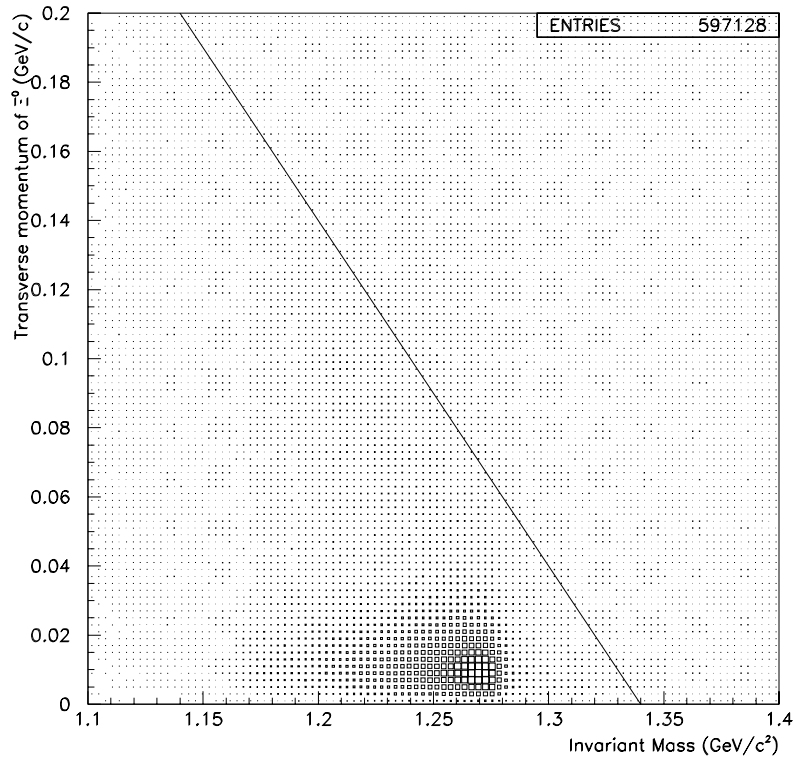


Figure 6.6:  $\Xi^0 \rightarrow \Sigma^+ e^- \bar{\nu}_e$  distribution of the reconstructed transverse momentum versus the reconstructed mass of  $\Sigma^+ e^-$ . The events above the line  $1.34 \Leftrightarrow M_{\Sigma^+ e^-} = p_t$  are rejected from data.

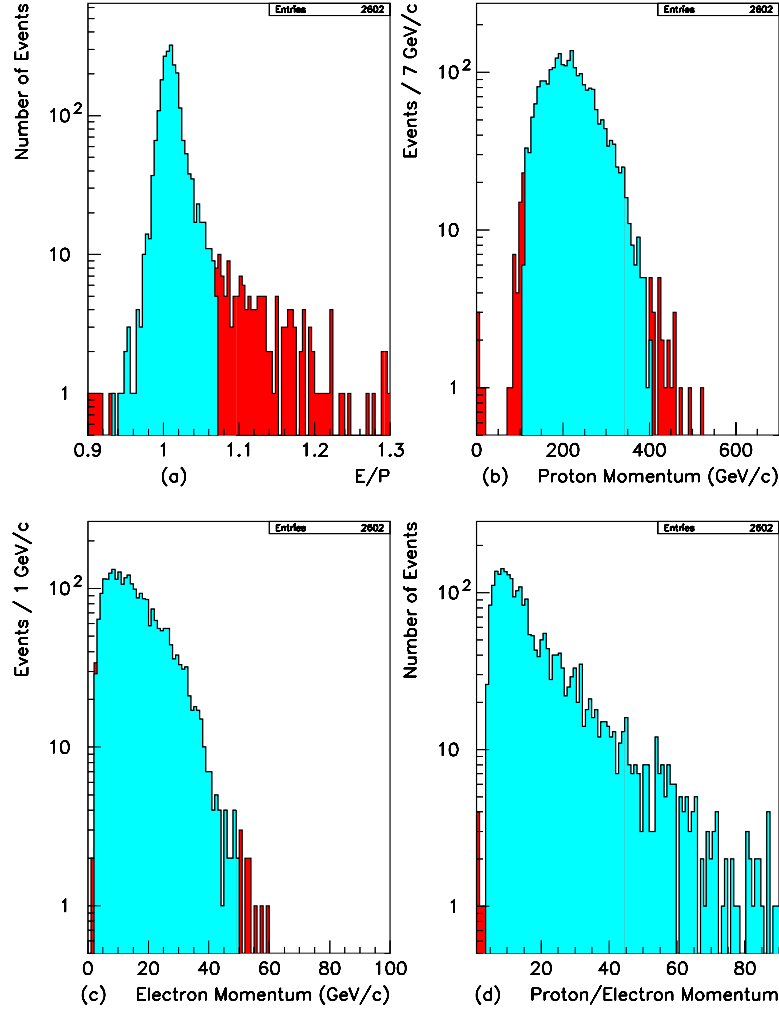


Figure 6.7: Monte Carlo simulation of the: (a) Ratio of the energy of the electron as measured by the calorimeter to the momentum of the electron as measured by the charged spectrometer. (b) Momentum of the positive charged track, assumed to be a proton. (c) Momentum of the negative charged track, assumed to be an electron. (d) Ratio of momentum of the positive track to the momentum of the negative track. The light grey shows the accepted events after applying the cuts and the dark grey is the rejected events.

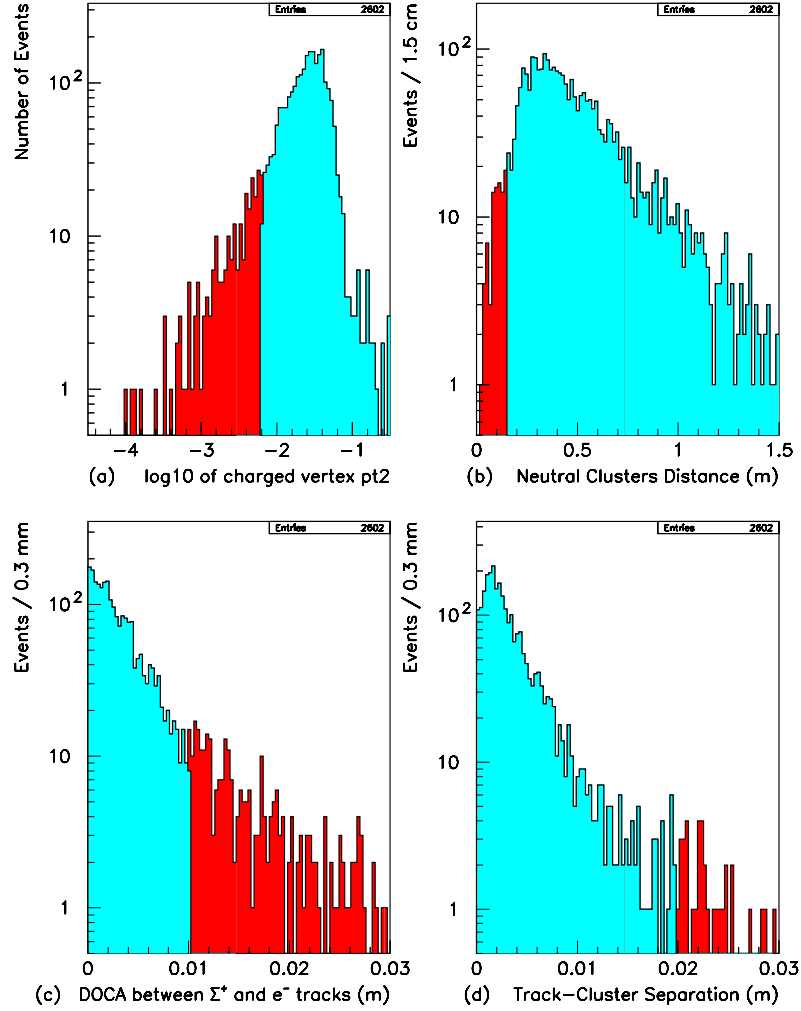


Figure 6.8: Monte Carlo simulation of the: (a) Square of the transverse momentum of the charged vertex. (b) Distance between the two neutral clusters (photons) in the calorimeter. (c) Distance of closest approach between the  $\Sigma^+$  reconstructed track and the electron track. (d) Separation distance between the center of the electron cluster and the track associated with that at CsI. The light grey shows the accepted events after applying the cuts and the dark grey is the rejected events.

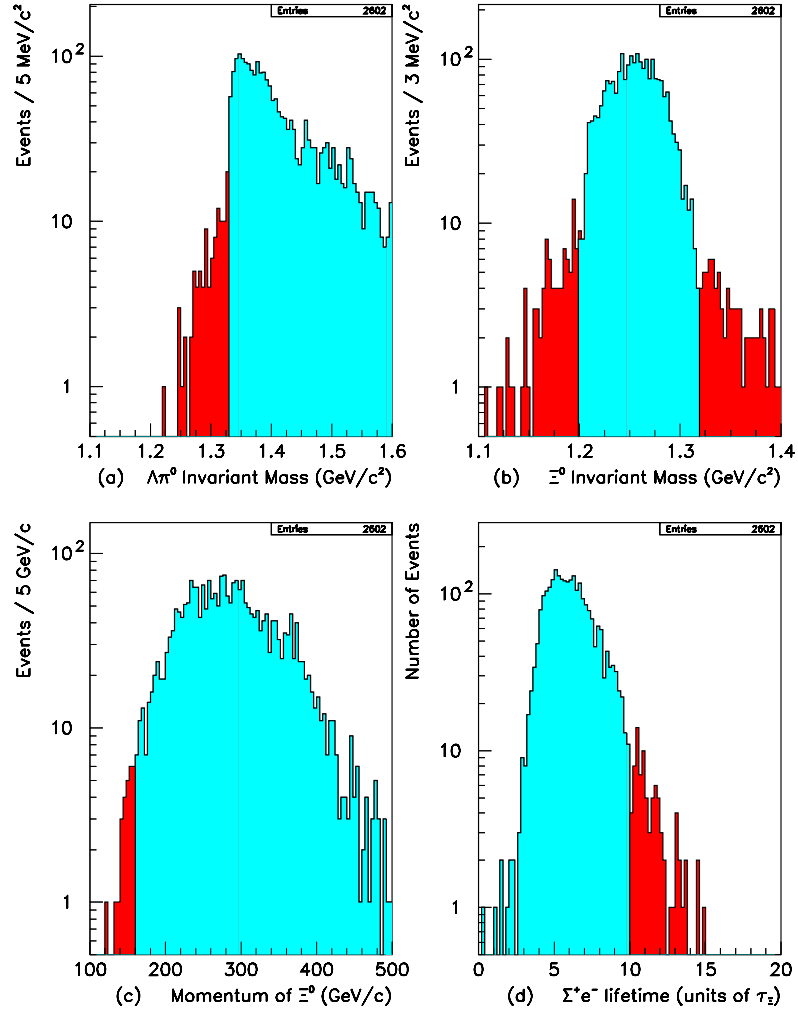


Figure 6.9: Monte Carlo simulation of the: (a) Reconstructed  $p\pi^-\pi^0$  principal decay mass. (b) Reconstructed mass of  $\Sigma^+e^-$ . (c) Reconstructed momentum of  $\Sigma^+e^-$ . (d) Reconstructed  $\Sigma^+e^-$  lifetime in units of  $\Xi^0$  lifetime. The light grey shows the accepted events after applying the cuts and the dark grey is the rejected events.

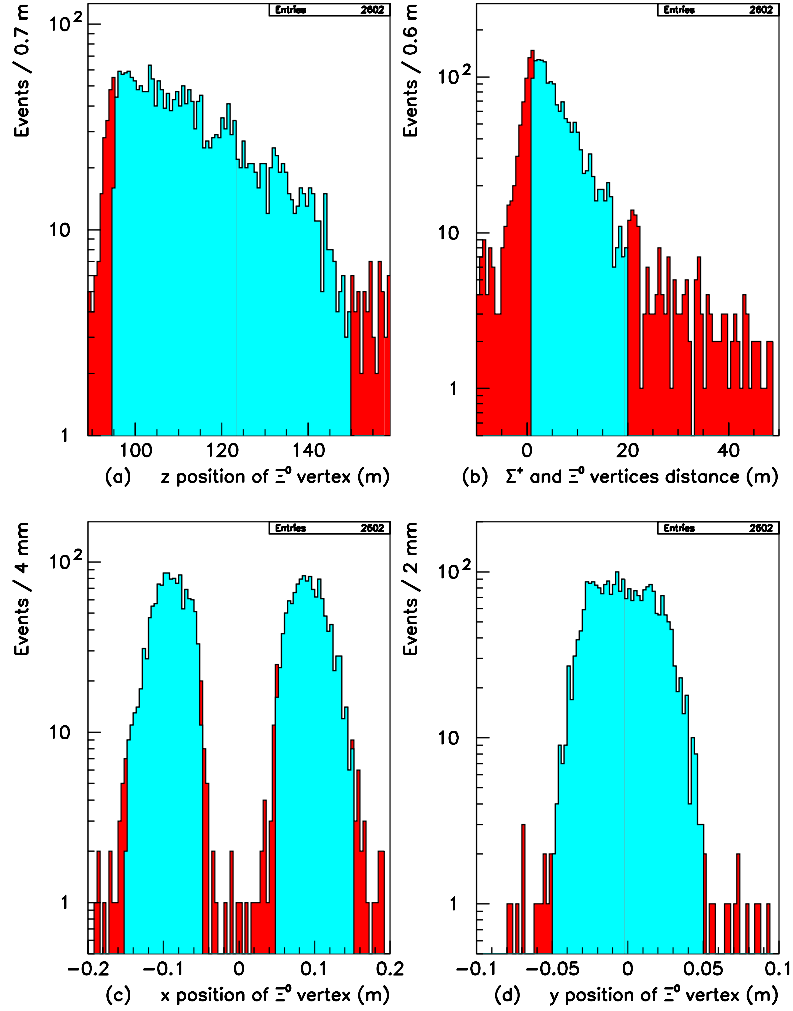


Figure 6.10: Monte Carlo simulation of the: (a) longitudinal position of  $\Xi^0$  vertex inside the decay volume. (b) Longitudinal distance between the  $\Sigma^+$  and  $\Xi^0$  vertices. (c,d) Transverse position of  $\Xi^0$  beta vertex. The light grey shows the accepted events after applying the cuts and the dark grey is the rejected events.

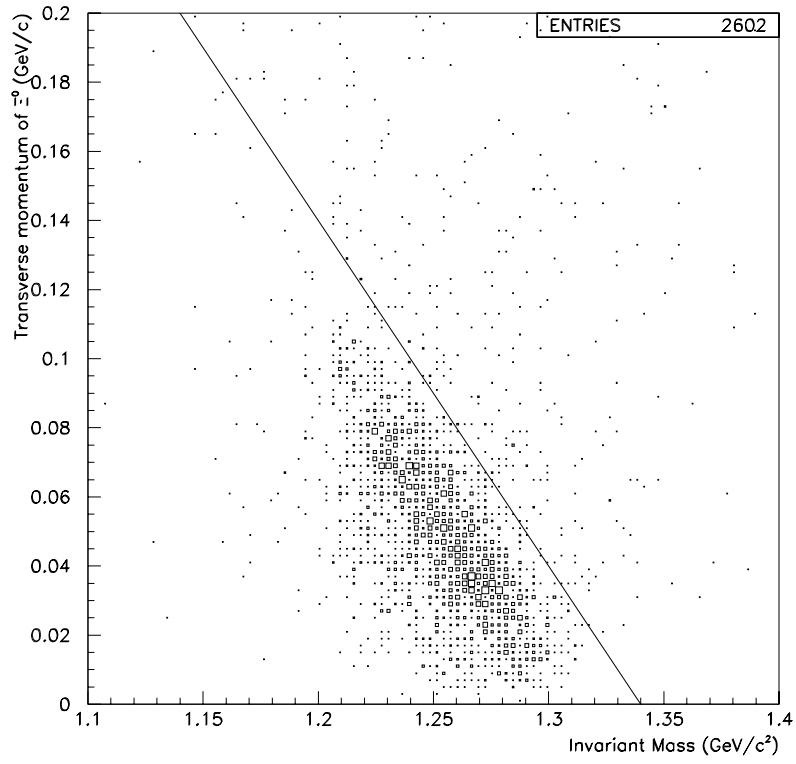


Figure 6.11: Monte Carlo simulation of the reconstructed transverse momentum versus the reconstructed mass of  $\Sigma^+e^-$ . The events above the line  $1.34 \Leftrightarrow M_{\Sigma^+e^-} = p_t$  rejected from data.



in the hole counter regions. The energy deposited in the calorimeter calculated from the sum of the charge and the two neutral clusters is above 18 GeV for all the events. They are all in a very good agreement with the expected  $\Xi^0 \rightarrow \Sigma^+ e^- \bar{\nu}_e$  events kinematics.

### 6.1.2 The $\Xi^0 \rightarrow \Lambda \pi^0$ Event Selection

This decay mode is the dominant  $\Xi^0$  decay. It is used as a flux normalization in the calculation of the  $\Xi^0$  beta decay branching ratio. Only events selected on-line by the “ $\Lambda$ -trigger” are kept. To minimize the differences between the two modes, most of the cuts used to select this dominant mode are similar to those used to select  $\Xi^0$  beta decay events. The  $\Xi^0$  decays into a  $\pi^0$  and  $\Lambda$  that may decay into a proton and a  $\pi^-$ . Events that can come from such a process are selected.

Thus, only two track events are kept and the momentum and momentum ratio cuts on both of tracks are the same as those used in the beta mode selection. Since a  $\pi^0$  is produced, two neutral clusters are required with the same cuts as before.

The  $\Lambda$  vertex is a charged vertex reconstructed from the closest approach between the two tracks. The high momentum and positive charged track is called proton and the low momentum and negative track is assigned as a  $\pi^-$ . The ratio of the energy deposited by the  $\pi^-$  over its momentum has to be below 0.8 since it does not produce an electromagnetic shower. The same energy over momentum ratio has to be below 0.1 for the proton or we alternatively require the positive track trajectory to pass through the beam holes at the CsI face. The reconstructed  $\Lambda$  mass has to be less than 10 MeV different from its known PDG value.

Table 6.1: Effect of each cut on the pre-selected data if all the others have been fulfilled. A large difference between the data and the simulation is indicative of the cut being mostly effective on the background and not on the signal events. Some of the cuts seem to be ineffective because of their earlier pre-selection.

Cut type	Candidate rejection DATA (778 Events)	Signal event loss MC (946 Events)
Proton momentum	1.1 %	0.7 %
Electron momentum	1.0 %	0 %
Proton down the hole	0 %	1.8 %
Electron E/P	10.2 %	5.3 %
Neutral cluster distance	0.4 %	0.4 %
Track-Cluster separation	0.9 %	0.5 %
$\Xi^0$ vertex $x \leftrightarrow y$ position	0.8 %	0.9 %
$\Xi^0$ vertex longitudinal position	8.3 %	6.7 %
$z_{\Sigma^+} \leftrightarrow z_{\Xi^0}$	82 %	24 %
Proton/electron momentum ratio	1.8 %	0 %
$Pt^2$ of the charged vertex	17 %	6.3 %
$p\pi^-\pi^0$ mass	31 %	0.8 %
$(e^-\Sigma^+)$ reconstructed mass	24 %	0.2 %
$(e^-\Sigma^+)$ reconstructed momentum	0.3 %	0 %
$(e^-\Sigma^+)$ transverse momentum	43 %	2.5 %
$(e^-\Sigma^+)$ reconstructed lifetime	9.7 %	1.3 %
$DOCA(e^-, \Sigma^+)$	6.5 %	5.5 %
Collar anti energy	7.7 %	0.9 %

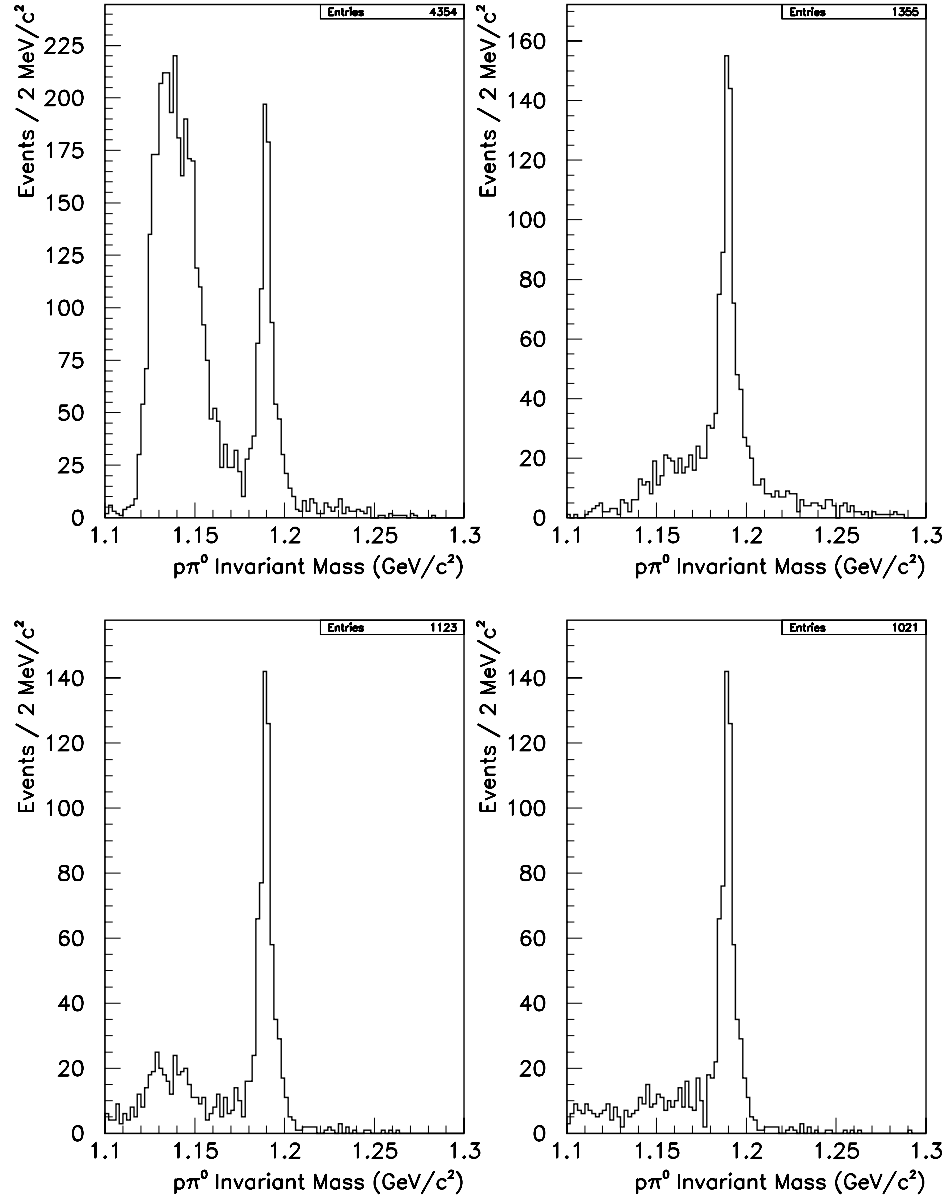


Figure 6.12: The  $\Sigma^+$  mass peak with all the cuts applied except one.  $z_{\Sigma^+} \leftrightarrow z_{\Xi^0}$ , reconstructed transverse momentum of  $e^-\Sigma^+$ ,  $p\pi^-\pi^0$  mass and the reconstructed mass of  $e^-\Sigma^+$  are the strongest cuts as shown in table 6.1.

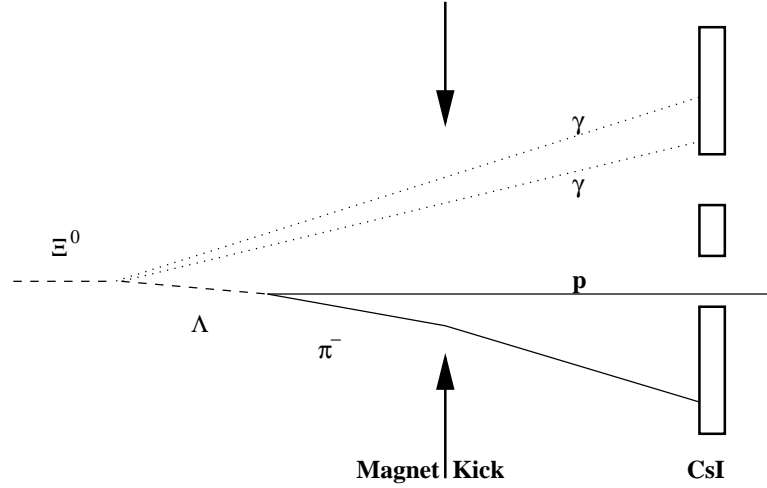


Figure 6.13: The geometry of the dominant decay of  $\Xi^0 \rightarrow \Lambda \pi^0$  where  $\Lambda \rightarrow p \pi^-$  and  $\pi^0 \rightarrow \gamma \gamma$ . This decay was used as the normalization mode.

The  $\Xi^0$  decay vertex is reconstructed to be the point along the extrapolated  $\Lambda$  path where the two neutral electromagnetic clusters, called photons, best match the  $\pi^0$  mass. The same fiducial cuts as for the beta decay mode are applied on the horizontal and vertical  $\Xi^0$  vertex positions. The longitudinal distance between the  $\Xi^0$  vertex and the  $\Lambda$  vertex has to be between 1 m and 20 m. The  $\Xi^0$  momentum and lifetime have to be in the same ranges as for the beta decay mode. The reconstructed  $\Xi^0$  mass is required to be between  $1.30 \text{ GeV}/c^2$  and  $1.33 \text{ GeV}/c^2$ . The reconstructed  $\Xi^0$  mass is shown on Fig. 6.14 for the selected events.

Figure 6.15 shows the distribution of the main variables which are different from Cascade beta decay. It also shows a comparison between the data and the Monte Carlo simulation of these variables. The dots represent the data with the *statistical* error bars and the histogram represents the Monte Carlo distribution

normalized to the number of data events for the  $\Xi^0$  principal decay. The relatively small  $\chi^2/ndf$  indicates a good Data/MC agreement.

## 6.2 The $\Xi^0$ Beta Decay Events

The distribution of the reconstructed  $\Sigma^+$  mass is shown in the Fig. 6.16, for all the events selected as  $\Xi^0$  beta decay candidates. A peak centered at the expected mass value of the  $\Sigma^+$  [28],  $1.1894 \pm 0.0001 \text{ GeV}/c^2$  can clearly be seen. A Gaussian fit that matches the signal peak has been performed on part of the distribution. The result of the fit gives a mean value of  $1.1897 \pm 0.0002 \text{ GeV}/c^2$ , in good agreement with the PDG  $\Sigma^+$  mass value. Between  $1.175 \text{ GeV}/c^2$  and  $1.205 \text{ GeV}/c^2$ , a signal peak of  $626 \pm 25$  events on top of a background of  $45 \pm 18$  events can be estimated. The background contribution has been calculated by counting the number of events in two mass regions of  $15 \text{ MeV}/c^2$  width each, located on both sides of the mass peak and interpolating linearly beneath the peak. Such a method can be applied since the background is small, continuous and relatively well understood. This issue will be addressed again in Sec. 6.4. Since there is no other possible source of  $\Sigma^+$  in vacuum, it is most likely that these events present under the peak centered at the mass of the  $\Sigma^+$  are coming from the beta decay of a  $\Xi^0$ .

To confirm that the reconstructed  $\Sigma^+$  of those events are real  $\Sigma^+$  coming from the decay of a  $\Xi^0$  particle, Fig. 6.17 represents the distribution of the calculated  $\Sigma^+$  proper time, in units of  $\Sigma^+$  lifetime ( $c\tau=2.396 \text{ cm}$ ) [28] on a logarithmic scale. The corresponding simulated distribution matches the data well. Furthermore, a crude exponential fit performed on the data gives a lifetime for the reconstructed data

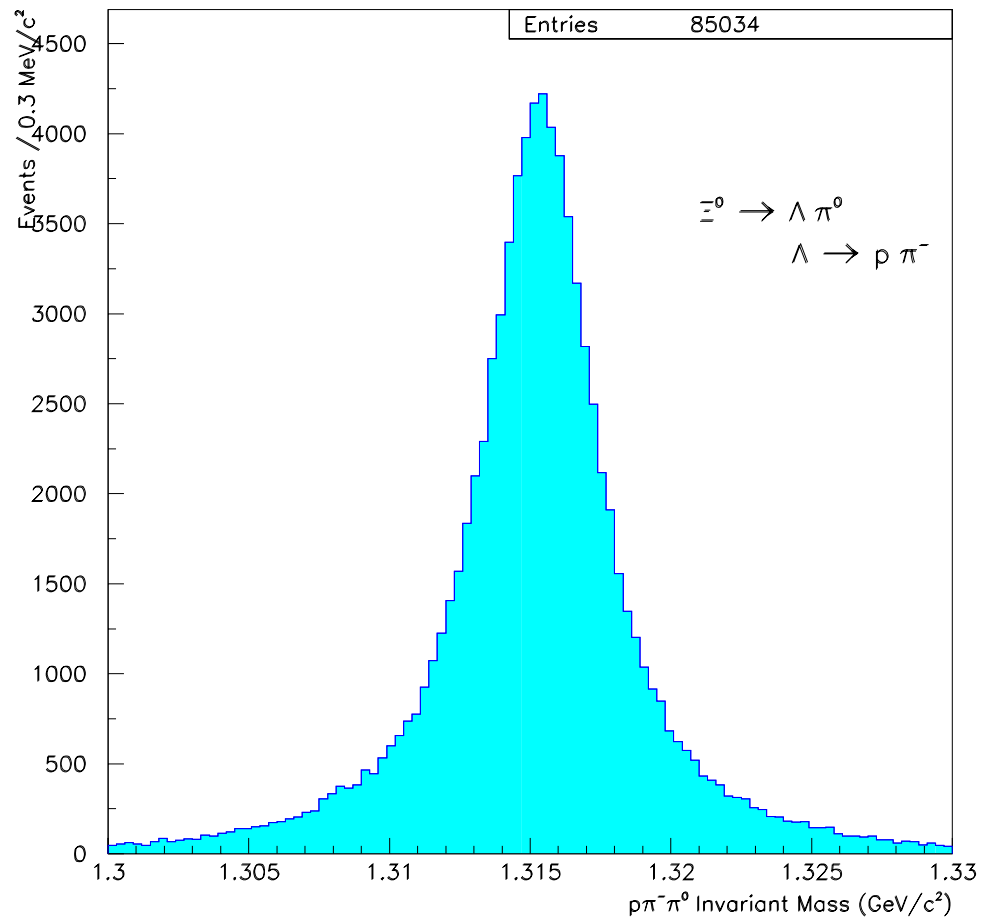


Figure 6.14: Distribution of the reconstructed  $\Xi^0$  mass from  $\Xi^0 \rightarrow \Lambda \pi^0$  candidates.

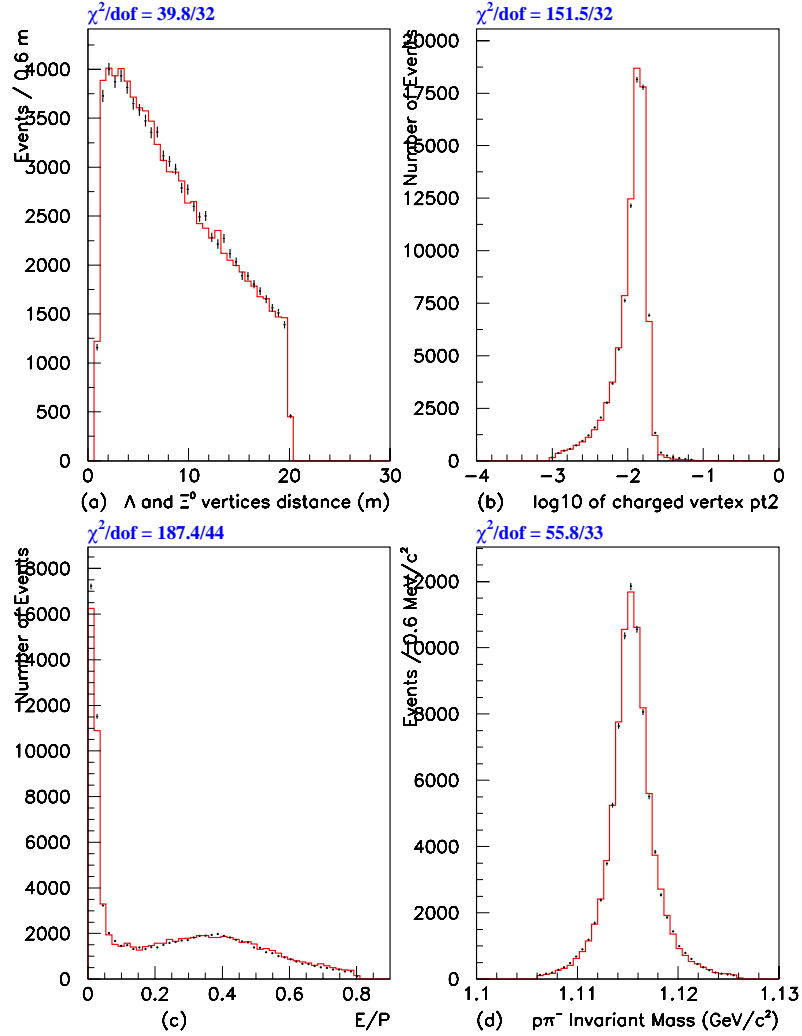


Figure 6.15:  $\Xi^0 \rightarrow \Lambda \pi^0$  decay's distribution of the: (a) Longitudinal distance between the  $\Lambda$  and  $\Xi^0$  vertices. (b) Square of the transverse momentum of the charged vertex. (c) Ratio of energy of the  $\pi^-$  as measured by the calorimeter to the momentum of the  $\pi^-$  as measured by the charged spectrometer. (d) Reconstructed  $p\pi^-$  mass. Dots are data and the histogram is MC in each plot.

of  $75.5 \pm 4.4$  psec in good agreement with the value of  $79.9 \pm 0.4$  psec given by the PDG. The same fit procedure is applied on the simulated distribution and gives a value of  $81.4 \pm 4.2$  psec. This is not claimed to be a precise lifetime measurement of  $\Sigma^+$  particle, since no attempt was made to correct for the acceptance as can be seen from the end points in the plot. However, it is a convincing double check to prove the majority of the particles in the mass peak are  $\Sigma^+$ .

Figures 6.18 to 6.22 show the distribution of the kinematical and several reconstructed variables, as described in section 6.1.1, for the final set of signal events which passed all the above cuts in comparison with the Monte Carlo simulation of the same variables. The dots represent the data with the *statistical* error bars and the histogram represents the Monte Carlo distribution normalized to the number of data events for the  $\Xi^0$  beta decay signal. The relatively small  $\chi^2/ndf$  indicates a good Data/MC agreement.

Hence, at the level of the analysis, the kinematics of the  $\Xi^0$  decay is well understood and the Monte Carlo simulation can be properly used for the acceptance corrections performed in the measurement of the branching ratio.

### 6.3 Background Studies

There is no competing two-body decay to the  $\Xi^0$  beta decay with the same final state baryon. The possible decay,  $\Xi^0 \rightarrow \Sigma^+ \pi^-$ , is not energetically allowed. However,  $\Xi^0$  formed the least fraction of neutral particles in beam. The total flux of  $\Xi^0$  for the summer run was estimated to be about  $1.3 \times 10^8$ . The ratio of the number of  $\Lambda$ 's to the number of  $\Xi^0$ 's was estimated to be 10:1 and that of  $K_L$ 's to  $\Lambda$ 's to be



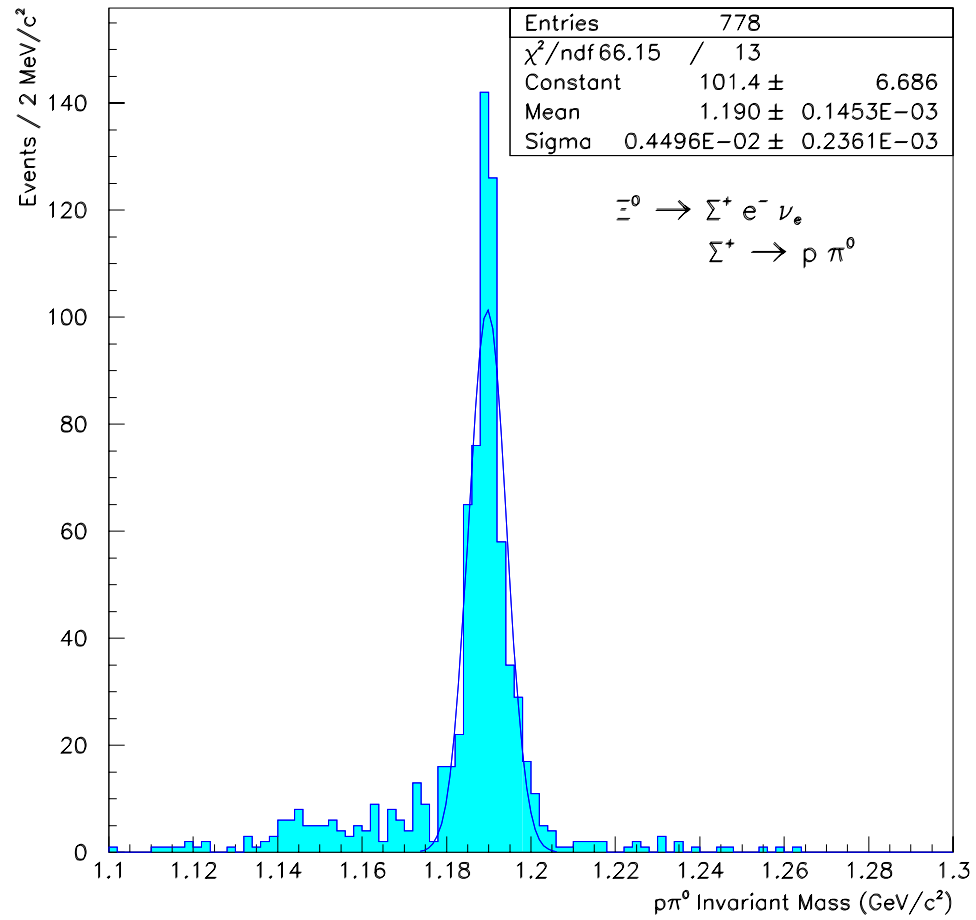


Figure 6.16: Reconstructed  $p\pi^0$  mass distribution for the events selected for the  $\Xi^0$  beta decay branching ratio measurement. The parameters of a Gaussian fit on the data distribution are given.

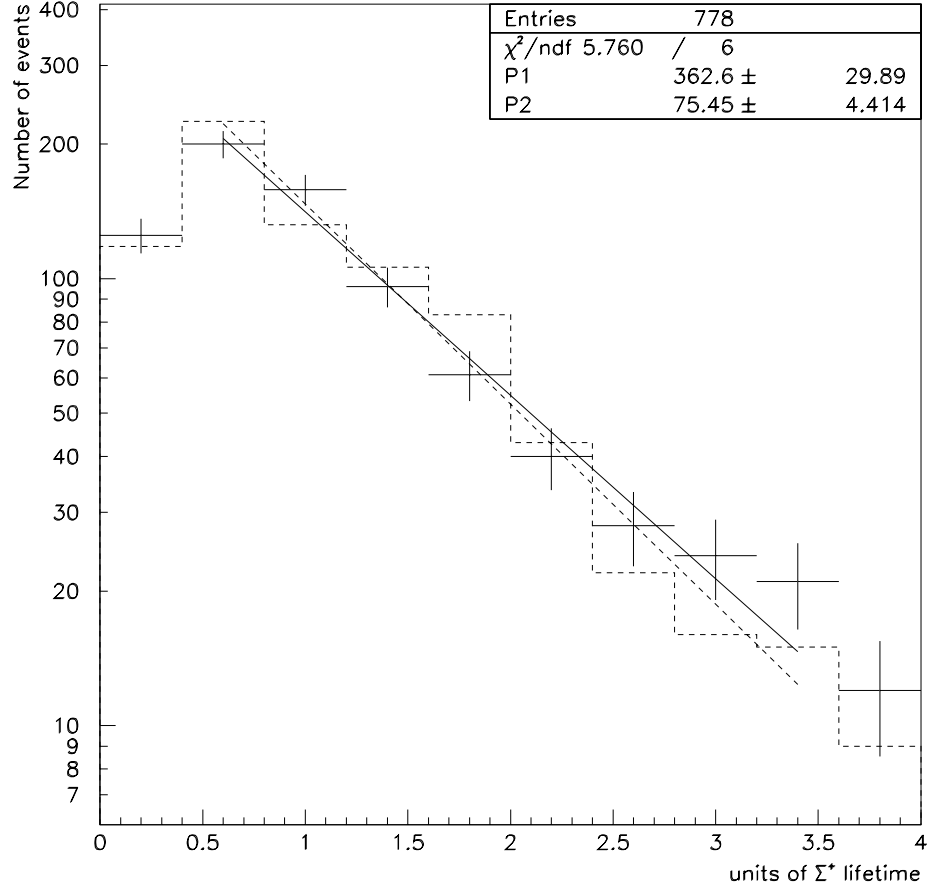


Figure 6.17: Proper time distribution of  $\Sigma^+$  from the  $\Xi^0$  beta decay event candidates, in  $\Sigma^+$  lifetime units. The plotted points are data (statistical errors only). The histogram is the corresponding MC distribution normalized to the number of data events. No acceptance correction has been applied. The results of an exponential fit done on the data and on the simulation are shown.

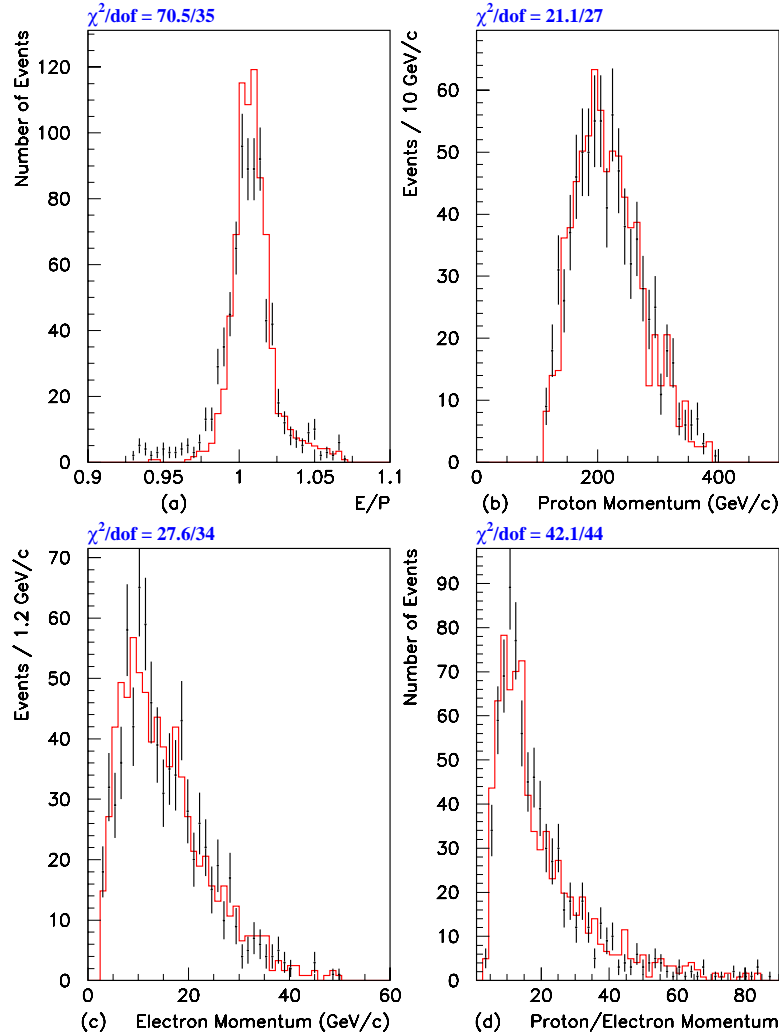


Figure 6.18:  $\Xi^0 \rightarrow \Sigma^+ e^- \bar{\nu}_e$  distribution of the: (a) Ratio of the energy of the electron as measured by the calorimeter to the momentum of the electron as measured by the charged spectrometer. (b) Momentum of the positive charged track, assumed to be a proton. (c) Momentum of the negative charged track, assumed to be an electron. (d) Ratio of momentum of the positive track to the momentum of the negative track. Dots are data and the histogram is MC in each plot.

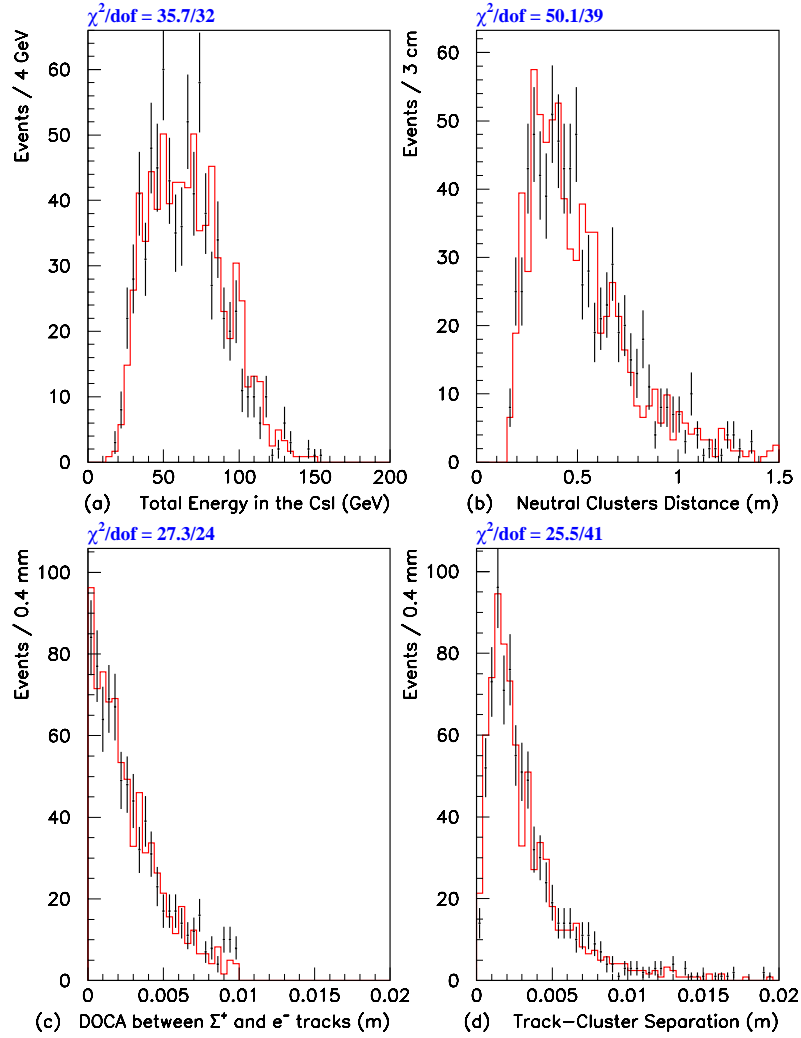


Figure 6.19: Distribution of the: (a) Total energy of the cluster deposited in the CsI calorimeter. (b) Distance between the two neutral clusters (photons) in the calorimeter. (c) Distance of closest approach between the  $\Sigma^+$  reconstructed track and the electron track. (d) Separation distance between the center of the electron cluster and the track associated with that at CsI. Dots are data and the histogram is MC in each plot.

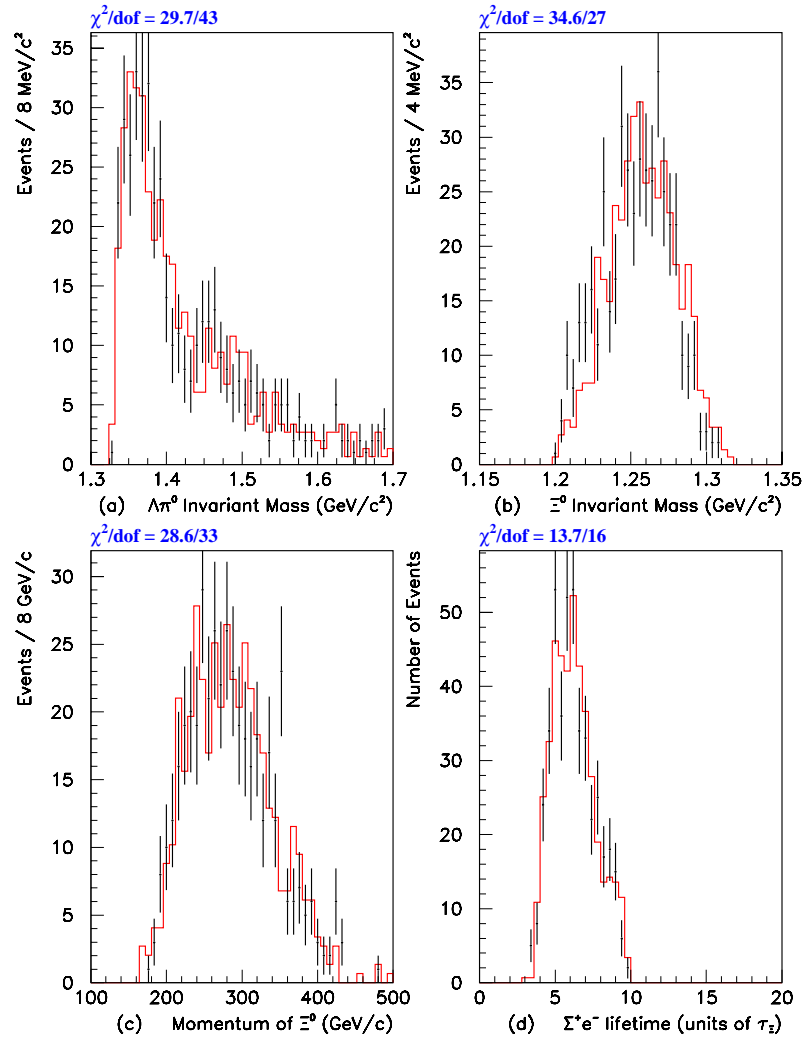


Figure 6.20:  $\Xi^0 \rightarrow \Sigma^+ e^- \bar{\nu}_e$  distribution of the: (a) Reconstructed  $p\pi^-\pi^0$  principal decay mass. (b) Reconstructed mass of  $\Sigma^+e^-$  beta decay. (c) Reconstructed momentum of  $\Sigma^+e^-$  beta decay. (d) Reconstructed  $\Sigma^+e^-$  lifetime in units of  $\Xi^0$  lifetime. Dots are data and the histogram is MC in each plot.

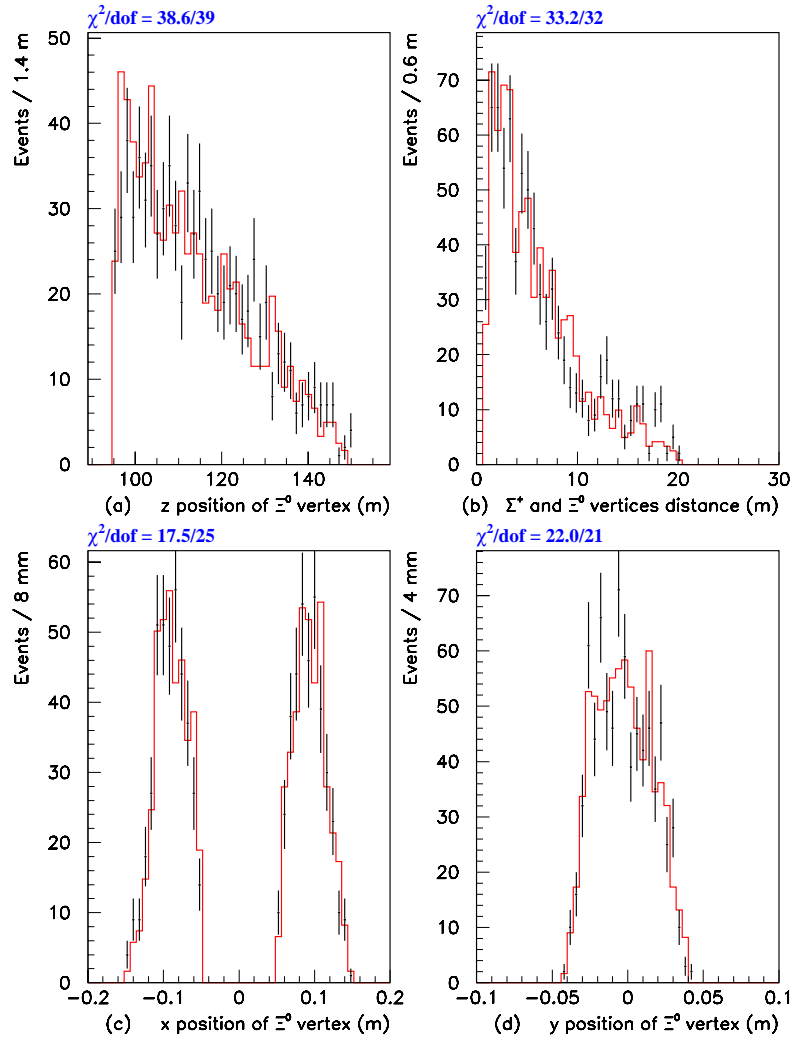


Figure 6.21: Distribution of the: (a) longitudinal position of  $\Xi^0$  vertex inside the decay volume. (b) Longitudinal distance between the  $\Sigma^+$  and  $\Xi^0$  vertices. (c,d) Transverse position of  $\Xi^0$  beta vertex. Dots are data and the histogram is MC in each plot.

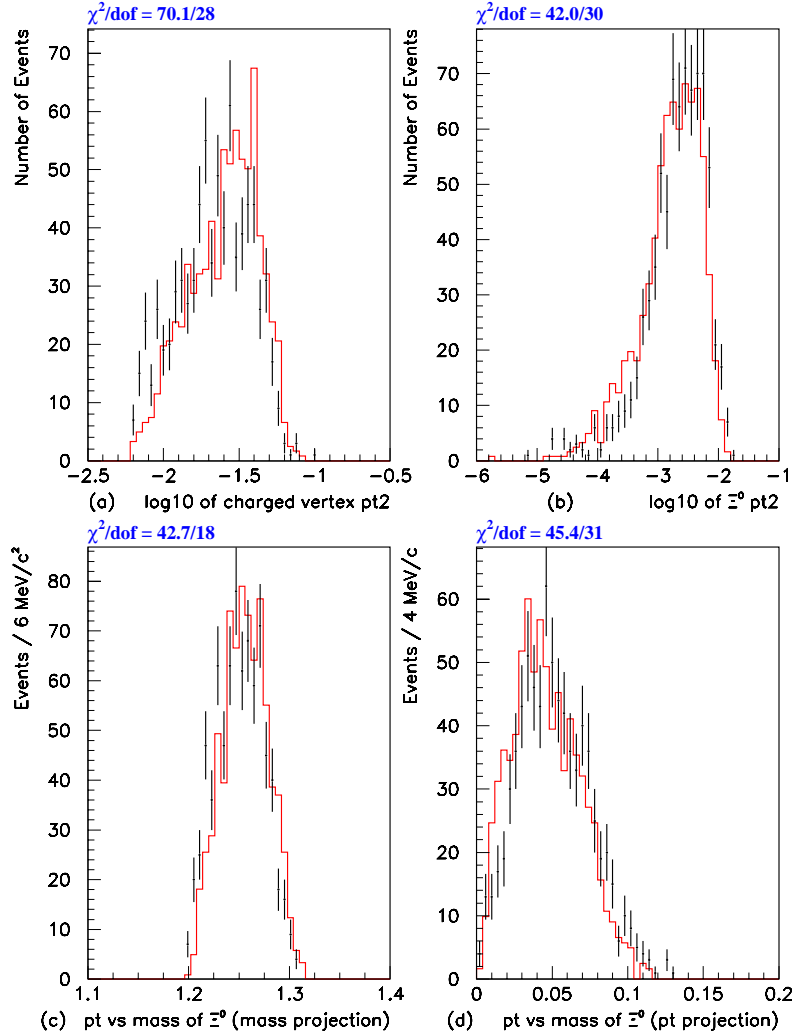


Figure 6.22: Distribution of the: (a) Square of the transverse momentum of the charged vertex. (b) Square of the transverse momentum of the reconstructed  $\Xi^0$  beta vertex. (c,d) Projection of the 2-dimensional distribution of transverse momentum vs reconstructed mass of  $\Sigma^+e^-$  on the mass and transverse momentum axis respectively. Dots are data and the histogram is MC in each plot.

50:1. Thus, besides other decay channels of  $\Xi^0$  decays, we studied all the possible decays of  $K_L$  and  $\Lambda$  which could fake the signal. These background decays are discussed in this section. Especially, we are interested to know the amount of their contribution to the signal and how we could reduce them in the data.

### 6.3.1 $K_L^0 \rightarrow \pi^0 \pi^+ \pi^-$

This is one of the dominant  $K_L$  decay modes with a branching ratio (BR) of 12.56% and could be a background when the negative pion is misidentified as an electron and the positive pion goes down the beam hole mistakenly called a proton. Figure 6.23 shows the geometry of this decay. This background can easily be identified and removed. First of all the cuts on the E/p of the negative track, on the momentum ratio, on the charged vertex transverse momentum and the lifetime of  $\Xi^0$  remove almost all of these events. Furthermore, by assuming a  $\pi$  mass for both the tracks and forcing the two photons to form a  $\pi^0$  at the charged vertex, one could reconstruct the mass of  $K_L$  and cut on that. Monte Carlo studies showed that this background is negligible. Even cutting on the mass  $K_L$  was unnecessary.

### 6.3.2 $K_L^0 \rightarrow \pi^+ e^- \bar{\nu}_e$

This decay mode known as  $K_{e3}^0$  is the dominant product of  $K_L$  with a BR of 38.8%, and is a possible source of background when accompanied with two accidental photons. Requiring three in-time hardware clusters is the most effective way to remove this background since the accidentals are mostly out-of-time. We generated a large MC sample of these events equivalent to the number expected from the



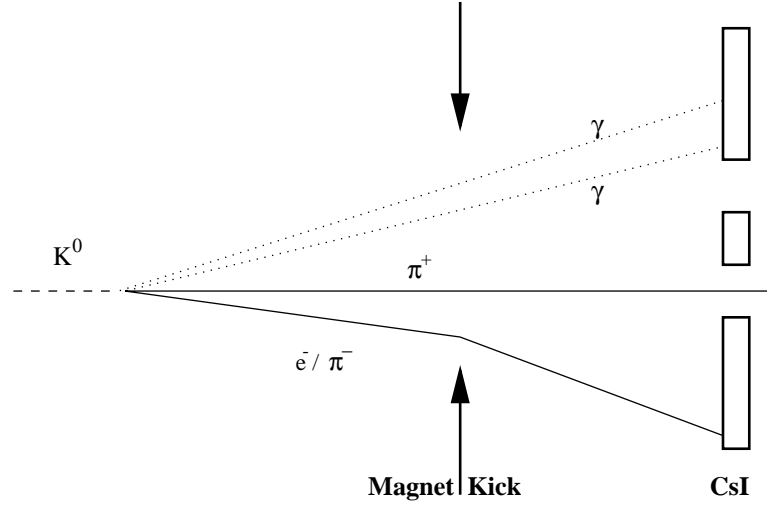


Figure 6.23: The geometry of the decays  $K_L \rightarrow \pi^+ \pi^- \pi^0$  and  $K_L^0 \rightarrow \pi^+ e^- \nu_e \gamma$  (+ an accidental photon).

data for the high momentum  $K_L$ 's <sup>2</sup>. Running the analysis code on these data showed there were 4 events left under the sigma reconstructed mass.

### 6.3.3 $K_L^0 \rightarrow \pi^+ e^- \bar{\nu}_e \gamma$

This decay mode known as radiative  $K_{e3}^0$  is suppressed by about two orders of magnitude compared to  $K_{e3}^0$  decays but producing one actual photon means only one accidental photon is needed to fake a  $\Xi^0 \rightarrow \Sigma^+ e^- \bar{\nu}_e$  decay. Requiring three in time hardware clusters again removes most of this background. A large MC

---

<sup>2</sup> $\pi^+$  tracks had to have a momentum above 100 GeV to be able to fake protons. For the MC generation, we required  $K_L$  with momentum above 100 GeV which is on the tail of the kaon momentum spectrum. This technique saved us a lot of CPU time and disk space to generate and store huge MC data

sample of these events equivalent to the number expected from the data for the high momentum  $K_L$  s showed 8 events under the sigma reconstructed mass.

#### 6.3.4 $K_L^0 \rightarrow \pi^0 \pi^+ e^- \bar{\nu}_e$

This decay mode known as  $K_{e4}^0$  is very similar to  $K_L \rightarrow \pi^+ \pi^- \pi^0$  except that it produces an electron (Fig 6.23) instead of a  $\pi^-$ . However, it has a much smaller BR of  $5.15 \times 10^{-5}$ . Similar cuts would remove this background as well. MC simulation of this decay mode shows no background event in the signal region.

#### 6.3.5 $\Xi^0 \rightarrow \Lambda \pi^0$ followed by $\Lambda \rightarrow p \pi^-$

Let us consider the backgrounds coming from decay of  $\Xi^0$  to other final states. The dominant  $\Xi^0$  decay mode into a  $\Lambda$  and a  $\pi^0$  with  $\Lambda$  going into a proton and a  $\pi^-$ , which was used as the normalization mode for the BR measurement, could be a background when the  $\pi^-$  is misidentified as an electron. The geometry of this decay is however, different than that of  $\Xi^0 \rightarrow \Sigma^+ e^- \bar{\nu}_e$  decay (Figs. 6.1 and 6.13). As shown in section 6.1, the reconstructed  $\Sigma^+$  that one would get for these events is not in the signal region but slightly aside (Fig. 6.12 top left). These events were completely removed by cuts on the relative  $z$ -position of  $\Xi^0$  and  $\Sigma^+$  vertices, transverse momentum of charged vertex and the reconstructed  $\Xi^0$  vertex, and most importantly by a cut on the reconstructed  $\Xi^0$  mass with the hypothesis of a decay into a  $\Lambda \pi^0$  and the  $\Lambda$  into a proton and a  $\pi^-$  as described in section 6.1. The generated MC of these events equivalent in number to the data showed no event in the signal region. Fig. 6.24 shows the distribution of the above variables and the cuts used for  $\Xi^0 \rightarrow \Sigma^+ e^- \bar{\nu}_e$  event selection. The dark grey area shows the

rejected events. These plots can be compared with the corresponding variables for  $\Xi^0 \rightarrow \Sigma^+ e^- \bar{\nu}_e$  in Figs. 6.7 to 6.11.

### 6.3.6 $\Xi^0 \rightarrow \Lambda \pi^0$ followed by $\Lambda \rightarrow p e^- \bar{\nu}_e$

Finally, the most difficult hyperon background is the one coming from the same  $\Xi^0$  decay into  $\Lambda \pi^0$  with a subsequent beta decay of  $\Lambda$ . This decay has exactly the same decay products as  $\Xi^0 \rightarrow \Sigma^+ e^- \bar{\nu}_e$  decay. The only difference is the topology of this decay is different<sup>3</sup>. The cut on the relative  $z$ -position of  $\Xi^0$  and  $\Sigma^+$  vertices allowed us to eliminate this background. Similar to the other background in section 6.3.5, the reconstructed  $\Sigma^+$  that one would get for these events is not in the signal. Knowing the branching ratio of Lambda beta decay, we generated a full MC sample of this decay equivalent to the entire data (roughly six times more than Cascade beta decay). Only two events were found under the sigma mass peak.

In conclusion, we believe we understood our various background sources to the  $\Xi^0$  beta decay signal and they were under control at the level of our analysis. Figure 6.25 shows the signal as we presented in Fig. 6.16 with the overlay of the sum of the background contributions of the above mentioned modes in dark gray. To see how well the MC generated background agrees with the level of background in the signal, the logarithmic scale is used. There are 14 events underneath of the signal between 1.175 and 1.205 GeV (3 sigmas on both sides of the peak) which will be used in the next section to extract the branching ratio.

---

<sup>3</sup>The decay geometry is the same as normal decay of  $\Xi^0$  in Fig. 6.13, if one replaces the  $\pi^-$  with an electron and a missing neutrino.

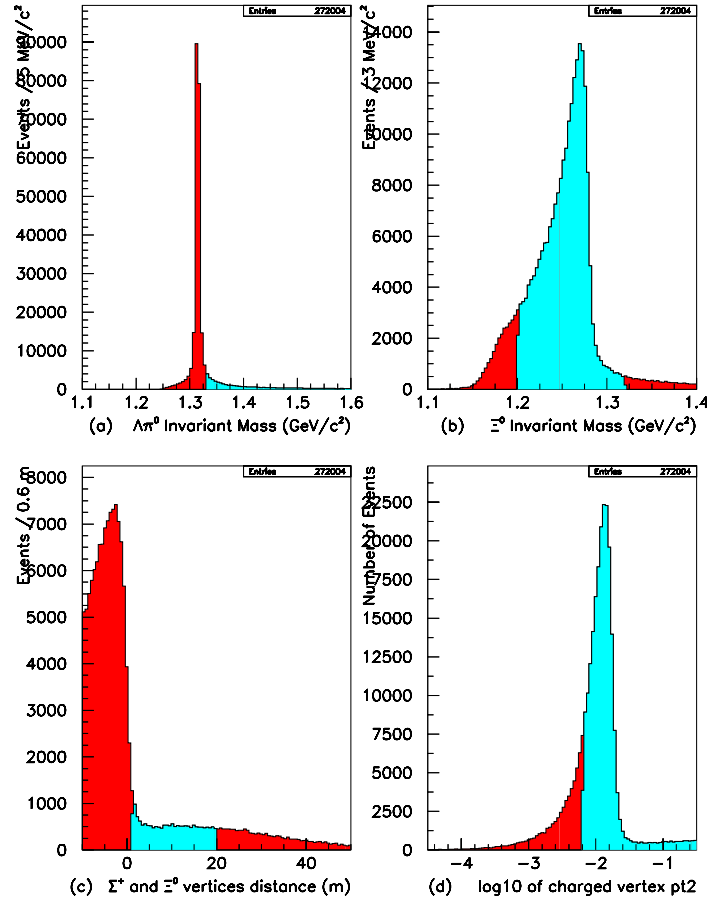


Figure 6.24: Monte Carlo simulation of  $\Xi^0 \rightarrow \Lambda \pi^0$  for: (a) Reconstructed  $\Xi^0$  mass. (b) Reconstructed mass of  $\Sigma^+ e^-$ . (c) Longitudinal distance between the  $\Sigma^+$  and  $\Xi^0$  vertices. (d) Square of the transverse momentum of the charged vertex. The light grey shows the accepted events after applying the cuts and the dark grey is the rejected events.

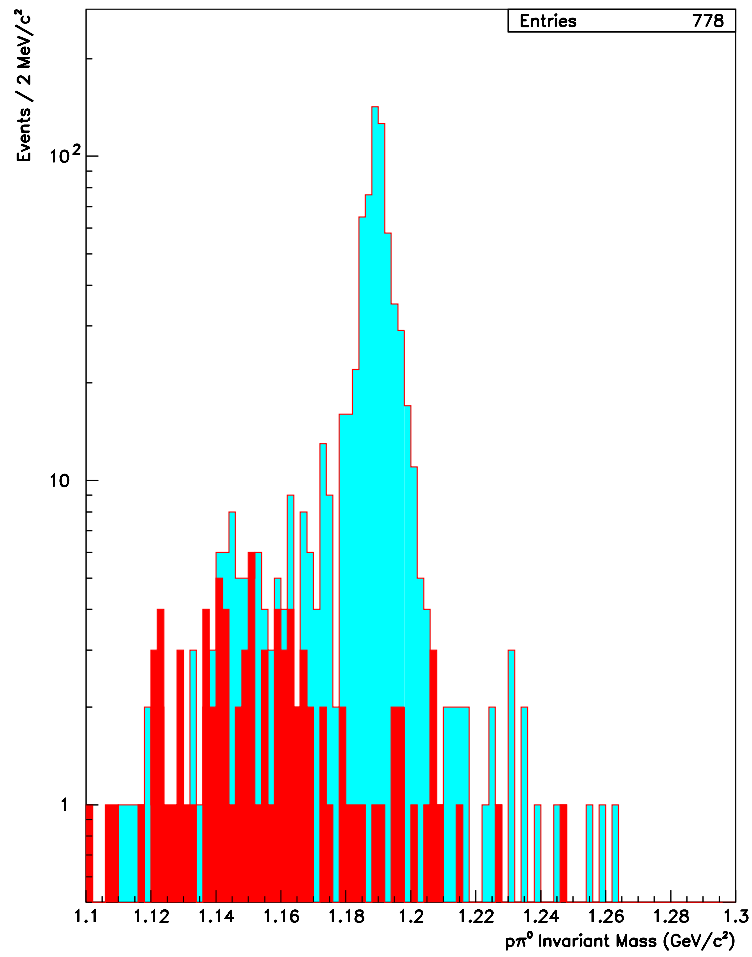


Figure 6.25: Reconstructed  $p\pi^0$  mass distribution for the  $\Xi^0$  beta events. The MC simulated background normalized to the flux is shown in dark grey.

## 6.4 Measurement of the Branching Ratio

The branching ratio of  $\Xi^0 \rightarrow \Sigma^+ e^- \bar{\nu}_e$  decay normalized to  $\Xi^0 \rightarrow \Lambda \pi^0$  decay can be calculated from the following relation:

$$\frac{BR(\Xi^0 \rightarrow \Sigma^+ e^- \bar{\nu}_e)}{BR(\Xi^0 \rightarrow \Lambda \pi^0)} = \frac{N_{beta}}{N_{norm}} \times \frac{Acc_{norm}}{Acc_{beta}} \times \frac{BR(\Lambda \rightarrow p \pi^-)}{BR(\Sigma^+ \rightarrow p \pi^0)} \times \frac{Ps(beta \leftrightarrow trigger)}{Ps(\Lambda \leftrightarrow trigger)}$$

where the value of each factor is determined as follows:

- $N_{beta}$  is the number of  $\Xi^0 \rightarrow \Sigma^+ e^- \bar{\nu}_e$  selected events. We counted the number of events in the reconstructed  $\Sigma^+$  mass peak in Fig. 6.16. There are 626 events between 1.175 GeV/ $c^2$  and 1.205 GeV/ $c^2$  (within 15 MeV/ $c^2$  or equivalently  $3\sigma$  of the known mass of  $\Sigma^+$ , 1.1894 GeV/ $c^2$ ). However, this includes background events in the peak. We used a sideband background subtraction method to estimate the level of background. Assuming a uniform background, one could count the number of events in two sides of the peak, 15 MeV each, which would have the same number of background events as the 30 MeV region under the peak. From Fig. 6.16, there are 38 events between 1.145 and 1.160 GeV/ $c^2$ , and 7 events between 1.220 and 1.235 GeV/ $c^2$ . Therefore,  $N_{beta} = 626 \leftrightarrow 45 = 581$ .
- $N_{norm}$  is the number of  $\Xi^0 \rightarrow \Lambda \pi^0$  selected events. From Fig. 6.14  $N_{norm} = 85034$ . The background for the normalization mode is less than 0.5% and therefore negligible.
- $BR(\Lambda \rightarrow p \pi^-) = (63.9 \pm 0.5)\%$  from the PDG.

- $BR(\Sigma^+ \rightarrow p\pi^0) = (51.57 \pm 0.30)\%$  from the PDG.
- $Acc_{beta}$  is the acceptance correction for the  $\Xi^0 \rightarrow \Sigma^+ e^- \bar{\nu}_e$  decay which was determined from the MC. 25,432  $\Xi^0 \rightarrow \Sigma^+ e^- \bar{\nu}_e$  were generated out of which 919 events reached the decay volume of the experiment, passed all the  $beta \Leftrightarrow trigger$  requirements and passed the reconstruction and the analysis cuts. The acceptance of the signal mode was  $(3.61 \pm 0.05)\%$ .
- $Acc_{norm}$  is the acceptance correction for the  $\Xi^0 \rightarrow \Lambda\pi^0$  decay which was determined from the MC. 1,457,136  $\Xi^0 \rightarrow \Lambda\pi^0$  were generated out of which 81,095 events reached the decay volume of the experiment, passed all the  $\Lambda \Leftrightarrow trigger$  requirements and passed the reconstruction and the analysis cuts. The acceptance of the signal mode was  $(5.57 \pm 0.07)\%$ .
- $Ps(beta \Leftrightarrow trigger)$  is the prescale factor of  $\Xi^0 \Leftrightarrow beta \Leftrightarrow trigger$  which was 1 for the data taking period in this calculation.
- $Ps(\Lambda \Leftrightarrow trigger)$  is the prescale factor of  $\Lambda \Leftrightarrow trigger$  which was 50 for the data taking period in this calculation.

The calculation leads to a BR result and statistical error of

$$\frac{BR(\Xi^0 \rightarrow \Sigma^+ e^- \bar{\nu}_e)}{BR(\Xi^0 \rightarrow \Lambda\pi^0)} = (2.61 \pm 0.11_{(stat.)}) \times 10^{-4}.$$

A systematic error of 6.1% is estimated for this calculation. The issue of systematic errors is discussed in Chapter 8 in detail. Therefore, we present the branching ratio of  $\Xi^0 \rightarrow \Sigma^+ e^- \bar{\nu}_e$  normalized to  $\Xi^0 \rightarrow \Lambda\pi^0$  decays:

$$\frac{BR(\Xi^0 \rightarrow \Sigma^+ e^- \bar{\nu}_e)}{BR(\Xi^0 \rightarrow \Lambda \pi^0)} = (2.61 \pm 0.11_{(stat.)} \pm 0.16_{(syst.)}) \times 10^{-4}$$

The BR of  $\Xi^0 \rightarrow \Lambda \pi^0$  is known to be  $(99.54 \pm 0.05)\%$  from the PDG. Therefore to calculate the absolute branching fraction, we multiply the above value by the BR of  $\Xi^0 \rightarrow \Lambda \pi^0$  decay:

$$BR(\Xi^0 \rightarrow \Sigma^+ e^- \bar{\nu}_e) = \frac{BR(\Xi^0 \rightarrow \Sigma^+ e^- \bar{\nu}_e)}{BR(\Xi^0 \rightarrow \Lambda \pi^0)} \times BR(\Xi^0 \rightarrow \Lambda \pi^0) = (2.60 \pm 0.11_{(stat.)} \pm 0.16_{(syst.)}) \times 10^{-4}.$$

## 6.5 $\Lambda \rightarrow pe^- \bar{\nu}_e$ Decay, An alternative Normalization Mode

In the branching ratio calculation of the decay  $\Xi^0 \rightarrow \Sigma^+ e^- \bar{\nu}_e$  presented in this chapter, we used the principal decay of  $\Xi^0 \rightarrow \Lambda \pi^0$  as the flux normalization mode where  $\Lambda \rightarrow p \pi^-$ , the dominant decay of  $\Lambda$  ( $BR = (63.9 \pm 0.5)\%$ ). This normalization mode has the advantage of being well measured, easy to reconstruct and background free. However, due to high statistics of this mode, we had to use a different trigger (prescaled by a factor of 50) to collect them which made the analysis a little difficult.

Another decay mode of  $\Lambda$  known as Lambda beta decay,  $\Lambda \rightarrow pe^- \bar{\nu}_e$  could be used instead of  $\Lambda \rightarrow p \pi^-$  whose branching ratio of  $(8.32 \pm 0.14) \times 10^{-4}$  is also known [28]. The sequence of  $\Xi^0 \rightarrow \Lambda \pi^0$  where  $\Lambda \rightarrow pe^- \bar{\nu}_e$  would be a perfect normalization mode for the  $\Xi^0 \rightarrow \Sigma^+ e^- \bar{\nu}_e$  decay, in a sense that it has exactly the same final decay products and is collected from the same trigger. The disadvantage of this mode however, is a lower statistics and a high level of background. Besides, the reconstruction of this mode is more challenging. In this section we discuss a



reconstruction method used to identify these events and present some preliminary results.

### 6.5.1 The Reconstruction Method

Figure 6.26 shows the topology of the decay in KTeV apparatus. It can be compared with figure 6.13. The only difference is having an electron (accompanied by a missing neutrino) instead of a pion in the final state. The  $\Lambda$  vertex is a charged vertex reconstructed from the closest approach between the two charged tracks. Unlike the  $\Lambda \rightarrow p\pi^-$  case, the missing neutrino doesn't allow us to reconstruct the 4-momentum of  $\Lambda$  precisely. Luckily, most of the momentum of  $\Lambda$  is being carried by the proton. In the first approximation, one could ignore the momentum kick from the missing neutrino and reconstruct the  $\Lambda$  trajectory from the known 4-momentum of the electron and the proton. The  $\Xi^0$  and its decay vertex are reconstructed to be the point, along the extrapolated  $\Lambda$  path where the two neutral electromagnetic clusters, called photons, best match the  $\pi^0$  mass. We should keep in mind that because of constraining the direction of the momentum of  $\Lambda$ , this decay vertex is an approximation.

The magnitude of the momentum of  $\Lambda$  and the momentum of the neutrino are then found by solving the problem of a three body decay with a missing particle (Appendix B). This relativistic problem has two solutions reflecting an ambiguity of direction of flight of the neutrino. We picked the solution which results in the better reconstructed mass of  $\Xi^0$  at the end. Regardless of this ambiguity, the method would work correctly in order to tag Lambda beta events from the decay

of  $\Xi^0 \rightarrow \Lambda \pi^0$ .

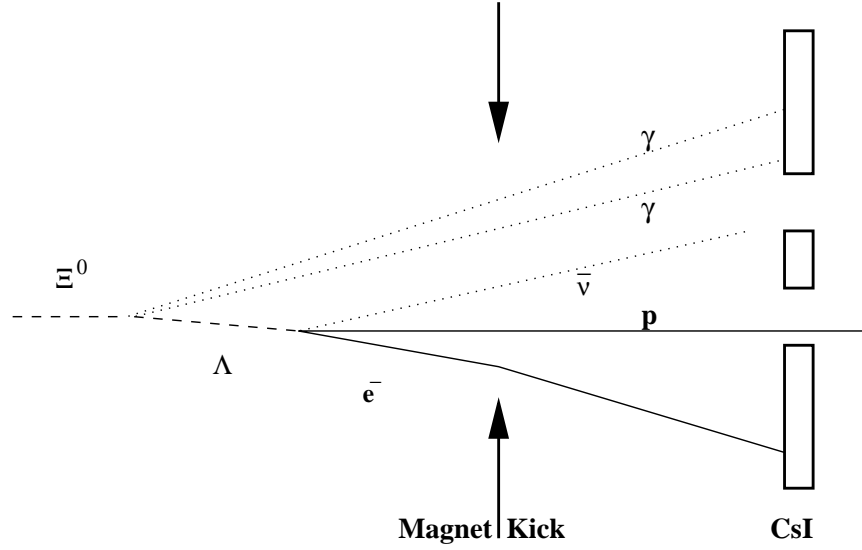


Figure 6.26: The geometry of the decay  $\Xi^0 \rightarrow \Lambda \pi^0$  where  $\Lambda \rightarrow p e^- \bar{\nu}_e$ .

### 6.5.2 The Event Selection

The event selection criteria and the analysis cuts were very similar to what we described in section 6.1.2, except that we searched for an  $e^-$  instead of a  $\pi^-$ . The ratio of the energy deposited by the low momentum track in the calorimeter to its momentum (measured by the spectrometer) was chosen to be between 0.93 and 1.07 like Cascade beta decay. Besides CsI, we had to use the Transition Radiation Detectors (Sec. 2.4) to enhance the  $e^-/\pi^-$  discrimination power by another factor of about 250; hence removing most of the main background from  $\Lambda \rightarrow p \pi^-$ . Furthermore, we applied a cut on the mass of  $p \pi^-$  to be more than 10 MeV away from the known mass of  $\Lambda$ . Figure 6.27 shows the reconstructed

mass of  $\Xi^0$  from this decay for the entire summer data.

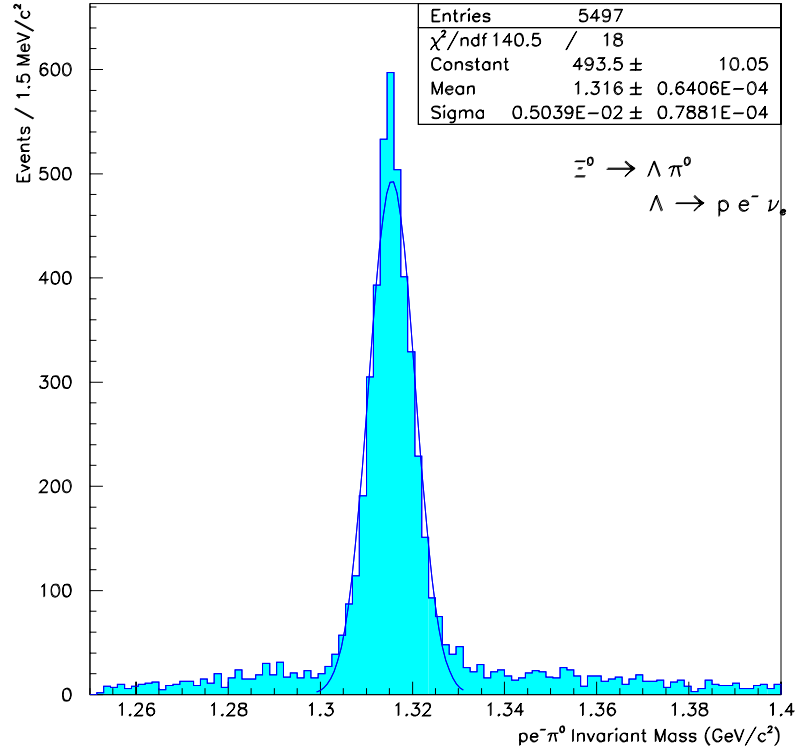


Figure 6.27: The reconstructed mass of  $\Xi^0$  for the decay  $\Xi^0 \rightarrow \Lambda \pi^0$  where  $\Lambda \rightarrow p e^- \bar{\nu}_e$  and  $\pi^0 \rightarrow \gamma \gamma$ .

Monte Carlo studies show most of the background is coming from  $K_{e3}^0$  decays ( $K_L \rightarrow \pi^+ e^- \bar{\nu}$ ) with two in-time accidental photons. Radiative  $K_{e3}^0$  decays ( $K_L \rightarrow \pi^+ e^- \bar{\nu} \gamma$ ) with one accidental, and the principal decay of  $\Xi^0 \rightarrow \Lambda \pi^0$  where  $\Lambda \rightarrow p \pi^-$  are the next largest backgrounds. There are  $4229 \pm 65$  estimated events over a background of  $440 \pm 41$  between 1.300 GeV and 1.330 GeV. A preliminary

branching ratio measurement of  $\Lambda \rightarrow pe^- \bar{\nu}_e$  decay using this sample agrees well with the world average. However, an improved method of event reconstruction and a better understanding of backgrounds for this mode is needed in order to use it as the flux normalization mode for  $\Xi^0 \rightarrow \Sigma^+ e^- \bar{\nu}_e$  branching ratio measurement at a level comparable or more precise than our current measured method.

## Chapter 7

### The Monte Carlo Simulation

This chapter discusses the Monte Carlo (MC) simulation of KTeV experiment which was referred to extensively in chapter 6. The MC serves two purposes. First, in order to measure the branching ratio (presented in the last chapter), the acceptance ratio of signal to normalization mode must be understood. The MC was used to calculate the detector acceptance for both the signal and normalization modes. Second, the MC was necessary in the background level estimation and in studying various analysis cuts for the event selection.

#### 7.1 Event Generation

A Monte Carlo simulated event is generated in three steps. First the momentum and direction of the parent particles ( $K_L$  or hyperons) of the decay is produced at the target. Then the directions and momentum of the decay products are determined. Finally, the decay products are propagated through the detector to determine the response of different detector elements to the particles.

### 7.1.1 Kaon Production

The first step is to parameterize the kaon production spectrum obtained in proton-Beryllium collisions. Our starting point is the parameterization by Malensek [80] for the  $K^+$  and  $K^-$  spectrum for protons incident on a beryllium target by 400 GeV/c protons. In this parameterization, the number of kaons with momentum  $p$  into a solid angle  $d\Omega$  was:

$$\frac{d^2 N}{dp d\Omega} = \frac{E_B}{400} B x \frac{(1 \leftrightarrow x)^A (1 + 5e^{-Dx})}{(1 + p_t^2/M^2)^4} \quad (7.1)$$

where,  $x$  is the ratio of the kaon momentum,  $p$ , to the beam energy,  $E_B$ ,  $x = p/E_B$ , and  $p_t$  represents the transverse momentum of the produced particle relative to the incident beam direction.  $B$ ,  $A$ ,  $D$ , and  $M^2$  are constants fit to the experimental data (Table 7.1).  $p$  and  $p_t$  are expressed in unit of GeV/c.

Table 7.1: Values of parameters describing the kaon production spectrum [80].

	$K^+$	$K^-$
A	2.924	6.107
B	14.15	12.33
$M^2$	1.164	1.098
D	19.89	17.78

Using quark-counting arguments (see reference [73] for example),  $K^0$  and  $\bar{K}^0$  production can be related to  $K^+$  and  $K^-$ :

$$N_{K^0} = \frac{N_{K^+} + N_{K^-}}{2} \quad (7.2)$$

$$N_{\bar{K}^0} = N_{K^-} \quad (7.3)$$

The KTeV spectrum was tuned further, to match kaon momentum measured by  $K_L \rightarrow \pi^+ \pi^-$  events in the real data. The details can be found elsewhere ([20], [73], [74]).

### 7.1.2 Hyperon Production

The first step in MC is the generation of the energy and directions of the parent particles. The probability of hyperon generation is provided by a model given by Pondrom [39, 40]:

$$E \frac{d^3\sigma}{dp^3} = \exp(C_1 + C_2 x^2 + C_3 x + C_4 x p_t + C_5 p_t^2 + C_6 p_t^4 + C_7 p_t^6) \times (1 \Leftrightarrow x)^{C_8 + C_9 p_t^2}$$

where  $x$  is defined as the ratio of the produced particle momentum,  $p$ , to the beam energy,  $E_B$ ,  $x = p/E_B$ ,  $p_t$  is the transverse momentum of the produced particle relative to the incident beam direction and  $E$  denotes the energy of produced particle. This formula was determined by fits on the experimental results from Fermilab Meson Center, and the coefficients known as Pondrom parameters are listed in Table 7.2. Based on the momentum spectrum produced by using these constants, the  $\Lambda$  spectrum was tuned so that the spectrum measured in  $\Lambda \rightarrow p\pi^-$  events matched to that in MC. As a result, the MC spectrum was scaled by 90% in  $E$ . For  $\Xi^0$ , the production spectrum based on the Table 7.2 was used without corrections. The decay position of hyperons was simply determined by their proper lifetimes and their momenta.

Table 7.2: Coefficients in empirical fits for hyperon spectrum.

	$p\text{Be} \rightarrow \Lambda$	$p\text{Be} \rightarrow \Xi$	$p\text{Be} \rightarrow \bar{\Lambda}$	$p\text{Be} \rightarrow \bar{\Xi}$
$C_1$	1.68	-1.21	1.45	0.61
$C_2$	0.44	1.16	-0.79	18.1
$C_3$	0.28	-0.72	1.28	-22.5
$C_4$	-0.58	-0.48	-1.09	-1.46
$C_5$	-2.62	-1.85	-2.21	-1.24
$C_6$	0.40	0.17	0.45	0.00
$C_7$	-0.03	-0.008	-0.07	-0.00
$C_8$	0.86	2.87	0.74	-
$C_9$	0.20	0.04	0.61	-



## 7.2 Hyperon Decays

The default KTEVMC simulated  $\Lambda$  and  $\Xi^0$  hyperon decays assuming unpolarized hyperons, and decays were generated according to a flat phase space<sup>1</sup>. However, the user could enable the following features [81]:

- The polarization of  $\Lambda$  and  $\Xi^0$  hyperons produced at the target.
- Distribution of decay products according to physics form factors as in:  $\Lambda \rightarrow p\pi^-$ ,  $\Lambda \rightarrow pe^-\bar{\nu}$ ,  $\Xi^0 \rightarrow \Lambda\pi^0$ ,  $\Xi^0 \rightarrow \Sigma^+e^-\bar{\nu}$ ,  $\Sigma^+ \rightarrow p\pi^0$ ,  $\Xi^0 \rightarrow \Lambda\gamma$ ,  $\Xi^0 \rightarrow \Sigma^0\gamma$ ,  $\Sigma^- \rightarrow n\pi^-$ ,  $\Lambda \rightarrow n\pi^0$ ,  $\Sigma^0 \rightarrow \Lambda\gamma$ .
- Polarization of decay products from hyperon decays as in:  $\Sigma^0 \rightarrow \Lambda\gamma$ ,  $\Xi^0 \rightarrow \Lambda\gamma$ ,  $\Xi^0 \rightarrow \Sigma^0\gamma$ ,  $\Xi^0 \rightarrow \Sigma^+e^-\bar{\nu}$ ,  $\Xi^0 \rightarrow \Lambda\pi^0$ .
- Production of anti-hyperons:  $\bar{\Lambda}$  and  $\bar{\Xi}^0$
- The decay  $\Xi^0 \rightarrow \Lambda\pi^0$  with  $\Lambda \rightarrow pe^-\bar{\nu}$  and the decay  $\Xi^0 \rightarrow \Lambda\pi^0$  with  $\Lambda \rightarrow p\mu^-\bar{\nu}$
- The decay  $\Xi^0 \rightarrow \Sigma^+\mu^-\bar{\nu}$

By “polarization”, we mean the ensemble average of the polarization vector of the particle in its own rest frame. The magnitude of this polarization vector is equal to the amount of polarization, so a polarization of  $\vec{P}_\lambda = 1.0\hat{z}$  refers to 100% polarization in the z-direction in the particle’s rest frame.

---

<sup>1</sup>A flat phase space generator chooses random directions and momenta for the decay products which conserve the 4-momentum.

### 7.2.1 Distribution of the Decay Products

#### Hyperon Non-Leptonic Decays

For decays of the type  $B \rightarrow B'\pi$ , where  $B$  and  $B'$  are initial and final state baryons, the final state baryon is distributed according to

$$\frac{1}{4\pi} \frac{d,}{d\Omega_{B'}} = \frac{1}{4\pi} (1 + \alpha \vec{P}_B \cdot \hat{p}_{B'}) \quad (7.4)$$

where  $\alpha$  is the decay symmetry,  $\hat{p}_{B'}$  is the unit vector of the final state baryon in the rest frame of initial state baryon, and  $\vec{P}_B$  is the polarization vector of the initial state baryon. The numerical values of  $\alpha$  for these decays can be found in [28]. The decays which implemented this were:

$$\Lambda \rightarrow p\pi^-, \Xi^0 \rightarrow \Lambda\pi^0, \Sigma^+ \rightarrow p\pi^0, \Sigma^- \rightarrow n\pi^-, \Lambda \rightarrow n\pi^0$$

For anti-hyperon non-leptonic decays, the same formula for decay distribution was used with the replacement  $\alpha \rightarrow \leftrightarrow\alpha$  [39].

#### Hyperon Semi-Leptonic Decays

The hyperon semi-leptonic decays  $\Lambda \rightarrow pe^-\bar{\nu}$  and  $\Xi^0 \rightarrow \Sigma^+e^-\bar{\nu}$  are three body decays, and hence there are 5 free parameters of the decay. We used the solid angles of the electron and neutrino and the energy of the electron,  $\Omega_{\bar{\nu}}$ ,  $\Omega_e$  and  $E_e$ , in the rest frame of the parent baryon. A random point in this 5-d space was chosen, and the weight of the decay was determined from a formula in [25]. This weight was then compared with a properly normalized random number, and if that random number was less than the “weight” then the decay was generated, and if not, a new random point was chosen, thus for many events the distribution

of decay products follows from the physics form factors. The normalized weight of each event must be less than 0.28.

The form factors of the decays  $\Lambda \rightarrow pe^- \bar{\nu}$  and  $\Xi^0 \rightarrow \Sigma^+ e^- \bar{\nu}$  were the SU(3) calculated values at  $q^2 = 0$  (Sec. 1.3.1).

For anti-hyperon semi-leptonic decays, the same decay formulae were used.

## 7.2.2 Polarization of the Decay Products

### Polarization of $\Sigma^+$ from $\Xi^0 \rightarrow \Sigma^+ e^- \bar{\nu}$

The polarization of the  $\Sigma^+$  from  $\Xi^0 \rightarrow \Sigma^+ e^- \bar{\nu}$  is determined by an approximation formula which can be found in [26]. No recoil approximation was used and the polarization of the target  $\Xi^0$  was neglected.

The magnitude of the  $\Sigma^+$  polarization vector should be equal to

$$|P_{\Sigma^+}^{\vec{}}| = \frac{8x}{3 + 9x^2} \sqrt{1 + x^2} \quad (7.5)$$

where  $x = g_1/f_1$ .

Anti-hyperon semi-leptonic decays used the same formulae as for hyperons.

### Hyperon Non-Leptonic Decays

For the decay  $\Xi^0 \rightarrow \Lambda \pi^0$ , where the  $\Lambda$  decays into  $p\pi^-$ , the polarization of the  $\Lambda$  is determined by the expression

$$\vec{P}_f = \frac{(\alpha + \vec{P}_i \cdot \hat{u})\hat{u} + \beta(\vec{P}_i \times \hat{u}) + \gamma(\hat{u} \times (\vec{P}_i \times \hat{u}))}{1 + \alpha\vec{P}_i \cdot \hat{u}} \quad (7.6)$$

Where  $\alpha, \beta, \gamma$  are decay parameters,  $\vec{P}_i$  and  $\vec{P}_f$  are the polarizations of the initial and final state baryons, and  $\hat{u}$  is the direction vector of the final state baryon in the rest frame of the initial state baryon.

For anti-hyperon non-leptonic decays, the same formulae are used with the replacement  $\alpha \rightarrow \Leftrightarrow\alpha$ ,  $\beta \rightarrow \Leftrightarrow\beta$ ,  $\gamma \rightarrow \gamma$  [39] .

### 7.3 Detector Response

Once the MC event was generated as described in the previous section, the detector response must be simulated as the next step. In addition, the response had to be correctly digitized so that analysis codes would work for both the real data and the MC generated data in a same manner. Especially for the CsI DPMT's, the simulation of digitization was a crucial task to reproduce the calorimeter response. This section describes the simulation of responses in the major detector elements.

#### 7.3.1 Drift Chambers

When charged particles traveled through the drift chambers, the drift distance, *i.e.* the distance from the particle trajectory to the closest wire in each of the two complementary planes, was converted to a drift time. The conversion factor was calibrated from the data so that the sum of drift distances in the two complementary planes (SOD) equaled 6.35 mm (Section 5.3). The drift time was smeared based on the calibration results to simulate 100  $\mu\text{m}$  resolution, and was recorded as TDC counts. The inefficiency for each plane was implemented by not recording the hit information randomly. Only the earliest hit in multiple hits was recorded

if they were within the same time window of 235 nsec.

The  $\delta$ -ray emission in the chamber gas was simulated as follows. First, when a relativistic particle passes through a  $L(\text{m})$  long material with Atomic Number  $Z$  and Mass number  $A$ , the emission probability is

$$P = 154(\text{KeV}) \times \frac{Z}{A} \times d(\text{g/cm}^3) \times L(\text{cm}) \times \frac{1}{E} ,$$

where  $d$  is the density of the material, and  $E$  represents the  $\delta$ -ray energy. With this probability,  $P$ , a  $\delta$ -ray was emitted perpendicular to the parent particle trajectory. Its range was determined based on the emitted energy. If the electron emitted as the  $\delta$ -ray was stopped outside the original cell, the flight distance was considered as the size of the cell. Finally, the distance from the  $\delta$ -ray to the closest wire was computed. The hits due to the  $\delta$ -rays were also recorded by the same method used for normal charged particles. The resulting hit information was used in the level 1 trigger for DC1 and DC2 simulation, which counted the number of hits in the defined in-time window (235 nsec).

There was a calibration task to extract the ionization density of the gas by fitting an empirical function to the data. This ionization density was used by the MC to simulate the so called high SOD problem in the experiment to some extent.

### 7.3.2 The Trigger Hodoscopes

When a charged particle hit the trigger hodoscope, the latch bit corresponding to the firing counter was set based on the efficiency of the counter measured from the data. The latch bits were used to simulate the first level triggering.

### 7.3.3 CsI Calorimeter

The simulation of the CsI calorimeter first determined the energy deposited in each crystal, based on the type, energy, and position of a particle hitting the calorimeter. Once the deposited energy was determined for an event, the scintillation light yield was simulated and digitized. The triggering elements,  $E_{tot}$  and HCC were also simulated using the result of the simulation of the calorimeter.

#### Showers in the CsI crystals

For the MC simulation, when electrons or photons reached the front face of the CsI, the transverse position was defined at shower mean depth approximated by;

$$z_e = 0.11 + 0.018 \times \ln E ,$$

$$z_\gamma = 0.12 + 0.018 \times \ln E ,$$

where  $E$  is the energy of the electron or the photon in GeV, and  $z$  in meters is the depth downstream of the front face of the crystal.

Using the transverse position and energy of electron or photon as inputs, the energy deposited in the CsI crystals was derived from the lookup tables referred to as the “shower library”. The shower library was created in advance by collecting the CsI response of electrons in  $K_{e3}^0$  events for which the position and momentum were measured by the spectrometer.

The showers were segmented in depth ( $z$ ) into 25 slices. They were also binned in 6 energy slices: 2, 4, 8, 16, 32 and 64 GeV, and binned in position. Each  $2.5 \text{ cm} \times 2.5 \text{ cm}$  crystal had six sizes of the position bins, varied from  $0.2 \text{ mm} \times$

0.2 mm to 0.7 mm  $\times$  0.7 mm with a difference of 0.1 mm with respect to the length of the side. The shower library was composed of  $13 \times 13$  small (2.5 cm  $\times$  2.5 cm) CsI crystal arrays. The segmentation in  $z$  was intended to correct for the position dependence along  $z$  of the light yield in each crystal. The correction factor was obtained before the installation of the CsI crystals by using cosmic ray muons. Once a sample shower was picked from the shower library, the energy scale was normalized to the original energy of the particle incident to the CsI.

The same shower library was used for both 2.5 and 5.0 cm crystals. If any 5.0 cm crystals were present in the shower, they were treated as four 2.5 cm crystals. This simplified the treatment around the boundary between the two different crystal sizes.

For charged pions reaching the face of the CsI, the calorimeter response was derived from a shower library created by GEANT simulation. The same shower library information was also used to simulate the energy from pions deposited in the HA.

For a muon, deposited energy was determined by Landau distribution based on  $dE/dx$  in the 50 cm long CsI crystals. Muons deposited only a minimum ionization energy in the calorimeter.

After determining the energy deposited in each crystal, the Monte Carlo simulated the digitization process. It started with the simulation of the scintillation light yield, and then the light was converted to a charge. Finally, the charge was digitized to ADC counts.

### **$E_t$ and HCC**

The energy deposited in each crystal was used as an input to the Energy Total ( $E_t$ ) and HCC simulation. Only the energy in the in-time slice was used for the  $E_t$  simulation. Summing over the energy for the whole calorimeter formed the  $E_t$  signal, to which a threshold was applied. HCC was simulated by tabulating crystals whose in-time energy was above the HCC threshold. The completed table was sent to the cluster counting algorithm described in Section 2.6.

## **7.4 Accidental Activity**

Accidental activities in the various parts of the detector had to be added to each single MC generated event. To simulate the accidentals, the data collected from the Accidental Trigger were overlaid on the MC generated events as follows. After the event generation, all the detector's response was recorded as ADC counts, TDC counts and latch bits by digitization. Then, the digitized quantities in an accidental data were added to the MC data. ADC counts were simply added together, latch bits were or-ed, and only the first hit in TDC reading was kept. Once the accidental data were appended, the trigger requirements were applied by reading the trigger sources as implemented in the hardware.



## Chapter 8

### Systematics

There were several sources of systematic errors in this analysis.

The trigger system contribution which was mainly due to inefficiency of the trigger elements and the fact that the events used to measure the branching ratio of the  $\Xi^0$  beta decay came from two different trigger sources, introducing some possible systematic effects.

The systematics due to selection of the cut values for both the signal and normalization modes reflects the uncertainty in the detector calibration, Monte Carlo imperfection, and the background level.

In order to find the systematic errors for the branching fraction of Cascade Beta Decay, we studied the efficiency of all the trigger elements during the entire data taking period which is described first. The trigger functionality was found to be fully reliable.

In Section 8.6, we present a method we used to estimate the contribution of cut variations in the systematic errors. This turned out to be the dominant contribution to the systematics. The uncertainties due to background subtraction and Monte Carlo acceptance corrections also contribute to the systematics.

Finally, various consistency checks on the final result will be discussed.

## 8.1 Hole Counters

By looking at events with an extrapolated track traveling down the beam hole and selected by an accidental event trigger, the efficiency of the hole counters was measured over the entire data taking period to be stable at  $95 \pm 1$  % for charged particles traveling down the beam hole. A possible systematic effect induced by such an efficiency on the ratio of acceptance between the two  $\Xi^0$  decay modes was calculated. Events selected as  $\Xi^0 \rightarrow \Lambda\pi^0$  decays and events selected as  $\Xi^0 \rightarrow \Sigma^+e^-\bar{\nu}_e$  decays have been used in that study. The assumption of an efficiency of 90 % for the two top half hole counters and 100 % for the other two halves, led to a shift smaller than 0.7 % and below the statistical errors on the ratio of acceptance between the two modes. Since such a difference in the hole counters is an extreme figure, no systematic contribution to the systematic error on the branching ratio measurement need to be taken into account from this shift.

## 8.2 Hadron Anti

The hadron anti detector was only used in the “ $\Xi^0$ -beta-trigger”. Thus its inefficiency was important to know because of the direct effect it has on the calculation of the  $\Xi^0$  beta decay branching ratio. Events, mostly  $K_L \rightarrow \pi^\pm e^\mp \nu_e$  events ( $K_{e3}^0$ ’s), have been extracted from the data selected by the hyperon minimum bias trigger. The energy deposited by these events in the CsI calorimeter was coming from the electron. Therefore, any hadron anti activity could come from residual out of time hadronic activity or from possible  $\pi$  shower back-splash on the back anti calorimeter. It was assumed that, at the precision level of the analysis, back-splash effects

from  $\pi$  were fairly similar to those from protons. From 15524 events with the  $\pi^+$  going through the beam hole, only 154 had the hadron anti high threshold latch bit of the first trigger level set on leading to an inefficiency of 1 %.

### 8.3 Total Energy in the Calorimeter

Simulated  $\Xi^0$  beta decays have a total energy of greater than 20 GeV deposited in the calorimeter. Figure 6.19-(a) shows the sum of energy of the electron and the two photons, for the selected  $\Xi^0 \rightarrow \Sigma^+ e^- \bar{\nu}_e$  events in the data. It agrees with the simulated results. For the summer run, “ $\Xi^0 \Leftrightarrow beta \Leftrightarrow trigger$ ” used the second lowest hardware threshold of Energy Total that accepts events with total energy deposited of at least 18 GeV.

In order to determine the efficiency of this element in the trigger, we looked at the hyperon-minimum-bias trigger (prescale of 20 000), which did not require any cuts on the total energy, for about 450 000 events over the entire run.

By counting the number of times the energy total latch bit in the first level trigger source was on, we measured the efficiency to be  $(0.999 \pm 0.001)$  for events with total energy of greater than 20 GeV deposited in the calorimeter (Fig 8.1 top plot).

### 8.4 Hardware Clustering

The “ $\Xi^0 \Leftrightarrow beta \Leftrightarrow trigger$ ” selected only events with one to four online hardware clusters in the CsI calorimeter. The measurement of the efficiency of such a requirement has been checked with about 450k events selected from the online

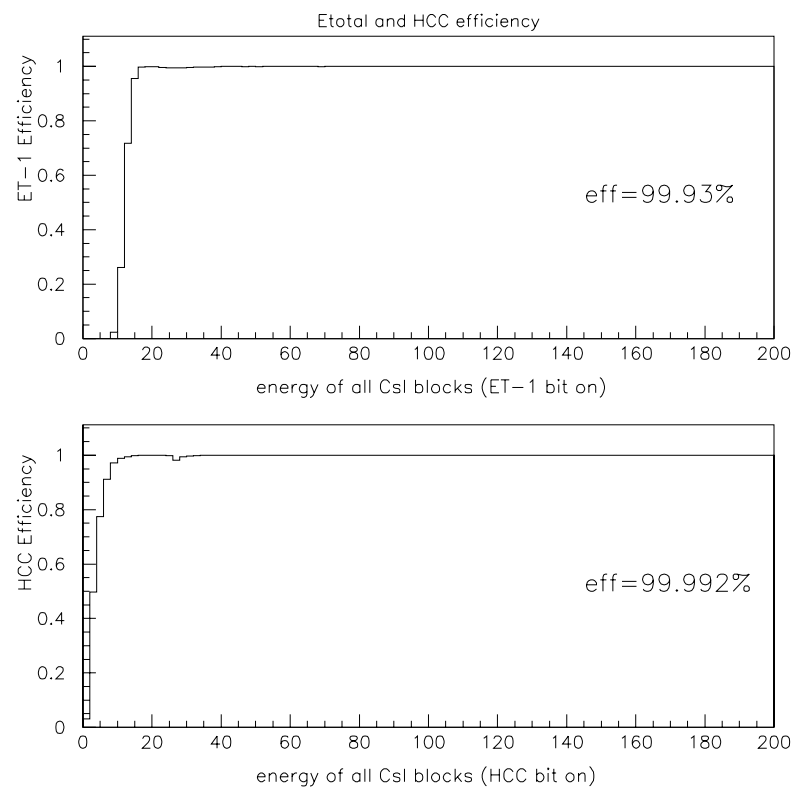


Figure 8.1: Energy total and HCC efficiency

hardware cluster minimum bias trigger (prescale of 20000). This trigger had the hardware cluster information read but no cut was applied.

Similar to Energy Total efficiency measurement, we checked the number of times that the level 1 trigger source latch bits were on. In Fig. 8.1 (bottom plot), the probability to have at least one online hardware cluster was given as a function of the deposited total energy.  $(99.9 \pm 0.1)$  % of the time this condition was fulfilled for events with more than 20 GeV deposited in the CsI calorimeter. Since the signal events had at most three CsI clusters, and since the probability to have fake noisy on-line clusters was extremely small, it was assumed that the condition to have a maximum of four online hardware clusters was fulfilled most of the time for both signal and normalization events and at an equal rate. Simulation confirmed such an assumption. The contribution of this trigger element to the systematic error on the branching ratio can also be neglected.

## 8.5 Drift Chamber Fast OR

The drift chamber FAST-OR (Sec. 3.1.1) was used in the first trigger level in combination with the hole counters to select events with a possible track going down a CsI beam hole. This FAST-OR used vertical wire ( $x$ -view) signals from the first two drift chambers. Its efficiency, defined as the average of the right and left hole efficiencies was measured by looking at tracks that went down the beam holes and that were selected by the hyperon minimum bias trigger which did not use the FAST-OR system. For tracks known to be in the beam hole area because of signal in the drift chamber wires related to this region, the latch bits of the first trigger

level of FAST-OR for both chambers were checked. Figure 8.2 shows the drift time distribution of hits on the tracks for the beam regions (histogram) and the similar distribution of the hits for which the FAST-OR system was inefficient (shaded histogram). These distributions are shown for each beam hole (upper plots) and as a combination of both beam holes. The last plot shows the corresponding extracted inefficiencies in %. From this plot an average efficiency of  $(0.995 \pm 0.001)$  is measured.

More detailed studies were done to understand the trend in the FAST-OR efficiency as presented in Figure 8.2. Since the FAST-OR signals basically consisted of signals from the drift chambers, any inefficiencies in this system could be highly correlated with inefficiencies in the chambers. As seen from the plots, the right (East) hole is more inefficient (1.1%) than the left (West) hole (0.1%) for the summer run. Looking at similar efficiency plots for each run number shows the same behavior, suggesting no particular range of runs responsible for that. Furthermore, we saw exactly the same effect in the winter run.

The TDC plots for both DC1 and DC2 left and right holes were also investigated. We concluded that the inefficiency in the right hole almost entirely came from DC2 (a right hole signal is “AND” of a DC1-right and a DC2-right signal), suggesting more extra activities in that area of chamber 2. A noisy wire would set the FAST-OR on before the real hit gets there. Since FAST-OR stretched a signal for about 90 nsec, it would miss the real hit. Figure 8.3 shows this effect. We were able even to specify a single noisy wire in that region using the above model. However, this was a very small effect which didn’t cause any bias in our analysis.

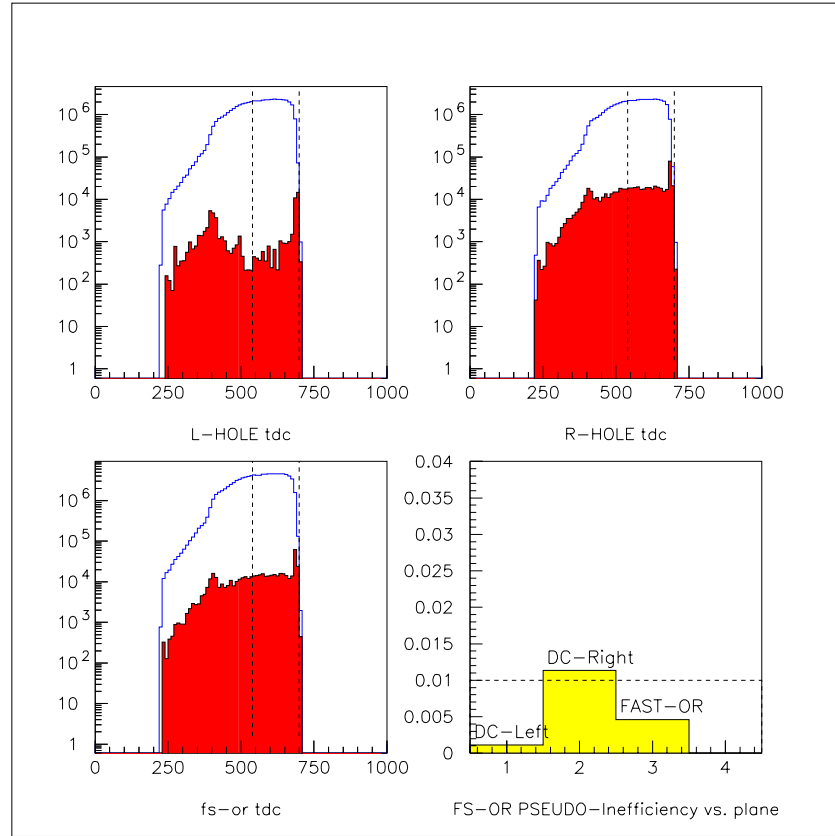


Figure 8.2: Drift chamber FAST-OR efficiency. Upper plots: hit wire distribution for track traveling down the left (west) and right (east) holes. Shaded, the corresponding distribution is shown for the tracks with no FAST-OR trigger latch bits set. Bottom plots: Same distribution for the OR of the holes and calculated inefficiencies in % from these previous three plots.

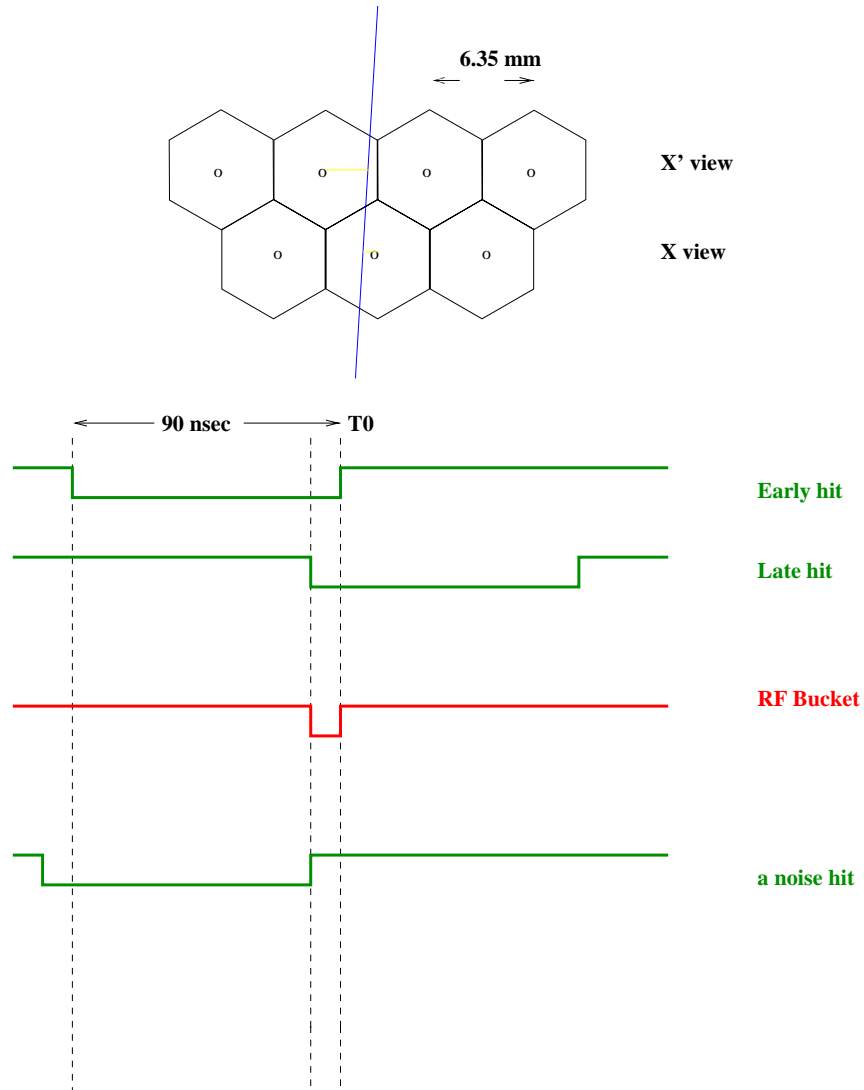


Figure 8.3: A DC signal from a real track is in coincidence with an RF signal. The top plot shows a track passing very close to a sense wire in the  $X$  plane of a chamber causing an early hit. The same track would be close to the edge of a cell in the  $X'$  plane causing a late hit. A noisy wire can set the FAST-OR on too early making the real hit miss the RF bucket. FAST-OR stretches a signal to about 90 nsec to cover any hits in a DC cell.



Moreover, the quoted FAST-OR efficiency is rather conservative. For the range of momentum which protons had in the hyperon data, this efficiency is estimated to be above  $(99.8 \pm 0.1)\%$ .

## 8.6 Cut Variation Studies

We used a set of “nominal” cuts for the  $\Xi^0 \rightarrow \Sigma^+ e^- \bar{\nu}_e$  signal and another set for the normalization mode  $\Xi^0 \rightarrow \Lambda \pi^0$  to measure the branching ratio as discussed in Chapter 6. These nominal sets of cuts were suggested by the Monte Carlo simulation of both modes, the kinematics of the decays, and how well they could reduce the background level. However, the exact choice of cuts is rather arbitrary and one could come up with another sets of similar but different cuts. Also updating the calibration constants in the database and modifying the Monte Carlo could slightly affect the function of the cuts. To determine the systematic error associated with the choice of the cuts, we calculated the branching ratio 100 times with 100 different sets of cuts for the signal and the normalization mode. Instead of assigning a fixed lower and upper limit value for each cut, reasonable windows (about 5-10%) of cuts around the nominal values were defined. A random value was picked within the cut windows for each cut. Doing this 100 times, Figure 8.4 shows the distribution of the measured branching ratios for the each set of cuts. If one fits a gaussian to this distribution, the mean should be around the measured branching ratio for the nominal set of cuts and the sigma of the gaussian fit would be a measure of the systematic error. As can be seen from Figure 8.4, the mean value of  $2.56 \times 10^{-4}$  is in agreement with the measured value of  $2.61 \times 10^{-4}$ .

However, there are statistical errors associated with each number, and the MC simulation was not perfect. To take these into account, we generated another sample of MC with almost the same size as the data sample and repeated the above procedure. The sigma of the gaussian fit in Figure 8.5 has to be subtracted from the sigma in Figure 8.4 in quadrature which results in  $0.12 \times 10^{-4}$  (about 4.6%) for the systematic uncertainty due to the cut variations.

## 8.7 Background Subtraction and Acceptance Correction Uncertainty

In Section 6.4, a sideband background subtraction method was used for the branching ratio calculation. That is a valid procedure, if there is a uniform background. Since most of the background is well understood (Sec. 6.3), another approach would be to subtract the simulated background which is normalized to the measured flux and then use the sideband subtraction method. Repeating the calculation steps in section 6.4 with MC background subtraction (the dark grey area in Fig. 6.25), one finds 586 events (subtracting 40 background events) instead of 581 (subtracting 45 background events) events. Also, if we used different sidebands around the peak the number of background would change by as much as 40% leading to a 2.9% uncertainty in the branching ratio. Therefore, our best estimate of the number of background events in the signal mass peak is  $45 \pm 18$ .

The sensitivity of the beta decay acceptance to reasonable variations of the form factors was checked by changing the form factors and the momentum spectrum of  $\Xi^0$ . A change of 50% to the SU(3) predicted value of  $g_1/f_1 = 1.26$ , changes the

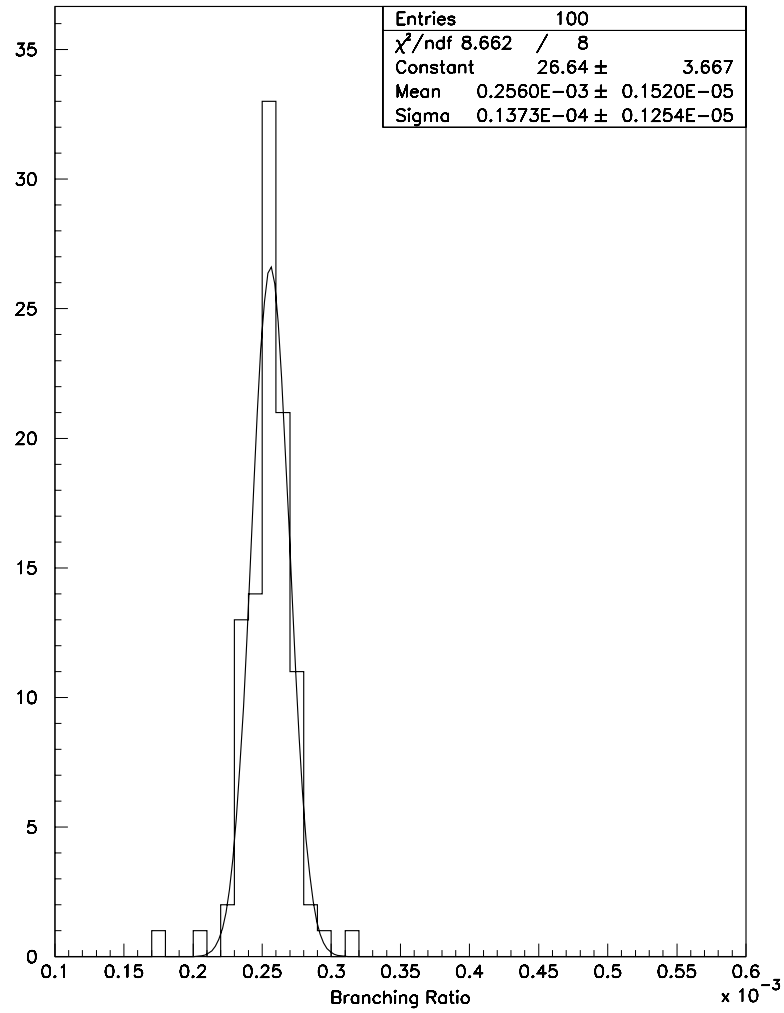


Figure 8.4: The distribution of branching ratio for 100 different sets of cuts applied on the data. The peak is around the measured branching ratio for the nominal set of cuts and the width of the gaussian fit is a measure of the systematic error.

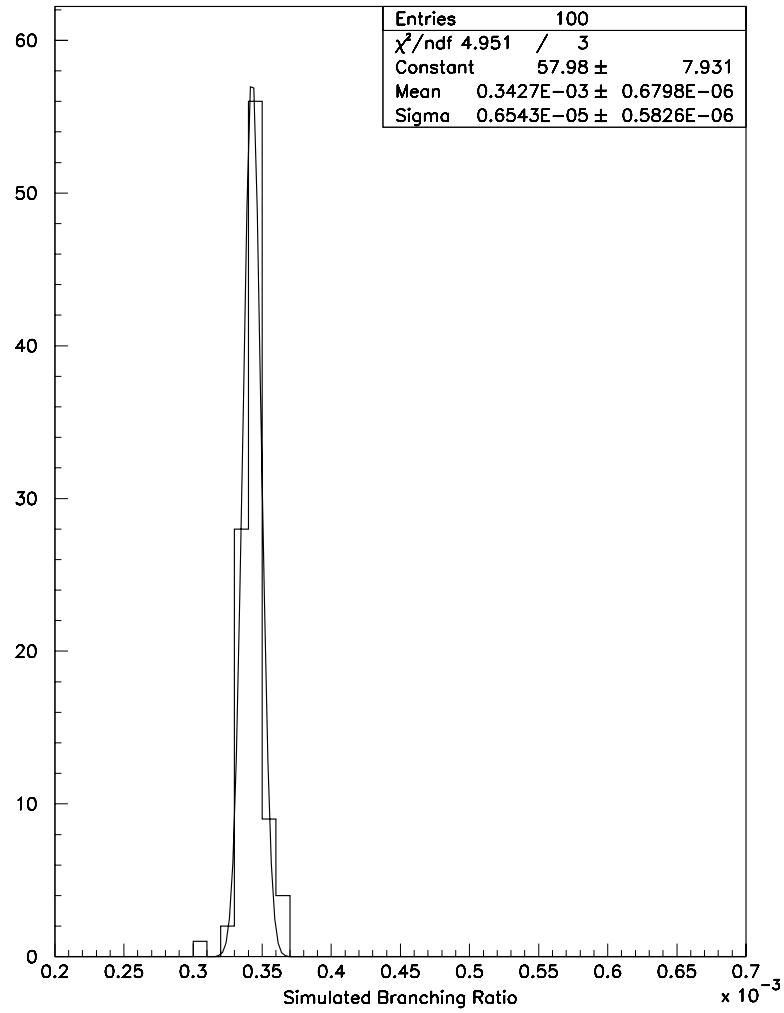


Figure 8.5: The distribution of branching ratio for 100 different sets of cuts applied on a Monte Carlo simulated sample. The width of the gaussian fit is a measure of the Monte Carlo imperfection.

beta decay acceptance by less than 2%.

## 8.8 Summary of the systamatics

The result of the systematic studies presented in this chapter is summarized in table 8.1. Adding the listed contributions in quadratures, we assign a systematic error of  $0.16 \times 10^{-4}$  for the BR measurement.

Systematic	$\times 10^{-4}$	in percent
uncertainty of cuts	0.12	4.6
background estimation	0.08	2.9
MC Acceptance	0.05	2.0
Trigger inefficiency	0.05	2.0
Total (quadrature)	0.16	6.1

Table 8.1: Summary of the systematic errors for the  $\Xi^0 \rightarrow \Sigma^+ e^- \bar{\nu}_e$  BR measurement.

We also performed several consistency checks on the branching ratio. The full sample of data was divided into 14 run ranges in a chronological order to investigate any aging of the apparatus or data acquisition problems. Figure 8.6 shows the branching ratio as a function of run time. The first point is the main result based on the entire data followed by 14 numbers representing different time periods. The error bars are statistical errors only. The fluctuations are within the known errors and no systematic biases are seen. The largest deviation from the

central value (a  $2.5 \sigma$  effect) corresponds to about 5% of the data known as the “day of summer data” which was selected and fully calibrated before the rest of the data became available. Even though this large deviation is not statistically unreasonable, a lot of investigation was done to look for any possible error or systematic bias. Nothing was found.

Furthermore,  $\Xi^0$  beta decay candidates selected with the “ $\Lambda$ -trigger” were used to extract a branching ratio. This method had the advantage of being trigger independent in the calculations since both the signal and normalization modes came from the same trigger. However, this trigger had a prescale of 50, so only 13 signal candidates were found. Applying the same techniques as before, a branching ratio of  $(2.19 \pm 0.61_{(stat.)}) \times 10^{-4}$  was measured in good agreement with our measurement  $((2.61 \pm 0.11_{(stat.)}) \times 10^{-4})$ .

To look for possible biases of the apparatus behavior, the data sample was separated in two beam regions. We found a branching ratio of  $(2.55 \pm 0.15_{(stat.)}) \times 10^{-4}$  for the West beam and a branching ratio of  $(2.65 \pm 0.15_{(stat.)}) \times 10^{-4}$  for the East beam.

The polarity of the analyzing magnet was flipped once a day to collect more or less the same number of events with both polarities. To look for magnetic field effects, the sample was separated by polarity sign of the analysis magnet. We found a branching ratio of  $(2.58 \pm 0.15_{(stat.)}) \times 10^{-4}$  for the magnetic field in the  $+y$  direction, and a branching ratio of  $(2.64 \pm 0.15_{(stat.)}) \times 10^{-4}$  for the magnetic field in the  $-y$  direction.

The above results are summarized in table 8.2. They are in a good agreement

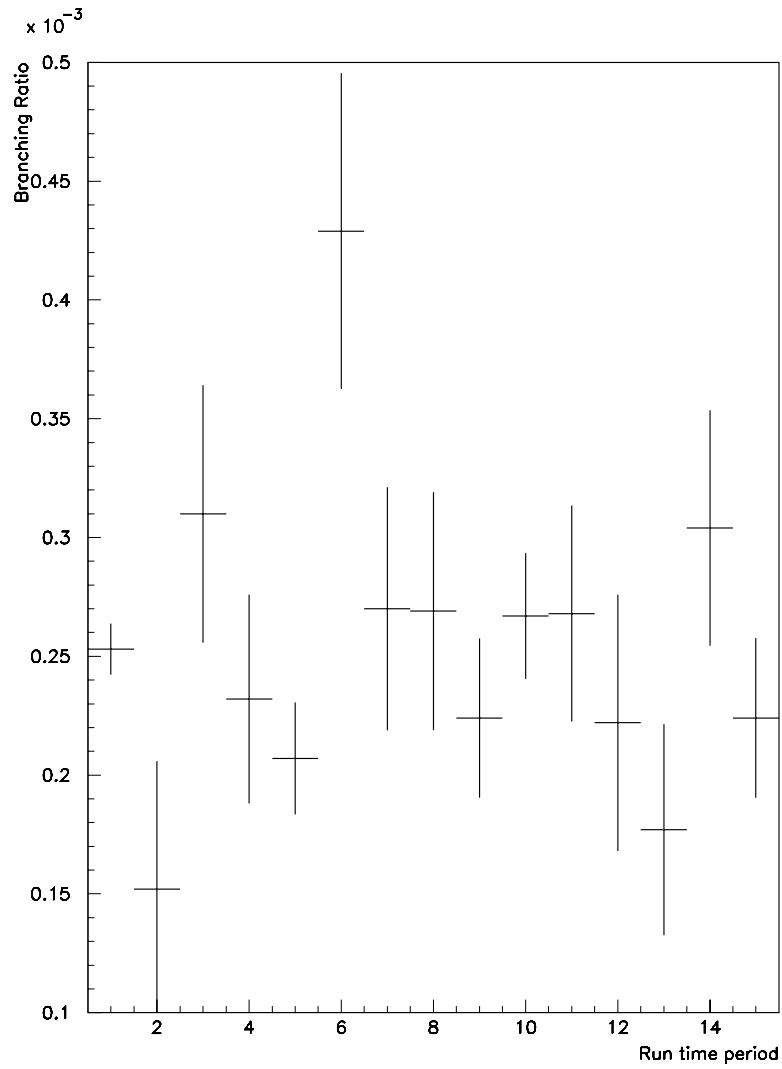


Figure 8.6: The measured branching ratio of  $\Xi^0 \rightarrow \Sigma^+ e^- \bar{\nu}_e$  decay as a function of time for 14 different run-ranges. The error bars are statistical only. The first point is the measured value for the full sample.

with the measured value within the statistical error.

Cut type	BR $\times 10^{-4}$	stat. err. $\times 10^{-4}$
Trigger 11 data	2.19	0.61
magnet polarity up	2.58	0.15
magnet polarity down	2.64	0.15
West beam	2.55	0.15
East beam	2.65	0.15

Table 8.2: Branching ratio for various separated data samples.



## Chapter 9

### Conclusion

The neutral Cascade beta decay,  $\Xi^0 \rightarrow \Sigma^+ e^- \bar{\nu}_e$  was observed for the first time by the KTeV collaboration at Fermilab. We measured a branching fraction of

$$(2.60 \pm 0.11_{(stat.)} \pm 0.16_{(sys.)}) \times 10^{-4}$$

from the E799-II experiment data, collected in the Summer of 1997 in agreement with our previous measurement of

$$(2.71 \pm 0.22_{(stat.)} \pm 0.31_{(sys.)}) \times 10^{-4}$$

from the earlier E799-II experiment data, collected in the Winter of 1997.

We used the principal decay of  $\Xi^0 \rightarrow \Lambda \pi^0$  where  $\Lambda$  decays to a proton and a  $\pi^-$  as the flux normalization mode. These measurements are in a good agreement with the Cabibbo model based on SU(3) flavor symmetry assumption for the Hyperon Semi-Leptonic Decays.

The branching fraction is directly related to the total decay rate of the decay which can be expressed in terms of a vector form factor  $f_1$ , and an axial-vector form factor  $g_1$  in the Cabibbo model. An independent ongoing measurement at KTeV is able to evaluate the  $g_1/f_1$  ratio by looking at the decay asymmetries with a precision of order 20 %.

Within the current precisions we may be able to verify or rule out some of the several models that predict the value of these form factors based on SU(3) symmetry breaking assumptions. The upcoming run of KTeV experiment in 1999 will increase the statistics, promising the possibility of a more precise measurement of the branching fraction and the form factor of  $\Xi^0 \rightarrow \Sigma^+ e^- \bar{\nu}_e$  decay.

## Appendix A

### First BR Measurement of the Decay $\Xi^0 \rightarrow \Sigma^+ e^- \bar{\nu}_e$

Cascade beta decay was observed for the first time during early data-taking of E799-II in the winter of 1997. In fact, some earlier Monte Carlo studies [79] had predicted this decay mode within capability of the KTeV experiment. During this period we collected 235 signal candidates as shown in Fig. A.1. A clear  $\Sigma^+$  mass peak is apparent, containing 183 events within  $\pm 15 \text{ MeV}/c^2$  ( $\pm 3$  standard deviations) of the  $\Sigma^+$  mass [28]. The gray region of the plot is the distribution for the primary predicted background, from  $\Xi^0$  decay, normalized to the beam flux. The tail of this distribution was estimated to contribute 7 events under the mass peak. After subtracting this known background from the mass distribution, the residual background was estimated to be negligible by counting events in two  $15 \text{ MeV}/c^2$  mass regions on either side of the peak ( $1.155\text{-}1.170 : 1.21\text{-}1.225$ ) GeV yielding a total sample of  $176 \pm 14 \Xi^0 \rightarrow \Sigma^+ e^- \bar{\nu}_e$  events.

We used the same technique as described in detail in Chapter 6 to extract the branching ratio. The trigger condition was slightly different [77] (also see Sec. 3.4). Figure A.2 shows 41 024 collected  $\Xi^0 \rightarrow \Lambda \pi^0$  events used as the flux normalization mode.

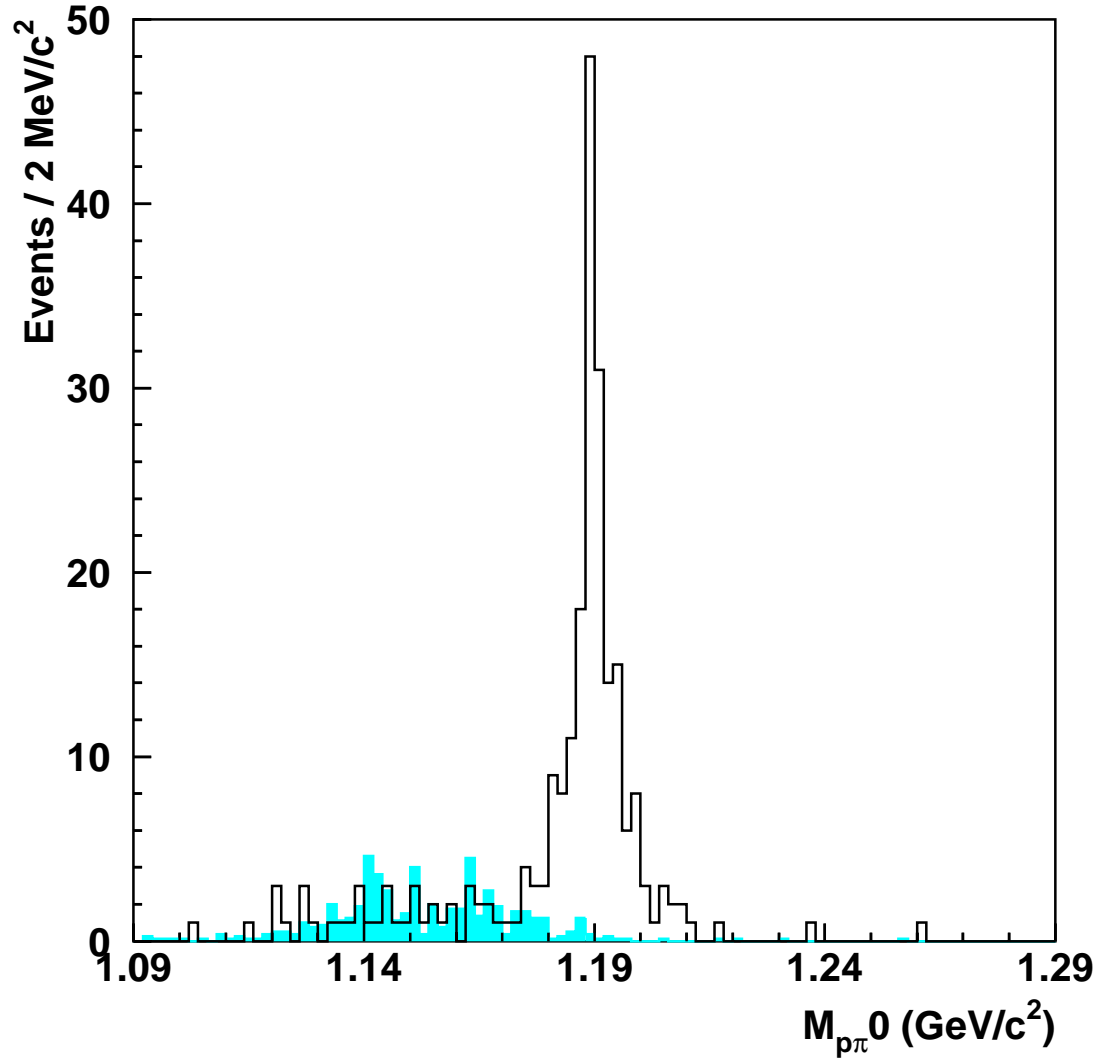


Figure A.1: Reconstructed  $p\pi^0$  mass distribution for the events selected for the first  $\Xi^0$  beta decay branching ratio measurement in the winter data. The parameters of a Gaussian fit on the data distribution are given.

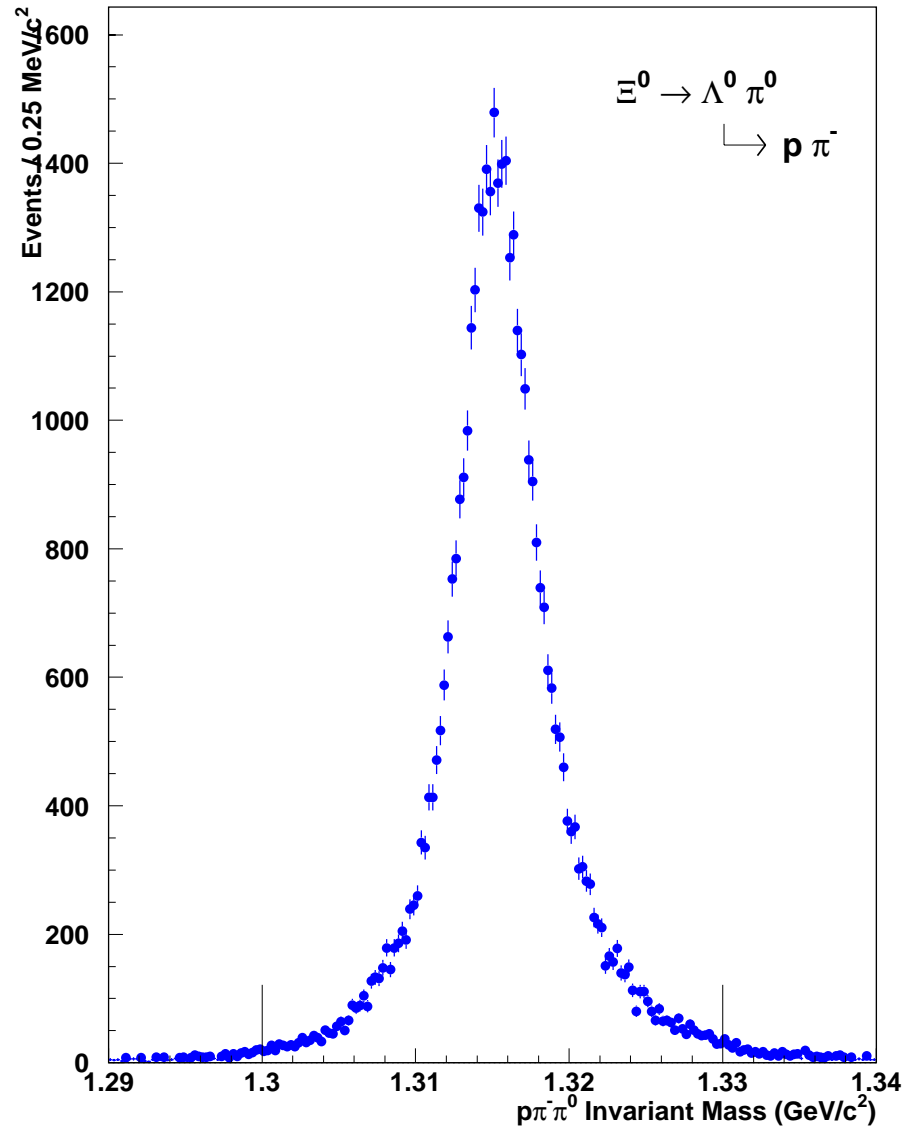


Figure A.2: Distribution of the reconstructed  $\Xi^0$  mass from  $\Xi^0 \rightarrow \Lambda^0 \pi^0$  candidates.

Monte Carlo studies gave a relative acceptance of

$$A(\Xi^0 \rightarrow \Sigma^+ e^- \bar{\nu}_e)/A(\Xi^0 \rightarrow \Lambda \pi^0) = 0.780 \pm 0.011_{(\text{stat.})} \pm 0.088_{(\text{syst.})}$$

Using this relative acceptance, the two event samples with their prescale factors, and known branching ratios [28], we found

$$BR(\Xi^0 \rightarrow \Sigma^+ e^- \bar{\nu}_e) = \frac{N(\Xi^0 \rightarrow \Sigma^+ e^- \bar{\nu}_e)}{N_{\text{total}}} = (2.71 \pm 0.22_{(\text{stat.})} \pm 0.31_{(\text{syst.})}) \times 10^{-4}$$

The first uncertainty is statistical and the second is systematic.

## Appendix B

### Kinematics With A Missing Particle

Both the hyperon beta decays in this experiment have a neutrino in the final state similar to the more familiar nuclear beta decay which can not be detected. Also in several of the hyperon analysis there are decays with a missing or ignored particle which contribute to the background. An example of the latter is the radiative decay of  $\Xi^0 \rightarrow \Lambda \gamma$  whose dominant background is the normal decay of  $\Xi^0 \rightarrow \Lambda \pi^0$  where one of the photons from the decay of  $\pi^0 \rightarrow \gamma \gamma$  is missing.

In the general situation, we have a parent particle with mass  $M$  and four momentum  $(E, \vec{P})$  which will decay into a set of reconstructible particles and one missing particle. Let  $m_u$  and  $p_u = (E_u, \vec{P}_u)$  be the mass and momentum of the unobserved particle. All of the reconstructed particles will be treated as a single system with an observed momentum  $p_o = (E_o, \vec{P}_o)$  and mass  $m_o$  defined as  $m_o^2 = E_o^2 \leftrightarrow p_o^2$ . All of the quantities with a superscript (\*) will refer to quantities in the center of mass of the decay particle. The energy and magnitude of momentum in the center of mass frame are of interest. Combining

$$P.P = M^2 = m_o^2 + m_u^2 + 2(E_o E_u \leftrightarrow \vec{p}_o \cdot \vec{p}_u) \quad (\text{B.1})$$

and

$$P.p_u = M E_u^* = m_u^2 + (E_o E_u \Leftrightarrow \vec{p}_o \cdot \vec{p}_u) \quad (\text{B.2})$$

we obtain

$$\begin{aligned} E_u^* &= \frac{M^2 \Leftrightarrow m_o^2 + m_u^2}{2M} \\ p_u^{*2} &= \frac{(M^2 \Leftrightarrow m_o^2 \Leftrightarrow m_u^2)/4 \Leftrightarrow m_o^2 m_u^2}{M^2} \end{aligned} \quad (\text{B.3})$$

In a fixed target experiment, the direction of vector of the decaying particle is known to be along the line of sight from the production target to the reconstructed decay vertex. The momentum of the missing particle transverse to this direction is the same as transverse momentum of the observed system  $\vec{p}_o$  which is an invariant measurable quantity. Thus the center of mass momentum of the missing particle along the direction of the decaying particle can be obtained

$$\begin{aligned} p_{u||}^{*2} = p_{o||}^{*2} &= p_u^{*2} \Leftrightarrow p_t^2 \\ &= \frac{(M^2 \Leftrightarrow m_o^2 \Leftrightarrow m_u^2)/4 \Leftrightarrow m_o^2 m_u^2}{M^2} \Leftrightarrow p_t^2 \end{aligned} \quad (\text{B.4})$$

This quantity is mostly sensitive to the measurement of  $p_t^2$  and should be positive. Although we have found the magnitude of the longitudinal component of momentum in the decay rest frame, we don't know whether the missing particle is aligned parallel or anti-parallel to the decay particle direction. This leads to a two-fold ambiguity in reconstructing the magnitude of the total momentum of the decay particle in the lab frame which can be verified by calculating P directly:

$$P.p_o = M E_o^* = E E_o \Leftrightarrow \vec{P} \cdot \vec{p}_o = E E_o \Leftrightarrow P p_{o||} \quad (\text{B.5})$$



After regrouping and squaring,

$$(E_o^2 \Leftrightarrow p_{o||}^2)P^2 \Leftrightarrow 2ME_o^*p_{o||}P + M^2(E_o^2 \Leftrightarrow E_o^{*2}) = 0. \quad (\text{B.6})$$

Using the more manifestly invariant form  $m_o^2 + p_t^2$  for  $E_o^2 \Leftrightarrow p_{o||}^2$  and solving for P, we obtain the boost expression

$$\gamma\beta = \frac{P}{M} = \frac{E_o^*p_{o||} \pm E_op_{o||}}{m_o^2 + p_t^2}. \quad (\text{B.7})$$

When the missing particle is massless, it e.g. neutrinos and photons, calculations can easily be done in the lab frame. In this case the momentum of the decaying particle will be the two-fold ambiguous solution of the quadratic equation

$$4(E_o^2 \Leftrightarrow p_{o||}^2)P^2 \Leftrightarrow 4p_{o||}(M^2 + m_o^2)P + [4E_o^2M^2 \Leftrightarrow (M^2 + m_o^2)^2] = 0 \quad (\text{B.8})$$

whose discriminant  $\Delta$  being

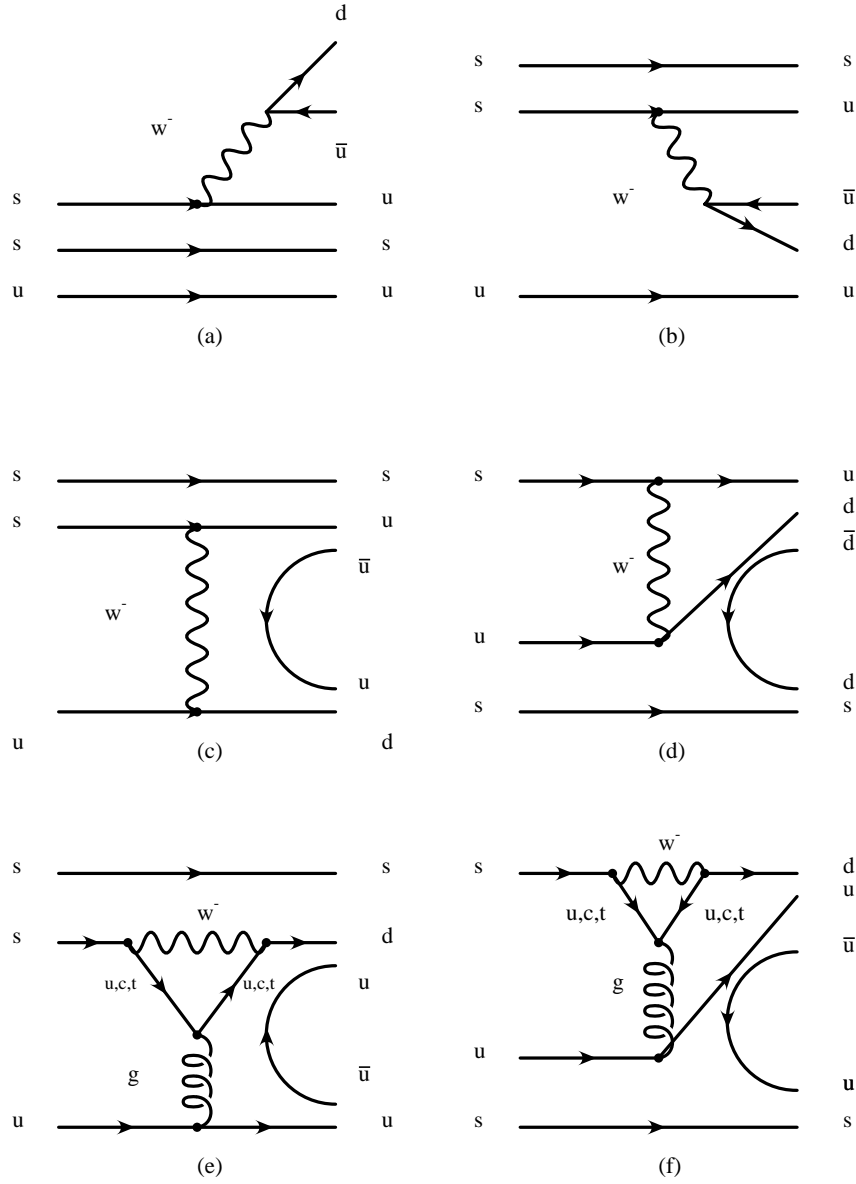
$$\Delta = 16E_o^2[(M^2 \Leftrightarrow m_o^2)^2 \Leftrightarrow 4M^2p_t^2] \quad (\text{B.9})$$

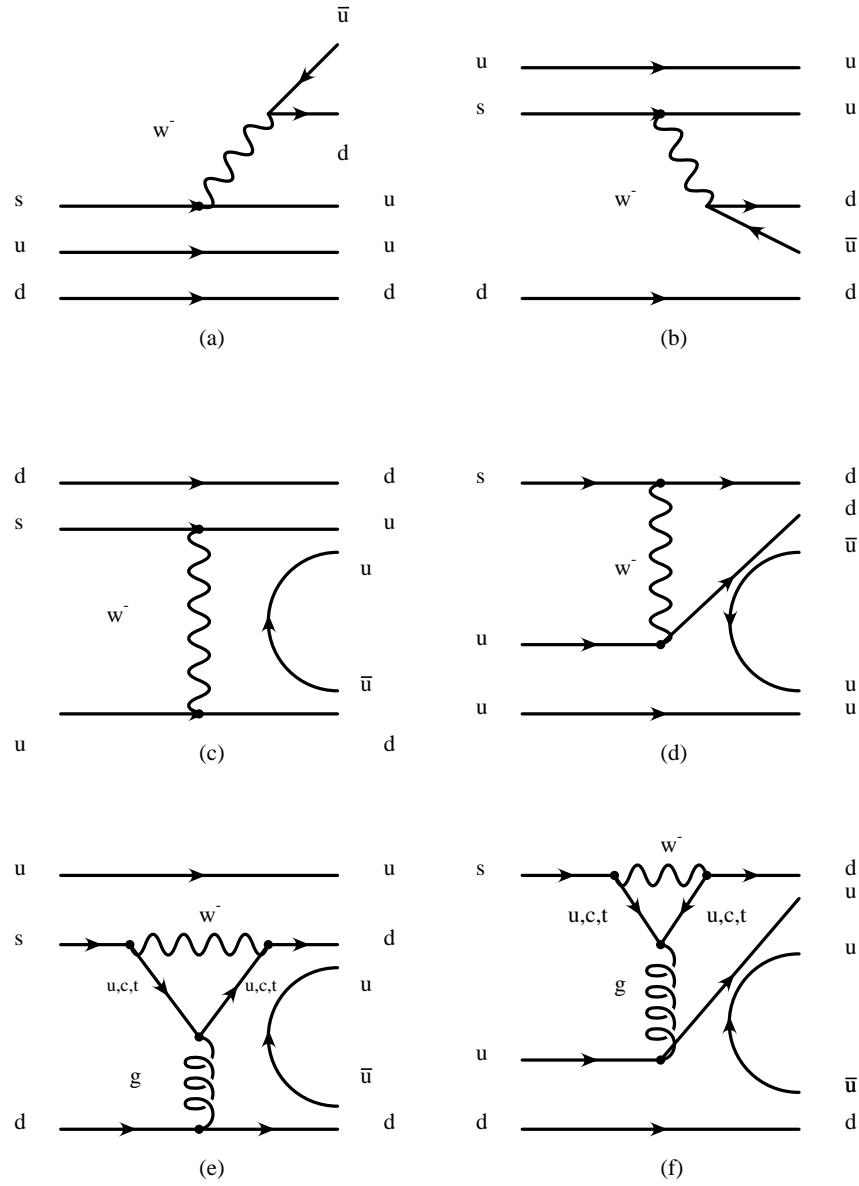
Again, the sign of  $\Delta$  is mostly sensitive to the measurement of  $p_t^2$ , and a negative  $\Delta$  means the missing particle won't be reconstructible.

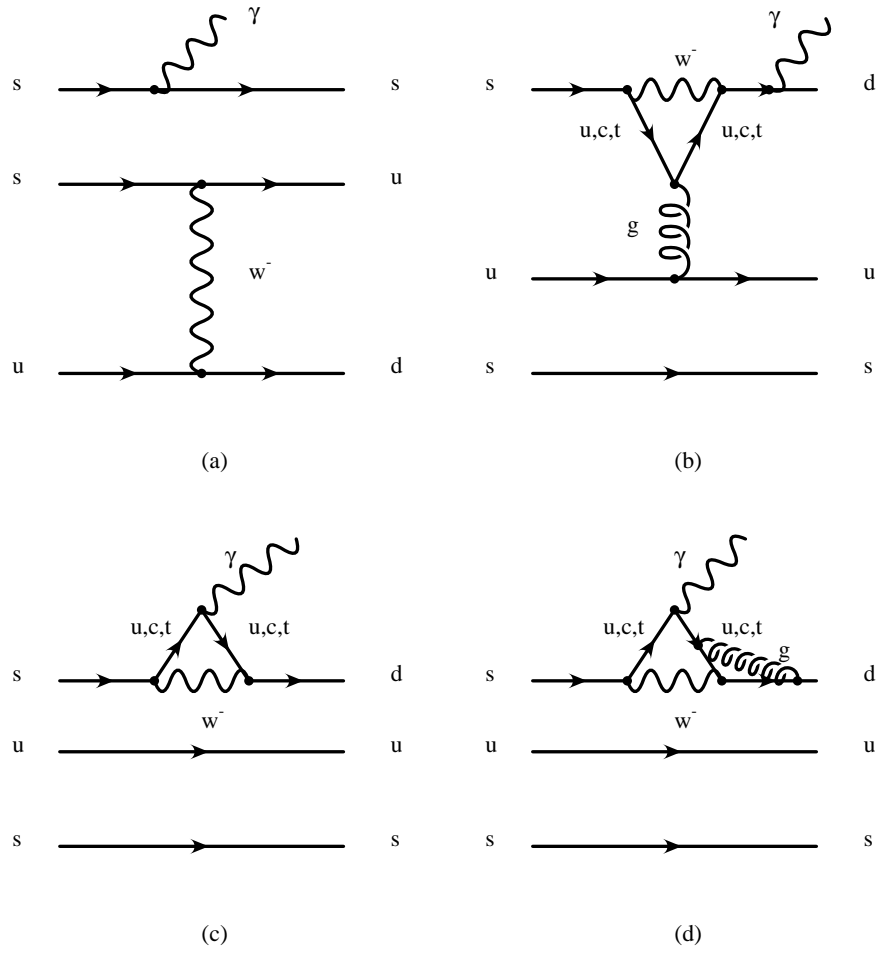
## Appendix C

# Feynman Diagrams of Non-Leptonic and Radiative Hyperon Decays

Feynman diagrams for the two-body non-leptonic decays of  $\Xi^0 \rightarrow \Lambda\pi^0$  and  $\Lambda \rightarrow p\pi^-$  discussed in Sec. 1.3.2 are presented in this Appendix. Also the Feynman diagrams for the weak radiative decays of  $\Xi^0 \rightarrow \Sigma^0\gamma$  and  $\Xi^0 \rightarrow \Lambda\gamma$  discussed in Sec. 1.3.3 are shown.

Figure C.1:  $\Xi^0 \rightarrow \Lambda \pi^0$

Figure C.2:  $\Lambda \rightarrow p\pi^-$

Figure C.3:  $\Xi^0 \rightarrow \Lambda \gamma$  and  $\Xi^0 \rightarrow \Sigma^0 \gamma$

## Appendix D

# Acronyms of Commonly Used Terms in Detector Control Systems

We present a list of the most commonly used terms in the Slow Control Systems.

- **AC:** Alternate Current
- **ADC:** Analog-to-Digital Conversion
- **AGP:** Advanced Graphics Port
- **AMD:** Active Matrix Display
- **ANSI:** American National Standards Institute
- **API:** Application Programming Interface
- **APT:** Application Productivity Tool
- **ASIC:** Application Specific Integrated Circuits
- **ATM:** Asynchronous Transfer Mode
- **BCD:** Binary-Coded Decimal

- **BIT3:** VME to VME inter-crate adaptors
- **CAMAC:** Computer Automated Measurement and Control
- **CAN:** Control Area Network
- **DAC:** Digital-to-Analog Conversion
- **DAQ:** Data Acquisition system
- **DA:** Data Acquisition
- **DB:** Data Base
- **DC:** Direct Current or Drift Chamber
- **DCS:** Detector Control System or Distributed Control System
- **DMA:** Direct Memory Access
- **DMACS:** Distributed Manufacturing Automation and Control Software
- **DRAM:** Dynamic Random Access Memory
- **DVD-ROM:** Digital Versatile Disk
- **ECL:** Emitter-Coupled Logic
- **EDA:** Easy Data Access
- **EDO-RAM:** Extended Data Out Random Access Memory
- **EMI:** Electro-Magnetic Interference

- **EPICS:** Experimental Physics and Industrial Control System
- **EPROM:** Erasable Programmable Read-Only Memory
- **EUROCARD:** European Packaging Specifications (IEC 60297, IEEE 1101.1, IEEE 1101.10, IEEE 1101.11)
- **FDDI:** Fiber Distributed Data Interface
- **FIFO:** First-In, First-Out shift registers
- **FIX:** Fully Integrated Control System
- **FSM:** Finite State Machine
- **FTMS:** Flexible Test Measurement System
- **FWHM:** Full-Width Half Maximum
- **GAC:** Geographical Address Control (in FASTBUS)
- **GPIB:** General Purpose Interface Bus
- **GUI:** Graphical User Interface
- **H-TMS:** High Performance Test Management System
- **HV:** High Voltage
- **IAC:** Inter-Application Communication
- **IC:** Integrated Circuit



- **IOC:** Input Output Controller
- **IOS:** Input Output Server
- **IPC:** Interprocess Communication
- **ISA:** Industry Standard Architecture; desktop PC,adapter board specification
- **ISO:** International Standards Organization
- **KS:** Kinetic Systems
- **LAN:** Local Area Network
- **LV:** Low Voltage
- **MCA:** Multi-Channel Analyzer (pulse height analyzer)
- **MLU:** Memory Lookup Unit
- **MMX:** Multimedia Extensions
- **MTBF:** Mean-Time Between Failure
- **MTTR:** Mean-Time To Repair
- **MURMUR:** Networked message reporting system
- **MUX:** Multiplexer
- **MXIbus:** Multi-system eXtension Interface bus from NI

- **NIM:** Nuclear Instrumentation Module
- **OCP:** Operator Control Program
- **ODMCS:** Open Distributed Monitoring and Control System
- **OPI:** Operator Interface
- **OS:** Operating System
- **PCI:** Peripheral Component Interconnect
- **PDT:** Program Data Transfer
- **PHA:** Pulse Height Analyzer
- **PISO:** Parallel-In Serial-Out shift register
- **PLC:** Programmable Logic Controller
- **PV:** Process Variable
- **PXI:** PCI eXtensions for Instrumentation
- **RAM:** Random Access Memory
- **RC:** Run Control
- **RF:** Radio Frequency
- **RFI:** Radio Frequency Interference
- **ROC:** ReadOut Controller

- **ROM:** Rear Only Memory
- **RPC:** Remote Procedure Call
- **RTD:** Resistance Temperature Detector
- **RTDB:** Real Time DataBase
- **SAD:** Simple Acquisition of Data (FNAL beam server)
- **SCA:** Single Channel Analyzer
- **SCADA:** Supervisory Control and Data Acquisition
- **SCC:** Smart Crate Controller (for CAMAC)
- **SCSI:** Small Computer System Interface
- **SCXI:** Signal Conditioning eXtensions for Instrumentation
- **SDRAM:** Synchronous Dynamic Random Access Memory
- **SIPO:** Serial-In Parallel-Out register
- **SNR:** Signal to Noise Ratio
- **SPC:** Statistical Process Control
- **SQL:** Structured Query Language
- **TCL/TK:** Tool Command Language/TK
- **TCP/IP:** Transmission Control Protocol/ Internet Protocol

- **TDC:** Time-to-Digital Conversion
- **TFT:** Thin Film Transistor
- **TTL:** Transistor-Transistor Logic
- **UART:** Universal Asynchronous Receiver/Transmitter
- **USB:** Universal Serial Bus
- **VISA:** Virtual Instrument Software Architecture
- **VITA:** VMEbus International Trade Association
- **VME:** Versa Module Europa
- **VPP:** VXIplug&play Specification
- **VSO:** VITA Standards Organization
- **VXI:** VMEbus eXtensions for Instrumentation
- **VxWorks:** real time operating system for embedded processors
- **WAN:** Wide Area Network

## Bibliography

- [1] K. Arisaka *et al.*, *KTeV Design Report*, FN-580 (1992)
- [2] W. Pauli, *Niels Bohr and the Development of Physics*. Pergamon Press, Elmsford, N.Y., (1955)
- [3] J. Schwinger, *Phys. Rev.* **91**, 713 (1953)
- [4] T.D. Lee and C.S. Wu, *Ann. Rev. Nuc. Sci.* **15**, 381 (1965)
- [5] T.D. Lee and C.N. Yang, *Phys. Rev.* **104**, 254 (1956)
- [6] C.S. Wu *et al.*, *Phys. Rev.* **105**, 1413 (1957)
- [7] R.L. Garwin, L.M. Lederman, and M. Weinrich, *Phys. Rev.* **105**, 1415 (1957)
- [8] J.I. Friedman and V.L. Telegdi, *Phys. Rev.* **105**, 1681 (1957)
- [9] R.P. Feynman and M. Gell-Mann, *Phys. Rev.* **109**, 193 (1958)
- [10] E.C.G. Sudarshan and R. Marshak, *Phys. Rev.* **109**, 1860 (1958)
- [11] T.D. Lee, R. Oehme, and C.N. Yang, *Phys. Rev.* **106**, 340 (1957)
- [12] L. Landau, *JETP* **5**, 336 (1957)
- [13] J.H. Christenson, J.W. Cronin, V.L. Fitch, and R. Turlay, *Phys. Rev. Lett.* **13**, 138 (1964)
- [14] M. Gell-Mann and A. Pais, *Phys. Rev.* **97**, 1387 (1955)
- [15] T.D. Lee, R. Oehme, and C.N. Yang, *Phys. Rev.* **106** 340 (1957)
- [16] T.T. Wu and C.N. Yang, *Phys. Rev. Lett.* **13** 380 (1964)
- [17] R.G. Sachs, *Ann. Rev.* **22** 239 (1963)
- [18] G.D. Barr *et al.*, *Phys. Lett.* **B317**, 233 (1993)
- [19] L.K. Gibbons *et al.*, *Phys. Rev. Lett.* **70**, 1203 (1993)

- [20] K. Hanagaki, *PhD thesis, Osaka University, Japan*, (1998)
- [21] M. Kobayashi and T. Maskawa, *Prog. Theory. Phys.* **49**, 652 (1973)
- [22] N. Solomey *et al.*, *KTeV Internal Note* **119**, (1993)
- [23] A. Alavi-Harati *et al.*, *KTeV internal note* **453**, (1997)
- [24] E. Monniere, *The 3rd Int. Conf. on Hyperons, Charm, and Beauty, Genoa, Italy* (1998) (Conference Proceedings to be published in Nucl. Phys. B)
- [25] A. Garcia and P. Kielanowski, *The Beta Decay of Hyperons. Lecture Notes in Physics*, **222**, Springer-Verlag (1985)
- [26] V. Linke, *Nucl. Phys.* **B12**, 669 (1969)
- [27] N. Cabibbo, *Phys. Rev. Lett.* **10**, 531 (1963)
- [28] Particle Data Group, C. Caso *et al.*, *Eur. Phys. J. C* **3**, 1 (1998)
- [29] E. Swallow, *Private notes*, (1998)
- [30] M. Ademollo, R. Gatto, *Phys. Lett.* **10**, 264 (1964)
- [31] M. Roos, *Phys. Lett.* **B246**, 179 (1990)
- [32] P. G. Ratcliffe, *Phys. Lett.* **B365**, 383 (1996)
- [33] R. Flores-Mendieta, E. Jenkins, and A. V. Manohar, *Phys. Rev. D* **58**, 094028 (1998)
- [34] J. Dai, R. Dashen, E. Jenkins, and A. V. Manohar, *Phys. Rev. D* **53**, 273 (1996)
- [35] J. Donoghue and R. Holstein, *Phys. Rev. D* **25**, 206 (1982)
- [36] J. Donoghue *et al.*, *Low-energy weak interactions of quarks*, *Phys. Rep.* **131**, 403 (1986)
- [37] E. Commins and P. Bucksbaum, *Weak interaction of leptons and quarks*, Cambridge University Press (1983)
- [38] G. Guglielmo, *PhD thesis, The University of Minnesota*, August 1994.
- [39] L.G. Pondrom, *Physics Report* **122**, 58 (1985)
- [40] Skubic, *et al.*, *Phys. Rev. D* **18**, 1355 (1978)

- [41] Ramberg *et al.*, *Phys. Lett.* **B338**, 403 (1994)
- [42] Lach, Zenczyskowski, *Int. Journal of Modern Physics* **A10**, 3817 (1995)
- [43] Timm, *et al.*, *Physical Review* **D51**, 4638 (1995)
- [44] Zenczyskowski, *et al.*, *Physical Review* **D44**, 1485 (1991)
- [45] Teige, *Physical Review Letters* **63**, 2717 (1989)
- [46] E. Ramberg, *The 3rd Int Conf on Hyperons, Charm, and Beauty, Genoa, Italy* (1998) (Conference Proceedings to be published in Nucl. Phys. B)
- [47] C. James, *et al.*, *Physical Review Letters* **64**, 843 (1990)
- [48] S. Barshay and R. Behrends, *Physical Review* **114**, 931 (1958)
- [49] Baggett, *et al.*, *Physis Letters* **B42**, 379 (1972)
- [50] Marshak, Riazuddin and Ryan, *Theory of weak interactions in particle physics*, John Wiley & Sons, Inc. (1969)
- [51] C. Alff, *et al.*, *Physical Review* **137**, B 1105 (1965)
- [52] Feinberg, *Physical Review* **109**, 1019 (1958)
- [53] V. Bocean, S. Childress, R. Coleman, R. Ford, D. Jensen, *KTeV Internal Note* **466** .
- [54] E. Bartz, *et al.*, *KTeV Internal Note* **190** (1994)
- [55] G. Graham, *et al.*, *KTeV Internal Note* **185** (1994)
- [56] N. Solomey, *KTeV Internal Note* **569** (1998)
- [57] A. Roodman, "The KTeV pure CsI calorimeter", *Proceedings of the VII International Conference on Calorimetry, Tucson, Arizona*, World Scientific (1998)
- [58] P. Shanahan, *Proceedings of ICHEP, Frascati, Italy* (1996)
- [59] A. Roodman, *Conference Record of ICHEP 96*, (1996)
- [60] N. Solomey *Private notes*, (1999)
- [61] S. Schnetzer, *KTeV Internal Note* **191** (1994)
- [62] R. Tesarek and S. Schnetzer, *KTeV Internal Note* **215** (1994)

- [63] R. Kessler, *KTeV Internal Note* **361**, (1996)
- [64] T. Alexopoulos, A. Erwin, and R. Kessler, *KTeV Internal Note* **207** (1994)
- [65] T. Alexopoulos and A. Erwin, *KTeV Internal Note* **264**. (1994)
- [66] G. Kassabian, H. Kobrak, R. Swanson, G. White, *KTeV Internal Note* **196**, (1994)
- [67] P. Mikelsons, *KTeV Internal Note* **347**, (1995)
- [68] P. Krolak, *et al.*, *KTeV Internal Note* **267**, (1994)
- [69] S. Bright, *KTeV Internal Note* **369**, (1996)
- [70] C. Bown, *et al.*, *Nucl. Inst. and Meth.* **A369**, 248 (1996)
- [71] P. Shawhan, *KTeV Internal Note* **328**. (1996)
- [72] A. Roodman, *KTeV Internal Note* **577**, (1998)
- [73] R.A. Briere, *PhD thesis, The University of Chicago*, (1995)
- [74] K.S. McFarland, *PhD thesis, The University of Chicago*, (1994)
- [75] V. O'Dell and T. Yamanaka, *KTeV Internal Note* **184**, (1994)
- [76] T. Alexopoulos *et al.*, *KTeV Internal Note* **256**, (1994)
- [77] A. Alavi-Harati *et al.*, *KTeV internal note* **453**, (1997)
- [78] A. Affolder *et al.*, *preprint FERMILAB-Pub-98/403-E* (to be published in Phys. Rev. Lett.)
- [79] A. A. Affolder, *A Monte Carlo study of the  $\Xi^0 \rightarrow \Sigma^+ e^- \bar{\nu}_e$  at KTeV*, *Bachelor's Thesis, The University of Chicago*, (1996)
- [80] A.J. Malensek, *Preprint FN-341, Fermi National Accelerator Laboratory*, (1981)
- [81] S. Bright, *Private notes*, (1997)